Imperial College London
Department of Earth Science & Engineering

Tarik M.A. Saif

Multi-scale Multi-dimensional Imaging and Characterization of Oil Shale Pyrolysis

A dissertation submitted in fulfilment of the requirements for the degree of Doctor of Philosophy

August 2017

Abstract

In recent years, oil shale has attracted renewed attention as an unconventional energy resource, with vast and largely untapped reserves. Oil shale is a fine-grained sedimentary rock containing a sufficiently high content of immature organic matter from which shale oil and combustible gas can be extracted through pyrolysis. Several complex physical and chemical changes occur during the pyrolysis of oil shale where macromolecular network structures of kerogen are thermally decomposed. The pyrolysis of oil shale leads to the formation of a microscopic pore network in which the oil and gas products flow. The pore structure and the connectivity are significant characteristics which determine fluid flow and ultimate hydrocarbon recovery. In this thesis, a state-of-the-art multi-scale multi-dimensional workflow was applied to image and quantify the Lacustrine Eocene Green River (Mahogany Zone) formation, the world's largest oil shale deposit. Samples were imaged before, during and after pyrolysis using laboratory and synchrotron-based X-ray Micro-tomography (μCT), Optical Microscopy, Automated Ultra-High Resolution Scanning Electron Microscopy (SEM), MAPS Mineralogy (Modular Automated Processing System) and Focused Ion Beam Scanning Electron Microscopy (FIB-SEM). Results of image analysis using optical (2-D), SEM (2-D), and μCT (3-D) reveal a complex fine-grained microstructure dominated by organic-rich parallel laminations in a tightly bound heterogeneous mineral matrix. MAPS Mineralogy combined with ultrafast measurements highlighted mineralogic textures dominated by dolomite, calcite, K-feldspar, quartz, pyrite and illitic clays. From high resolution backscattered electron (BSE) images, intra-organic, inter-organic-mineral, intra and inter-mineral pores were characterised with varying sizes and geometries. A detailed X-ray μCT study with increasing pyrolysis temperature (300-500°C) at 12 μm, 2 μm and 0.8 μm voxel sizes illuminated the evolution of pore structure, which is shown to be a strong function of the spatial distribution of organic content. In addition, FIB-SEM 3-D visualisations showed an unconnected pore space of 0.5% with pores sizes between 15 nm and 22 nm for the un-pyrolysed sample and a well-connected pore space of 18.2% largely with pores of equivalent radius between 1.6 μm and 2.0 μm for the pyrolysed sample. Synchrotron 4-D results at a time resolution of 160 seconds and a voxel size of 2 μm revealed a dramatic change in porosity accompanying pyrolysis between 390-400°C with the formation of micron-scale heterogeneous pores followed by interconnected fracture networks predominantly along the organic-rich laminations. Combining these techniques provides a powerful tool for quantifying petrophysical properties before, during and after oil shale pyrolysis. Quantitative 2-D, 3-D and 4-D imaging datasets across nm-μm-mm length scales are of great value to better understand, predict and model dynamics of pore structure change and hydrocarbon transport and production during oil shale pyrolysis.

Declaration of Originality

I hereby declare that this work is original research undertaken by me and that no part of this thesis has been submitted for consideration towards another degree at this or any other institution. Any work in this thesis which is not my own work has been properly referenced.

Tarik Saif
August 2017

Copyright Declaration

The copyright of this thesis rests with the author and is made available under a Creative Commons Attribution Non-Commercial No Derivatives licence. Researchers are free to copy, distribute or transmit the thesis on the condition that they attribute it, that they do not use it for commercial purposes and that they do not alter, transform or build upon it. For any reuse or redistribution, researchers must make clear to others the licence terms of this work.

Tarik Saif
August 2017

Publications

1. **Saif, T.**, Lin, Q., Butcher, A.R, Bijeljic, B. and Blunt, M.J., (2017). Multi-scale Multi-dimensional Microstructure Imaging of Oil Shale Pyrolysis using X-ray Micro-tomography, Automated Ultra-high Resolution SEM, MAPS Mineralogy and FIB-SEM, *Applied Energy*, 202, 628-647.

2. **Saif, T.**, Lin, Q., Bijeljic, B. and Blunt, M.J., (2017). Microstructural Imaging and Characterization of Oil shale before and after Pyrolysis. *Fuel*, 197, 562-574.

3. **Saif, T.**, Lin, Q., Singh, K., Bijeljic, B. and Blunt, M.J. (2016). Dynamic imaging of oil shale pyrolysis using Synchrotron X-ray micro-tomography. *Geophysical Research Letters*, 43(13), 6799-6807

4. **Saif, T.**, Lin, Q., Gao, Y., Al-Khulaifi, Y., Marone, F., Bijeljic, B. and Blunt, M.J., (2017). A 4-D *in situ* synchrotron X-ray tomographic microscopy and laser-based heating study of oil shale pyrolysis, in preparation for *Scientific Reports*.

5. **Saif, T.**, Lin, Q., Gao, Y., Al-Khulaifi, Y., Marone, F., Bijeljic, B. and Blunt, M.J., (2017). Hydrocarbon Recovery from Oil Shale Pyrolysis: Dynamic Multi-Scale Imaging using Synchrotron-based X-ray tomographic microscopy and a Laser-based Heating System, in preparation for *Journal of Visualized Experiments (JoVE)*.

6. **Saif, T.**, Lin, Q., Bijeljic, B. and Blunt, M.J., (2017). Imaging of Worldwide Oil Shales, in preparation for *Earth Science Reviews*.

Acknowledgements

I would like to express my gratitude to Professor Martin Blunt and Dr Branko Bijeljic for their valuable guidance, encouragement and outstanding supervision throughout the entire period of my PhD and for giving me the opportunity to conduct this research. This work could not have been accomplished without their continuous motivation and fantastic support. Your leadership and mentorship has helped me grow my academic potential. I will remain forever grateful for your trust and confidence in me and for inspiring me to always keep moving forward and to never give up. You are truly the greatest supervisors a student could ask for. In addition, I would like to acknowledge funding from the Consortium on Pore-Scale Modelling and the Department of Earth Science & Engineering at Imperial College London.

I am tremendously grateful to Dr Qingyang Lin for his exceptional support, invaluable discussions and his ever insightful scientific comments during my research. I thank him sincerely for always pushing me to never let it rest until my good is better and my better is best. It has been an incredible privilege to work with you and I am forever grateful to have you as a colleague and a great friend.

I would also like to extend my sincere appreciation to my amazing colleagues and friends: Ying Gao, Yousef Al-Khulaifi, Kamaljit Singh, Hannah Menke, Ben Niu, Peter Lai, Rodolfo Oliviera, Yacine Debabi, Hasan Nourdeen, Amer Alhammadi, Ali Raeini, Ahmed Alratrout, Matthew Andrew, Bagus Muljadi, Zaki Al-Nahari, Thomas Serafini de Oliveira, Joseph Marsden, Tony Luong and Karwan Mustafa. I also extend my thanks to Norman Nicholls, Graham Nash, Gary Jones, Saurabh Shah and Alex Toth for their brilliant technical support throughout my research.

I am exceptionally grateful to the many experts for sharing their technical knowledge and scientific intuition: Professor Alan Butcher, Professor Mark Sephton, Dr Fivos Spathopoulos, Dr Lin Ma, Professor Omar Al-Ayed, Dr Federica Marone, Dr Christoph Rau, Daniel Melo, Hanish Yadav, Erin Honse, Leonardo Salazar, Pradeep Bhattad, Gwenole Tallec, Michael Owen, Erin Summerlin and Rob Hanson.

My heartfelt appreciation to my loving wife and all my family for their encouragement, patience, unwavering support and for being a continuous source of inspiration in every aspect of my life. Special thanks to my father for truly being my greatest inspiration - I appreciate and treasure everything you have taught me.

Table of Contents

ABSTRACT ..... **I**

DECLARATION OF ORIGINALITY ..... **II**

COPYRIGHT DECLARATION ..... **III**

PUBLICATIONS ..... **IV**

ACKNOWLEDGEMENTS ..... **V**

TABLE OF CONTENTS ..... **VI**

LIST OF FIGURES ..... **IX**

LIST OF TABLES ..... **XXI**

LIST OF ABBREVIATIONS ..... **XXII**

CHAPTER 1 INTRODUCTION AND RESEARCH OBJECTIVES **1**

1.1 INTRODUCTION 1
1.2 RESEARCH OBJECTIVES 3
1.3 SCIENTIFIC ACHIEVEMENTS 5
1.4 THESIS STRUCTURE 6

CHAPTER 2 LITERATURE REVIEW **8**

2.1 INTRODUCTION 8
2.2 DEFINING OIL SHALE 8
2.3 OIL SHALE DEPOSITS 10
2.4 OIL SHALE TYPES 12
2.5 OIL SHALE COMPOSITION 16
2.5.1 ORGANIC MATTER 16
2.5.2 MINERAL MATTER 20
2.6 OIL SHALE GRADE 21
2.7 OIL SHALE PYROLYSIS PROCESS 22
2.8 OIL SHALE TECHNOLOGIES 27
2.9 PYROLYSIS PARAMETERS 31
2.9.1 TEMPERATURE 31
2.9.2 HEATING RATE 32
2.9.3 PARTICLE SIZE 32
2.9.4 MINERAL CONTENT 33
2.9.5 PRESSURE 33
2.10 OIL SHALE IMAGING 34
2.11 SUMMARY 41

CHAPTER 3 EXPERIMENTAL METHODS AND ANALYTICAL TECHNIQUES.....42

3.1 INTRODUCTION.....42
3.2 SAMPLE SELECTION.....43
3.3 GEOCHEMICAL & ROCK ANALYSIS.....47
3.3.1 X-RAY DIFFRACTION (XRD).....47
3.3.2 TOTAL ORGANIC CARBON (TOC) ANALYSIS.....49
3.3.3 PROGRAMMED PYROLYSIS (ROCK-EVAL, SOURCE ROCK ANALYSIS).....50
3.3.4 THERMOGRAVIMETRIC ANALYSIS (TGA).....53
3.3.5 ELEMENTAL ANALYSIS (CHNOS).....54
3.3.6 MODIFIED FISCHER ASSAY (MFA).....55
3.4 OPTICAL MICROSCOPY.....56
3.5 SCANNING ELECTRON MICROSCOPY (SEM) AND ENERGY DISPERSIVE X-RAY SPECTROSCOPY (EDS) ANALYSIS.....59
3.5.1 SAMPLE PREPARATION.....62
3.5.2 LARGE SCALE AUTOMATED IMAGING AND MINERALOGY.....66
3.6 FIB-SEM.....69
3.7 X-RAY MICRO-TOMOGRAPHY.....74
3.7.1 X-RAY BEAM SOURCES.....81
3.7.1.1 LABORATORY-BASED M-CT.....83
3.7.1.2 SYNCHROTRON-BASED X-RAY MICRO-TOMOGRAPHY.....86
3.7.2 ARTEFACTS.....88
3.7.2.1 BEAM HARDENING.....88
3.7.2.2 RING ARTEFACTS.....89
3.7.3 IMAGE PROCESSING.....90
3.7.3.1 IMAGE FILTERING.....90
3.7.3.2 IMAGE SEGMENTATION.....92
3.8 PYROLYSIS OF OIL SHALE SAMPLES.....93
3.9 SUMMARY.....94

CHAPTER 4 MICROSTRUCTURAL IMAGING AND CHARACTERIZATION OF OIL SHALE PYROLYSIS USING 2-D OPTICAL MICROSCOPY, SEM AND 3-D LAB-BASED X-RAY MICRO-TOMOGRAPHY.....95

4.1 INTRODUCTION.....96
4.2 OIL SHALE COMPOSITION ANALYSIS.....96
4.2.1 X-RAY DIFFRACTION (XRD).....96
4.2.2 TOTAL ORGANIC CARBON (TOC).....98
4.2.3 PROGRAMMED PYROLYSIS (ROCK-EVAL, SOURCE ROCK ANALYSER).....98
4.2.4 ELEMENTAL ANALYSIS (CHNOS).....100
4.2.5 MODIFIED FISHER ASSAY (MFA).....101

4.3 VISUALIZATION USING OPTICAL MICROSCOPY 102
4.4 VISUALIZATION USING SCANNING ELECTRON MICROSCOPY (SEM) 104
4.5 VISUALIZATION AND QUANTIFICATION USING X-RAY MICRO-TOMOGRAPHY 106
4.5.1 PYROLYSIS OF OIL SHALE SAMPLES 106
4.5.2 X-RAY MICRO-TOMOGRAPHY 107
4.5.3 IMAGE VISUALIZATION AND PROCESSING 107
4.5.4 12 μM 3-D μCT ANALYSIS 109
4.5.5 2 μM 3-D μCT ANALYSIS 112
4.6 SUMMARY 116

CHAPTER 5 IMAGING AND ANALYSIS OF OIL SHALE PYROLYSIS USING SUB-MICRON X-RAY MICRO-TOMOGRAPHY, AUTOMATED ULTRA-HIGH RESOLUTION SEM, MAPS MINERALOGY AND FIB-SEM 118

5.1 INTRODUCTION 119
5.2 3-D ORGANIC MATTER (KEROGEN) AND PORE STRUCTURE ANALYSIS USING SUB-MICRON X-RAY MICRO-TOMOGRAPHY (μCT) 119
5.3 2-D ULTRA-HIGH RESOLUTION SEM AND MAPS MINERALOGY 125
5.4 3-D NANO-SCALE IMAGING USING FOCUSED ION-BEAM SCANNING ELECTRON MICROSCOPY (FIB-SEM) 138
5.5 SUMMARY 146

CHAPTER 6 DYNAMIC IMAGING OF OIL SHALE PYROLYSIS USING SYNCHROTRON X-RAY MICRO-TOMOGRAPHY 148

6.1 INTRODUCTION 149
6.2 OPERATING PARAMETERS 150
6.3 PORE SPACE SEGMENTATION 151
6.4 PORE STRUCTURE EVOLUTION 153
6.5 PORE SPACE CONNECTIVITY 160
6.6 PORE VOLUME ANALYSIS: IMAGING VS TGA 161
6.7 SUMMARY 163

CHAPTER 7 CONCLUSIONS AND FUTURE WORK 164

7.1 CONCLUSIONS 164
7.2 FUTURE WORK 166
7.2.1 CORRELATIVE IMAGING 166
7.2.2 DYNAMIC IMAGING 167
7.2.3 MODELLING 167
7.2.4 CHEMICAL VARIATIONS IN OIL SHALES 168
7.2.5 HYDROUS PYROLYSIS 169

REFERENCES 170

List of Figures

Figure 1.1 Oil shale exhibits significant structural and compositional heterogeneity, which can be characterised by several levels of hierarchy. In this thesis, a multi-scale multi-dimensional workflow is successfully applied to meet the research objectives. (A) Green River (Mahogany Zone) Oil Shale Formation, (B) 3-D Computed Tomography (CT) scan, (C) 3-D micro-tomography (μCT) at lower and higher resolutions, (D) 2-D SEM mosaic image captured under BSE mode, (E) 3-D FIB-SEM oil shale volume, and (F) 3-D Ultra-high resolution SEM image. 4

Figure 2.1 Oil shale is found in many places around the world with more than 600 known deposits. The largest oil shale resources are in the USA, Brazil, Jordan, Russia and Morocco. The most well-known and explored deposits include the Green River deposits in the western United States, the Tertiary deposits in Australia, deposits in Sweden and Estonia, the El-Lajjun deposit in Jordan, and deposits in France, Germany, Brazil, China, and Russia. 11

Figure 2.2 A classification of oil shales developed by Hutton (1987; 1991; 1995), who established the use of blue/ultraviolet fluorescent microscopy in the study of oil shale deposits. Oil shales are considered one of three broad groups of organic-rich sedimentary rocks: (1) bitumen-impregnated rock, (2) oil shales, and (3) humic coals. Hutton (1991) divided oil shales into three groups based on their depositional environment – terrestrial, lacustrine, and marine. Within this threefold grouping of oil shales, Hutton (1991) identified six specific oil shale types: cannel coal, lamosite, torbanite, kukersite, tasminite and marinate. The most common and largest deposits are marinites and lamosites. 13

Figure 2.3 Oil shales (photographed in fluorescence mode; sections perpendicular to bedding: (1) Tertiary cannel coal, from Freshford (New Zealand), Field width = 0.34 mm. (2) Permian torbanite, from Newnes (New South Wales, Australia), Field width = 0.56 mm. (3) Tertiary lamosite, from Condor deposit (Queensland, Australia), Field width = 0.28 ram. (4) Very low grade lamosite, from the Rundle deposit (Queensland, Australia), Field width = 0.28 mm. (5) Tertiary lamosite, from the Green River Formation (Colorado, U.S.A.), containing abundant layered lamalginite, Field width = 0.22 mm, (6) Cretaceous marinite, from the Toolebuc Formation (Queensland, Australia), Field width = 0.28 mm. (7) Permian tasmanite, from the Mersry River area (Tasmania, Australia), composed of abundant telalginite, Field width = 0.44 mm. (8) Ordovician kuckersite, from Estonia, composed of telalginite derived from the alga Gloeocapsomorpha, Field width = 0.44 mm (Hutton 1987). 14

Figure 2.4 H/C atomic ratios in various hydrocarbon materials (Strizhakova and Usova, 2008).... 17

Figure 2.5 (A) Oil shale molecular model $C_{645}H_{1017}O_{17}S_4N_{15}$ proposed by Siskin and Katritzky (1995) and Liu et al. (2015). (B) 3-D representation, using the XMol software, of a type III kerogen structure at the end of catagenesis. Only C atoms (aromatic in white, aliphatic in blue), O atoms (in dark green) and N atoms (in red) are represented (Vandenbroucke, 2003)..... 18

Figure 2.6 Van Krevelen diagram showing kerogen type and evolutionary path. Van Krevelen diagram (left) displays kerogen type and evolution with thermal maturity (Ro). The table and schematic model (right) show the timing and relative abundance gas generated with maturity (adapted from Boyer et al., 2006; Glorioso and Rattia, 2012; Mastalerz et al., 2013; Seewald, 2003). 20

Figure 2.7 General flow diagram of the oil shale retorting process. Oil shale is a complex mixture of kerogen, minerals and water. The kerogen, the organic fraction present as a complex combination of carbon, hydrogen, sulfur and oxygen, cannot be extracted with ordinary solvents due to its macromolecular character. Therefore, heating is required to break down the kerogen network structure and release the shale oil. Upon heating oil shale in the absence of air, residual moisture is first driven off and then the kerogen is initially converted to bitumen. Formed bitumen thermally degrades to shale oil, gas, carbonaceous residues and pyrolytic water, among which shale oil, gas and water leave (vaporize) from the shale particle matrix. Carbonaceous residues remain mixed in with the minerals, forming the solid residues known as semicoke (Han et al., 2014).....23

Figure 2.8 Simplest mechanism of oil shale pyrolysis. 24

Figure 2.9 Oil Shale *ex situ* and *in situ* conversion processes. *Ex situ* retorting is carried out above the ground after the oil shale is mined and crushed, whereas *in situ* processes are carried out in the subsurface, within the existing formation.....28

Figure 2.10 Alberta Taciuk Processor (ATP) retort (adapted from Cameron & Gani 2011). A horizontal, rotating vessel, the ATP retort has four main zones: preheat, retort, combustion, and cooling zone. (1) The Preheat Zone: oil shale enters the retort and moves through the preheat zone where it is heated to about 250°C by the outgoing spent shale. Water is driven off as steam at this stage. (2) The Retort Zone: preheated feed mixes with hot solids recycled from the combustion zone. The resulting heat liberates the kerogen in an oxygen-deficient atmosphere, yielding hydrocarbon vapour and residual char containing ashes. The vapour is condensed externally to recover shale oil and fuel gas. (3) The Combustion Zone: air is added to burn the char off the solids. A significant amount of hot spent shale is recycled to the Retort Zone. (4) The Cooling Zone: hot solids and flue gases are cooled through indirect heat transfer to fresh oil shale feed. Spent shale is discharged for disposal or further processing. Flue gases are disposed of through an off-gas treatment system.....30

Figure 2.11 Imaging and characterisation techniques for shales at varying scales (adapted from Ma et al. 2017). 37

Figure 2.12 X-ray CT images of Australian Oil Shales (A) parallel to bedding, (B) perpendicular to bedding (Coshell et al., 1994). 39

Figure 2.13 CT scan greyscale images of the oil shale sample (cylindrical sample 0.82 diameter × 7 mm length) at different temperatures acquired at a voxel size of 0.54 μm (Kang et al., 2017).....39

Figure 2.14 Micro-CT images of Green River (US) oil shale before (A) and after (B) pyrolysis. Shows the pore-space and connectivity created after pyrolysis (Tiwari et al., 2013). ...40

Figure 2.15 Schematic illustration of (A) Micro-CT 3-D imaging technique and (B) FIB-SEM 3-D imaging technique (Ma et al., 2016). 40

Figure 3.1 Map showing oil shale resource areas of Utah, Colorado and Wyoming. This area contains the lacustrine Eocene Green River Formation, which contains the world's largest deposit of oil shale.....45

Figure 3.2 (A) Enefit oil shale research site, Utah, United States, (B) Oil shale box cut, (C) Oil shale sampling site; note the black horizontal streaks of the Mahogany Zone, and (D) Mahogany Zone oil shale sample used in this study; note the dark colour indicating an organic-rich rock. 45

Figure 3.3 Generalized stratigraphic section of the Green River Formation and associated rocks in the north-central part of the Piceance Creek Basin, northwestern Colorado, United States (Dyni, 2003). The shale-oil resource data, converted from U.S. barrels to metric tons, are from (Pitman et al., 1990). 46

Figure 3.4 (A) Schematic illustration of an X-ray diffractometer, (B) Reflection of X-rays at atomic lattices (Moore and Reynolds, 1989). 48

Figure 3.5 Image of a powder X-ray diffractometer. The incident beam enters from the tube on the left, and the detector is housed in the black box on the right side of the instrument. 49

Figure 3.6 For geochemical analysis (XRD, TOC, Elemental, TGA and MFA), powdered samples were prepared using a pestle and mortar. (A) initial bulk oil shale rock samples, (B) samples crushed using a pestle and mortar, and (C) fine oil shale powder samples used for analysis. 49

Figure 3.7 (A) Source Rock Analyser (SRA), (B) Rock-Eval and (C) Pyrogram obtained from programmed pyrolysis. The first step is to heat the oil shale sample to 300°C to volatize the pre-existing free hydrocarbons in the sample. The amount of these hydrocarbons is measured from a peak area S1. The next step is to pyrolyze the kerogen present in the sample at higher temperatures and measure it at peak area S2. The carbon dioxide generated from the cracking of kerogen (up to 390°C) is measured from the S3 peak. 53

Figure 3.8 Thermogravimetric analysis (TGA) apparatus. (A) Crushed oil shale sample is placed in a highly calibrated platinum pan, which is placed over a hook and attached to a high precision scale. This is directly above the heating chamber which consists of electrical heating coils and ceramic insulation. (B) Perkin-Elmer Pyris 1 TGA instrument used in this study which measures oil shale sample mass loss with increasing temperature in a controlled inert atmosphere. 54

Figure 3.9 Modified Fisher Assay pyrolysis incorporates a defined heating rate and condenser to determine the amount of oil, gas, and water that can be extracted from oil shale. (A) and (B) MFA retorting vessels, (C) Retort assembly, where the oil shale sample is placed in an aluminium can and three aluminium heat transfer disks are placed at regular intervals in the sample. The sample and container are then placed in the steel retort. 56

Figure 3.10 (A) Optical microscope main components: light source, the condenser, the objective and the ocular (eyepiece), (B) Zeiss SteREO Discovery V12 microscope used in this study, (C) Oil shale resin filled block (left) and prepared thin section (right) of the Green River (Mahogany Zone) oil shale. 57

Figure 3.11 Examples of Airy disks of 2 point sources in the vicinity of one another where (A) the sources are separated by a large distance (B) a smaller separation distance but resolvable (C) the Rayleigh criterion where they are just resolvable (D) where they are unresolvable. 58

Figure 3.12 Schematic drawing of the major components of a scanning electron microscope (SEM). Various detectors are used to register the signals arising from various electron–matter interactions. (adapted from Amelinckx et al. 2008). 60

Figure 3.13 A schematic overview of the signals that are generated when an electron beam interacts with a solid sample which are used in the scanning electron microscope (SEM) for microstructural characterization. The most frequently detected signals are high-energy backscattered electrons (BSE), low-energy secondary electrons (SE) and X-rays (EDS/EDX), while less common signals include Auger electrons, cathodoluminescence, and measurements of beam-induced current. 61

Figure 3.14 An example of an X-ray spectrum acquired from a shale sample. Individual peaks indicate an increased concentration of a given element. C = carbon, O = oxygen, Mg = magnesium, Al = aluminium, Si = silicon, Ca = calcium (Huang et al., 2013). 62

Figure 3.15 Oil shale samples in this study were hand-polished using (A) sandpaper (600, 1200 and 2000 grit) and (B) diamond lapping film (6 µm, 3 µm and 1 µm). 63

Figure 3.16 (A) Fischione 1060 SEM Mill used in this study for Argon (Ar) Ion beam polishing. (B) Green River (Mahogany Zone) oil shale sample loaded into the chamber. (C) With the sample stage fixed in position, the ion sources were tilted to 2° operating at energy of 6kV for 22 hours milling an oil shale surface area of 18 mm × 14 mm. 64

Figure 3.17 (A) Q150T carbon coating system used to apply 100-Å thick elemental carbon film on the surface of the oil shale samples to minimise charge build up during SEM imaging. (B) High purity, 3.05 mm diameter carbon rod inserted. (C) Thin conductive layers of carbon are generated by resistive evaporation of the carbon rod. (D) and (E) Oil shale samples following carbon coating. 64

Figure 3.18 Oil shale BSE image under (A) mechanical polishing and, (B) argon ion beam polishing. Mechanical polishing is not suitable for shale samples, as this technique tends to destroy the fine structure of the pore network (e.g., smearing grain boundaries, embedment of grit into surface of sample). A non-contact polishing technique with argon ions is used to obtain a smooth surface. 65

Figure 3.19 (A) FEI QEMSCAN 650F system used in this study to image Green River (Mahogany Zone) oil shale samples. (B) Oil shale samples secured onto sample stage in preparation for ultra-high resolution mosaic imaging and MAPS Mineralogy. 65

Figure 3.20 Energy-dispersive X-ray spectroscopy calibration using copper standard (A) Copper sample, (B) BSE image of copper sample and (C) Copper spectrum; the K-alpha peak being the taller than the K-beta peak. 66

Figure 3.21 A 2 × 2 set of high-resolution BSE images; before (top) and after stitching (bottom) for the Green River (Mahogany Zone) oil shale acquired at 5 keV with a 15 nm pixel size. Tiles acquired with a 10% overlap using MAPS (Modular Automated Processing System) Tiling and Stitching software. 67

Figure 3.22 Modular Automated Processing System (MAPS) tiling and stitching system. (A) Grid system of 19 × 16 tiles with each tile being 1.024 mm × 1.024 mm, (B) and (C) Real-time acquisition and stitching of tiles with 10% overlap, (D) Close-up on an individual tile showing the acquired BSE image and energy-dispersive X-ray spectrometry (EDS) data acquired (red colour indicated areas rich in calcium). 69

Figure 3.23 (A) FIB-SEM DualBeam configuration used in image acquisition In a DualBeam, the electron and ion beams intersect at a 52° angle at a coincident point near the sample surface, allowing immediate, high resolution SEM imaging of the FIB-milled surface. (B) 2-D FIB-SEM 2-D image stacks are computationally converted to a 3-D volume. 70

Figure 3.24 (A) FEI Helios 660 FIB-SEM system used in this study to acquire high-resolution 3-D datasets of un-pyrolysed and pyrolysed samples of Green River (Mahogany Zone) oil shale. (B) Oil shale sample secured onto stage in preparation FIB-SEM acquisition. 71

Figure 3.25 FIB-SEM setup consisting of an (1) electron source, FIB ion source (Ga^+), Platinum (Pt) gas injection needle, specimen stage and oil shale sample for analysis. The ion beam and electron beam were set a 52° angle to each other. 72

Figure 3.26 (A) SEM image following platinum deposition of 40 µm × 5 µm × 2µm, which act as a protective layer. This is vital to protect the area of interest from any stray ions and prevent any damage to the area, which will otherwise cause curtaining artefacts. (B) and (C) Trenches milled around region of interest for debris / redeposited material to collect in which would otherwise cause obscuration of the region of interest or shadowing effects. (D) A 7 µm x 7 µm × 2 µm platinum pad was deposited above the right side of the trench and an X placed in the centre. This is a fiducial marker, which acts as a reference point and allows for image alignment. 73

Figure 3.27 Schematic illustration of X-ray micro- tomography images acquisition and reconstruction (adapted from Landis & Keane 2010). X-ray micro-tomography images are generated based on the principle that X-ray intensity is linearly attenuated when passing through different materials. A decrease in X-ray intensity is a function of the X-ray energy, path length and material linear attenuation coefficient. The sample rotates around a specific axis and the detector measures the degree of attenuation, creating 2-D radiographs (projections) in greyscale. Individual 2-D projections are then reconstructed to produce a 3-D volume. 74

Figure 3.28 The interaction modes of X-rays with matter depending on elemental atomic number Z and the X-ray photon energy hν. There are three dominant physical processes responsible for attenuation of an X-ray signal: photoelectric absorption, Compton scattering, and pair production. In general, for geological materials, the photoelectric effect is the dominant attenuation mechanism at low X-ray energies, up to approximately 50–100 keV. Compton scatter is dominant at higher energies up to 5–10 MeV, after which pair production predominates. Thus, unless higher-energy sources are used, only photoelectric absorption and Compton scattering need to be considered (Ketcham and Carlson, 2001). 75

Figure 3.29 Linear attenuation coefficient as a function of incident X-ray energy for four common materials found in oil shale rock samples: pyrite, calcite, dolomite, illite, quartz and carbon. Note that the linear attenuation coefficients for calcite, dolomite, illite and quartz are very similar but rather different from pyrite and carbon (organic matter). 77

Figure 3.30 Illustration of (A) Projection, and (B) Backprojection. The object is rotated, pauding at discrete angles to collect 2-D projection images. The projection images are combined together to produce a 3-D reconstruction of the object's volume. Simple back-projection reconstructs an image by taking each projection and smearing (or backpojecting) it along the line it was acquired. As a result of this simple procedure, the backprojected image is blurred. In filtered backprojection (FBP), a filter is applied to each projection before the backprojection is done to counteract the blur. FBP is the most commonly used algorithm for computed tomography systems. 79

Figure 3.31 Reconstruction process using Zeiss proprietary software (Zeiss XMReconstructor) with centre shift at (A) -4.163, (B) 3.739, (C) 7.817 and (D) 11.837. For this oil shale dataset, a centre shift of 3.739 resulted in the best image quality. 79

Figure 3.32 Oil shale sample (A) 2-D projections, (B) 2-D grey-level and (C) Line-plot indicating the intensity along the yellow line across image (B) with red markers for reference 80

Figure 3.33 Example of oil shale laboratory-based X-ray micro-CT data visualization showing XY, XZ and YZ slices and a tri-planar image revealing 3-D microstructure of the scanned sample. 80

Figure 3.34 X-ray optical geometries. Illustration of a (A) parallel X-ray beam, (B) conical X-ray beam (Menke, 2015). Conical beams are typical used in bench-top X-ray μCT systems and parallel beams are typical of synchrotron X-ray μCT systems. 82

Figure 3.35 X-ray micro-tomography (μCT) apparatus used to capture 3-D scans of Green River (Mahogany Zone) oil shale samples. (A) The laboratory-based μCT consists of three main components: an X-ray micro-focus source, a rotation stage to mount and control the sample and an X-ray detector. (B) Zeiss Versa XRM-500 μ-CT system used in this research study. 84

Figure 3.36 Zeiss Versa XRM-500 μ-CT schematic. An X-ray source fires X-rays through the sample which fluoresce when they hit the scintillator. The visible light is focused by the objective lens and digitised by the CCD array. 84

Figure 3.37 The geometric and optical magnification capabilities available in a laboratory-based micro-CT. Geometric magnification allows for high resolution scans at shorter source distances than traditional optical magnification (Menke, 2015). 85

Figure 3.38 Illustration of the Zeiss Versa XRM-500 μ-CT source-sample-detector setup with *a* representing the source to sample distance and *b* representing sample to detector distance. 86

Figure 3.39 A schematic for a typical synchrotron consisting of: (1) Electron gun, (2) Linear accelerator (Linac), (3) Booster ring, (4) Storage ring, (5) Beamline, and (6) End station. 87

Figure 3.40 A synchrotron undulator. (1) The periodic structure of magnets, (2) Bending the electron beam, and (3) Generation of intense light (Menke, 2015). 88

Figure 3.41 The Diamond Lightsource pink beam apparatus. The beam passing through the undulator generates intense light. The spectrum is narrowed by mirrors and filters and is then transmitted through the sample. The scintillator fluoresces in the visible spectrum and the light is focused and measured by the objective lens and CCD camera array (Menke, 2015). 88

Figure 3.42 (A) Uncorrected initial image of a water phantom showing beam hardening (B) corrected image using reconstruction software (Kyriakou et al., 2009). 89

Figure 3.43 (A) Uncorrected initial image of a water phantom showing ring artefacts sand (B) corrected image using based on median filtering of the reconstructed image and working on a transformed version of the reconstructed images in polar coordinates. This post-processing method reduced ring artefacts in the reconstructed images and improved image quality (Kyriakou et al., 2009). 90

Figure 3.44 (A) Oil shale raw image, (B) Non-local means filtered image and (C) Histogram of the tomography data indicating the number of voxels (counts) with a particular grey value. A clear separation is observed in the histogram peaks corresponding to the pore space (left peak) and the solid phase (right peak). 91

Figure 3.45 Overview of X-ray micro-CT imaging and analysis workflow for an oil shale sample: 2-D projections are acquired, followed by reconstruction to generate a 3-D volume, then segmentation is completed to separate key phases and finally analysis of the segmented volume is done to compute petrophysical properties. 92

Figure 3.46 One-dimensional example of watershed segmentation. (A) Grey-level profile of image data. (B) Watershed segmentation - local minima of grey-level (altitude) yield catchment basins with local maxima defining the watershed lines (Sonka et al., 2014). 93

Figure 3.47 (A) Custom-built furnace designed for use at a synchrotron facility, (B) schematic of furnace indicating key dimensions including 10 mm holes to allow the X-ray beam to directly pass through the sample during heating. 94

Figure 4.1 XRD pattern (diffractogram) for the Green River oil shale sample (Mahogany Zone) with characteristic mineral peaks identified. 98

Figure 4.2 Modified Fisher Assay (MFA) results for the Green River oil shale sample (Mahogany Zone) including mineral decomposition and organic products, oil density and oil yield. The clean oil density represents the density of the oil recovered as liquid in the receiver following the test. The oil yield represents the amount of potentially extractable shale oil present in the sample as determined the MFA method..... 101

Figure 4.3 Thin section mosaic images of the Green River oil shale sample (Mahogany Zone) generated by digitally stitching 1152 individual images into one all-encompassing view. 102

Figure 4.4 Thin section images of oil shale from the organic –rich Green River Formation (Mahogany Zone) at low (A), medium (B-D) and high (E-G) magnification. The images taken in plane polarized light (PPL) show a series of laminated structures of organic material in a distribution of fine grained inorganic minerals. 103

Figure 4.5 SEM images revealing organic matter, inorganic minerals and porosity with increasing magnification (A-E). The Oil Shale of the Green River Formation is characterised by alternating horizontal and folded layers of organic (black) and inorganic (grey) minerals. (F) Composite elemental map for the Green River Oil Shale displaying the spatial distribution of elements in the sample with organic-rich regions shown in red. 105

Figure 4.6 Photograph of the raw and pyrolysed Green River oil shale sample (Mahogany Zone) (A) Raw oil shale sample of size 10 mm (diameter) by 70 mm (length) (B) Oil shale sample pyrolysed at 500°C, note the vertical expansion linked to development porous layers predominantly along the kerogen-rich laminations. 106

Figure 4.7 (A) Raw 2-D grey scale image at a 2 μm voxel size, (B) Non-local means filtered 2-D grey scale image, (C) Segmented image with pore space shown in blue (D) 3-D volume rendered image the pore space shown in blue and the matrix in grey, (E) Histogram of the tomography data showing the number of voxels with a particular grey value. A clear separation is observed in the histogram peaks corresponding to the pore space and the rest of the solid phase..... 108

Figure 4.8 2-D grey scale images following reconstruction of the μCT 12 μm voxel size dataset for (a) raw oil shale, (b) pyrolysed oil shale at 500°C. (c) Segmented image with pore space shown in white. (d) The porosity profile per slice. The grey scale level indicates variations in the X-ray attenuation coefficients which depend on the density and atomic number of the material within each voxel. Pores and micro-fractures are observed in the kerogen-rich laminations..... 110

Figure 4.9 (A) 2-D segmented image with pore space shown in white and solid material in black. (B) REV analysis method where a volume of *x* thickness is moved up by one slice up to slice *n*, with each slice representing one voxel of 12 µm and porosity computed at each stage. (C) Porosity profile for analysed REV thicknesses. 111

Figure 4.10 2-D grey scale images for oil shale sample at 20°C, 400°C, 450°C and 500°C with their respective porosity profiles per slice. 112

Figure 4.11 (A) 2-D segmented image for pyrolysed oil shale sample at 500°C with pore space shown in white and solid material in black. (B) 2-D image where pores of the same color are connected, (C) 3-D rendering of the pore space revealing the extensive laterally connectivity of the pore space following pyrolysis. 113

Figure 4.12 Oil shale porosity as a function of pyrolysis temperature. A comparison between static laboratory based analysis, presented here, and dynamic synchrotron µCT data (Saif et al., 2016). 115

Figure 4.13 (A) Porosity of 10 oil shale samples after pyrolysis at 500°C, (B) – (D). 2-D grey scale images for organic-rich, organic-mixed and organic-lean regions respectively. (E) – (G) 3-D rendered volumes with the pore space visualized in blue. 115

Figure 5.1 2-D greyscale and tri-planar images of Green River (Mahogany Zone) oil shale before pyrolysis acquired at (A)-(B) 12 µm, (C)-(D) 2 µm and (E)-(F) 0.8 µm voxel size. 121

Figure 5.2 X-ray micro-tomography (µCT) for immature Green River (Mahogany Zone) oil shale acquired at a 0.8 µm voxel size. (A) Raw 2-D greyscale image, (B) Non-local means filtered 2-D greyscale image, (C) Segmented image with organic matter (kerogen) shown in blue (D) 3-D volume rendered image with the organic matter shown in blue and the mineral matrix in grey. 122

Figure 5.3 (A)-(C) Backscattered electron (BSE) images of the Green River (Mahogany Zone) oil shale with increasing amount of organic matter (total organic carbon (TOC)) within the same sample. (D)-(F) Segmented images with organic matter shown in blue. 122

Figure 5.4 Micro-fracture development in the Green River (Mahogany Zone) oil shale sample during pyrolysis at (A) 20°C, (B) 350°C, (C) 380°C, (D) 390°C, (E) 400°C and (F) 420°C. The red arrows indicate reference pyrite minerals used to monitor the same 2-D µCT image slice, and the yellow arrows show developing micro-fractures within the oil shale sample. 123

Figure 5.5 Oil shale porosity for the Green River (Mahogany Zone) samples as a function of pyrolysis temperature. A comparison is made between static laboratory based analysis, presented here, and dynamic synchrotron µCT data (Saif et al., 2016). 125

Figure 5.6 (A) Carbon-coated argon ion milled Green River (Mahogany zone) oil shale samples, un-pyrolysed (sample 1, left) and pyrolysed (sample 2, right), prepared for large-area automated SEM imaging and MAPS Mineralogy, (B) Two independently adjustable ion sources used to rapidly mill the oil shale samples creating highly polished ultra-flat surfaces for ultra-high resolution SEM imaging. 126

Figure 5.7 Automated SEM and MAPS Mineralogy measurement and analysis workflow. The area of interest is divided into multiple tiles and backscattered electron (BSE) images are recorded in sequence and subsequently stitched to generate 7one single image. The full surface is also mapped using energy-dispersive (EDS) X-ray analysis with a user-defined spacing. The EDS X-ray spectrum for each analysis point is compared to a database of known mineral species. This process is automated on a pixel by pixel basis to create high resolution mineral maps. 127

Figure 5.8 (A) Stitched BSE image of 18 mm × 14 mm raw Green River (Mahogany zone) oil shale. The large area image has been created by stitching 19 × 16 tiles, resulting in an image of 34,733 × 28,839 pixels with a pixel size of 500 nm captured at 15 keV. (B) - (D) From the full overview of the stitched image of a sample, zooming exposes the high resolution details without losing correlation and allows regions of interest to be located for further investigation. (E) - (F) Higher resolution BSE images acquired at 5 keV with a 10 nm pixel size. 128

Figure 5.9 The pores identified in the un-pyrolysed Green River (Mahogany Zone) oil shale sample can be categorized into: Intra-OP (Organic Pore), Inter-OMP (Organic-Mineral Pore), Intra-MP (Mineral Pore), Inter-MP (Mineral Pore). (A) Marcasite grain (FeS_2, orthorhombic), the dimorph of pyrite with characteristic tabular-bladed morphology, BSE image captured at 5 keV with a 15 nm pixel size. (B) Individual rhomboid shaped grains characteristic of dolomite, BSE image captured at 5 keV with a 15 nm pixel size. (C) Porous carbonate grain, BSE image captured at 5 keV with a 10 nm pixel size. (D) Clay platelets with local ordering within organic matter and submicron-scale pores between clay mineral platelets, BSE image captured at 3 keV with a 3 nm pixel size. 129

Figure 5.10 (A) Lenticular shaped intra-OP (Organic Pore) of micron-scale, BSE image captured at 5 keV with a 50 nm pixel size, (B) Intra-MP (Mineral Pore) within dolomite grain and inter-OMP (Organic-Mineral Pore) between organic matter and potassium feldspar grain, BSE image captured at 5 keV with a 50 nm pixel size, (C) Intra-OP within the range from several tens to a few hundred nanometres, BSE image captured at 5 keV with a 50 nm pixel size, (D) Fracture pores within organic matter of a few micrometres, BSE image captured at 5 keV with a 10 nm pixel size. 130

Figure 5.11 High-resolution BSE images for immature Green River (Mahogany Zone) oil shale, (A) Dolomite grain with sub-µm pores, (B) Kerogen encapsulated within calcite minerals, (C) Mineral hosted nano-porosity within a Marcasite (FeS_2) grain, and (D) Nano-scale clay platelets within kerogen. 131

Figure 5.12 (A) Backscattered electron (BSE) greyscale mosaic image; (B) Mineral map based on EDS analysis with an X-ray spacing of 10 µm and acquisition time of 8ms per pixel with automated mineral identification performed using NanoMin software; and (C) Quantification of minerals present in the Green River (Mahogany Zone) oil shale sample indicating a highly calcareous mineral matrix. (D) An overlay of (a) and (b) showing the spatial distribution of minerals and the micro-texture of the inorganic mineral grains dispersed within organic matter (kerogen). 132

Figure 5.13 Backscattered electron (BSE) images of Green River (Mahogany Zone) with point identification of inorganic mineral grains by comparing measured X-ray spectra with a mineral spectral library: (A) Quartz (SiO_2), (B) Dolomite ($CaMg(CO_3)_2$) and (C) Pyrite (FeS_2). 133

Figure 5.14 (A)-(C) Backscattered electron (BSE) images of the Green River (Mahogany Zone) oil shale of same region of interest with decreasing pixel size: (A) 500 nm, (B) 50 nm and (C) 10 nm. (D)-(F) Three-phase segmented images with organic matter shown in blue, mineral phases in green and pores in red, (G)–(I) Zoom-in within segmented images with finer pixel size revealing more well-defined boundaries between organic, mineral and pore phases. 135

Figure 5.15 (A) Stitched BSE image of 18 mm × 14 mm Green River (Mahogany zone) oil shale pyrolysed at 500°C. The large area image has been created by stitching 19 × 16 tiles, resulting in an image of 35,417 × 29,216 pixels with a pixel size of 500 nm captured at 15 keV. (B) - (D) From the full overview of the stitched image of a sample, zooming exposes the high resolution details without losing correlation and allows regions of interest to be located for further investigation. Fractures formed during oil shale pyrolysis, which essentially constitute the loss of organic matter, are observed from the μm-to- mm scales. (E) - (F) Higher resolution BSE images acquired at 5 keV with a 10 nm pixel size. 136

Figure 5.16 BSE images of the Green River (Mahogany Zone) oil shale pyrolysed at 500°C. (A) An open micro-fracture of approximately 200 μm in length as the solid kerogen is converted to fluid hydrocarbons, image captured at 5 keV with a 30 nm pixel size. (B) A fracture of approximately 80 μm in length with connecting smaller fractures as the organic matter thermally decomposes, BSE image captured at 5 keV with a 20 nm pixel size. (C) - (D) Partially decomposed organic matter, with solid kerogen remaining attached to inorganic mineral grains, BSE image captured at 5 keV with a 10 nm pixel size. (E) - (F) Images showing the formation of pores within the oil shale microstructure from tens of nanometres to a few micrometres in size and varying in shape from nearly circular to irregular polygon pores hosted within the organic matter and between the organic material and inorganic mineral grains, BSE image captured at 5 keV with a 10 nm pixel size. 137

Figure 5.17 (A) Schematic diagram of the sectioning and imaging procedure in a focused ion beam–scanning electron microscopy (FIB-SEM) system, (B) FIB-SEM configuration, and (C) FIB-SEM site preparation: first, a trench is milled around the volume that will be analyzed; then, FIB milling and SEM imaging are used sequentially to generate a 3-D data set of parallel, high-resolution images. Fiducial markers are placed as reference features to allow for image alignment/registration. ... 139

Figure 5.18 FIB-SEM locations selected for sample 1 (un-pyrolysed, top) and sample 2 (pyrolysed, bottom) of the Green River (Mahogany Zone) oil shale. (A) Immature oil shale in the SEM sample chamber. (B) BSE mosaic image revealing a moderately organic-rich region. (C) An enlarged section of the FIB-SEM image with trenches milled by FIB around the region of interest (ROI) prior to serial sectioning and imaging of the ROI using the FIB and SEM. (D) Pyrolysed oil shale sample (500°C). (E) BSE image revealing a network of parallel fractures. (F) FIB-SEM region precisely selected to capture developed pores/fractures, the solid phase of minerals and remaining organic material. 139

Figure 5.19 (A) Raw greyscale image acquired using FIB-SEM. (B) The filtered image processed using a non-local means edge preserving smoothing filter. (C) Placement of markers with pore phase (including pore backs) marked in red and solid phase (organic + mineral) marked in yellow followed by the application of 2-D watershed segmentation. (D) Pore phase (red) is locked in place and a 2-D watershed segmentation is applied to separate the organic phase (blue) from the mineral phase (green). 140

Figure 5.20 (A) 3-D reconstructed greyscale FIB-SEM volume of the raw Green River (Mahogany Zone) oil shale, sample 1. (B) Three-phase segmentation of minerals (green), organic matter (blue) and pores (red). (C) Mineral grains representing 47. 7% of the FIB-SEM volume. (D) Fully connected organic matter (kerogen) representing 51.8% of the FIB-SEM volume. (E) Isolated pores from nano to micron-scales representing 0.5% of the total FIB-SEM volume. 142

Figure 5.21 (A) 3-D reconstructed greyscale FIB-SEM volume of the Green River (Mahogany Zone) oil shale pyrolysed at 500°C, sample 2. (B) Three-phase segmentation of minerals (green), organic matter (blue) and pores (red). (C) Mineral grains representing 42.2% of the FIB-SEM volume. (D) Residual organic matter representing 39.6% of the FIB-SEM volume. (E) Pores predominantly in the form of micro-fractures along the organic-rich laminations representing 18.2% of the total FIB-SEM volume. 142

Figure 5.22 3-D FIB-SEM rendering of the pore space where the colors indicate clusters of connected pores. (A) Immature Green River (Mahogany Zone) oil shale where the pore space appears disconnected —the large range of colors indicates a poorly connected pore network. (B) Pyrolysed (500°C) Green River (Mahogany Zone) oil shale displaying a well-connected pore space in the form of micro-fractures predominantly along the organic-rich laminations. 143

Figure 5.23 (A) Immature Green River (Mahogany Zone) Oil Shale pore size distribution showing that pores between 15 nm and 22 nm in equivalent radius dominate in number. (B) Pore volume contribution, showing that pores approximately ranging from 140 nm to 390 nm in equivalent radius have the greatest volumetric contribution occupying 75.9% of the pore volume. 144

Figure 5.24 (A) Pyrolysed Green River (Mahogany Zone) Oil Shale pore size distribution showing that pores between approximately 9 nm and 18 nm in equivalent radius dominate in number. (B) Pore volume contribution, showing that pores approximately ranging from 1.6 μm and 2 μm in equivalent radius have the greatest volumetric contribution occupying 98.7% of the pore volume. 145

Figure 6.1 A comparison of segmentation results between Otsu's thresholding method and watershed segmentation. The results indicate a difference in segmented pore volume of less than 2%. 152

Figure 6.2 Schematic of experimental apparatus used at Diamond Light Source (DLS). 152

Figure 6.3 Temperature profile used in the experiment, with each point (red) representing an acquisition of a 3-D tomogram. In total 52 scans were recorded. 153

Figure 6.4 (A) – (D) Filtered greyscale images at different temperatures. (E) - (G) segmented images with pore space shown white. The greyscale cross-sections show organic-rich laminations (dark grey) tightly bound in an inorganic mineral matrix (light grey) with no resolvable pore space between 20°C and 380°C. The first resolvable pore space appears at 390°C. There then follows a dramatic increase in porosity to form micro-fracture networks along the organic-rich laminations (c and f) with a small but detectable increase in porosity with a further increase in sample temperature to 500°C (D and E). 154

Figure 6.5 BSE image of the Green River Oil Shale sample with four EDS spot analysis points and corresponding spectra results. The organic-rich material is shown as the darker coloured area and the denser mineral mineral-rich matrix appears lighter. The red box represents the area used to acquire an elemental map. 155

Figure 6.6 Individual elemental maps for the Green River Oil Shale displaying the spatial distribution of carbon (C), silicon (Si), Ca (calcium), sulphur (S), magnesium (Mg), sodium (Na), aluminium (Al) and potassium (K). 156

Figure 6.7 Composite elemental map for the Green River Oil Shale displaying the spatial distribution of elements in the sample. Organic-rich areas are shown in red, calcium-rich minerals in blue and silicon-rich minerals in pink. 157

Figure 6.8 Porosity as a function of experimental time. The temperature is indicated by the arrows. Between 20°C and 380°C no resolvable porosity was observed; at 390°C the first micro-scale pores were detected contributing to a porosity of 2.7%; at 400°C a dramatic increase in porosity is observed resulting in a total porosity of 21.9%; and a further increase in pyrolysis temperature to 500°C leads to a smaller increase in porosity to 24.9%. 158

Figure 6.9 3-D rendered volumes of the oil shale sample at 390°C (A) and 400°C (B). The dramatic increase in porosity is visualized with the pore phase (blue) and remaining matrix phase (grey). The porosity profile across the sample from line A to B for both 390°C and 400°C reveals a variable porosity distribution related to the thermal decomposition of organic material. 159

Figure 6.10 3-D rendering of the pore space where the colors indicate clusters of connected pores. At 20°C no pores can be resolved. At 390°C all the pore space appears disconnected at the resolution of the image - the large range of colors indicates a poorly connected pore network. At 400°C and 500°C the vast majority of the pore space is connected, 96.5% and 97.8% respectively, shown in blue. 161

Figure 6.11 (A) Thermogravimetric (TGA) data showing the fraction of the mass remaining as a function of temperature (solid line) and the fractional change in mass (dashed line) between two measured temperature points. $m0$ is the initial mass, mi is the mass at some temperature and Δmi is the change in mass for a 10°C temperature increase. (B) Image derived data showing the matrix (non-pore) volume loss due to pore space development (solid line) and the fractional change in matrix volume. ΔVi is the change in volume for a 10°C temperature increase. 162

List of Tables

Table 2.1 Estimate of Oil Shale Reserves (Metric Tons × 10^6) 11

Table 2.2 Examples of kerogen elemental composition (CHNOS) for various oil shale deposits (Probstein and Hicks, 2006). A major advantage of oil shales over other solid fossil fuels is the relatively high hydrogen to carbon atomic ratios (H/C) in the organic matter, which allows for the production of a wide range of chemical products. 17

Table 2.3 Kerogen type, form and origin (adapted from Glorioso and Rattia (2012)). There are four types of kerogen: (1) Type I, which consists mainly of algal and amorphous constituents; (2) Type II, which consists of mixed terrestrial and marine source material; (3) Type III, which consists of woody terrestrial source material; and (4) Type IV, which is derived from reworked organic matter or from highly oxidised material. 19

Table 2.4 Mineral Matter composition for selected oil shale deposits presented as oxides in ash, wt%. 21

Table 2.5 A summary of oil shale pyrolysis reactions (Parker and Zhang, 2006). 26

Table 2.6 Comparison of commercial oil shale retort technologies (adapted from Qian et al. 2008). 29

Table 3.1 Acquired parameters during programmed pyrolysis, associated units, measurement properties and related comments. 52

Table 3.2 Calculated parameters from programmed pyrolysis, their units, equations and names. 52

Table 4.1 Composition analysis for the Green River oil shale sample (Mahogany Zone) including mineralogy, TOC and elemental analysis. 100

Table 4.2 Oil shale μCT acquisition settings. 108

Table 5.1 Oil shale μCT acquisition settings 121

List of Abbreviations

2-D	Two-dimensional
3-D	Three-dimensional
4-D	Four-dimensional
XRD	X-ray Diffraction
TOC	Total Organic Carbon
CHNOS	Carbon, Hydrogen, Nitrogen, Oxygen and Sulphur
MFA	Modified Fischer Assay
PPL	Plain Polarized Light
SEM	Scanning Electron Microscopy
BSE	Back-Scattered Electron
SE	Secondary Electron
ESEM	Environmental SEM
EDS	Energy Dispersive X-ray Spectroscopy
MAPS	Modular Automated Processing System
TEM	Transmission Electron Microscopy
FIB	Focused Ion Beam
XCT	X-ray Computed Tomography
μCT	Micro Computed Tomography
BET	Brunauer– Emmett–Teller
MICP	Mercury Injection Capillary Pressure
REV	Representative Elementary Volume
DLS	Diamond Light Source

Chapter 1

Introduction and Research Objectives

1.1 *Introduction*

Global energy demand is set to rise spectacularly in the coming decades as a result of population growth and economic development (BP, 2016; ExxonMobil, 2017; IEA, 2015). In many parts of the world, focus on energy reliability and security has brought significant attention to the exploration and production of unconventional hydrocarbon deposits transforming energy markets worldwide (Aguilera and Radetzki, 2013; McGlade et al., 2013). Oil shale is an unconventional energy resource which represents a tremendous and predominantly untapped natural energy resource with many known deposits across the world. These deposits, which range from Cambrian to Tertiary age, may occur as minor accumulations of little or no economic value or giant deposits that occupy thousands of square kilometres and reach thicknesses of 700 m or more (Dyni, 2003; Dyni and U.S. Geological Survey, 2010; Johnson et al., 2009). Oil shales range widely in organic content and oil yield with commercial grades of oil shale, as determined by their yield of shale oil, ranging from about 100 to 200 litres per metric ton (l/t) of rock. As with most mineral deposits, the value of an oil shale deposit depends upon its depth, thickness and grade. The Lacustrine Eocene Green River Formation, located in Utah, Colorado and Wyoming contains the largest oil shale deposit in the world with an estimated 1.5 to 1.8 trillion barrels of oil originally in place (Bartis et al., 2005) and is the focus of this study.

Oil shale is broadly defined as a very fine-grained sedimentary rock containing sufficiently high contents of immature organic matter (Dyni, 2003). It is a potential petroleum source rock that would have generated hydrocarbons if it had been subjected to geological burial at the requisite temperatures and pressures for a sufficient time. Kerogen, which constitutes most of oil shale's organic matter, is a highly cross-linked, insoluble, macromolecular solid material that is the dominant source of carbon for hydrocarbon generation in the subsurface. The organic matter in

oil shale includes the remains of algae (cyanobacteria), spores, pollen, plant cuticle and corky fragments of herbaceous and woody plants, and other cellular remains of lacustrine, marine, and land plants. The kerogen material is a complex combination of carbon, hydrogen, oxygen, nitrogen and sulphur and cannot be extracted with ordinary solvents due to its macromolecular character. Hydrocarbon recovery from oil shale is principally through *ex situ* (surface retorting) and *in situ* (within the subsurface geologic formation) technologies. The source rock is heated above pyrolysis temperatures (300-500°C) at which the immobile organic matter is transformed to mobile oil and gas which can be upgraded and used for a wide variety of fuels and chemical products.

The pyrolysis of oil shale refers to its thermal processing by heating in the absence of air or oxygen at a temperature of 300-500°C. The first stage involves the heating of oil shale where heat transfer occurs from the heat carrier to the oil shale surface, and then from the surface to its interior. Pyrolysis of oil shale occurs at approximately 300°C, the temperature at which the endothermic energy barrier is overcome. The second stage is the pyrolysis of the organic matter where kerogen is thermally decomposed to produce shale oil vapour, non-condensable gases, pyrolysis water and a carbonaceous residue. The decomposition rate accelerates as the temperature increases. The third step involves diffusion and flow of shale oil vapour, non-condensable gas and water vapour through an interconnected pore and fracture network.

The raw oil shale microstructure is complex and is considered to be impermeable. In the oil shale pyrolysis extraction of hydrocarbons, both the chemical and physical properties of oil shale change significantly. A suite of traditional laboratory-based analytical techniques are normally used to characterise oil shale samples which include the Modified Fischer Assay (MFA) and Elemental Analysis (CHNS). MFA is a standard test method which determines the yield of oil from oil shale; whilst elemental analysis reveals the composition of shale oil based on the mass fractions of carbon, hydrogen, nitrogen, and sulphur. To enhance our understanding of oil and gas transport phenomena involved in the pyrolysis of oil shale and ultimate recovery, a comprehensive characterization of the variations in petrophysical properties is

essential, in particular, the direct visualization and quantification of the kerogen network, mineralogical phases and the evolution of the pore space during pyrolysis.

The geological setting and microstructural characteristics of an oil shale resource are of significant importance to its commercial development. Ultimately, the availability and price of petroleum affects the viability of a large-scale oil-shale industry. Today, few oil shale deposits can be economically developed for shale oil in competition with conventional petroleum. However, given that global conventional oil supplies have plateaued and are slowly decreasing, greater use of oil shale for the production of electric power, transportation fuels, petrochemicals, and other industrial products seems likely.

1.2 *Research Objectives*

The aim of this research is to provide comprehensive information on the microstructure of oil shales including the evolution of the pore structure during pyrolysis. The thermal decomposition of oil shale involves complex physical and chemical changes, including the development of microscopic pore structures. Currently, there is a fundamental gap in knowledge on detailing pore space evolution of oil shale during pyrolysis as the oil shale rock acts as a porous medium with the pores and fractures being conduits for the storage and percolation of oil and gas. The pore properties of oil shales directly influence the inward and outward diffusion of oil vapour and gas, and the availability of reactions during the thermal decomposition of organic matter. Further understanding on describing this subject, including visualizations and quantification, is crucial for the development of applied oil shale utilization technologies.

The main objectives of the research presented in this thesis are:

(1) To develop a multi-scale workflow from the nanoscale to macroscale and to systematically characterise the distribution, connectivity and relationships of the pore system, organic matter and minerals in the Green River (Mahogany Zone) oil shale.

(2) To visualize and quantify the development of the pore space and microstructure before and after pyrolysis using two dimensional (2-D) and three-dimensional

imaging techniques, including X-ray micro-tomography (lab-based), Scanning Electron Microscopy (SEM) and Focused Ion Beam Scanning Electron Microscopy (FIB-SEM).

(3) To capture the constantly evolving porous structure of oil shale during pyrolysis (300 - 500°C) using dynamic synchrotron-based X-ray micro-tomography and to determine the critical temperature window at which initiation and propagation of fractures takes place, this in turn acts as the main conduits for the storage and percolation of evolved oil and gases.

This comprehensive study provides a better insight and understanding into the structural and compositional heterogeneity of oil shale (Figure 1.1), and the change in petrophysical properties during pyrolysis. The results from this study offer valuable datasets to academics and industry to better model oil shale pyrolysis processes and to more accurately predict and optimize hydrocarbon recovery.

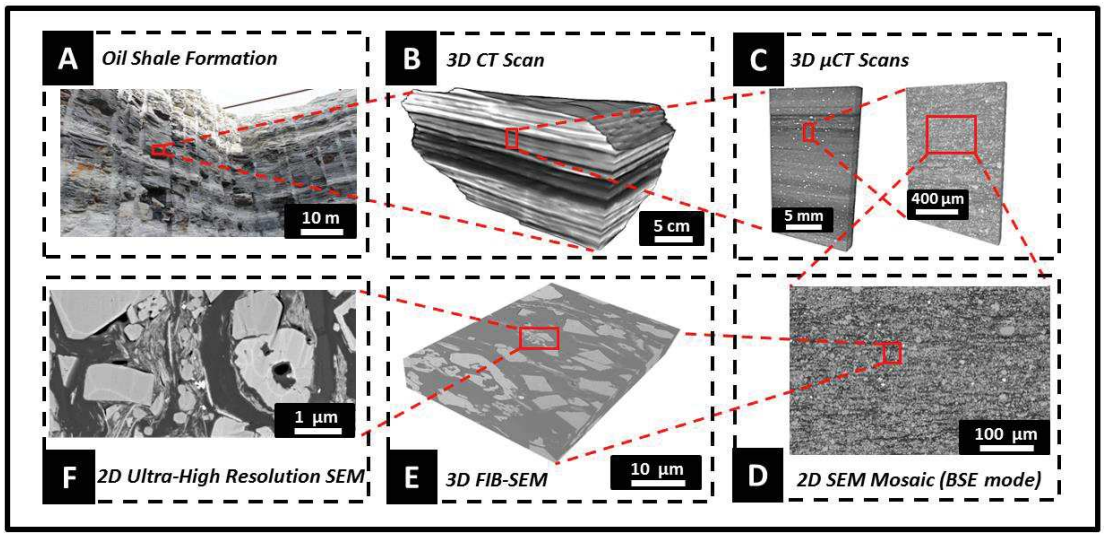

Figure 1.1 Oil shale exhibits significant structural and compositional heterogeneity, which can be characterised by several levels of hierarchy. In this thesis, a multi-scale multi-dimensional workflow is successfully applied to meet the research objectives. (A) Green River (Mahogany Zone) Oil Shale Formation, (B) 3-D Computed Tomography (CT) scan, (C) 3-D micro-tomography (µCT) at lower and higher resolutions, (D) 2-D SEM mosaic image captured under BSE mode, (E) 3-D FIB-SEM oil shale volume, and (F) 3-D Ultra-high resolution SEM image.

1.3 *Scientific Achievements*

The main achievements in this research are:

(1) For the first time, a multi-scale (nm- μm-mm) multi-dimensional (2-D, 3-D and 4-D) workflow has been successfully applied to comprehensively characterise the Green River (Mahogany Zone) oil shale. Such an integrated imaging strategy provides valuable petrophysical characterization of heterogeneous fabrics in oil shales revealing important microstructural and mineralogical complexities. This contribution presents important scientific advances into one of the largest and mostly untapped unconventional energy resource with impact in the oil shale science and engineering community and in wider areas.

(2) State-of-the-art 2-D ultra-high resolution SEM imaging combined with MAPS Mineralogy allows for rapid spatial understanding and quantification of pore-mineral associations and oil shale rock fabrics. Automated tiling and stitching has proven to be a valuable tool to generate mosaic images of gigapixel size and can provide the simultaneous retrieval of nano-scale oil shale microstructural information, whilst maintaining correlation and association with oil shale heterogeneous fabric domains. In addition, this technique is valuable for selecting more representative FIB-SEM locations.

(3) High-resolution 3-D datasets from FIB-SEM has illuminated valuable qualitative and quantitative characterizations of the network and distributions of pores, organic matter and inorganic mineral phases over nm-μm scales for un-pyrolyzed and pyrolyzed samples. The gain in resolution to detect nano-scale features comes at the expense of the volume analysed. It is recommended that multiple oil shale sampling volumes be obtained to achieve statistical significance.

(4) X-ray micro-tomography at micron and sub-micron scale has provided valuable 3-D visualization and quantification of the organic matter network and the evolution of pore space in organic-rich and organic-lean zones with increasing pyrolysis temperatures (300-500°C). The results convincingly indicate that the pore structure evolution during pyrolysis is a strong function of the spatial distribution of organic content within oil shales.

(5) A novel experimental technique using dynamic synchrotron-based X-ray micro-tomography (4-D) has been applied to image the time evolution of the pore structure and connectivity during oil shale pyrolysis. The key finding is that there is a dramatic change in porosity accompanying pyrolysis between 390-400°C which results in a connected micro-fracture network predominantly along the kerogen-rich laminations. This is due to the build-up in internal vapour pressure of isolated pores to such an extent that the local mechanical strength of the oil shale matrix breaks down.

1.4 *Thesis Structure*

The unifying theme of this thesis is the development of an effective workflow of multi-scale multi-dimensional imaging and quantification of oil shale pyrolysis across a wide range of observational length scales over three orders of magnitudes.

This thesis is organised as follows:

Chapter 2 introduces a review of the literature relevant to this work and background information is presented related to oil shale including global deposits, oil shale types, composition (organic and mineral matter) and extraction technologies. A review of research conducted on oil shale pyrolysis reaction mechanisms, effect of oil shale pyrolysis parameters and oil shale imaging are presented.

Chapter 3 describes the experimental methods and analytical techniques used in this research including: sample selection, geochemical and rock analysis methods (XRD, TOC, programmed pyrolysis, thermogravimetric analysis, elemental analysis, modified fischer assay), optical microscopy, scanning electron microscopy, focused ion beam scanning electron microscopy and X-ray micro-tomography (laboratory and synchrotron-based). In addition, details of the pyrolysis of the oil shale samples are provided.

Chapter 4 provides results of the Green River (Mahogany Zone) oil shale samples characterised in 2-D using optical microscopy and SEM and in 3-D using X-ray micro-tomography. The impact of temperature on pore structure development during oil shale pyrolysis from 300-500°C is described along with 3-D visualization and quantification of the pore space in organic-rich and organic-lean regions.

Chapter 5 introduces imaging and analysis of oil shale pyrolysis using 3-D X-ray μCT at the sub-micron scale to capture the pore and organic network distributions. Ultra-high resolution SEM images under BSE mode resolve organic and mineral structures at the micro to nanometre scale. MAPS mineralogy is used to quantify the spatial distribution of minerals and 3-D FIB-SEM is applied to visualize organic and mineral hosted porosity and connectivity.

Chapter 6 provides results from dynamic oil shale imaging under pyrolysis conditions performed using synchrotron X-ray micro-tomography. This chapter offers analysis of the evolution of pore space as a function of temperature and time in organic-rich and organic-lean regions.

Chapter 7 presents the main conclusions and accomplishments of this research and provides suggestions for future work including studies related to correlative imaging, dynamic imaging, modelling, chemical variations in oil shales and hydrous pyrolysis.

Chapter 2

Literature Review

2.1 *Introduction*

The volume of literature on oil shale pyrolysis is comprehensive covering various aspects, including compositional analysis of oil shale rock and products formed as well as the effects of retorting conditions on product distribution. However, due to the very complex nature of the organic matter in oil shale, the exact mechanism of the complex kerogen decomposition process at the pore-scale and the flow behaviour of the produced oil and gas through the created pore network structure are yet to be fully characterised. Therefore, with state-of-the-art imaging techniques, this research is intended to make a valuable contribution to the oil shale industry. In this chapter, a review of the literature and background pertinent to this research is presented, including an overview of oil shale deposits (Section 2.3), oil shale types (Section 2.4), composition (Section 2.5) as well as a discussion on the complexities involved in the oil shale pyrolysis process (Section 2.7), oil shale technologies (Section 2.8) and the impact of various pyrolysis parameters on shale oil yield and quality (Section 2.9). Moreover, a review on advanced imaging techniques is given (Section 2.10) and an examination of the shortcomings of existing studies to characterise oil shales is provided. Moreover, a discussion is presented on how the application of particular imaging methods can lead to a better understanding of the evolution in petrophysical properties during oil shale pyrolysis.

2.2 *Defining Oil Shale*

Oil shale can be defined as a fine-grained sedimentary rock comprising organic matter that yields significant amounts of oil and combustible gas upon destructive distillation (Dyni, 2003). Most of the organic matter is insoluble in ordinary organic solvents; therefore, it must be decomposed by heating to release hydrocarbons in a process known as pyrolysis (Durand, 1980).

Oil shale is essentially a source rock, which is a geologically immature form of petroleum. Unlike crude oil, oil shale has not been subjected to high enough temperatures over an extended period of time to break the complex solid hydrocarbons down into lighter, liquid and gaseous compounds. Oil shale has received several names over the years including cannel coal, boghead coal, alum shale, stellarite, albertite, kerosene shale, bituminite, gas coal, algal coal, wollongite, schistes bitumineux, torbanite, and kukersite. Some of these names are still used today for certain types of oil shale. Also, oil shale was referred to as *the rock that burns* by The Ute Native Americans, as they observed oil shale outcrops bursting into flames as they were hit by lightning (Lee et al., 2014).

Oil shales from various deposits differ in their inorganic mineral content, chemical composition of organic matter, geological period of deposition, depositional environment, etc. (Cane, 1976; Duncan, 1976). In the literature, there are several definitions for oil shale based upon application, operational, or scientific point of view (Hutton, 1995). Similarly there are various oil shale classification schemes (Coshell et al., 1994; Durand, 1980; Hutton, 1995, 1987; Lee, 1990).

Schlatter (1968) described oil shale as "a heterogeneous mixture of organic and mineral matter. It is a fine-grained, tight rock with essentially no permeability or porosity". Ozerov and Polozov (1968) defined oil shale as "a hard foliated combustible rock formed by joint accumulation of pelagic plants and animals and mineral mass which had been transformed by the action of geographic conditions and chemical, biochemical and hydro-chemical processes". Gavin (1924) describe oil shale as a "compact laminated rock of sedimentary origin, yielding over 33% of ash and containing organic matter that yields oil when distilled, but not appreciably when extracted with ordinary solvents for petroleum." Therefore, no precise definition for the term "oil shale" exists, but in general it can be described as a fine-grained organic-rich sedimentary rock that yields substantial amounts of hydrocarbons upon pyrolysis.

2.3 *Oil Shale Deposits*

Oil shale is distributed widely throughout the world with known deposits in every continent. More than 600 oil shale deposits have been discovered around the world (Francu et al., 2007) with nearly 100 major deposits in 27 countries (Speight, 2014). These oil shale formations range from Cambrian to Tertiary in age and in extent from small deposits of little or no economic value to those of enormous size that dominate thousands of square kilometres and comprise many billions of barrels of potentially recoverable shale oil (Figure 2.1).

Currently, petroleum-based crude oil is cheaper to produce than hydrocarbons from oil shale because of the extra costs of mining and energy input required during the pyrolysis process. Given the higher costs, currently only oil shale deposits in Estonia, China and Brazil are being exploited. Estonia has been using its oil shale resources for oil and power production for near 100 years with 95% of the electrical needs of Estonia being produced from oil shale. China and Brazil already use oil shale as an energy source, while in the USA – which is estimated to hold approximately 72% of the world's oil shale reserves – significant research on oil shale technology developments are taking place. In addition to shale oil extracted from oil shale, by-products can add value to oil shale deposits. Uranium, vanadium, zinc, alumina, phosphate, sodium carbonate minerals, ammonium sulphate, and sulphur are some of the potential by-products. The spent shale after retorting has previously been used to manufacture cement, predominantly in Germany and China. Also, the heat energy acquired by the combustion of the organic material in oil shale can be used in the cement-making process.

Oil shale resources can be quantified in two different ways: (1) as tons of oil shale, and (2) as crude-shale-oil equivalents contained in the oil shale. Global deposits have been estimated to be about 411 metric gigatons (Oja and Suuberg, 2012) or to range from 2.8 to 3.3 trillion barrels (4.5×10^{11} to 5.2×10^{11} m^3) of recoverable oil equivalent (Caillé et al., 2007). This exceeds the world's proven conventional oil reserves, estimated at 1.3 trillion barrels (210×10^9 m^3). Estimates of oil shale reserves are provided in Table 2.1.

For oil shale deposits, it is important to distinguish between two terms: *resources* and *reserves*. Resources often refer to estimates of all deposits of oil shales, whereas reserves typically refer only to those from which oil extraction can be economically profitable with the use of existing technologies. Given that oil shale extraction technologies are constantly developing, oil shale reserve estimates will not remain constant over time, irrespective of use or discovery of new oil shale resources (Oja and Suuberg, 2012).

Table 2.1 Estimate of Oil Shale Reserves (Metric Tons × 10^6)

Region	Shale Reserves	Kerogen Reserves	Kerogen in Place
North America	3,340,000	80,000	140,000
South America	-	400	10,000
Europe	54,180	600	12,000
Middle East	35,360	4,600	24,000
Australia	32,400	1,700	37,000
Asia	20,570	1,100	-
Africa	12,373	500	5,900

Source: World Energy Council, WEC Survey of Energy Resources. To convert tons to barrels, multiply by 7 indicating approximately 620 billion barrels of known recoverable kerogen, which has been estimated to be capable of producing 2600 billion barrels of shale oil. This compares with 1200 billion barrels of known worldwide petroleum reserves (Source: BP Statistical Review of World Energy, 2008).

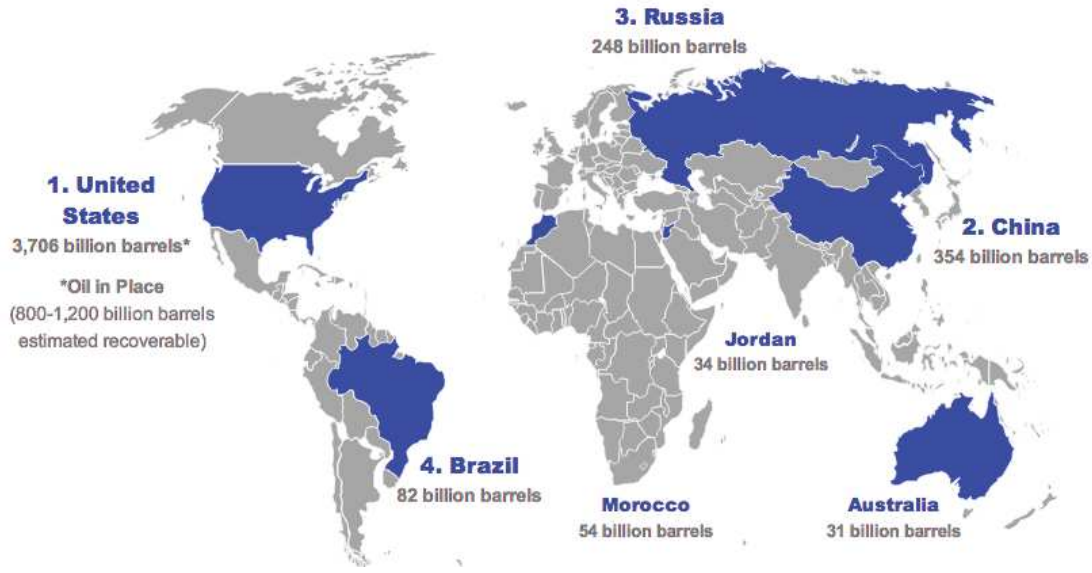

Figure 2.1 Oil shale is found in many places around the world with more than 600 known deposits. The largest oil shale resources are in the USA, Brazil, Jordan, Russia and Morocco. The most well-known and explored deposits include the Green River deposits in the western United States, the Tertiary deposits in Australia, deposits in Sweden and Estonia, the El-Lajjun deposit in Jordan, and deposits in France, Germany, Brazil, China, and Russia.

2.4 Oil Shale Types

Significant efforts have been made to systematically classify the different types of oil shales based on the depositional environment, petrographic character of the organic matter, and precursor organisms from which the organic matter was derived. A useful and often used classification of oil shales was developed by A.C. Hutton (1987; 1991; 1995), who pioneered the use of blue/ultraviolet fluorescent microscopy in the study of oil-shale deposits. Modifying petrographic terms from coal terminology, Hutton advanced a classification of oil shale based primarily on the origin of the organic matter. This classification has proved to be valuable for correlating various types of organic matter in oil shale with the chemistry of the hydrocarbons derived from oil shale.

Hutton (1987) divided organic-rich sedimentary rocks into three broad groups: (1) humic coals and carbonaceous shales, (2) bitumen-impregnated rock, and (3) oil shale (Figure 2.2). On the basis of the depositional environment, three basic groups of oil shales were recognised: terrestrial, lacustrine, and marine. Terrestrial oil shales include those composed of lipid-rich organic matter such as plant resins, spores, waxy cuticles, and corky tissue of roots and stems of vascular terrestrial plants commonly found in coal-forming swamps and bogs. Lacustrine oil shales are those containing lipid-rich organic matter derived from algae that lived in freshwater, brackish, or saline lakes. Marine oil shales are composed of lipid-rich organic matter derived from marine algae, acritarchs (unicellular microorganisms of questionable origin), and marine dinoflagellates (one-celled organisms with a flagellum).

Three major macerals (organic components) were recognised in oil shale: telalginite, lamalginite, and bituminite (Hutton, 1987). Telalginite is considered to be structured organic matter composed of large colonial or thick-walled unicellular algae such as Botryococcus and Tasmanites (Tyson, 1995). Lamalginite includes thin-walled colonial or unicellular algae that occur as distinct laminae, but displays little or no recognisable biologic structures (Hutton, 1995, 1988). Under the optical microscope, telalginite and lamalginite are easily identified by their bright shades of yellow under ultraviolet/blue fluorescent light (Figure 2.3). The third maceral, bituminite, is another important constituent in many oil shales. It is mostly amorphous, lacks

recognisable biologic structures, and displays relatively low fluorescence under the optical microscope. This material has not been fully characterised with respect to its composition or origin, although it is often a quantitatively important component of the organic matter in many marine oil shales (Cook and Sherwood, 1991). Other organic constituents include vitrinite and inertinite, which are macerals derived from the humic matter of land plants. These macerals are usually found in relatively small amounts in most oil shales (Hutton, 1991, 1995, 1987; Hutton et al., 1994).

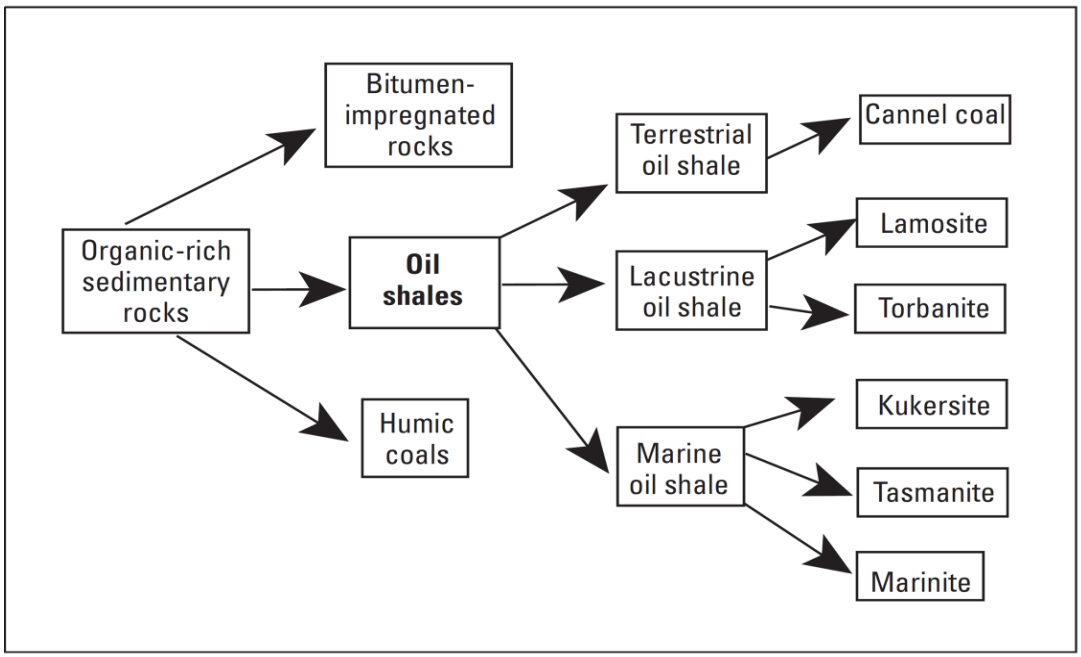

Figure 2.2 A classification of oil shales developed by Hutton (1987; 1991; 1995), who established the use of blue/ultraviolet fluorescent microscopy in the study of oil shale deposits. Oil shales are considered one of three broad groups of organic-rich sedimentary rocks: (1) bitumen-impregnated rock, (2) oil shales, and (3) humic coals. Hutton (1991) divided oil shales into three groups based on their depositional environment – terrestrial, lacustrine, and marine. Within this threefold grouping of oil shales, Hutton (1991) identified six specific oil shale types: cannel coal, lamosite, torbanite, kukersite, tasminite and marinate. The most common and largest deposits are marinites and lamosites.

Within the three-fold grouping of oil shales (terrestrial, lacustrine, and marine), Hutton (1987; 1991) distinguished six specific oil-shale types: (1) cannel coal, (2) lamosite, (3) torbanite, (4) kukersite, (5) tasmanite, and (6) marinate. The most abundant and largest deposits are lamosites and marinites (Dyni, 2003).

Cannel coal is a brown to black oil shale consisting of resins, spores, waxes, and cutinaceous and corky materials derived from terrestrial vascular plants together with varied amounts of vitrinite and inertinite. Cannel coals originate in oxygen-deficient

ponds or shallow lakes in peat-forming swamps and bogs (Dyni, 2003; Speight, 2012a).

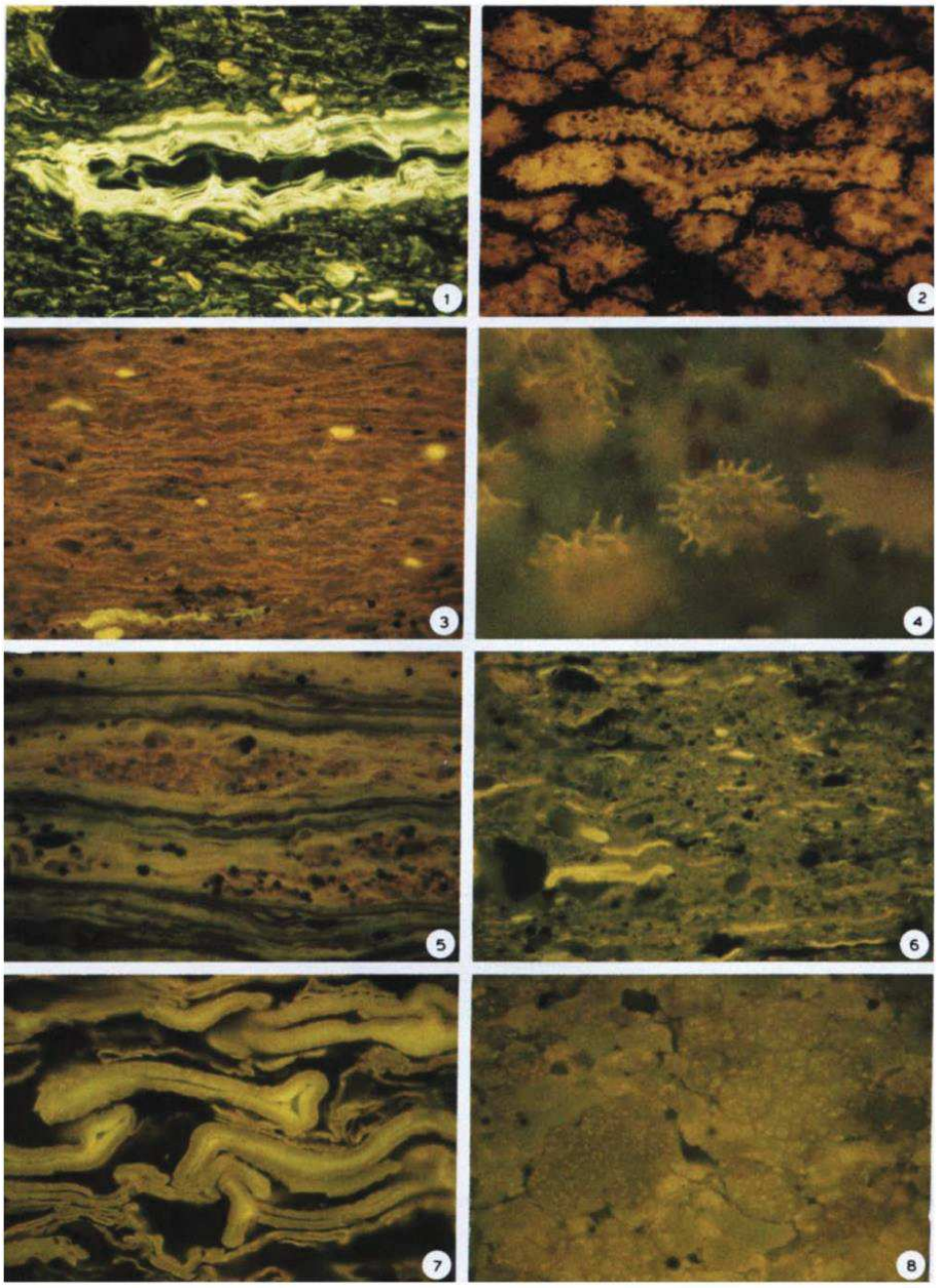

Figure 2.3 Oil shales (photographed in fluorescence mode; sections perpendicular to bedding: (1) Tertiary cannel coal, from Freshford (New Zealand), Field width = 0.34 mm. (2) Permian torbanite, from Newnes (New South Wales, Australia), Field width = 0.56 mm. (3) Tertiary lamosite, from Condor deposit (Queensland, Australia), Field width = 0.28 ram. (4) Very low grade lamosite, from the Rundle deposit (Queensland, Australia), Field width = 0.28 mm. (5) Tertiary lamosite, from the Green River Formation (Colorado, U.S.A.), containing abundant layered lamalginite, Field width = 0.22 mm, (6) Cretaceous marinite, from the Toolebuc Formation (Queensland, Australia), Field width = 0.28 mm. (7) Permian tasmanite, from the Mersry River area (Tasmania, Australia), composed of abundant telalginite, Field width = 0.44 mm. (8) Ordovician kuckersite, from Estonia, composed of telalginite derived from the alga Gloeocapsomorpha, Field width = 0.44 mm (Hutton 1987).

Lamosite oil shales can appear as both pale- and greyish-brown and dark grey to black where the main organic constituent is lamalginite derived from lacustrine (lake-like) planktonic algae. Minor constituents in lamosite oil shales include vitrinite, inertinite, telalginite, and bitumen. The Green River oil-shale deposits in western United States and a number of the Tertiary lacustrine deposits in eastern Queensland, Australia, are lamosites (Gibson, 1989; Hutton, 1995).

Torbanite, kukersite and tasmanite are associated to particular types of algae from which the organic matter was derived; the names are based on local geographic features. Torbanite, named after Torbane Hill in Scotland, is a black oil shale whose organic matter consists predominantly of telalginite derived largely from lipid-rich Botryococcus and related algal forms found in fresh- to brackish-water (slightly salty) lakes (Speight, 2012a). It also contains small quantities of vitrinite and inertinite. The deposits are typically small, but can be extremely high grade (Dyni, 2003).

Kukersite, which takes its name from Kukruse Manor near the town of Kohtla-Järve, Estonia, is a light brown marine oil shale. Its main organic constituent is telalginite originating from the green alga, Gloeocapsomorpha prisca (Derenne et al., 1990; Hutton, 1982). The Estonian oil-shale deposit in northern Estonia along the southern coast of the Gulf of Finland and its eastern extension into Russia, the Leningrad deposit, are considered to be kukersite oil shales(Cook and Sherwood, 1991). Compared with other rocks containing telalginite, kukersites have low atomic H/C (1.48) and high atomic O/C (0.14) ratios and generally plot as type II kerogen on the van Krevelen diagram (further details provided in Section 2.5.1).

Tasmanite, named from oil-shale deposits in Tasmania, is a brown to black marine oil shale. It is commonly associated with high-latitude, nutrient-rich, marginal marine settings in Permina of Tasmania (Energy, 2008). The organic matter consists of telalginite derived chiefly from unicellular tasmanitid algae of marine origin and lesser amounts of vitrinite, lamalginite, and inertinite.

Marinite is a grey to black oil shale of marine origin in which the chief organic components are lamalginite and bituminite derived chiefly from marine

phytoplankton. Marinite may also contain small amounts of bitumen, telalginite, and vitrinite. Marinites are deposited typically in epeiric (inland) seas such as on broad shallow marine shelves or inland seas where wave action is restricted and currents are minimal. The Devonian–Mississippian oil shales of eastern United States are typical marinites. Such deposits are generally widespread covering hundreds to thousands of square kilometres, but they are relatively thin, often less than about 100 m. The Irati oil shale (Permian) in Brazil is another example of a marintie oil shale which extends for more than 1000 kilometres from north to south (Dyni, 2003). The Jurassic marine shales of western Europe, the Cambrian shales of northern Siberia and northern Europe and the Silurian shales of North Africa are further examples of marinite oil shales (Tissot and Welte, 1978).

2.5 Oil Shale Composition

2.5.1 Organic Matter

Oil shale organic matter consists of solvent-soluble and insoluble organic materials. The organic matter in oil shales is mostly in the form of solvent insoluble cross-linked macromolecular structure referred to as kerogen. Oil shales also contain a small amount of bitumen which is a benzene-soluble organic material (generally not exceeding 1-2% (Allred, 1966; Gao, 2009)). The term *kerogen* was first applied by Crum-Brown in 1912 to denote specifically the insoluble organic matter in oil shale (Hutton, 1995; Yen, 1976). Nowadays, the term kerogen is often used to characterise solid organic matter in all sedimentary rocks (Lee et al., 2007; Oja and Suuberg, 2012; Speight, 2012a)

The composition of kerogens is typically presented based on carbon (C), hydrogen (H), nitrogen (N), oxygen (O) and sulphur (S) content. Table 2.2 presents some example kerogen elemental compositions from major oil shale deposits. The composition and properties of kerogen vary somewhat from deposit to deposit, but may also differ within a deposit.

Table 2.2 Examples of kerogen elemental composition (CHNOS) for various oil shale deposits (Probstein and Hicks, 2006). A major advantage of oil shales over other solid fossil fuels is the relatively high hydrogen to carbon atomic ratios (H/C) in the organic matter, which allows for the production of a wide range of chemical products.

Oil Shale	C	H	N	O	S	H/C	O/C
Kukersite (Estonia)	77.3	9.8	0.4	10.8	1.7	1.52	0.105
Green River (USA)	78.3	9.9	2.1	8.1	1.6	1.52	0.078
Dictyonema (Estonia)	70.5	7.4	2.5	15.4	4.2	1.26	0.164
Kasphir (Russia)	67.1	8.0	1.2	13.5	10.2	1.43	0.151
Timahdit (Morocco)	68.9	8.5	3.0	12.6	7.0	1.48	0.137
Eastern Devonian (USA)	82.0	7.4	2.0	6.3	2.3	1.08	0.058

One of the important advantages of oil shale over other solid fossil fuels is that they possess relatively high hydrogen to carbon atomic ratios (H/C) (typically 1.2–1.6), at least in comparison to coals for which this ratio is typically less than unity. It is the high hydrogen to carbon ratio (combined with low oxygen to carbon ratio) which allows the production of a wide range of chemical products, including motor fuels and premium lubricating oils. Figure 2.4 shows the H/C atomic ratios in various hydrocarbon materials (Raja et al., 2017; Strizhakova and Usova, 2008).

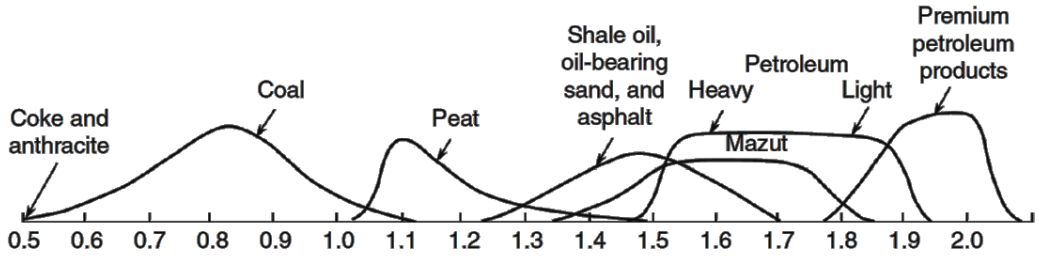

Figure 2.4 H/C atomic ratios in various hydrocarbon materials (Strizhakova and Usova, 2008).

The macromolecular structure of kerogen in oil shale is a complex mixture of organic compounds. It is composed of highly variable structural units, both in terms of size and chemical character. The average molecular weight is in the order of 3000, and an approximate empirical formula would be $C_{200}H_{300}N_5O_{11}S$ (Deo and Tiwari, 2008). Siskin and Katritzky (1995) investigated the chemical properties of kerogen and proposed a kerogen model in the form of $C_{647}H_{1017}N_{19}O_{17}S_4$ (Figure 2.5). More recently, Bousige et al. (2016) performed X-ray scattering, neutron diffraction and inelastic neutron scattering experiments to construct molecular models of mature and immature kerogens using a combined approach of molecular dynamics and hybrid reverse Monte Carlo (MD-HRMC) simulations.

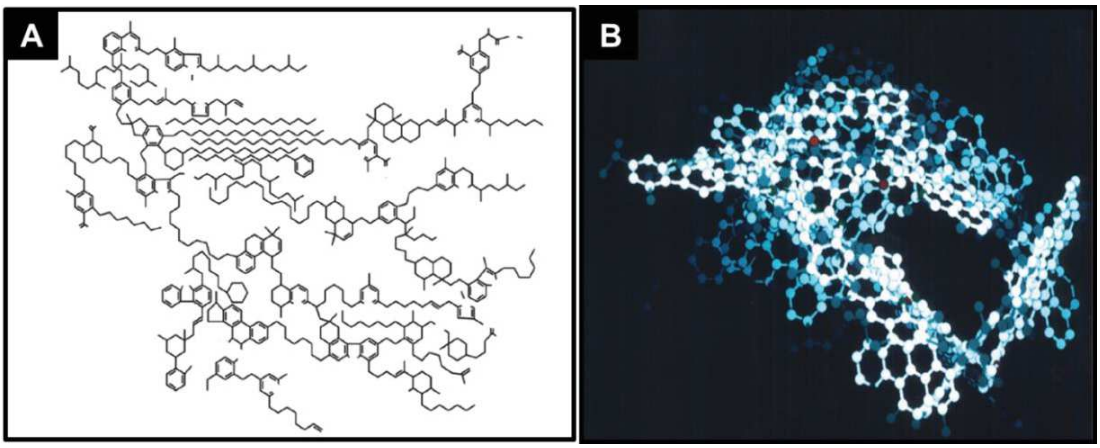

Figure 2.5 (A) Oil shale molecular model $C_{645}H_{1017}O_{17}S_4N_{15}$ proposed by Siskin and Katritzky (1995) and Liu et al. (2015). (B) 3-D representation, using the XMol software, of a type III kerogen structure at the end of catagenesis. Only C atoms (aromatic in white, aliphatic in blue), O atoms (in dark green) and N atoms (in red) are represented (Vandenbroucke, 2003).

Given kerogen's insolubility in organic solvents (Koel et al., 2001), it has been difficult to characterise its chemical character. Attempts to liberate it from the oil shale rock involve the risk of chemical degradation. Even if the approach involves dissolving away the mineral matter, there are concerns regarding whether the kerogen has been altered. In addition, there is also the difficulty of reliably characterizing the chemical structure of a solid organic macromolecular substance once it is isolated.

The chemical structure of kerogen is determined by several factors including the composition of initial organic matter and the process of chemical conversion during diagenesis. The chemical composition of the kerogen has been the subject of many studies (Behar and Vandenbroucke, 1987; Burnham, 2017a; De Leeuw and Largeau, 1993; Durand, 1980; Wang et al., 2016), but whether or not the data are indicative of the true nature of the kerogen is extremely speculative, as one can do little more than characterise average structures or structural elements.

Kerogens can be classified in various ways on the basis of elemental composition. One of the most common is based on the Van Krevelen diagram originally developed for classifying coals (Van Krevelen, 1950) . Kerogens are placed into certain groups on the basis of the atomic ratios of hydrogen to carbon and oxygen to carbon. Kerogens can be classified as Type I, II, III or IV (Table 2.3), with further

subgrouping according to sulphur content. Oil shale kerogens are predominantly Type I (Green River Oil Shale from Uinta Basin is a typical kerogen of this group) and II (Torcian Oil Shale from the Paris Basin is an example from this group). The less common coaly shales belong to Type III (Upper Cretaceous sedimentary rock from the Doula Basin, as one example) (Durand and Monin, 1980; Vandenbroucke and Largeau, 2007).

Kerogen form can be classified into four major groups: alginate, exinite, vitrinite and inertinite (Table 2.3). The alginate/exinite macerals are characterised by high hydrogen content and therefore have excellent liquid hydrocarbon-generating potential (Zou, 2017). Type I kerogens are composed mainly of alginite and characteristically have a high atomic H/C ratio. Typically, for Type I kerogens H/C > 1.25 and O/C < 0.15. Type II kerogen has intermediate properties between type I and type III and is mainly derived from organic matter deposited in a marine setting. Typically, for Type II kerogens H/C < 1.25 and 0.03 < O/C < 0.18. Type III kerogens are derived from terrestrial plant material and have a low H/C ratio. Generally for Type III H/C < 1.0 and 0.03 < O/C < 0.3 (Figure 2.6). Type IV kerogens contain mainly reworked organic debris and highly oxidized material of various origins. They are generally considered to have essentially no hydrocarbon-source potential (Vandenbroucke and Largeau, 2007).

Table 2.3 Kerogen type, form and origin (adapted from Glorioso and Rattia (2012)). There are four types of kerogen: (1) Type I, which consists mainly of algal and amorphous constituents; (2) Type II, which consists of mixed terrestrial and marine source material; (3) Type III, which consists of woody terrestrial source material; and (4) Type IV, which is derived from reworked organic matter or from highly oxidised material.

Environment	Kerogen type	Kerogen form	Origin
Aquatic	I	Alginite	Algal bodies
		Amorphous Kerogen	Structureless debris of algal origin
	II		Structural planktonic material, primarily of marine origin
Terrestrial		Exinite	Skins of spores and pollen, cuticle of leaves and herbaceous plants
	III	Vitrinite	Fibrous and woody plant fragments and structureless, colloidal humic matter
	IV	Inertinite	Oxidised, recycled woody debris

Hydrocarbon potential	Oil	Gas	None

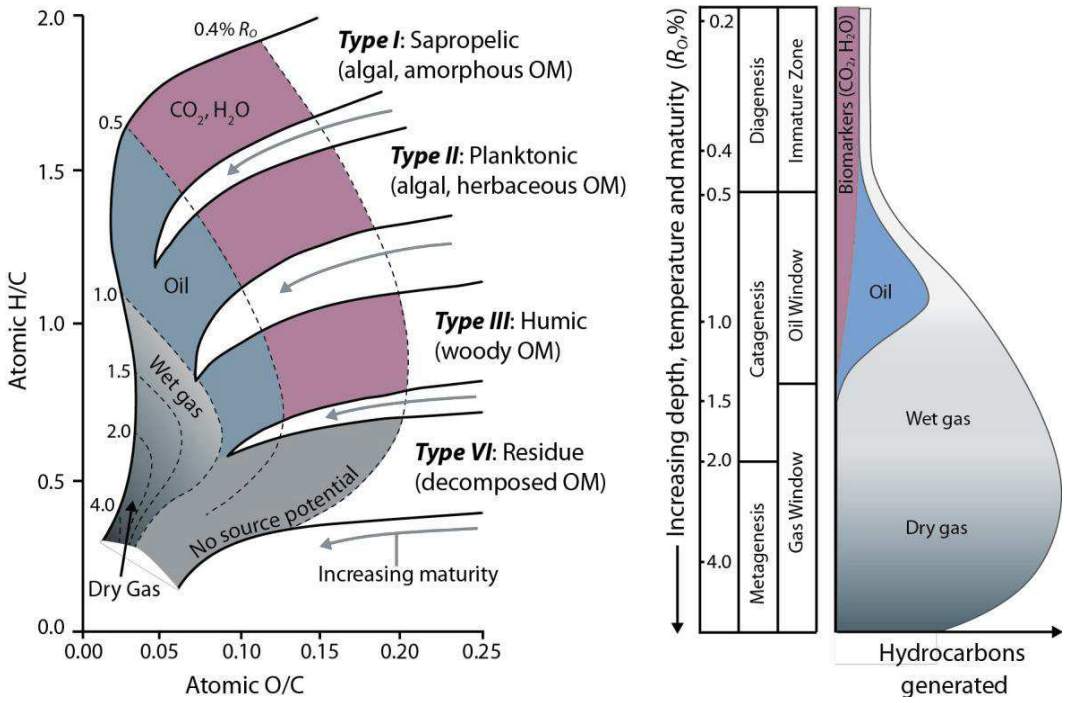

Figure 2.6 Van Krevelen diagram showing kerogen type and evolutionary path. Van Krevelen diagram (left) displays kerogen type and evolution with thermal maturity (Ro). The table and schematic model (right) show the timing and relative abundance gas generated with maturity (adapted from Boyer et al., 2006; Glorioso and Rattia, 2012; Mastalerz et al., 2013; Seewald, 2003).

2.5.2 Mineral Matter

Oil shale mineral matter includes several classes of minerals such as carbonates (calcite and dolomite), silicates, sulphides, and others. From one oil shale deposit to another, the inorganic composition can vary widely. The mineralogical composition of some oil shales is composed of carbonate minerals such as calcite and dolomite with lesser amounts of aluminosilicate minerals whereas, for other oil shales, the reverse is true (quartz, feldspars and clay minerals are dominant). In many deposits, small but ubiquitous quantities of sulphide minerals (pyrite, marcasite and pyrrhotite etc.) indicate to dysaerobic or anoxic waters in which the organic matter accumulated and was preserved.

A typical mineral composition (in weight percent of the mineral matter) of carbonate-rich Kukersite oil shale from Estonia is 65% calcite, 3% dolomite, 8% quartz, 15% illite, 5% orthoclase, 1% chlorite, and 3% pyrite (Puura, 1999). By comparison, the siliceous Eastern US Devonian oil shale (Probstein and Hicks, 2006) has a typical mineral composition of 28% quartz, 40% illite, 12% feldspar and 14% pyrite.

Frequently, mineral matter composition is represented by the chemical composition of oil shale ash, in which the mineral components have been converted to their oxides during combustion. This is shown in Table 2.4. However, it is important to note that mineral matter can be fundamentally altered by the combustion process, and therefore the ash composition can only be an approximate guide to the mineral content of the raw oil shale.

Table 2.4 Mineral Matter composition for selected oil shale deposits presented as oxides in ash, wt%.

Compound	Green River (USA)	Kukersite (Estonia)	El-lajjun (Jordan)	Dictyonema (Estonia)
SiO_2	40-60	28.25	28.86	63.72
Al_2O_3	10-15	9.84	7.43	16.43
Fe_2O_3	5-10	5.44	3.70	8.80
CaO	10-25	41.02	52.79	0.85
MgO	5-10	5.05	1.30	0.50
K_2O	-	3.60	-	8.72
Na_2O	-	-	0.3	-
SO_3	-	6.07	1.30	0.70
P_2O_5	-	-	5.9	-

2.6 *Oil Shale Grade*

The grade of oil shale can be determined by several methods and the results can be expressed in variety of units. One method is to use a calorimeter to determine the heating value of an oil shale. The results can be reported in British thermal units per pound of oil shale (Btu), calories per gram of rock (cal/gm), kilocalories per kilogram of rock (kcal/kg) and mega joules per kilogram of rock (MJ/kg) (Dyni, 2003). The heating value is useful for determining the quality of an oil shale used as a solid fuel in a power plant to produce electricity. Although the heating value of a given oil shale is a useful and fundamental property of the rock, it does not provide information on the amounts of shale oil or combustible gas that an oil shale is capable of producing (Gao, 2009).

An alternative method to determine the grade of an oil shale is to measure the yield of oil that an oil shale can produce in a laboratory retort (destructive distillation). This is considered the most common method to evaluate oil shale resources. This method is often referred to as the *Modified Fischer Assay*, initially developed in Germany, then adapted by the U.S. Bureau of Mines (Stanfield and Frost, 1949). The procedure was then standardized as the American Society for Testing and Materials

Method D-3904-80 (1984). Some laboratories have further modified the Fischer Assay method to enhance the evaluation of different types of oil shales and various methods of oil-shale processing (Dyni, 2003).

When oil shale is retorted, the organic matter breaks down into oil, gas, and residual organic carbon char that remains with the retorted shale. In the Fischer assay method, the amounts of individual gases (commonly methane, ethane, hydrogen and carbon dioxide) are not often individually determined but are typically reported collectively as *gas plus loss* which is the difference of 100 weight percent minus the sum of the weights of oil, water, and spent shale (solid residue from oil shale retorting).

A further shortcoming of the Fischer assay method is that it does not necessarily determine the total available energy or maximum amount of oil that can be produced by an oil shale sample. Retorting methods such as the Tosco II process, is known to produce in excess of 100% of the oil yield reported by the Fischer assay method (Crawford et al., 2008a). Other retorting methods, such as the Hytort process can increase oil yields of some oil shales by as much as 300 to 400% of that obtained from the Fischer assay technique (Oja and Suuberg, 2012). Therefore, Fischer assay analyses can only provide an approximation to the energy potential of an oil shale deposit.

2.7 *Oil Shale Pyrolysis Process*

The organic matter (kerogen) within oil shale is typically less than one third of the shale weight and cannot be extracted by solvent methods. The principal method of producing oil from oil shale is by heating up the resources between 300 to 500°C, in a process known as pyrolysis (William et al., 2010; Lee et al., 2007; Speight, 2012a). Kerogen is a cross-linked high molecular weight solid and under thermal heating, breaks down into lighter hydrocarbon products. Among the oil shale technologies, retorting is a pyrolysis process and is often considered to be the most effective method for extracting shale oil from oil shales (Hascakir et al., 2008; Jiang et al., 2015). This process is performed by heating the oil shale resource within a vessel known as a retort which promotes pyrolysis efficiency (Oja and Suuberg, 2012). The composition of the products formed during oil shale pyrolysis strongly depends on

the fundamental chemistry of the organic matter in the oil shale and the configuration of the reactor configuration.

The processes or mechanisms of thermo-oxidative decomposition (in air/combustion) and pyrolysis (without air) are different. The presence of oxygen leads to oil shale oxidation and consequently, to the formation of CO, CO_2 and oxygen-containing volatile substances having negative influences on the yield and quality of shale oil (Avid et al., 2000).

Oil shale pyrolysis can be considered analogous to geological processes that lead to the generation of conventional oil. Oil shale is often classed as an unconventional resource because the resource has to be artificially heated at a much faster rate than the geological timescale. With the input of energy in the form of heat, the breakdown of the organic material into volatile components is accelerated. The volatile components can range from light organic and inorganic gases to very heavy liquid including bitumen (Chilingarian and Yen, 2011). Upon condensation of the gaseous products, shale oil is produced (Figure 2.7). In addition to the shale oil, a carbonaceous residue is produced in the form of char/coke due to hydrogen deficiency (Braun and Rothman, 1975; Lee, 1990).

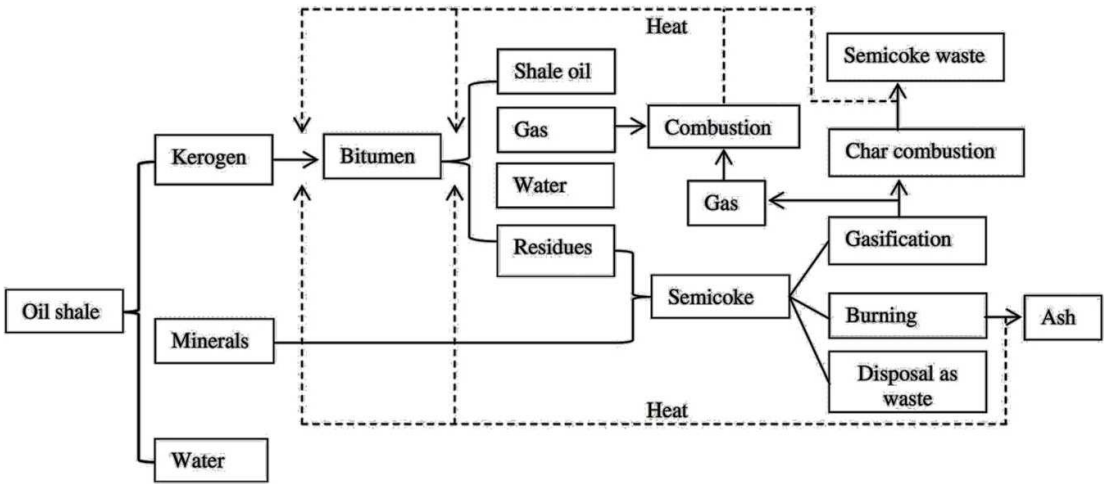

Figure 2.7 General flow diagram of the oil shale retorting process. Oil shale is a complex mixture of kerogen, minerals and water. The kerogen, the organic fraction present as a complex combination of carbon, hydrogen, sulfur and oxygen, cannot be extracted with ordinary solvents due to its macromolecular character. Therefore, heating is required to break down the kerogen network structure and release the shale oil. Upon heating oil shale in the absence of air, residual moisture is first driven off and then the kerogen is initially converted to bitumen. Formed bitumen thermally degrades to shale oil, gas, carbonaceous residues and pyrolytic water, among which shale oil, gas and water leave

(vaporize) from the shale particle matrix. Carbonaceous residues remain mixed in with the minerals, forming the solid residues known as semicoke (Han et al., 2014).

Oil shale pyrolysis products evolve when kerogen approaches a critical temperature. The pyrolysis reaction continues to completion given sufficient temperature and/or time. The consensus in the literature is that the oil shale pyrolysis temperature range for laboratory condition is 300 to 500°C (Gregg et al., 1981; Jaber et al., 1999; Kok and Pamir, 2003; Lee, 1990). Given that the chemical structure of kerogen is a complex heterogeneous mixture of organic compounds, the exact sequence of reactions that take place during oil shale pyrolysis is largely unknown (Gregg et al., 1981; Lee et al., 2014; Tiwari and Deo, 2012). A number of researchers have concluded that kerogen demonstrates properties of pyro-bitumen and when heated, kerogen decomposes by a consecutive reaction into bitumen. The bitumen does not vaporize but rather stays in the oil shale (Hubbard and Robinson, 1950) and can act as a solvent for the remaining organic matter (Allred, 1966). With further heating, this bitumen breaks down or cracks to produce oil, gas, and a carbonaceous residue (char/coke) (Motlep et al., 2007; Niu et al., 2013; Qian and Wang, 2006; Wang et al., 2011).

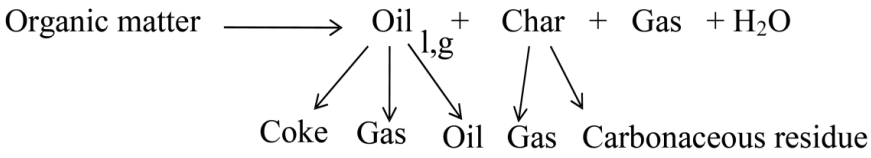

Figure 2.8 Simplest mechanism of oil shale pyrolysis.

Hubbard and Robinson (1950) investigated Colorado (Parachute and Rifle) oil shale samples with varying quantities of organic material, at a range of pyrolysis temperatures (350 to 525°C) under atmospheric pressures. The oil shale samples were extracted by removing the naturally present bitumen and the insoluble kerogen material. The results indicated that the bitumen (soluble organic material) in the raw oil shale had no significant effect upon the rate of thermal decomposition of kerogen. It was concluded that extracted kerogens from oil shales originating from different sources follow relatively the same reaction rate at corresponding temperatures. Allred (1966) reinterpreted this data and determined that the bitumen has a catalytic or solvent effect on the breakdown of kerogen.

It is understood that kerogen is predominantly a loosely interconnected structure of partly unsaturated chains and rings (Orendt et al., 2013; Solum et al., 2014; Tong et al., 2011; Van Den Berg, 1975; Vitorovic, 1980). The rupture of cross-linkage of these interconnected structures takes place first mainly from the rupture of weak chemical bonds such as C–O and C–S bonds, and/or the rupture of branched functional groups in the kerogen long molecular structure. The complexity of the thermal decomposition process of oil shale has been hypothesized based on experimental observations and measurements, such as the formation of bitumen as an intermediary phase followed by subsequent reactions (Bai et al., 2015; Burnham, 2015; Fletcher and Pugmire, 2016; Lü et al., 2014; Tiwari and Deo, 2012; Wang et al., 2014). A number of competitive reactions are thought to take place during oil shale pyrolysis (Parker and Zhang, 2006). A summary of oil shale pyrolysis reactions are presented in Table 2.5 (Parker and Zhang, 2006).

Rajeshwar et al. (1979) proposed several mechanisms for oil shale pyrolysis. However, the most common pyrolysis decomposition mechanism has been the two-step mechanism: (1) primary pyrolysis and (2) secondary pyrolysis. These reactions progress with competitive reaction mechanisms and with varying rates depending on pyrolysis conditions. The gaseous products consist of very light hydrocarbons and inorganic gases, CO_2 and H_2, while the shale oil is a mixture of condensable hydrocarbons (heavy and light oils) in vapour-liquid equilibrium. The fraction of oil in vapour and liquid phases is dependent on the boiling point distribution of the mixture components and pyrolysis temperature and pressure. Water can be generated from sources such as free water and bound water from organic and mineral decomposition.

Table 2.5 A summary of oil shale pyrolysis reactions (Parker and Zhang, 2006).

Description	Reaction
Primary pyrolysis	$kerogen_{(s)} \rightarrow oil_{(l)} + gas_{(v)} + H_{2(v)} + CH_{4(v)} + CO_{2(v)} + H_2O_{(v)} + char1_{(s)}$
Secondary pyrolysis	$char1_{(s)} \rightarrow H_{2(v)} + CH_{4(v)} + char2_{(s)}$
	$char2_{(s)} \rightarrow H_{2(v)} + ROC_{(s)} + ROH_{(s)}$
Carbon gasification	$ROC_{(s)} + CO_{2\,(v)} \rightarrow CO_{(v)}$
Dolomite decomposition	$MgCa(CO_3)_{2(s)} \rightarrow CaCO_{3(s)} + MgO_{(s)} + CO_{2\,(v)}$
Calcite decomposition	$CaCO_{3(s)} + SiO_{2(s)} \rightarrow Ca_2SiO_{4(s)} + CaO_{(s)} + CO_{2(v)}$
Oil coking	$oil_{(l)} \rightarrow H_{2(v)} + CH_{4(v)} + ROC_{(s)} + coke_{(s)}$
Water-gas shift	$CO_{(v)} + H_2O_{(v)} \rightarrow CO_{2(v)} + H_{2(v)}$
Bound water floss	$H_2O_{(s)} \rightarrow H_2O_{(v)}$
Water distillation/ condensation	$H_2O_{(l)} \rightarrow H_2O_{(v)}$
Oil distillation/ condensation	$oil_{(l)} \rightarrow oil_{(v)}$

Burnham (2017a; 2017b) used multiple datasets to argue that this two-step decomposition mechanism (kerogen → bitumen → oil) is not appropriate to fully describe the decomposition mechanism of oil shale pyrolysis. More complex kinetic analysis procedures have also been used in deriving kinetics of decomposition of oil shales (Bai et al., 2015; Deo and Tiwari, 2008; Kök and Iscan, 2007).

During the pyrolysis of oil shale, several coupled physical and chemical phenomena occur simultaneously, including heat transfer, chemical reaction kinetics, multiphase flow, phase changes, and mineral alteration and interaction. These processes are highly coupled and interrelated, therefore, isolating each phenomenon accurately is challenging. The changes in the physical properties (density, heat capacity, permeability, porosity, etc.) due to the local thermodynamic conditions may also

alter the product distribution. For example, the chemical reaction kinetics of oil shale pyrolysis is relatively complex with several hundred products being formed during decomposition. The distribution of these products (vapour or liquid) and their formation rates depend on the local conditions.

2.8 *Oil Shale Technologies*

In recent decades, energy companies have developed, tested, modified, and in many cases, established promising technologies for extracting shale oil from oil shale resources. A single approach to the thermal processing of oil shale is difficult to determine and process parameters and implementation are difficult to optimize because of differences in the composition and properties of oil shale from various deposits. The composition and quantitative ratios between the pyrolysis products of oil shale depend on many factors: the type and origin of the organic matter of oil shale, the final process temperature, the rate of heating, the residence time in a high-temperature zone, grain-size composition and pressure.

Production processes generally fall into two broad categories: (1) *ex situ* (above ground) *and (2) in situ* (underground). *Ex situ* production, which involves mining near surface oil shale deposits and retorting under anaerobic conditions at temperatures near 500°C, for times on the order of an hour (Han et al., 2009; Lee et al., 2007). On the other hand, *in situ* production technologies, which involve heating oil shale in the geological formation in the range of 300−350°C from days to months (Brandt, 2008; Liu et al., 2009; Scouten, 1990; Qian and Wang, 2006; Biglarbigi et al., 2009; Oja and Suuberg, 2012; Lee et al., 2014). Both ex-situ and *in situ* methods are summarised in Figure 2.9.

In general, surface processing consists of three major steps: (1) oil shale mining and ore preparation, (2) pyrolysis of oil shale to produce kerogen oil, and (3) processing kerogen oil to produce refinery feedstock and high-value chemicals (Biglarbigi et al., 2009; Speight, 2012a). For deeper, thicker deposits, not as amenable to surface or deep-mining methods, the shale oil can be produced by *in situ* technology. *In situ* processes minimize the requirement for mining and surface pyrolysis, by heating the oil shale resource in its natural depositional setting.

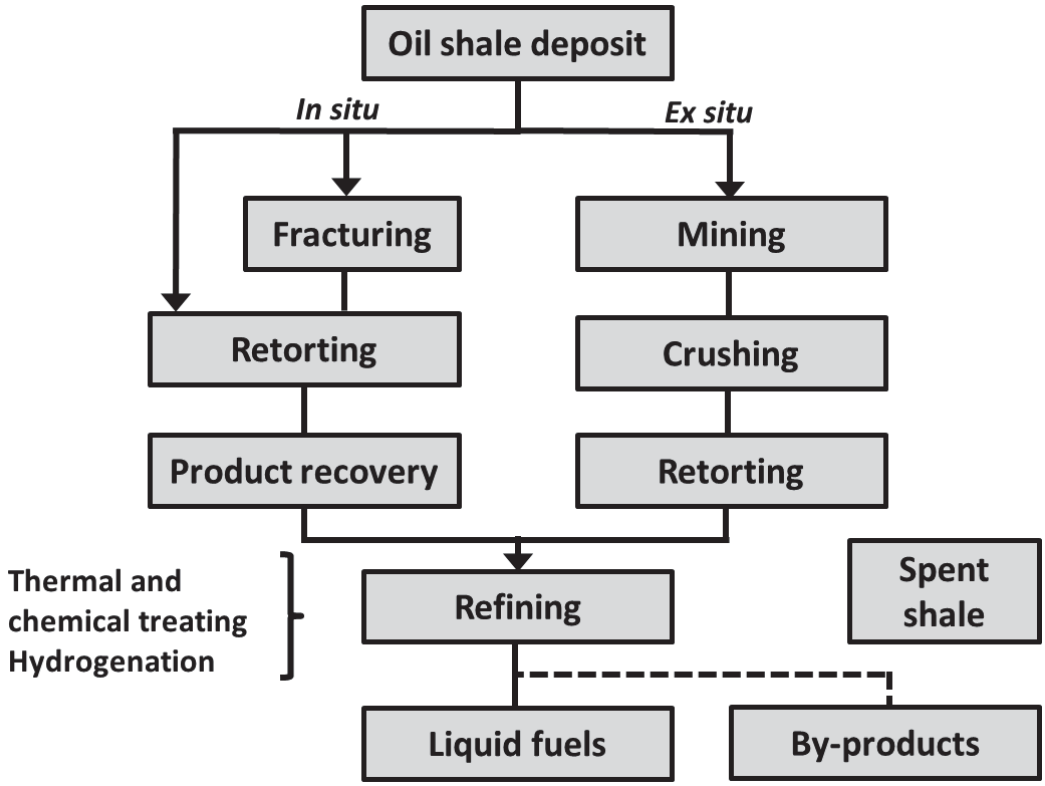

Figure 2.9 Oil Shale *ex situ* and *in situ* conversion processes. *Ex situ* retorting is carried out above the ground after the oil shale is mined and crushed, whereas *in situ* processes are carried out in the subsurface, within the existing formation.

Depending on the depth and other characteristics of the target oil shale deposits, either surface mining or underground mining methods may be used. Another way in which the various retorting processes differ is the manner by which heat is provided to the shale by hot gas: (1) by a solid heat carrier or (2) by conduction through a heated wall. After mining, the oil shale is transported to a facility for retorting, after which the oil must be upgraded by further processing before it can be sent to a refinery. Following this, the spent shale must be disposed of, often by putting it back into the mine.

At present, the commercial surface retorting technologies are: Estonian Kiviter lump shale retorting, Estonian Galoter particulate oil shale retorting, Brazilian Petrosix lump shale retorting, Chinese Fushun retorting; and Australia has scaled up Canadian Taciuk particulate shale retorting, called Aostra Taciuk Processing (ATP).

Table 2.6 Comparison of commercial oil shale retort technologies (adapted from Qian et al. 2008).

Retort	Chinese Generator	Kiviter	Galoter	Petrosix	Alberta Taciuk
Company	Fushun Shale Oil	Viru Keemia	Narva Power	Petrobras	SPP
Country	China	Estonia	Estonia	Brazil	Australia
Location	Fushun	Kohtla Jarve	Narva	Sao Mateus do Sul	Stuart
Oil Shale T/d	100	1000/200	3000	6200/1600	6000
Size, mm	10-75	10-125	0-25	6-50	0-25
Configuration	Vertical Cylinder	Vertical Cylinder	Horizontal Cylinder	Vertical Cylinder	Horizontal Cylinder
Heat Carrier	Gas	Gas	Ash	Gas	Ash
Oil Yield, % Fischer Assay	65	75-80	85-90	90	85-90

Currently, the Fushun and Kiviter type retorts are both in commercial use. In these technologies, a vertical cylindrical type retort is used to process oil shale with gas serving as a heat carrier (Qian et al., 2008). These retorts are classified as internal combustion technologies. Oil shale breaks down in the upper section of the retort, and semicoke is gasified with rising air–steam and smoulders in the lower part, serving to heat the gases necessary for retorting oil shale in the upper part. Given that any excess air escaping from the bottom into the upper section will burn out part of the generated shale oil, the oil yield is often not high, and is typically below 80% of Fischer assay (Han et al., 2014).

The Galoter retorting process is generally considered to be a lower environmental impact technology and has been recommended in the national development plan of Estonia. It is an above-ground oil shale retorting technology that uses hot recycled solids as a heat carrier (Qian et al., 2008). The process uses a horizontal cylindrical rotating kiln-type reactor for retorting particulate oil shale, and a separate but integrated aero-fountain furnace for burning the semi coke (Shuzhao et al., 2011). The concentration of organic substance in the ash finally discharged from this process is below 1% (Golubev, 2003). Up to now, two Galoter retorts, each with unit throughput rate of 3000 t/d raw oil shale, have been in operation at the Oil Factory of Narva Elektrijaamad (Han et al., 2014).

Brazil's Petrosix vertical retort consists an upper retorting and a lower semi coke cooling section (Crawford et al., 2008a; Martignoni and Rodrigues, 2002). Fuel gases produced during the retorting of oil shale are mainly divided into three parts: one part is used as fuel in a tubular heater, the second is heated in the heater's pipes to above 500 °C and recirculated back to the retort as hot carrier gas for heating and pyrolysing oil shale, and the third is circulated and enters into the bottom of the retort as a cooling medium for the hot semi coke (Qian et al., 2008). Two large Petrosix retorts with capacities of 1500 and 6200 t/d oil shale respectively, have been built by the Petrobras Company at Sao Mateus do Sul (Han et al., 2014).

The Alberta Taciuk Processor (ATP) retort (Figure 2.10) is another solid heat carrier technology that has been scaled up to 6000 t/d oil shale capacity at Stuart, Australia by the Australian SPP Company in 1999. Its distinctive characteristic is that drying and retorting of oil shale, as well as the combustion, recycling, and cooling of spent materials and residues, all occur within a single rotating multi-chamber horizontal retort (Brandt, 2008; Qian et al., 2008). Semi coke from the pyrolysis zone is burned in a combustion zone, heating recycled solids as heat carrier, and forming ash discharged with total organic carbon of less than 3% (Johnson et al., 2004).

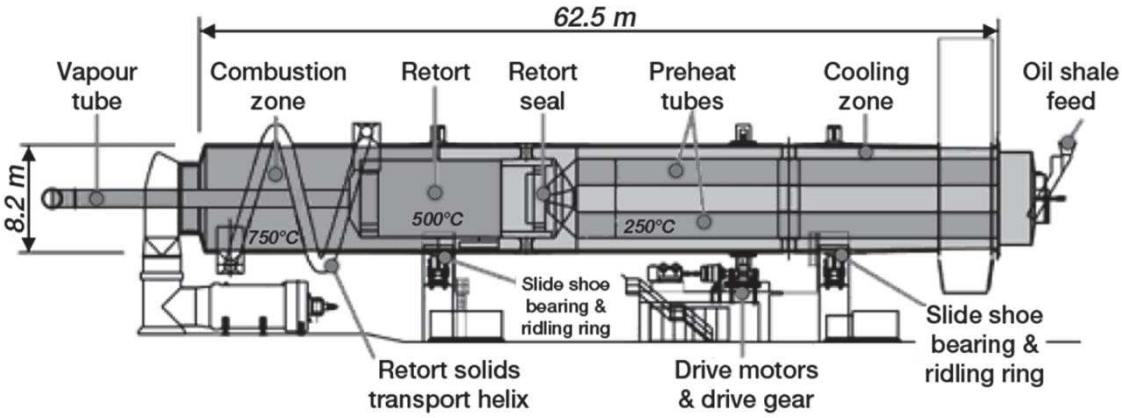

Figure 2.10 Alberta Taciuk Processor (ATP) retort (adapted from Cameron & Gani 2011). A horizontal, rotating vessel, the ATP retort has four main zones: preheat, retort, combustion, and cooling zone. (1) The Preheat Zone: oil shale enters the retort and moves through the preheat zone where it is heated to about 250°C by the outgoing spent shale. Water is driven off as steam at this stage. (2) The Retort Zone: preheated feed mixes with hot solids recycled from the combustion zone. The resulting heat liberates the kerogen in an oxygen-deficient atmosphere, yielding hydrocarbon vapour and residual char containing ashes. The vapour is condensed externally to recover shale oil and fuel gas. (3) The Combustion Zone: air is added to burn the char off the solids. A significant amount of hot spent shale is recycled to the Retort Zone. (4) The Cooling Zone: hot solids and flue gases are cooled through indirect heat transfer to fresh oil shale feed. Spent shale is discharged for disposal or further processing. Flue gases are disposed of through an off-gas treatment system.

In situ retorting is the technology for directly retorting oil shale underground by using heat input from either electrical heating elements, externally generated hot gas or other methods, such as underground partial combustion (Burwell et al., 1970, 1969; Lekas et al., 1991). More recent approaches have attempted to improve the pyrolysis and recovery efficiency of *in situ* processes by fracturing the resource to improve heat transfer and fluid flows through the shale (Crawford et al., 2008b). Although *in situ* retorting has the major advantage of avoiding oil shale mining, it has the disadvantages of potential environmental impact to ground water by loss of shale oil and retorting water (Fox, 1980; Qian et al., 2008). Shell Oil Company is exploring use of a freeze wall around the retorting area to diminish the leakage of shale oil vapour, however, creating this wall of frozen earth will consume significant power (Brandt, 2008).

2.9 *Pyrolysis Parameters*

Pyrolysis conditions such as temperature, heating rate, particle size, mineral content and pressure can impact the shale oil yield and quality. Given that pyrolysis conditions affect the composition and yields of hydrocarbon products; it is important to understand the effects of these conditions to optimise oil shale pyrolysis processes.

2.9.1 Temperature

Wang and Liang (2010) examined the influence of pyrolysis temperature on Huadian (China) oil shale samples. The maximum yield of shale oil was obtained when the pyrolysis temperature reached 530°C. Above 530°C, the yield of shale oil decreased, while the gaseous contents of CO, CO_2, H_2 and CH_4 in the retorting chamber increased. Han et al. (2009) also studied the pyrolysis of Huadian oil shale, establishing that the yield of shale oil could be increased to 80% when extending the residence time to 69 min at 430°C. However, increasing pyrolysis temperature was more efficient than extending residence time to enhance the yield of shale oil. Sun (2006) investigated the characteristics of pyrolysis of Fushun (China) oil shale. It was reported that organic material commenced pyrolysis at 400°C with significant CO_2 released at 500–550 °C. Williams and Ahmad (1999) reported that the optimal pyrolysis temperature was 500 °C for Pakistani oil shale samples (Kohat basin area and Salt Range areas of northern Pakistan).

2.9.2 Heating Rate

In addition to pyrolysis temperature and residence time, heating rate is also one of the key factors in oil shale pyrolysis. Nazzal (2008) showed that for Sultani (Jordan) oil shale rock samples, the shale oil yield was improved with increasing heating rate in the range of 2–10 °C/min. Above a heating rate of 30 °C/min, the yield of shale oil decreased slightly. Al-Harahsheh et al. (2010) showed that for El-lajjun (Jordan) oil shale sample, the fraction of saturated hydrocarbons increased when increasing heating rate in the range of 0.2–6 °C/min. Burnham and Happe (1984) acquired NMR data for five shale oil samples (Green River formation, USA) and reported that slow heating rates cause hetroaromatic compounds in the oil to be converted to coke, and excessive temperatures result in aliphatic moieties to crack to gas. At higher heating rates, the external surface of an oil shale particle will be at a different temperature than its core, with the temperature gradient being more prominent at higher heating rates. This temperature difference results in reactions occurring on the inside of the oil shale particle at lower temperatures generating oil and gas, which pass through a higher temperature region leading to secondary reactions (Jaber and Probert, 1999; Williams and Ahmad, 2000).

2.9.3 Particle Size

Particle size can also play a significant role in the pyrolysis process. However, there is some disagreement in the literature regarding the influence of particle grain size on the yield of oil from oil shales. Wallman et al. (1981) reported higher oil yields for smaller particle grain sizes compared to larger particle sizes using the Fischer assay method. Also, Rubel and Davis (1985) demonstrated that there was an increase in oil yield as the particle grain size was decreased from 2.36–4.75 to 0.25–0.60 mm for the Fischer assay of Kentucky (USA) oil shale. Guffey and McLendon (1984) encountered higher oil yields for smaller grain sizes compared to larger blocks of oil shale. Matzick et al. (1966) showed that larger oil shale particles require a longer residence time in the retorting hot zone affecting the complete decomposition of the kerogen. Harak et al. (1974) demonstrated that large blocks of oil shale yield less oil than the smaller particles. Matzick et al. (1966) explained that the oil shale particle is influenced by heat transfer and pressure drop, and it is a factor in the conversion of kerogen and in the diffusion of volatile products out of the oil shale particle.

On the other hand, Bartke and Duvall (1977) reported lower oil yields for smaller particle sizes compares to larger particle sizes in three narrow size ranges between 0.12 and 1.9 mm. Sohns and Long (1975) also reported that lower oil yields were produced for smaller particle sizes. More recently, Nazzal (2008), Ahmad et al. (1998) and Yu and Jian (2007) showed that the yield of shale oil increased with increasing particle size within the particle size range of 6 to 75 mm. In particular, Nazzal (2008) showed that the oil yield increased as the particle grain size was increased from 0.2–0.6 to 3.33–5.6 mm under both nitrogen and nitrogen/steam pyrolysis atmospheres. Increasing the particle grain size caused a decrease in the derived hydrocarbon gases and an increase in the carbon and hydrogen content in the derived oil.

2.9.4 Mineral Content

The mineral content of oil shale could also affect the thermal decomposition process of oil shales. The effect of the mineral matrix of Turkish oil shales on conversion of kerogen to hydrocarbon products was investigated by Karabakan and Yürüm (1998). It was reported that pyrolysis reactions were catalysed by alkaline earth metal cations of carbonates and inhibited by silicates. The activation energy decreased by 1.2−8.9% for Göynük oil shale when carbonates were removed by a HCl treatment. The interaction of alkaline earth metal cations with —COOH and —OH functional groups could result in the formation of the alkaline M^{2+} —O surface groups. It has been proposed that these groups can act as active sites on oil shale surfaces and, therefore, the alkaline earth metal cations may have some catalytic effect in the pyrolysis reactions of the organic structure (Karabakan and Yürüm, 2000, 1998). In addition, Borrego et al. (2000) reported that inherent montmorillonite in Spanish oil shale lowered the initiation temperature of kerogen cracking.

2.9.5 Pressure

Noble et al. (1981) reported that increasing pressure significantly retards all phases of the organic matter decomposition process. It was demonstrated that pressure affects not only the fractional distribution of liquid and vapour of the primary oil but also the degree of oil degradation during secondary reactions. Bae (1969)

demonstrated that higher pressures reduce the oil yield significantly and generates a larger volume of light hydrocarbon gases. The crude oil obtained at high pressure has higher aromaticity and a lower pour point than the lower pressure material. Also, it was noted that the sulphur and nitrogen content in shale oil does not change significantly with increasing pressure.

Burnham and Singleton (1983) investigated the oil yield, composition, and rate of evolution from Green River (USA) oil shale for heating rates from 1 to 100°C/hour and pressures of 0.15 MPa and 2.7 MPa. They concluded that higher pressures and lower heating rates during oil shale pyrolysis cause a decrease in oil yield. Moreover, vacuum pyrolysis has been shown to enable higher yield and improved quality shale oil in comparison with pyrolysis under atmospheric pressure (Hoekstra et al., 2012; Pakdel et al., 1999; Roy et al., 1985; Siramard et al., 2016). A reduced pressure facilitates the transport of pyrolysis products by providing quicker escape of primary oil from the reaction zone, thus reducing the secondary cracking reactions (Pakdel et al., 1999; Siramard et al., 2016).

2.10 *Oil Shale Imaging*

The complexity of oil shale is demonstrated both in compositional heterogeneity of the matrix and variance in the pore space. In oil shale, the organic matter is tightly bound within a heterogeneous matrix. The inorganic matrix consists of minerals, including clays, carbonates, feldspars, quartz, and pyrite (Alstadt et al., 2012; Dyni, 2003; Karabakan and Yürüm, 1998; Wang et al., 2009). Heterogeneity within oil shale formations exists across multiple length scales due to complex sedimentary and diagenetic processes (Lee et al., 2007; Picard, 1955; Speight, 2012b; Taylor and Ritts, 2004). This heterogeneity renders oil shale rocks difficult to characterise petrophysically (mineral composition, organic matter type and distribution, pore volume, pore size distribution, geometry and connectivity) and our ability to distribute these properties in oil shale pyrolysis models. Pores within oil shale rocks are orders of magnitude smaller (nanometre scale) than those in conventional carbonate and sandstone samples (micrometre scale). Nano-scale porosity associated with organic matter and how well that organic matter is connected is crucial for the creation of flow channels to allow the generated hydrocarbon fluids to escape. Thus

far, characterizing oil shales has proven to be a complex and challenging task, hindered by the lack of tools and techniques to investigate the broad structural and mineralogical heterogeneities over many length scales. Moreover, the development of pore networks and micro-fractures within the fine-grained oil shale microstructure during pyrolysis is not well understood and remains largely unknown. Hence, it is vital to comprehensively characterise the pore space and organic connectivity and mineralogical heterogeneity before and after pyrolysis across multiple length scales and to determine the nano- and microstructural controls on pore space evolution and hydrocarbon flow behaviour.

Quantifying the pore structure of oil shales is still challenging due to their extremely low porosity and permeability. Conventional laboratory porosity measurements such Mercury Injection Capillary Pressure (MICP) to obtain the porosity values and pore size distributions and gas adsorption Brunauer, Emmett and Teller (BET) to determine the specific surface area can be used to characterize pore systems down to a few nanometres (Brunauer et al., 1938; Van Brakel et al., 1981; Washburn, 1921; y Leon, 1998). The current limitations of MICP apparatus (pressure up to 60,000 psi) theoretically make it impossible to measure pores smaller than 3.6 nm, while the practical threshold is likely to be higher. The main advantage of gas adsorption techniques utilising nitrogen, argon, carbon dioxide, helium and methane is the ability to examine very fine pores in the range of 1.7 - 300nm, which captures the majority of pores in mudstones and shales. However, MICP and gas adsorption are macroscopic averaging methods which only provide data related to the accessible porosity, do not involve direct observation of individual pores and are based on models which may not reflect the complexity of the natural geological pore space (Clarkson et al., 2013; Conner et al., 1986; Gregg and Sing, 1982; Mastalerz et al., 2013; Olson and Grigg, 2008; Scholten, 1967; Washburn, 1921). Previous experimental studies have used nitrogen adsorption-desorption isotherms to estimate the pore properties of Green River (Western USA) (Tisot, 1962), New Albany (Eastern US) (Schrodt and Ocampo, 1984) and Huadian (China) oil shales (Han et al., 2008, 2006; Qing et al., 2010; Sun et al., 2008) before and after pyrolysis. However, the majority of these studies used powdered oil shale samples and an investigative method that lacks direct information about pore geometry, isolated pores and the association of porosity to the surrounding microstructure and

mineralogy. Moreover, in raw oil shale, naturally occurring porosities are negligible, although porosity may exist to some degree in formations where fractures, faults, or other structural defects have occurred. Overall, it is believed that a substantial proportion of pores in raw oil shale are isolated or inaccessible to gases and mercury even at high pressures (Speight, 2012b).

A wide range of complementary imaging techniques can be used to directly visualize and quantify oil shale structures across multiple scales (Figure 2.11). With optical thin sections, a useful initial visualization of the microstructure can be acquired to assess the mineralogy and microscopic features in 2-D. However, with traditional optical petrography, the resolution is limited to approximately 0.23 μm (diffraction barrier of visible light) which prevents the fine grain characteristics within oil shales from being characterised (Bultreys et al., 2016). To visualize and quantify the pores, inorganic mineral grains, fine clay structures and organic matter (kerogen) within oil shale, an imaging technique that resolves features from the optical regime down to the nanometre scale is required. Scanning electron microscopy (SEM) is well-suited to study fine-grained sedimentary rock features from the micrometre to nanometre scales (Lemmens et al., 2011; Loucks et al., 2009; Milliken et al., 2013; Milner et al., 2010; Pommer and Milliken, 2015; Qing et al., 2010; Wang et al., 2016). For shale samples, mechanical polishing is not suitable, as this technique tends to introduce artefacts and destroy the fine microstructure (e.g. abrasion marks, smearing grain boundaries, embedment of grit into surface of sample) (Loucks et al., 2009; Rine et al., 2013; Sondergeld et al., 2010). With advanced SEM instruments, even a minimal amount of damage can limit our ability to fully resolve or analyse the surface of an oil shale sample. To overcome this difficulty and obtain ultra-flat samples, argon (Ar) ion beam milling can be used resulting in high-quality SEM images that reveal nano- and microstructures in 2-D with minimal artefacts (Desbois et al., 2011; Loucks et al., 2012, 2009; Sondergeld et al., 2010). However, with this imaging method there is an inherent limitation in only being able to characterise a sample in 2-D and not being able to collect internal information such as 3-D pore, mineral and organic network structures. Some studies have used multiple-point statistics from 2-D images to generate 3-D networks of sandstone and carbonate samples (Hajizadeh et al., 2011; Okabe and Blunt, 2007, 2005, 2004), however, this becomes a

significant challenge for heterogeneous anisotropic media involving complex microstructures such as in oil shales.

Automated image acquisition for SEM systems has become increasingly common over recent years (Blackson et al., 2008; Buckman, 2014; Gu, 2003; Tovey and Wang, 1997). In general, these are concerned with capturing single images, or groups of associated images, for image analysis purposes. More recently, examples of automated image capture and stitching, designed to produce high-resolution large format images have been developed (Buckman, 2014; Ogura et al., 2010). These systems typically have the capability of producing images that are several gigabytes or larger in size, and can often use a variety of detector types such as backscattered electron (BSE), secondary electron (SE) and cathodoluminescence (CL).

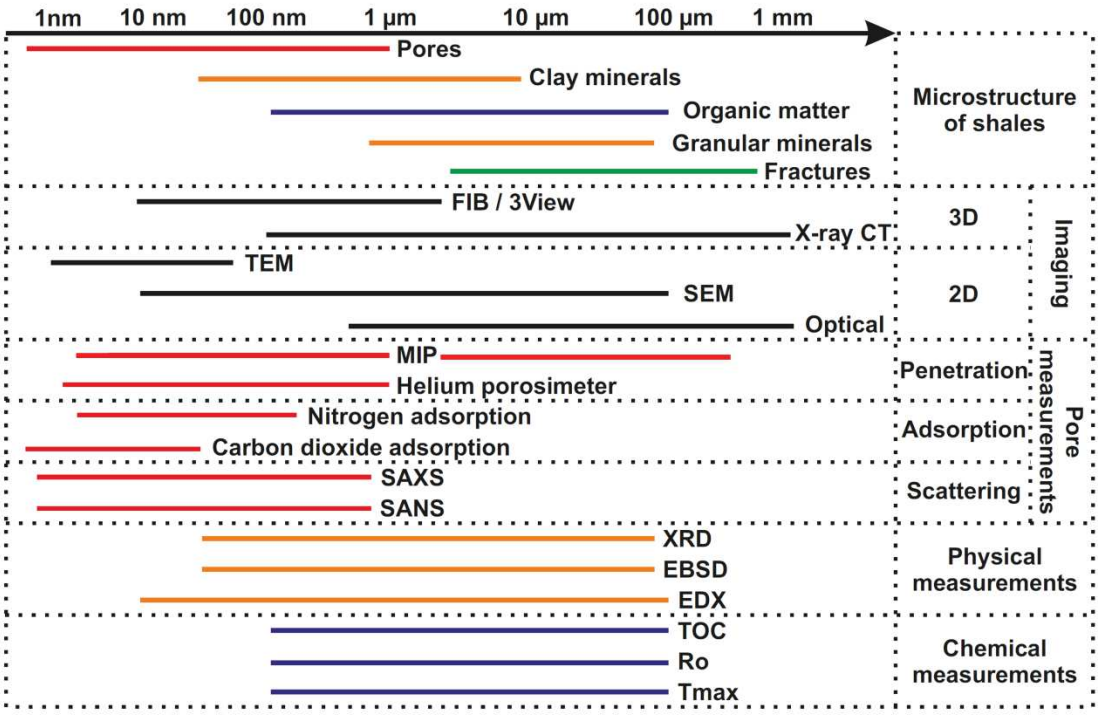

Figure 2.11 Imaging and characterisation techniques for shales at varying scales (adapted from Ma et al. 2017).

Recently, the use of automated mineralogy, in the form of QEMSCAN technology (Quantitative Evaluation of Minerals by Scanning Electron Microscopy) has allowed users to non-destructively quantify the amount, type and distribution of minerals present in a sample (Al-Otoom et al., 2005; Allen et al., 2012; Grauch et al., 2008; Jordens et al., 2016; Pirrie et al., 2004). Mineral identification is performed through

particle identification by BSE intensity and X-ray analysis for quantitative mineral identification based on energy dispersive spectrometry (EDS) and a mineral database or Species Identification Protocol (SIP). Automated mineralogy has provided significant advances in mineralogical mapping at high resolutions allowing a detailed evaluation far beyond the resolution of conventional thin section petrography and bulk compositional data from X-ray Diffraction (XRD) and X-ray Fluorescence (XRF) analysis. More recently, MAPS Mineralogy (Modular Automated Processing System) (FEI) has been developed which does not constrain the number of minerals per pixel, unlike a standard QEMSCAN analysis. Rather, it allows multiple minerals to be reported within a single pixel and avoids the need to manage complex mineral chemistry within the analytical software.

Techniques that allow direct 3-D imaging and quantification are of significant benefit in characterizing the evolution and connectivity of the pore space during oil shale pyrolysis. In recent years, X-ray micro-computed tomography (μCT) and Focused Ion Beam and Scanning Electron Microscopy (FIB-SEM) have emerged as powerful 3-D imaging tools to capture the internal structures of geological samples, in particular being effective at studying complex pore-scale processes (Al-Khulaifi et al., 2017; Bera et al., 2011; Blunt et al., 2013; Curtis et al., 2010; Dobson et al., 2017; Lemmens et al., 2011; Lin et al., 2017, 2016, 2015; Menke et al., 2016; Reyes et al., 2017; Singh et al., 2016; Wildenschild and Sheppard, 2013). For oil shales, in addition to determining pore space characteristics, a 3-D approach allows us to obtain important information on the spatial distribution of organic matter and constituent inorganic minerals. Quantitative analysis can provide useful insights by characterizing component volume fractions and fundamental pore space geometric attributes, including pore size, shape, tortuosity and connectivity. μCT offers several advantages: it is non-destructive, provides 3-D imaging, achieves high spatial resolutions at scales down to the micron level, gives good contrast between phases, and is adaptable to many types of experimental procedures. μCT has been applied to characterise oil shale samples from the United States (Green River, Figure 2.14) (Tiwari et al., 2013), China (Fushun, Figure 2.13) (Kang et al., 2017, 2011) and Australia (Queensland, Figure 2.12) (Coshell et al., 1994) . Tiwari et al. (Tiwari et al., 2013) characterised pore structures before and after pyrolysis based on 42 μm voxel size scans reporting pores as large as 500 μm after pyrolysis (Figure 2.14).

Using a Lattice Boltzmann simulation model, Tiwari et al. (2013) predicted ultra-high permeabilities in the range of 173 to 2919 Darcy.

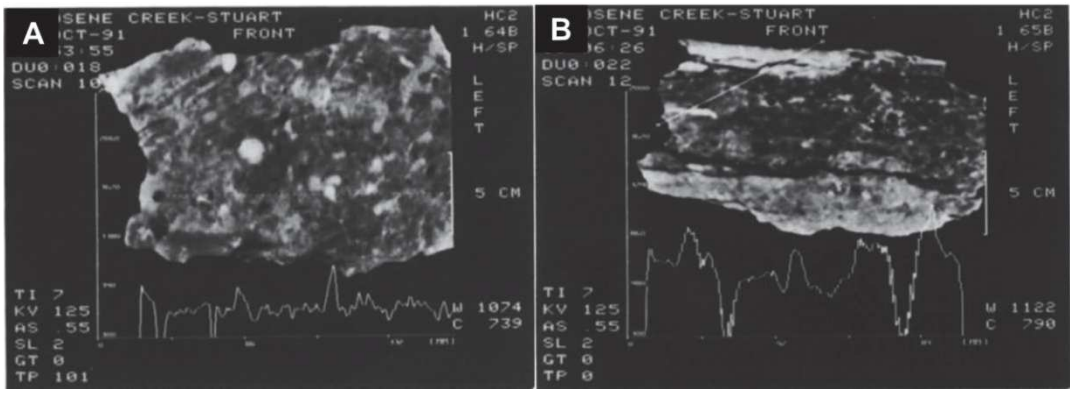

Figure 2.12 X-ray CT images of Australian Oil Shales (A) parallel to bedding, (B) perpendicular to bedding (Coshell et al., 1994).

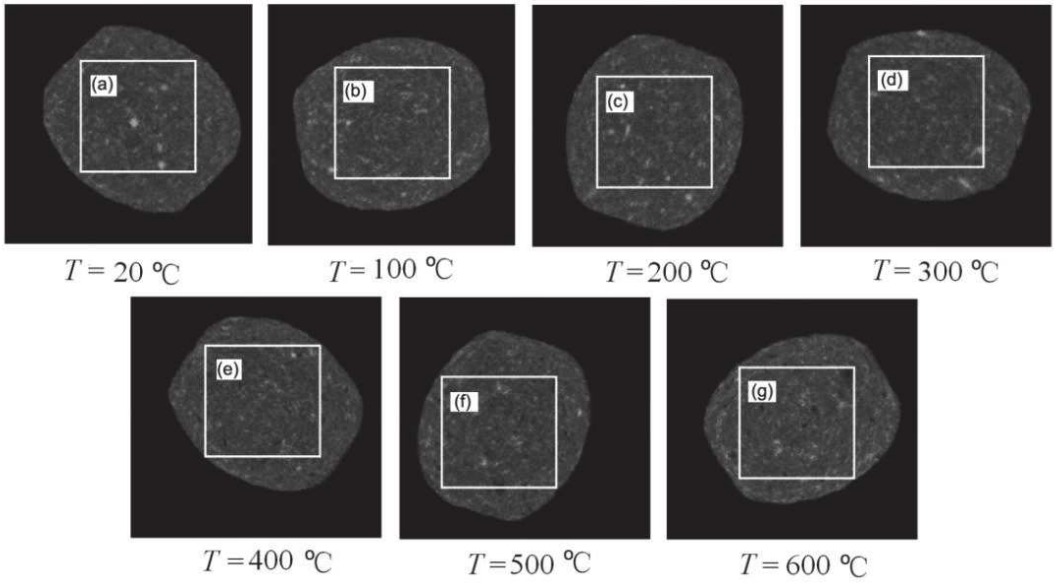

Figure 2.13 CT scan greyscale images of the oil shale sample (cylindrical sample 0.82 diameter × 7 mm length) at different temperatures acquired at a voxel size of 0.54 μm (Kang et al., 2017).

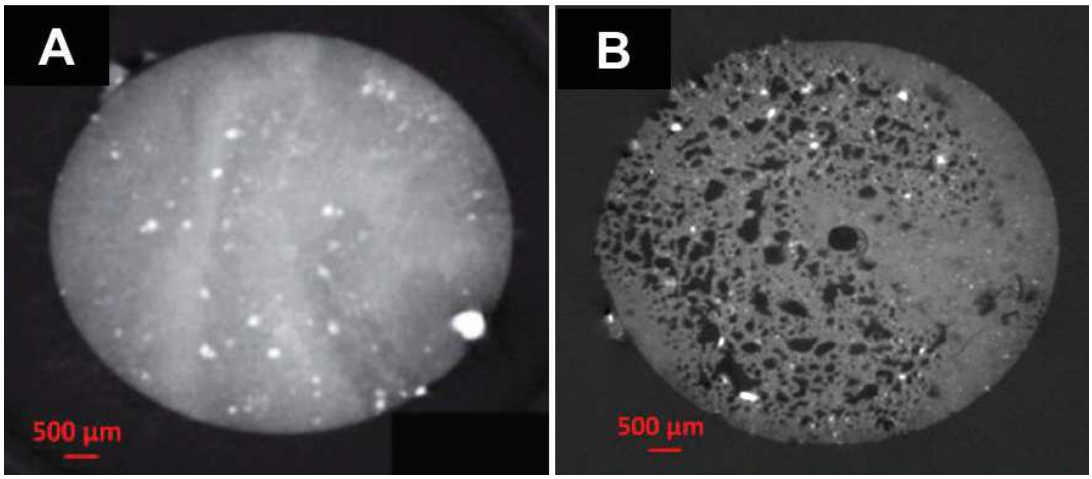

Figure 2.14 Micro-CT images of Green River (US) oil shale before (A) and after (B) pyrolysis. Shows the pore-space and connectivity created after pyrolysis (Tiwari et al., 2013).

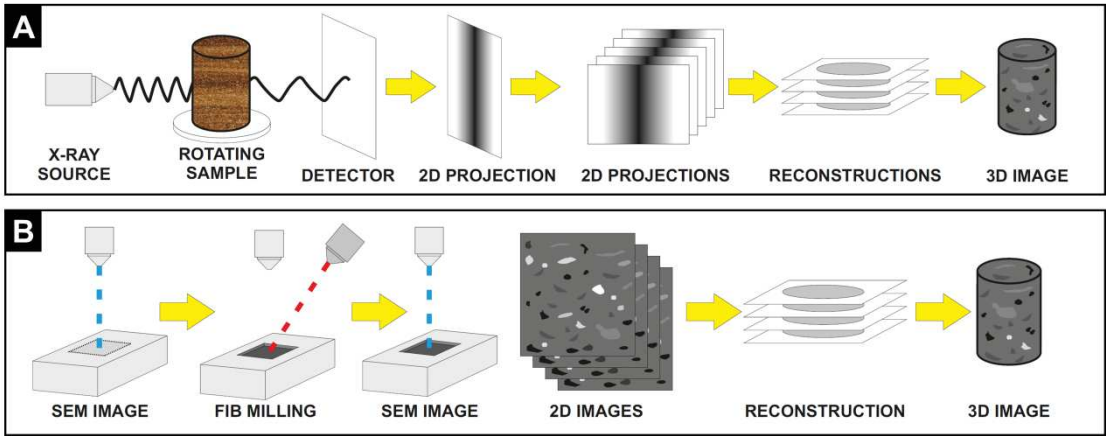

Figure 2.15 Schematic illustration of (A) Micro-CT 3-D imaging technique and (B) FIB-SEM 3-D imaging technique (Ma et al., 2016).

The complex microstructure of oil shales spans multiple orders of magnitude from centimetre scale laminations to nanometre scale pores within organic material and minerals. µCT can resolve features at the millimetre to micrometre scale, but lacks the capability to determine nano-scale structures such as the pore space in immature samples and the developing pore network during pyrolysis. The first experiments with a focussed ion beam (FIB) were reported in 1974 by Seliger and Fleming (1974) who were able to focus a beam of boron ions to about 3.5 micrometres. A number of different ions were tested and the liquid gallium (Ga^{+}) was found to be most suitable. (reviewed in Sugiyama and Sigesato 2004). Recent developments in FIB-SEM systems allow for direct 3-D visualization of a variety of samples at the nanometre-scale resolution (Curtis et al., 2010; Haswell et al., 2008; Krueger, 1999; Schiffbauer

and Xiao, 2009; Sivel et al., 2004; Tomutsa et al., 2007; Winter et al., 2009). The system allows the user to mill (with the FIB) and image (with the SEM) in a region of interest (ROI) to obtain a sequence of 2-D cross-sectional images which are then reconstructed to generate a digital 3-D visualization of the analysed volume. The FIB-SEM technique enables structural features within fine-grained samples to be resolved at the nano-scale including porosity, grain morphologies and organic networks.

2.11 *Summary*

In this chapter, a comprehensive review of the literature and scientific background relevant to this thesis has been presented. An overview of known oil shale deposits, types of oil shales has been provided illustrating the variation in organic matter origin and inorganic mineral content across oil shale resources. Details on the pyrolysis process used to transform solid kerogen into volatile hydrocarbons have been reviewed including an overview of current commercial retorting technologies. A review of the literature related to the effect of pyrolysis parameters on shale pyrolysis has been presented, with particular emphasis on shale oil yield and quality. Moreover, a review of literature pertinent to oil shale imaging highlighted the current lack of studies in characterizing the microstructural changes in oil shale pyrolysis including limited work on visualizing and quantifying the evolution of pore space that can elucidate the pyrolysis process. This has motivated a comprehensive multi-scale multi-dimensional study to be undertaken in this thesis.

Chapter 3

Experimental Methods and Analytical Techniques

3.1 Introduction

This chapter focuses on imaging methods and analytical techniques to observe and quantify the microstructure of oil shales with increasing pyrolysis temperature using a multi-scale, multi-dimensional integrated approach consisting of advanced 2-D, 3-D and 4-D (3-D + time). A significant challenge in the identification and characterization of oil shale heterogeneity is the need to obtain a balance between inspection volume and spatial resolution. Any characterization workflow must incorporate sufficient resolution to identify nanometre scale features while being able to assess how these features correlate to larger-scale volumes, on the scale of hundreds of microns to millimetres and beyond. Collectively, the methods discussed in this chapter, provide a workflow across multiple length scales with appropriate image processing to adequately visualize and analyse oil shale petrophysical properties during pyrolysis.

In this work, oil shale samples were prepared and analysed using X-ray Diffraction (XRD), Total Organic Carbon (TOC), Programmed Pyrolysis (Rock-Eval, Source Rock Analyzer), Elemental Analysis and Modified Fisher Assay (MFA). Following an understanding of the chemical composition, the samples were then prepared and observed using optical microscopy, scanning electron microscopy (SEM) to obtain 2-D qualitative and quantitative data, followed by X-ray tomography (laboratory and synchrotron X-ray sources) and Focused Ion Beam- Scanning Electron Microscopy (FIB-SEM) to acquire valuable 3-D information on organic matter, mineral and pore/fracture characteristics at multiple length scales (micron-scale, submicron-scale and nano-scale). The quantitative data derived from these imaging techniques were compared with XRD, TOC and Elemental (CHNSO) analysis.

To initially characterise the Mahogany oil shale, samples were prepared and analysed to characterise bulk properties including mineralogy (XRD), Total Organic Carbon (TOC), thermal maturity (Rock-Eval and Source Rock Analyzer (SRA), elemental analysis (CHNOS) and oil yield (Modified Fischer Assay (MFA)). However, given the complexity and heterogeneity of oil shale, samples were also cut and prepared for petrographic analysis, SEM-EDS (Mineral Mapping) and μCT image characterization. These imaging techniques offer local information on the spatial distribution of organic material, mineral phases and pore structures. With these bulk analytical techniques and imaging methods, a full characterization of oil shales can be achieved to better understand the internal microstructure and chemical composition which allows for improved modelling and prediction of fluid flow during oil shale pyrolysis.

To address the research objectives outlined in Section 1.2, this chapter presents experimental method and analytical techniques used for the multi-scale multi-dimensional work flow used in this study. Section 3.2 describes oil shale sample selection, oil composition analysis and Section 3.3 introduces the geochemical and traditional rock analysis techniques that have been used in this research. A description of the methods used for the 2-D imaging techniques of optical microscopy and SEM is provided in Section 3.4 and 3.5 respectively. Section 3.6 explains the FIB-SEM methodology to generate high-resolution 3-D datasets and Section 3.7 describes the X-ray micro-tomography methods used in this research for both laboratory-based (Section 3.7.1.1) and synchrotron-based (Section 3.7.1.2) sources along with image processing techniques (Section 3.7.3). Finally, given that the acquired oil shale samples are thermally matured, a description on the pyrolysis conditions used is provided in Section 3.8.

3.2 Sample Selection

Oil shale samples were obtained from an outcrop (Enefit Oil Shale Research Site, Figure 3.2) of the organic-rich Mahogany zone of the Green River Formation (Uinta Basin, Utah). The Eocene Green River Formation epitomises a classic example for lacustrine (lake-like) source rock deposition and is the frequent reference rock for Type I kerogen (Ruble et al., 2001; Vandenbroucke and Largeau, 2007). It is

considered to be the largest known oil shale deposit in the world with an estimated 4.3 trillion barrels of oil originally in place (Birdwell et al., 2012).

Lacustrine sediments of the Green River Formation were deposited in two large Eocene lakes (Lake Uinta in the Uinta and Piceance Basins, and Lake Gosiute in the Greater Green River Basin) that dominated 65,000 km^2 in many sedimentary-structural basins in Utah, Wyoming and Colorado (Figure 3.1). The Uinta Mountain uplift and its eastward extension, the Axial Basin anticline, divide these basins. The Green River lake system was in existence for more than 10 million years during a time of a warm temperate to subtropical climate.

During arid times, the lakes contracted in size and the lake waters became increasingly saline and alkaline (Dyni, 2003). The warm alkaline lake waters of the Eocene Green River lakes provided excellent conditions for the abundant growth of blue-green algae (cyanobacteria) that are thought to be the major precursor of the organic matter in the Green River oil shale.

Samples from this study were from the Mahogany zone (R-7) (Figure 3.3). This zone is the richest oil shale horizon which is a primary target for shale oil production due to its high oil yield which can exceed 250 litres per tonne of rock recovered as liquid fuel by pyrolysis (Johnson et al., 2009).

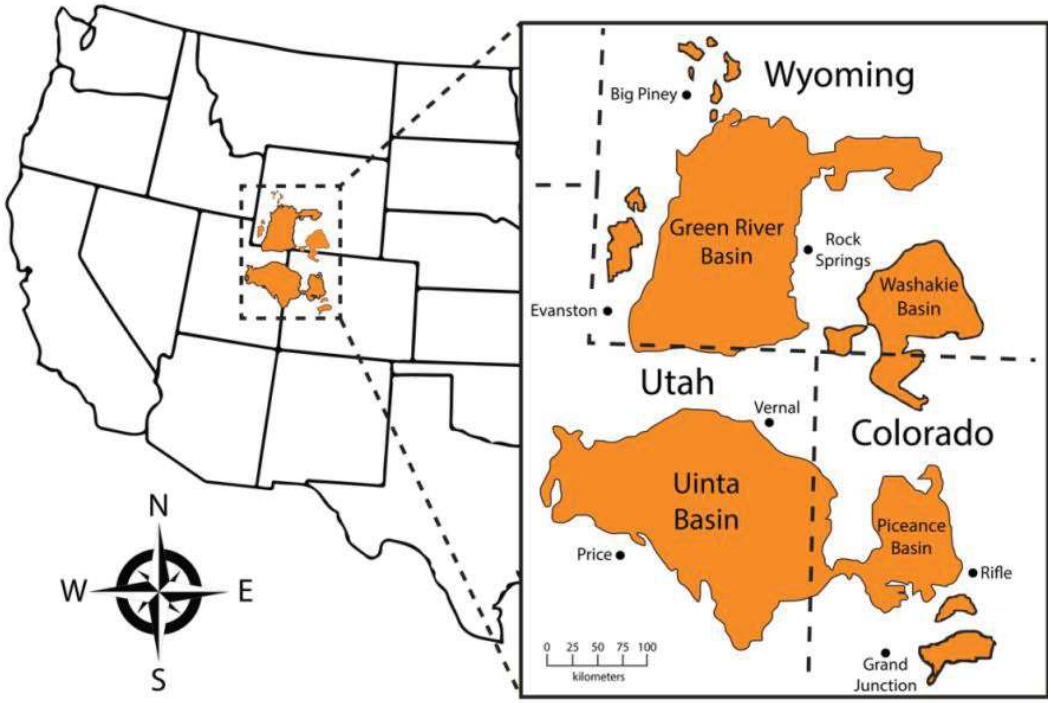

Figure 3.1 Map showing oil shale resource areas of Utah, Colorado and Wyoming. This area includes the lacustrine Eocene Green River Formation, which contains the world's largest deposit of oil shale.

Figure 3.2 (A) Enefit oil shale research site, Utah, United States, (B) Oil shale box cut, (C) Oil shale sampling site; note the black horizontal streaks of the Mahogany Zone, and (D) Mahogany Zone oil shale sample used in this study; note the dark colour indicating an organic-rich rock.

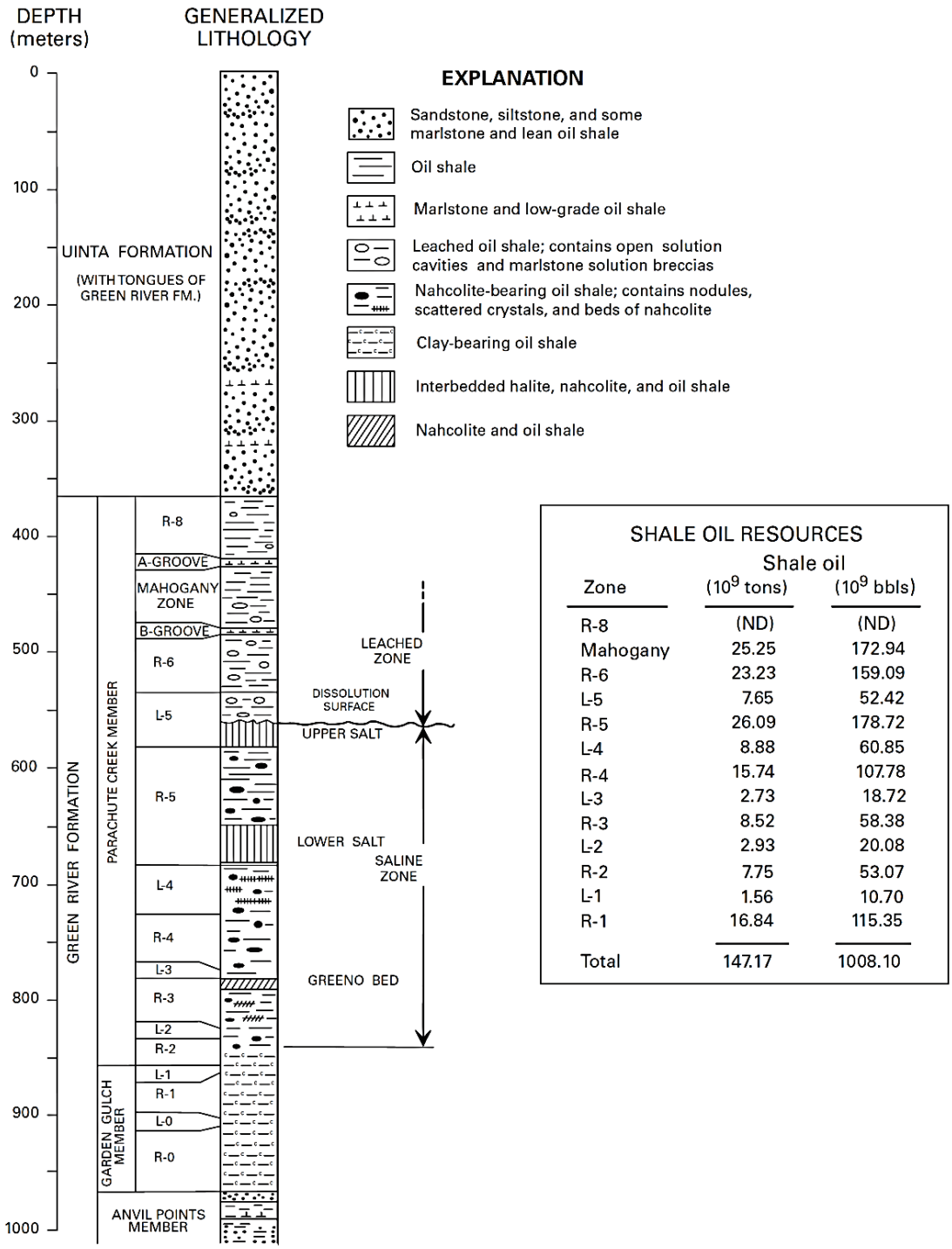

SHALE OIL RESOURCES

Zone	Shale oil (10^9 tons)	Shale oil (10^9 bbls)
R-8	(ND)	(ND)
Mahogany	25.25	172.94
R-6	23.23	159.09
L-5	7.65	52.42
R-5	26.09	178.72
L-4	8.88	60.85
R-4	15.74	107.78
L-3	2.73	18.72
R-3	8.52	58.38
L-2	2.93	20.08
R-2	7.75	53.07
L-1	1.56	10.70
R-1	16.84	115.35
Total	147.17	1008.10

Figure 3.3 Generalized stratigraphic section of the Green River Formation and associated rocks in the north-central part of the Piceance Creek Basin, northwestern Colorado, United States (Dyni, 2003). The shale-oil resource data, converted from U.S. barrels to metric tons, are from (Pitman et al., 1990).

3.3 Geochemical & Rock Analysis

3.3.1 X-ray Diffraction (XRD)

X-ray diffraction (XRD) is a widely used analytical technique to identify mineral phases in a sample. Each mineral has a unique diffraction pattern while interacting with X-rays. The characteristic diffraction patterns are used to identify minerals by comparing the diffraction data against a database maintained by the Inorganic Crystal Structure Database (ICSD). The ICSD maintains a database of powder diffraction patterns, *d*-spacings (related to angle of diffraction) and relative intensities of observable diffraction peaks . Furthermore, the areas under the peak are related to the amount of each phase present in the sample.

The structure of crystalline materials, such as minerals, is defined by regular, repeating planes of atoms that form a crystal lattice. X-rays are diffracted by each mineral differently, depending on the type and arrangement of atoms that make up the crystal lattice. When an X-ray beam hits a sample and is diffracted, it is possible to measure the distances between the planes of the atoms that constitute the sample by applying Bragg's Law:

$$n\lambda = 2d \cdot \sin(\theta) \tag{3.1}$$

Where n is a natural number, λ is the X-ray wavelength, d is the distance between atomic lattices and θ is the angle of incidence of the X-ray. Bragg's law can be understood by looking at two reflected X-rays (Figure 3.4). The first ray is reflected by the atomic lattice. The second ray is transmitted by the first atomic lattice and reflected by the second one. The difference between these two ray paths is a function of the angle of incidence (θ) and the distance between the atomic lattices (d). If this difference between these two ray paths is a multiple of the X-ray wavelength (λ), reflections of these two rays interfere constructively. During X-ray diffraction, the angle of incidence is varied while the intensity of the reflected X-rays is recorded resulting in an X-ray diffractogram. Since no two minerals have the same spacings of interatomic planes in three dimensions, the angles at which diffraction occurs can be used for identification.

For this study, XRD was used to quantify the mineralogical composition of Green River (Mahogany zone) oil shale samples. This was performed at Weatherford Laboratories (UK). The sample was first disaggregated gently using a pestle and mortar (Figure 3.6). A 2 g split of this material was then 'micronised' using a McCrone Micronising Mill to obtain an X-ray diffraction 'powder' with a mean particle diameter of between 5 - 10 microns. This powder was front-packed into an aluminium cavity mount, producing a randomly orientated sample for presentation to the X-ray beam.

Samples were analysed using a Bruker D8 Advance XRD between 2° and 75° 2θ with a step size of 0.05°/sec using X-ray radiation from a copper anode at 35kV, 30mA (Figure 3.5). Identification of unknown minerals was achieved by using a "Traces" and "Search-Match" software to compare the X-ray diffraction pattern from the oil shale samples with the International Centre for Diffraction Data PDF-4 Minerals database containing reference patterns for more than 157,000 phases. The maximum intensity of each mineral identified was measured and compared to a standard intensity for a pure sample of that mineral. The method does not take into account any amorphous content and the results were normalised to 100% based on the assumption that the complete mineral content of the sample was accounted for in the diffractogram.

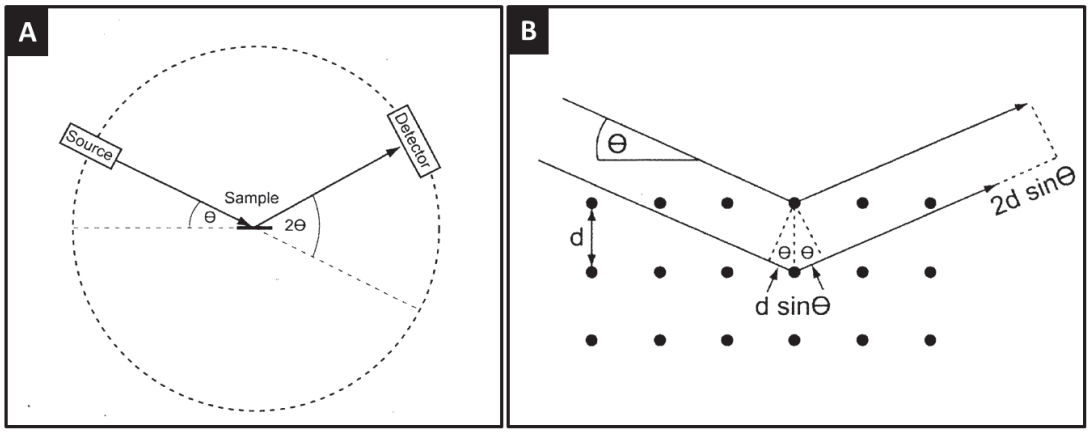

Figure 3.4 (A) Schematic illustration of an X-ray diffractometer, (B) Reflection of X-rays at atomic lattices (Moore and Reynolds, 1989).

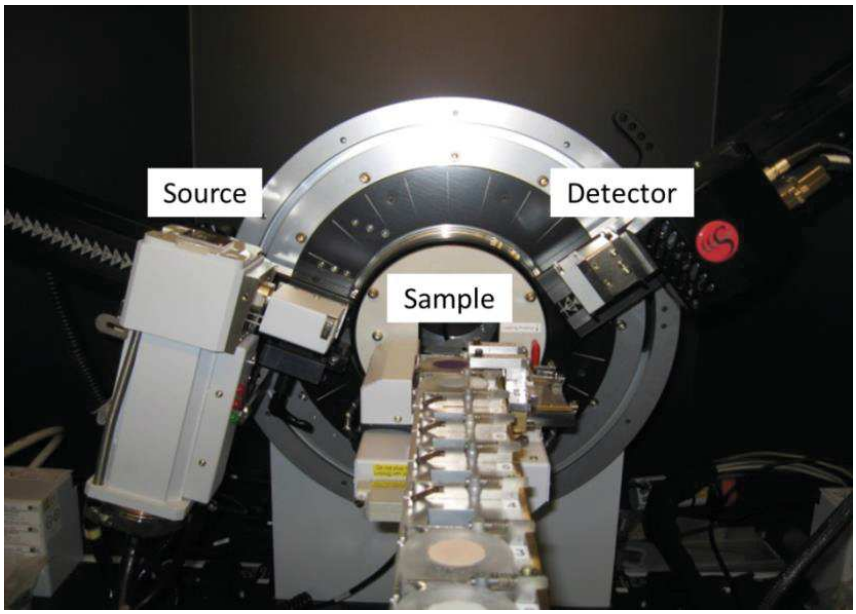

Figure 3.5 Image of a powder X-ray diffractometer. The incident beam enters from the tube on the left, and the detector is housed in the black box on the right side of the instrument.

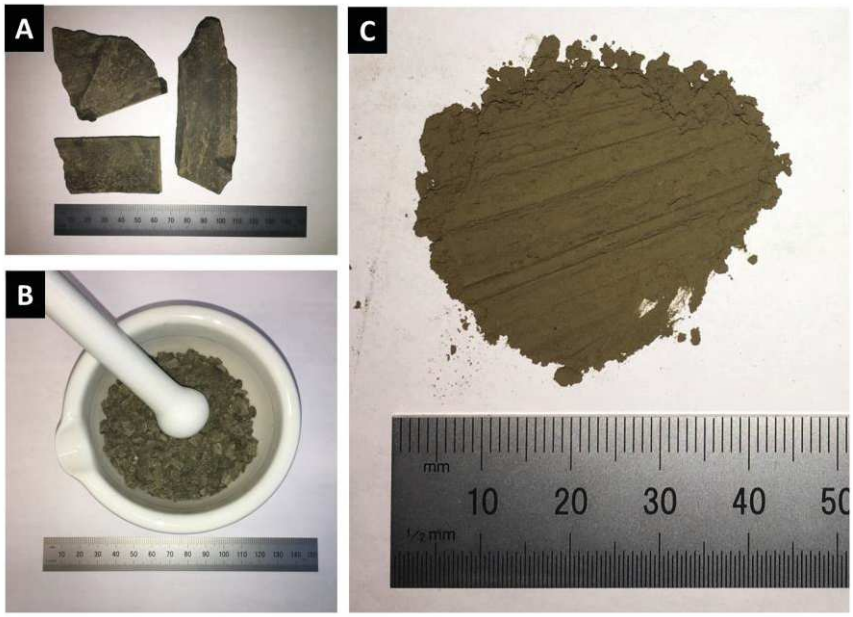

Figure 3.6 For geochemical analysis (XRD, TOC, Elemental, TGA and MFA), powdered samples were prepared using a pestle and mortar. (A) initial bulk oil shale rock samples, (B) samples crushed using a pestle and mortar, and (C) fine oil shale powder samples used for analysis.

3.3.2 Total Organic Carbon (TOC) analysis

Determination of the Total Organic Carbon (TOC) is a fundamental part of oil shale evaluation. Organic carbon is distinguished from inorganic carbon by its derivation. Organic carbon is derived from biogenic matter, whereas inorganic carbon is derived

from mineral matter. In this study, TOC by weight percent was determined for the Green River (Mahogany zone) oil shale samples at Weatherford Laboratories (UK).

TOC determination is most commonly performed indirectly by acid treatment of the sample to effervesce the carbon dioxide from the inorganic carbonate species. Instruments are then used for total carbon combustion based on either a high-temperature resistance furnace or a high-temperature induction furnace to achieve complete decomposition of the sample. The carbon is oxidized by the pure oxygen environment and converted to CO_2. The gas is swept through the instrument to the infrared detectors where the infrared absorbance of CO_2 is measured and converted to a quantifiable concentration based on initial sample mass.

Approximately 0.10 g of crushed rock was accurately weighed and then treated with concentrated hydrochloric acid to remove carbonates. The sample remained in acid for a minimum of 2 hours. The acid was then removed from the sample with a filtration apparatus fitted with a glass microfiber filter paper. The filter was placed in a LECO crucible and dried at 110° C for a minimum of 1 hour. After drying, the sample was analysed with a LECO 744 Carbon Analyser with detection limits to 0.01 weight percent.

3.3.3 Programmed Pyrolysis (Rock-Eval, Source Rock Analysis)

Programmed pyrolysis allows for the characterization of the quantity, type and thermal maturity of organic matter in a sample. The generalized analytical method consists of heating about 100 mg crushed rock sample in a furnace, under an inert atmosphere, using a specific temperature program, in order to measure the Flame Ionization Detector (FID) response during heating. The results are computed and presented as a pyrogram (a trace of FID response versus time, overlain with a temperature profile). Three groups of compounds (S1, S2, and S3), are measured as three peaks on the pyrogram (Figure 3.7).

Rock-Eval and Source Rock Analysis (SRA) methods of programmed pyrolysis are widely used as standard tools for source rock evaluation. (Bordenave, 1993). In this study, programmed pyrolysis using Rock-Eval II and SRA was used to analyse the Green River (Mahogany Zone) oil shale samples at Weatherford Laboratories (UK).

The Rock-Eval II and SRA methodologies are near identical. Sample heating at 300°C for 3 minutes produces the S1 peak by vaporizing the free (unbound) hydrocarbons. High S1 values indicate either large amounts of kerogen-derived bitumen (as in an active source rock) or the presence of migrated hydrocarbons. The furnace then increases in temperature by 25°C/minute to 600°C, and the S2 and S3 peaks are measured from the pyrolytic degradation of the kerogen in the sample.

The S2 peak is proportional to the amount of hydrogen-rich kerogen in the rock, and the S3 peak measures the carbon dioxide released (to 390°C) providing an assessment of the oxygen content of the rock. The temperature at which the S2 peak reaches a maximum, T_{max}, is a measure of the source rock maturity. Accuracy of T_{max} is 1-3°C, depending on the instrument, program rate and sample size, but can also vary by organic matter type. T_{max} values for samples with S2 peaks less than 0.2 mg HC/g rock are often inaccurate and should be rejected unless a definitive kerogen peak is noted from the pyrogram. A summary of acquired parameters and calculated parameters are presented in Table 3.1 and Table 3.2 respectively.

Table 3.1 Acquired parameters during programmed pyrolysis, associated units, measurement properties and related comments.

Acquired Parameter	Unit	Measurement	Comment
S1	mg HC/ g rock	Free hydrocarbon	The amount of free hydrocarbon liberated at 300°C (without cracking the kerogen).
S2	mg HC/ g rock	Residual potential	The amount of hydrocarbon released from cracking of kerogen and heavy hydrocarbons during temperature programed pyrolysis (300–600°C) and represents the existing potential of a rock to generate petroleum.
S3	mg CO_2 / g rock	Organic carbon dioxide	Represents the amount of CO_2 from breaking carboxyl groups and other oxygen-containing compounds in kerogen, obtained at 300–390°C.
$\mathbf{T_{max}}$	Degrees Celsius (°C)	Temperature at maximum evolution	Indicator of source rock maturity

Table 3.2 Calculated parameters from programmed pyrolysis, their units, equations and names.

Calculated Parameter	Unit	Equation	Name
HI	mg HC/ g TOC	$\frac{S2 \times 100}{TOC}$	Hydrogen Index
OI	mg CO_2 / g TOC	$\frac{S3 \times 100}{TOC}$	Oxygen Index
PI	Dimensionless	$\frac{S1}{S1 + S2}$	Production Index
S1/TOC	mg HC/ g TOC	$\frac{S1 \times 100}{TOC}$	Normalized Oil Content

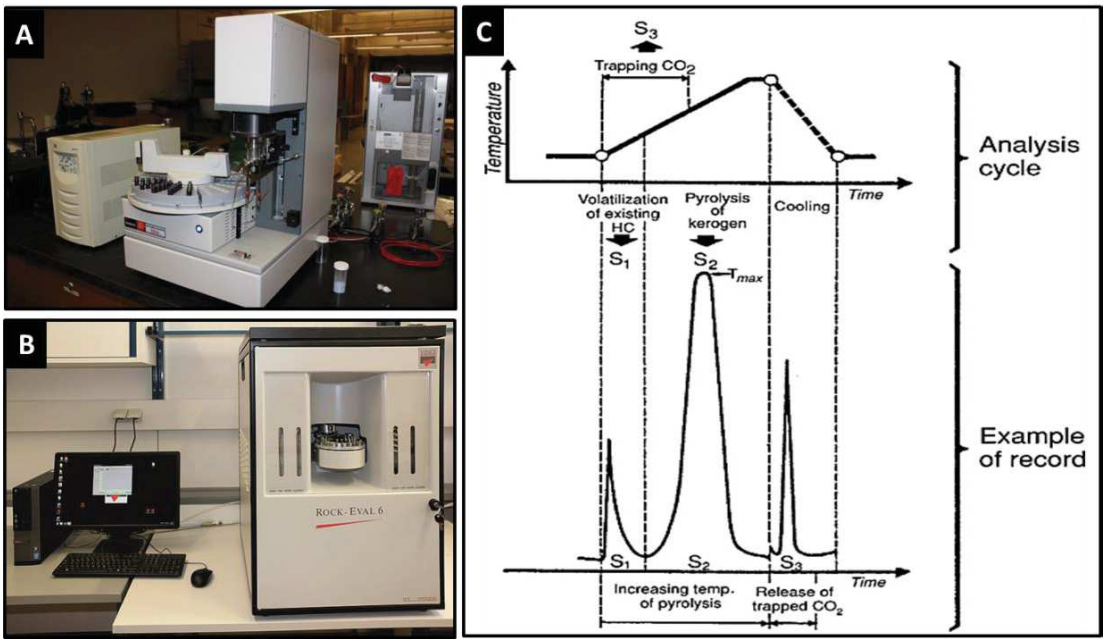

Figure 3.7 (A) Source Rock Analyser (SRA), (B) Rock-Eval and (C) Pyrogram obtained from programmed pyrolysis. The first step is to heat the oil shale sample to 300°C to volatize the pre-existing free hydrocarbons in the sample. The amount of these hydrocarbons is measured from a peak area S1. The next step is to pyrolyze the kerogen present in the sample at higher temperatures and measure it at peak area S2. The carbon dioxide generated from the cracking of kerogen (up to 390°C) is measured from the S3 peak.

3.3.4 Thermogravimetric Analysis (TGA)

Thermogravimetric Analysis (TGA) is a technique in which the mass change of a substance is measured as a function of temperature whilst the substance is subjected to a controlled heating programme. It is a useful technique for the analysis of materials where volatiles are lost upon heating, such as oil shales.

The TGA unit consists of a microbalance with a suspended inert crucible which is placed within a temperature programmable furnace (Figure 3.8). The oil shale sample should be as small as possible to enable as best as possible isothermal conditions, but large enough to enable accurate weight measurement, and representative of the bulk sample. The sample is then pyrolysed in an atmosphere of flowing/sweeping gas to ensure a steady gas concentration and temperature and to remove volatiles. Nitrogen is often used to create an inert environment without oxidation.

In this study, the TGA of the Green River (Mahogany Zone) oil shale sample was conducted using a Perkin-Elmer Pyris 1 instrument (Perkin Elmer, USA) at the Department of Chemistry, The University of Sheffield. Initially 100 g sample of the oil shale rock sample was crushed and milled, and 20 mg of this powdered sample was heated to 850°C at a heating rate of 10°C/min using nitrogen as the purge gas at flow rate of 60mL/min.

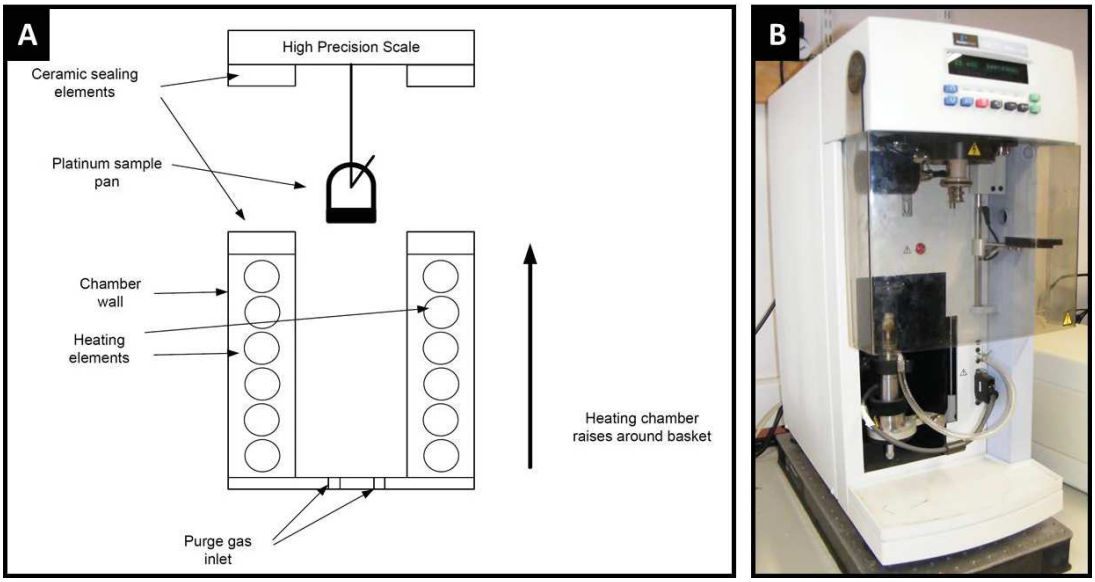

Figure 3.8 Thermogravimetric analysis (TGA) apparatus. (A) Crushed oil shale sample is placed in a highly calibrated platinum pan, which is placed over a hook and attached to a high precision scale. This is directly above the heating chamber which consists of electrical heating coils and ceramic insulation. (B) Perkin-Elmer Pyris 1 TGA instrument used in this study which measures oil shale sample mass loss with increasing temperature in a controlled inert atmosphere.

3.3.5 Elemental Analysis (CHNOS)

The presence and concentration of a variety of elements in oil shale can provide valuable insights. Carbon, hydrogen and nitrogen for the oil shale samples were determined on a Flash EA 1112 Series Analyser at Weatherford Laboratories (UK). The technique is the classical Dumas method, with thermal conductivity detection (TCD). The method is described in ASTM D5373 (coal) and ASTM D5291 (petroleum products). Weighed samples were combusted in oxygen at 1000 °C. The combustion products (including N and NOx) were swept by the helium carrier gas through combustion catalysts, scrubbers and through a tube filled with reduced copper. The copper removes excess oxygen and reduces NOx to N_2. The

gases were swept onto a chromatography column and measured with a TCD. Detection limits were 0.05% for Carbon and H, 0.01% for Nitrogen.

Oxygen was determined on a LECO RO-478 Oxygen Analyser. This method is described in ASTM D5622. An oil shale sample was pyrolysed at 1200 °C in a carbon pyrolysis tube to convert oxygen in the sample to CO and CO_2 which were then measured by non-dispersive infrared detection. The method is generally applicable to organically bound oxygen. Oxygen from water was determined. Refractory metal oxides such as those of silicon, aluminium and boron were not determined. Detection limit was 0.1% for Oxygen.

Sulphur and iron were determined after a $HNO_3/HClO_4$ total digestion and dissolution followed by analysis on a Perkin Elmer DV 5300 ICP-AES. A modified EPA 200.7 method was used for ICP-AES analysis. All the samples were duplicated several times and the results were averaged to determine the percentage of the elements in the sample.

3.3.6 Modified Fischer Assay (MFA)

The Modified Fischer Assay (MFA) extracts all hydrocarbons from the sample using pyrolysis - simulating industrial retorting conditions, and requires only 100 g of sample per test. The MFA results provide ore grade assessment and basic, oil, gas, and coke products for analysis.

The grade of oil shale can be determined by measuring the yield of oil of a shale sample in a laboratory retort (Figure 3.9). This is perhaps the most common type of analysis that is currently used to evaluate an oil-shale resource. For this study, MFA was performed on the Green River (Mahogany zone) oil shale samples at UMATAC laboratories (Calgary, Canada). The Modified Fischer Assay method consisted of heating a 100 g sample crushed to a particle size that passes through an 8 mesh (2.38-mm mesh) screen in a small aluminium retort to 500ºC at a rate of 12ºC per minute and held at that temperature for 40 minutes. The distilled vapours of oil, gas, and water were passed through a condenser cooled with ice water into a graduated centrifuge tube. The oil and water were then separated by centrifuging. The

quantities reported are the weight percentages of shale oil (and its specific gravity), water, shale residue, and "gas plus loss" by difference.

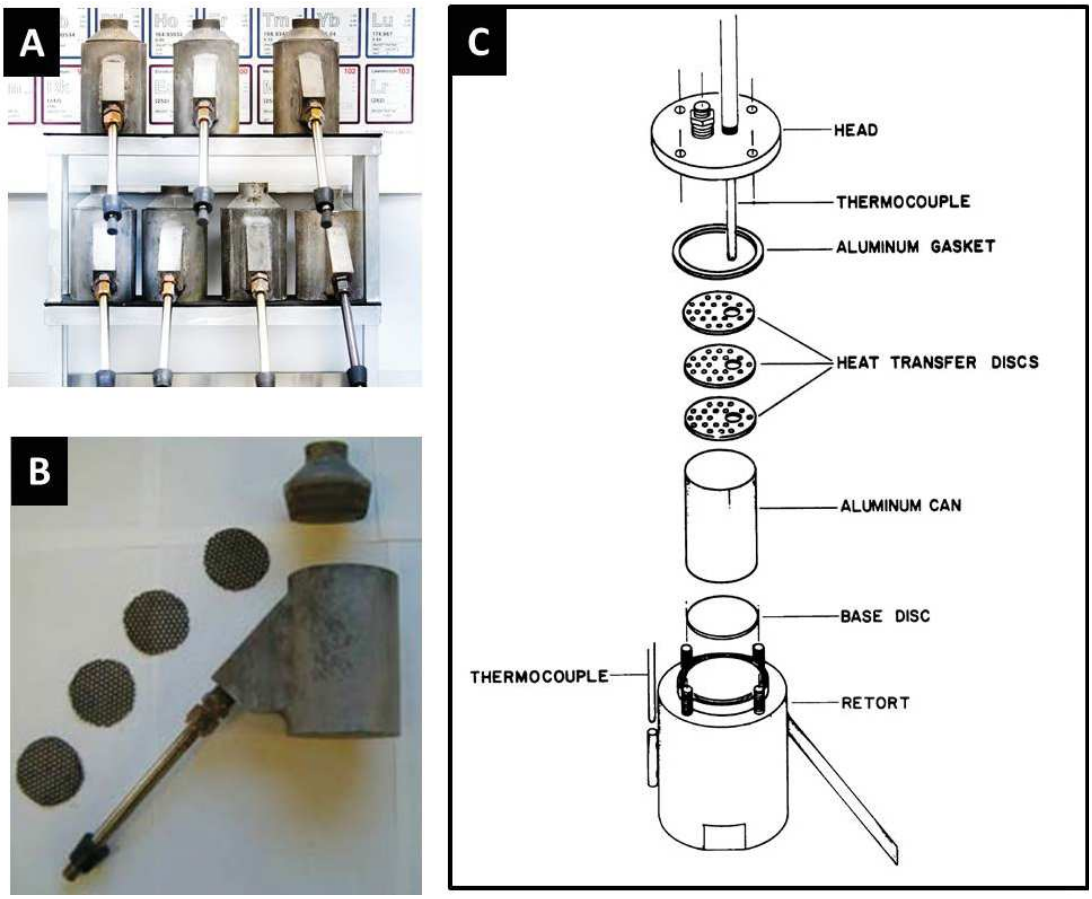

Figure 3.9 Modified Fisher Assay pyrolysis incorporates a defined heating rate and condenser to determine the amount of oil, gas, and water that can be extracted from oil shale. (A) and (B) MFA retorting vessels, (C) Retort assembly, where the oil shale sample is placed in an aluminium can and three aluminium heat transfer disks are placed at regular intervals in the sample. The sample and container are then placed in the steel retort.

3.4 Optical Microscopy

Optical microscopy provides a useful imaging technique to characterise the fine-grained structure of oil shale rocks. Thin section analysis serves as a basis for Petrography and Petrology studies. Shale rock specimens are often friable and brittle by nature, therefore thin section preparation requires meticulous, reliable slabbing, grinding, lapping and polishing machines. For this study, geological thin sections from the Green River Formation were prepared at Precimat Laboratories (Texas, USA).

Thin sections of 20 μm thickness were prepared using the following procedure:

1. Oil shale samples were air dried before impregnation.
2. Samples were then vacuum impregnated with epoxy.
3. Samples were hand lapped and polished down to 0.05 microns on both front and back, using silicon carbide, diamond, and alumina media and a high-purity hydrocarbon lubricant.

The oil shale thin sections were then optically examined using a Zeiss SteREO Discovery.V12 microscope with AxioVision LE64 software (Carl Zeiss, Germany) using plane-polarized light (PPL). Mosaic photomicrographs were generated by automatically stitching thousands of individual images into one all-encompassing view.

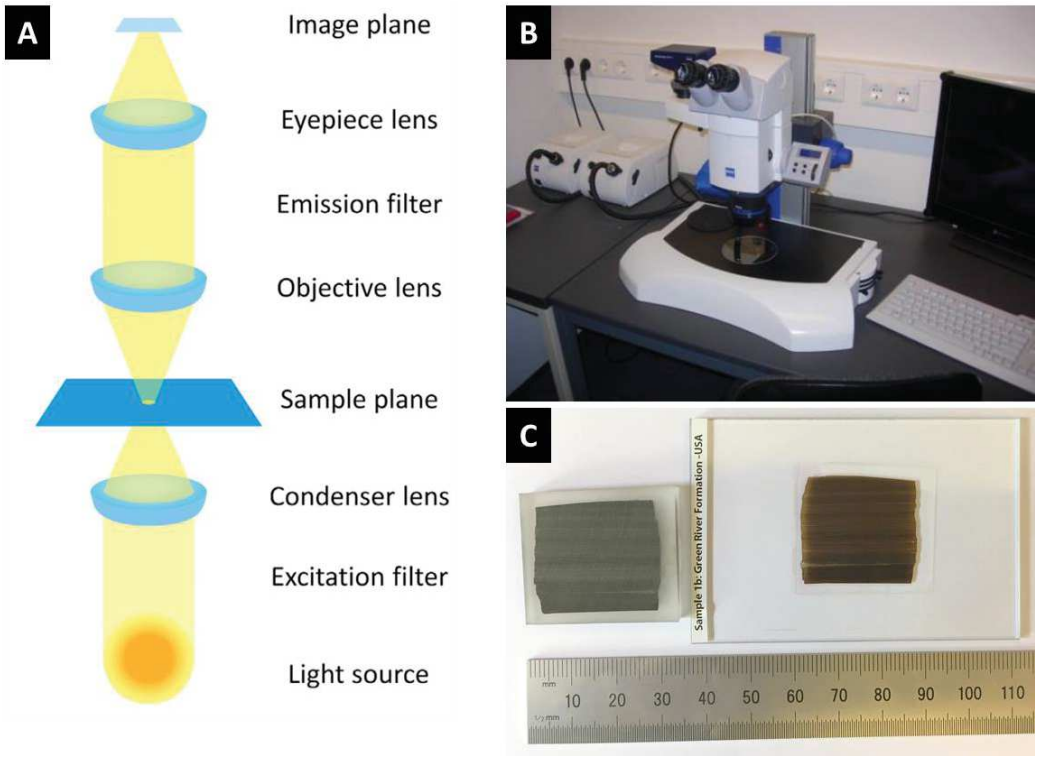

Figure 3.10 (A) Optical microscope main components: light source, the condenser, the objective and the ocular (eyepiece), (B) Zeiss SteREO Discovery V12 microscope used in this study, (C) Oil shale resin filled block (left) and prepared thin section (right) of the Green River (Mahogany Zone) oil shale.

A compound light microscope is an optical instrument that uses visible light to generate a magnified image of an object. There are components in an optical microscope that are critical in producing an image: (1) the objective lens, which collects light diffracted by the sample and forms a magnified real image at the real intermediate image plane near the eyepieces or oculars, and (2) the condenser lens, which focuses light from the illuminator onto a small area of the specimen (Figure 3.10)

Optical microscopes are ultimately limited by their resolution, the smallest distance at which two points can be resolved (Figure 3.11). In 1873, *Ernst Abbé* recognised that this was not just a technical limit in the manufacture of optics/microscopes but also rather a physical limit known as the diffraction limit. According to *Abbé*, the limiting spot size resolution that could be achieved by a microscope is given below:

$$r \geq \frac{\lambda}{2NA} \tag{3.2}$$

Where λ is the illumination wavelength of light, NA is the numerical aperture of the objective where NA = n sin α: n is the refractive index of the material and α is half the angle of acceptance of the lens, the maximum critical angle defined by the lens and focused light.

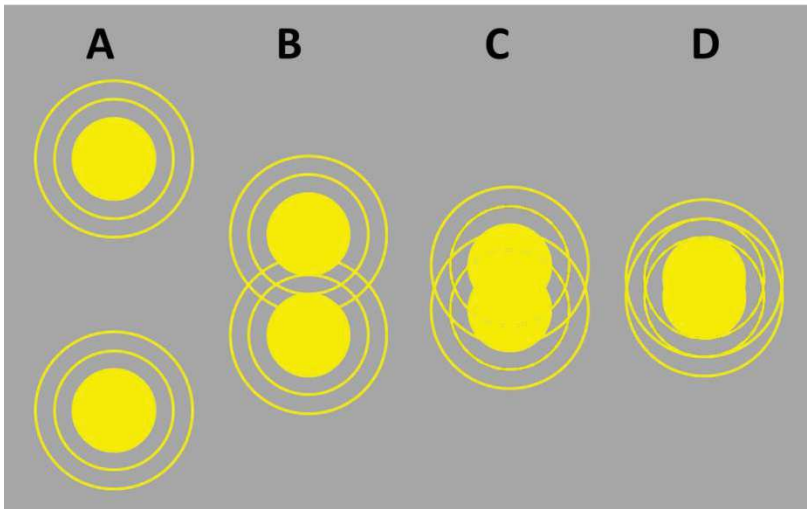

Figure 3.11 Examples of Airy disks of 2 point sources in the vicinity of one another where (A) the sources are separated by a large distance (B) a smaller separation distance but resolvable (C) the Rayleigh criterion where they are just resolvable (D) where they are unresolvable.

3.5 Scanning Electron Microscopy (SEM) and Energy Dispersive X-ray Spectroscopy (EDS) Analysis

Scanning Electron Microscopy (SEM) allows for the observation and analysis of the surface microstructure of a bulk sample using a finely focused beam of electrons. The mechanics of the modern scanning electron microscope (SEM) system allow for various imaging and detecting techniques that can be used to analyse various aspects of the composition of oil shale samples at very high resolution. Scanning electron microscopy, unlike conventional light microscopy, generates images by recording various signals resulting from interactions of an electron beam with the sample as it is scanned in a raster pattern across the sample surface. A fine electron probe, with a spot size from a few angstroms to several hundred nanometres, is generated by focusing electrons emanating from an electron source (conventionally called the electron gun) onto the surface of the specimen using a series of electro-optical lens elements. The combination of the source and the lens elements is called the electron column.

The main components of the SEM are: (1) electron source, (2) focusing- and scanning magnets, (3) detectors and (4) sample stage. A schematic of a typical SEM set-up is shown in Figure 3.12. The source of electrons in an electron microscope is the electron gun. In the gun, the electrons are emitted from the cathode either due to heating (thermionic source) or due to expelling electric field (field emission gun, FEG).

In this study, the FEI Quanta 650 microscope was used. In this system, a Field Emission Gun (FEG) is used to produce an electron beam that is smaller in diameter, more coherent and with up to three orders of magnitude greater current density or brightness than can be achieved with conventional tungsten tipped filaments. The result in scanning electron microscopy is significantly improved signal-to-noise ratio and spatial resolution, and greatly increased emitter life and reliability compared with thermionic devices.

After acceleration the electrons are focused and scanned by magnetic lenses. The electron lenses work on the basis of the Lorentz force. The focal length of magnetic lenses and the size of the beam spot can be changed by changing the current flowing through the coils. The minimum diameter of the beam spot is ~1 nm.

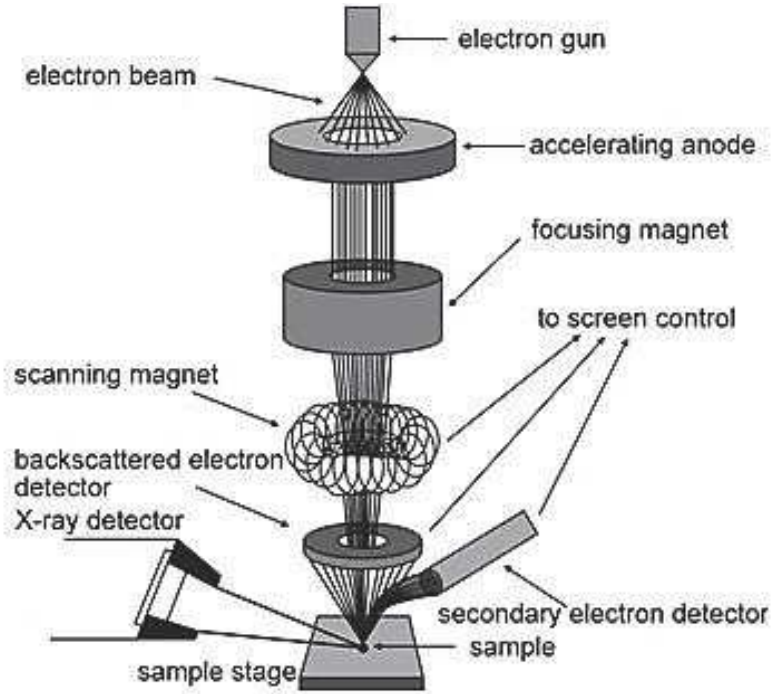

Figure 3.12 Schematic drawing of the major components of a scanning electron microscope (SEM). Specific detectors are used to register the signals arising from various electron–matter interactions. (adapted from Amelinckx et al. 2008).

Several types of electrons are generated as the result of the energetic bombardment of the specimen by the primary beam (Figure 3.13). All of these electrons carry distinct structural information about the sample and differ from one another in origin, energy, and traveling direction. The secondary electrons (SE) are specimen electrons, knocked out of the surface by inelastic collisions with the incoming beam electrons and their majority are emitted with energies of a few electron volts (3-5 eV) providing only near-surface (topographic) information. In this case, the resolution is determined by the diameter of the focused electron beam. The ultimate resolution in case of secondary electrons is ~1 nm.

The backscattered electrons (BSE) are beam electrons experiencing large angle (or multiple) elastic scattering and are closely linked to compositional contrast. The

order of magnitude of their energy is some tens of kilo electron volts (10-30 keV). Owing to their energy range they provide information from deeper layers. Accordingly, in this case the resolution is poorer, ~2-4 nm, but valuable compositional contrast is acquired.

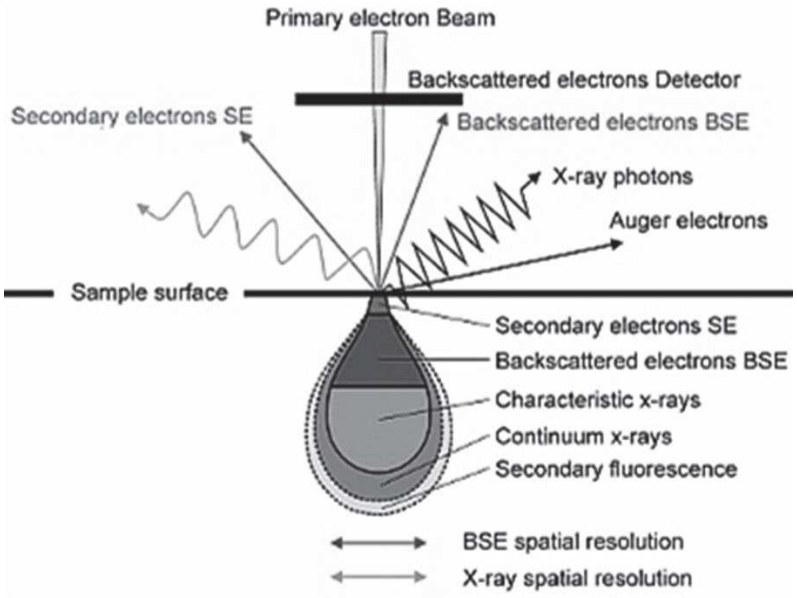

Figure 3.13 A schematic overview of the signals that are generated when an electron beam interacts with a solid sample which are used in the scanning electron microscope (SEM) for microstructural characterization. The most frequently detected signals are high-energy backscattered electrons (BSE), low-energy secondary electrons (SE) and X-rays (EDS/EDX).

Photons can also be generated from the excitation by the primary electron beam. For example, X-rays with a continuous spectrum in energy (bremsstrahlung) are generated as a result of the deceleration of the electrons. Additionally, characteristic X-ray lines are generated from electron excitation within specimen atoms that interact with the primary electron beam. The latter form of X-ray is particularly useful in chemical analysis with SEM. The characteristic X-rays originate from the inner-shell ionization process, where an electron from the electron beam interacts with the tightly bound inner-shell electrons, ejecting an atomic electron and leaving a vacancy in that shell. The atom relaxes to its ground state through a limited set of transitions of outer-shell electrons to fill the inner-shell vacancy. The energies of the electrons in the shells are sharply defined, with values characteristic of the binding energies of the electrons; therefore, the characteristic X-rays are elemental specific, creating a powerful tool for elemental analysis in SEM.

To take advantage of the element-specific information caused by X-ray excitation, EDS (or EDX) can be performed. As the electron beam scans the sample surface pixel by pixel, a full X-ray spectrum can be acquired from each pixel (Figure 3.14). Elemental distribution can therefore be mapped using the relative peak intensity to build an image of the scanned area. This can then be interpreted to estimate mineral phase composition. In this study, automated mineralogy measurements were performed on an FEI QEMSCAN 650F instrument (Figure 3.19) with two Bruker XFlash 6 series EDS detectors and Nanomin software (FEI, Hillsboro, OR, USA) was used to map the mineral distributions based on elemental compositions coupled to a library of mineral phases. For EDS calibration, a copper standard was used (Figure 3.20).

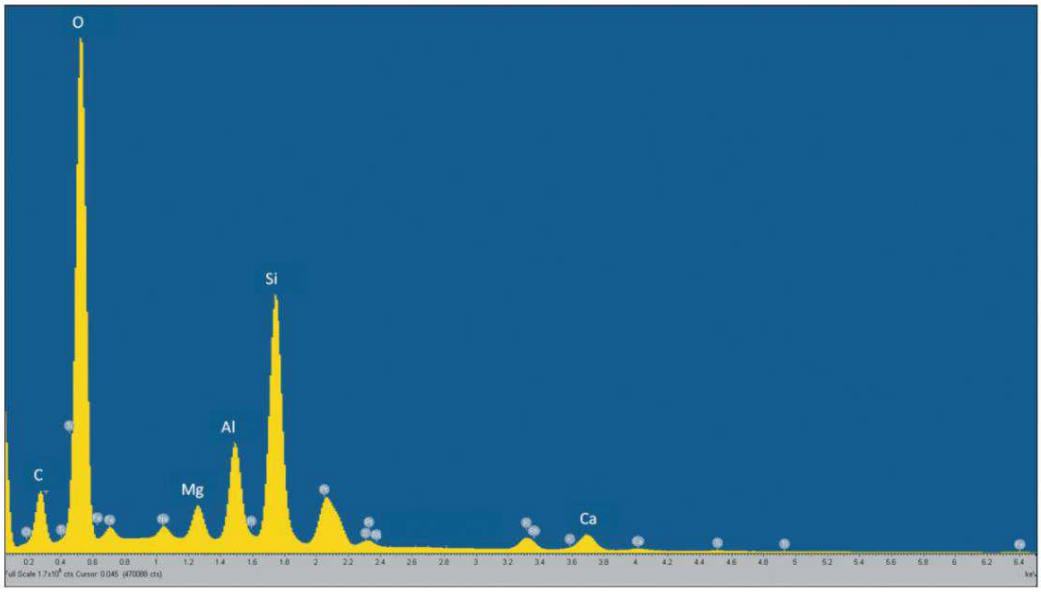

Figure 3.14 An example of an X-ray spectrum acquired from a shale sample. Individual peaks indicate an increased concentration of a given element. C = carbon, O = oxygen, Mg = magnesium, Al = aluminium, Si = silicon, Ca = calcium (Huang et al., 2013).

3.5.1 Sample Preparation

Observations of oil shale samples using SEM requires specific sample preparation. In this study, oil shale (Mahogany Zone) samples of about 18 mm × 14 mm × 5 mm were hand-polished using sandpaper (600, 1200 and 2000 grit) and diamond lapping film (6 µm, 3 µm and 1 µm) (Figure 3.15). However, traditional mechanical sample preparation using grinding and polishing alone can result in deformation, flaws, and artefacts that obscure the true structure of the oil shale microstructure (Figure 3.18).

Figure 3.15 Oil shale samples in this study were hand-polished using (A) sandpaper (600, 1200 and 2000 grit) and (B) diamond lapping film (6 µm, 3 µm and 1 µm).

A non-contact polishing technique using argon ions can be used to obtain a smooth surface. For oil shale samples in this study, the Fischione 1060 SEM Mill was used with 6 keV ions under a 2˚ incident angle and 360˚ sample rotation produce a polished surface after 22 hours. Figure 3.16 shows the setup of the two argon ion beams polishing the sample. Samples were then attached to a 25 mm diameter pin–type stub using carbon tape, and coated with less than a 100-Å thick elemental carbon film using a vacuum evaporator (Quorum Q150T) to mitigate charge build-up (Figure 3.17). Compared with mechanical polishing, ion beam polishing provides smoother surfaces and less curtaining effects for high-resolution microstructural analysis using the SEM.

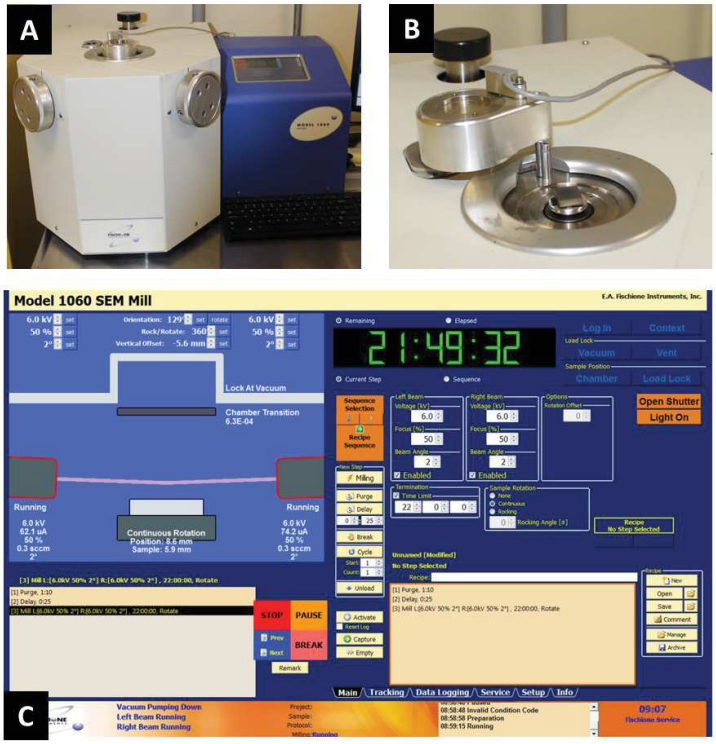

Figure 3.16 (A) Fischione 1060 SEM Mill used in this study for Argon (Ar) Ion beam polishing. (B) Green River (Mahogany Zone) oil shale sample loaded into the chamber. (C) With the sample stage fixed in position, the ion sources were tilted to 2° operating at energy of 6kV for 22 hours milling an oil shale surface area of 18 mm × 14 mm.

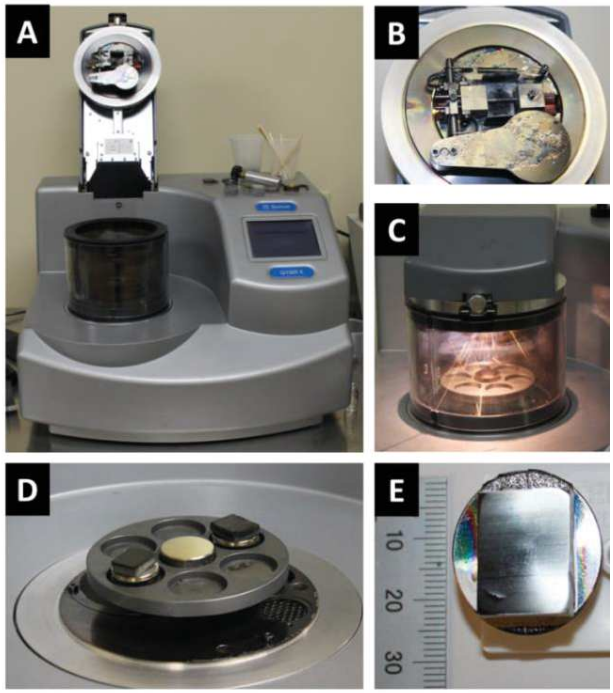

Figure 3.17 (A) Q150T carbon coating system used to apply 100-Å thick elemental carbon film on the surface of the oil shale samples to minimise charge build up during SEM imaging. (B) High purity, 3.05 mm diameter carbon rod inserted. (C) Thin conductive layers of carbon are generated by resistive evaporation of the carbon rod. (D) and (E) Oil shale samples following carbon coating.

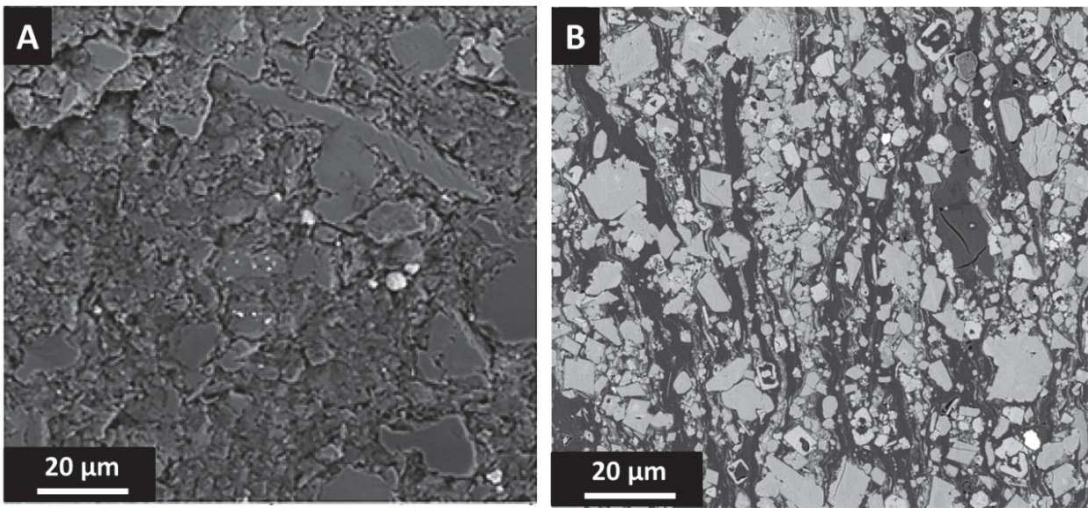

Figure 3.18 Oil shale BSE image under (A) mechanical polishing and, (B) argon ion beam polishing. Mechanical polishing is not suitable for shale samples, as this technique tends to destroy the fine structure of the pore network (e.g., smearing grain boundaries, embedment of grit into surface of sample). A non-contact polishing technique with argon ions is used to obtain a smooth surface.

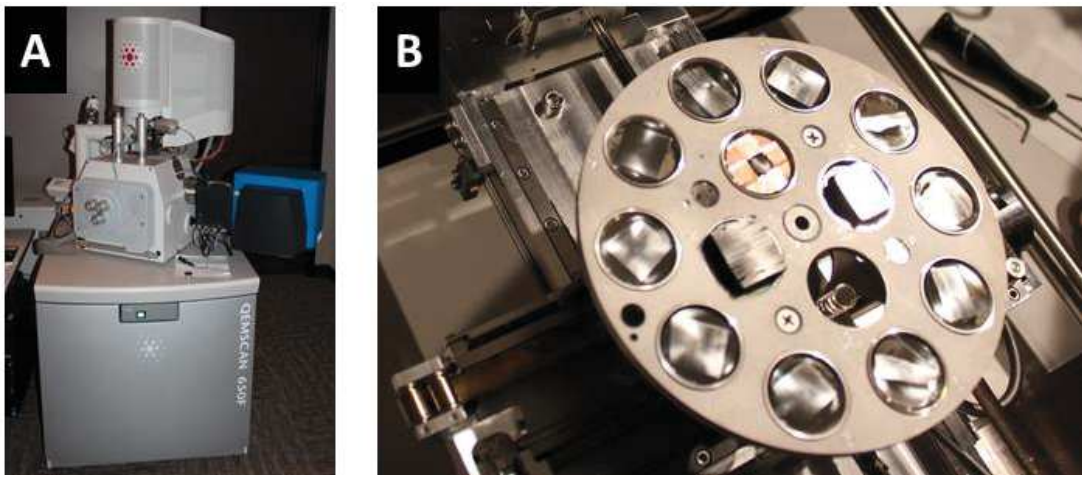

Figure 3.19 (A) FEI QEMSCAN 650F system used in this study to image Green River (Mahogany Zone) oil shale samples. (B) Oil shale samples secured onto sample stage in preparation for ultra-high resolution mosaic imaging and MAPS Mineralogy.

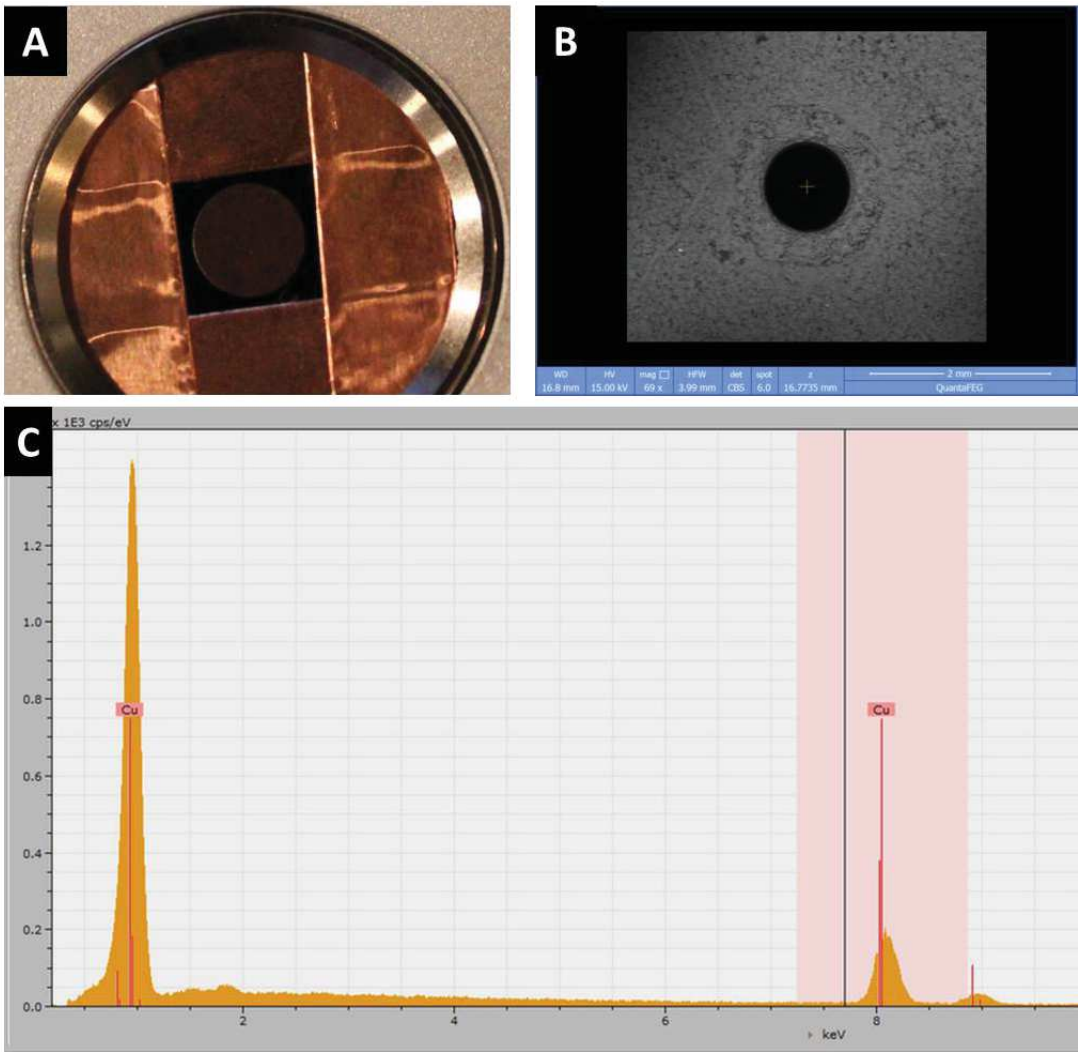

Figure 3.20 Energy-dispersive X-ray spectroscopy calibration using copper standard (A) Copper sample, (B) BSE image of copper sample and (C) Copper spectrum; the K-alpha peak being the taller than the K-beta peak.

3.5.2 Large Scale Automated Imaging and Mineralogy

Large scale imaging was performed using the FEI MAPS (Modular Automated Processing System) Tiling and Stitching software to generate high-resolution image mosaics and mineral maps where the size is limited only by time constraints. Auto-imaging controls (focus, brightness, contrast) contribute to an image that is near seamless; even when it is composed of many thousands of individual SEM images. Figure 3.21 shows a set of 2 × 2 individual tiles and the resulting seamless mosaic. Overlap between the images could be kept to a minimum because of the high accuracy provided by piezo-electric stages deployed on high resolution SEMs and DualBeams.

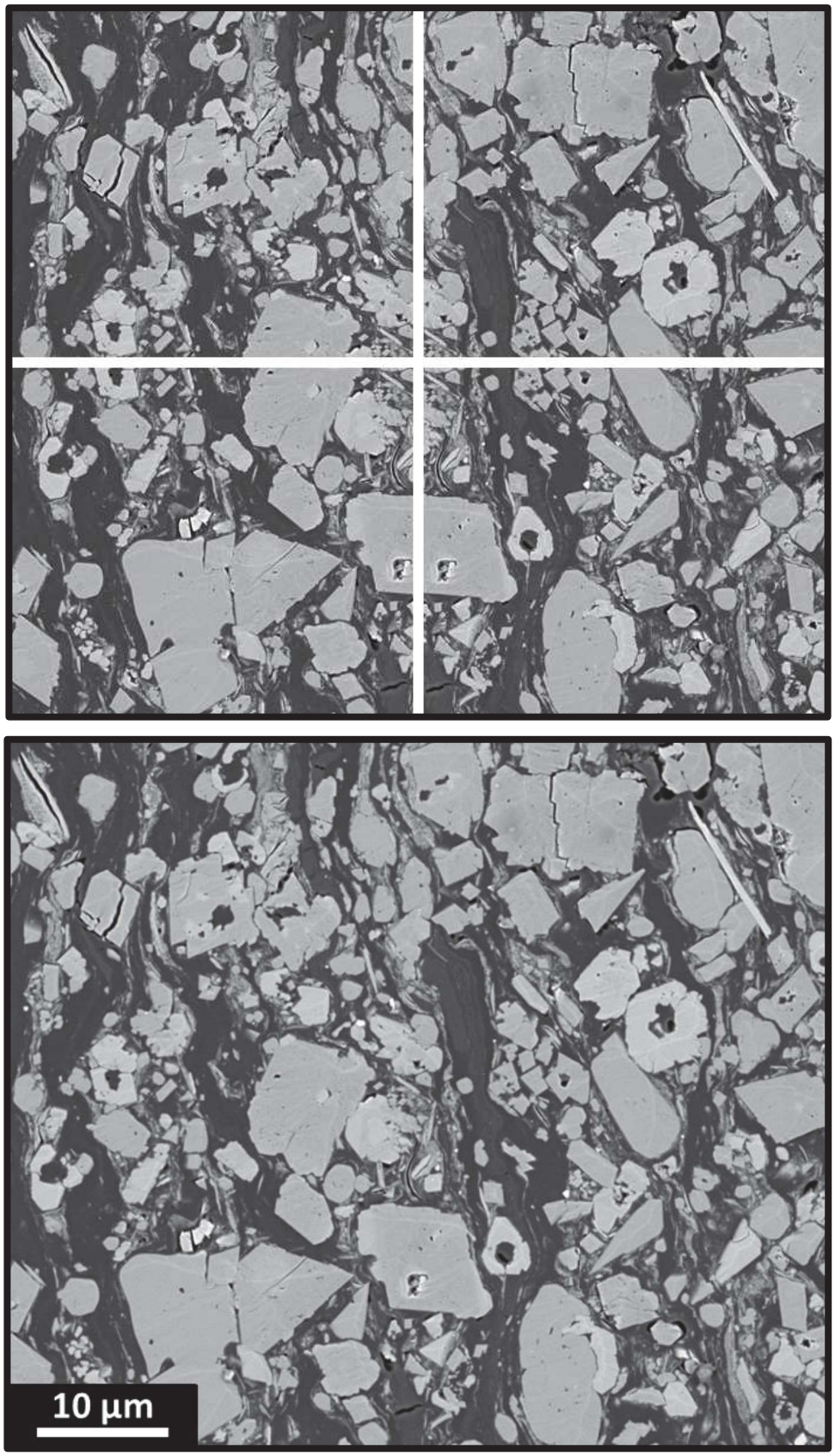

Figure 3.21 A 2 × 2 set of high-resolution BSE images; before (top) and after stitching (bottom) for the Green River (Mahogany Zone) oil shale, acquired at 5 keV with a 15 nm pixel size. Tiles acquired with a 10% overlap using MAPS (Modular Automated Processing System) Tiling and Stitching software.

MAPS is software for automated acquisition of high resolution images from large areas. It enables the navigation, tiling, stitching, correlation and analysis of image data. Automated imaging of large areas is a principal feature of MAPS. The area of interest is divided in multiple tiles, which are recorded in a sequence and subsequently stitched to generate one single image. The size of the area is limited by the size of the stage rather than the image acquisition hardware. As a result, high-resolution images of gigapixel size can be acquired. Another benefit of dividing a large area in multiple tiles is an improvement of overall image quality. To acquire data from a single large area at high resolution would take too much time, resulting in image quality loss due to stability and drift issues inherent in any system. With tiling and stitching approach, drift is kept to a minimum because the acquisition of data of every tile can be achieved much faster, leading to higher quality results.

MAPS uses real-time acquisition of tiles with a small pixel size that have a programmable overlap (Figure 3.22). Dividing the area into smaller tiles has two important advantages: (1) image distortions are kept to a minimum reducing the need for post-processing and improving the image quality; (2) acquired data is immediately available for review and further processing.

In this study, individual tiles were stitched by MAPS to create an overview of the oil shale sample as one large image using FEI's stitching algorithms. The system was configured to start the stitching process during image acquisition. Stitching accuracy was constantly monitored and in the event that the stitching quality confidence level was low, the software highlighted the issue enabling manual alignment. Images were stored in RAW, Tiff and HD View compatible formats.

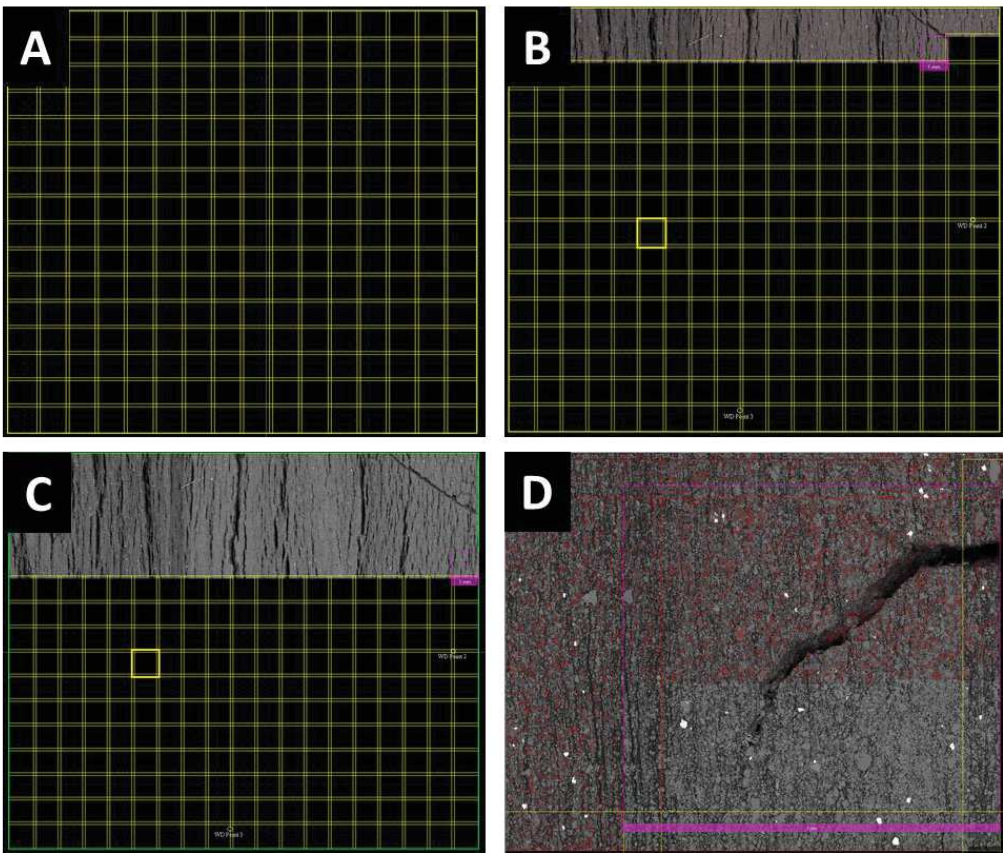

Figure 3.22 Modular Automated Processing System (MAPS) tiling and stitching system. (A) Grid system of 19 × 16 tiles with each tile being 1.024 mm × 1.024 mm, (B) and (C) Real-time acquisition and stitching of tiles with 10% overlap, (D) Close-up on an individual tile showing the acquired BSE image and energy-dispersive X-ray spectrometry (EDS) data acquired (red colour indicated areas rich in calcium).

3.6 FIB-SEM

A dual beam focused ion beam (FIB) scanning electron microscope (SEM) uses a beam of focused ions to mill away material allowing for *slice and view*, which is a technique based on using a FIB to create a cut at a designated site in the specimen. The cuts are then followed by viewing or imaging the newly generated surface with an SEM. During milling, the beam is maintained normal to the sample surface with the electron beam typically at an angle of 52° from the ion beam. The iteration of these two steps results in the generation of a series or stack of 2-D images of the specimen at regularly spaced intervals, which can be reconstructed into a 3-D digital grey-scale volume representation of the sample (Figure 3.23). This technique is particularly useful in revealing the 3-D distribution of mineral types, organic matter and porosity for oil shale samples.

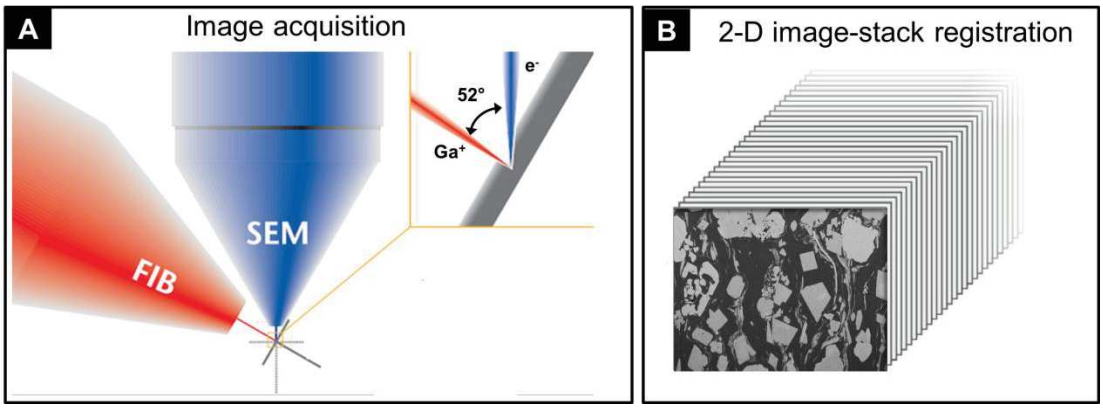

Figure 3.23 (A) FIB-SEM DualBeam configuration used in image acquisition In a DualBeam, the electron and ion beams intersect at a 52° angle at a coincident point near the sample surface, allowing immediate, high resolution SEM imaging of the FIB-milled surface. (B) 2-D FIB-SEM 2-D image stacks are computationally converted to a 3-D volume.

The ion source often consists of a liquid metal such as gallium (Ga^+). The ions are extracted from the liquid applying a strong electric field. The extracted Ga^+ ions are accelerated through an electric potential down the ion column passing through apertures that define the beam size, and finally, they are focused through lenses onto the target to interact with the target material. Momentum transfer from the accelerated Ga^+ ion to the atoms of the target material removes surface atoms from their lattice position into the vacuum if the transferred momentum is large enough to overcome the binding energy. Details on the ion– solid interaction are presented elsewhere (Giannuzzi et al., 2005; Nastasi et al., 1996; Orloff et al., 2003). Gallium is used as source material because it has a low melting point (29.8°C) and Ga^+ is a comparatively heavy ion that transfers a large momentum to the target material resulting in a high sputtering yield. Details of the physics of a FIB device and the sputtering process are given elsewhere (Giannuzzi et al., 2005; Orloff et al., 2003).

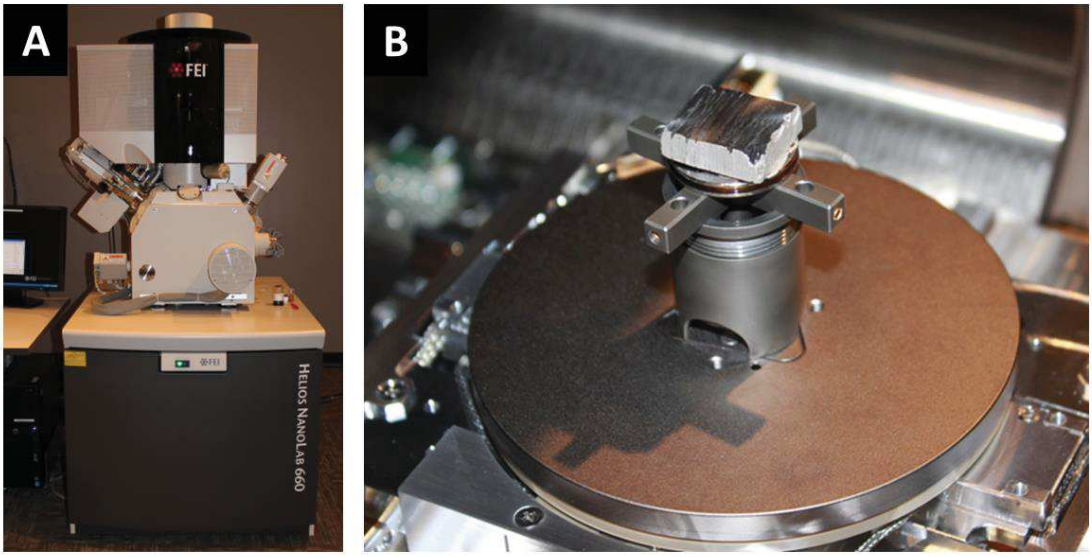

Figure 3.24 (A) FEI Helios 660 FIB-SEM system used in this study to acquire high-resolution 3-D datasets of un-pyrolysed and pyrolysed samples of Green River (Mahogany Zone) oil shale. (B) Oil shale sample secured onto stage in preparation FIB-SEM acquisition.

In this study, the FEI Helios NanoLab 660 DualBeam system was used to generate 3-D oil shale volumes of Green River (Mahogany Zone) oil shale samples (Figure 3.24, Figure 3.25). The first step necessary for the acquisition of a good quality image in 3-D was coating the sample with carbon to avoid charging of the region of interest (Figure 3.17). Charging would cause a deflection of the ion or electron beam. In addition, a thin layer (~4µm) of a conducting material (Platinum, Pt) was deposited just above the region of interest to avoid damage of the target by the ion beam.

The Pt layer was deposited on the surface using the following procedure (Figure 3.26). The needle of the gas injection system was inserted and positioned very close to the location where the Pt should be deposited. An organic Pt-containing gas flowed through the needle and was adsorbed at the target surface. The Ga^+ ions broke the bonds between the organic molecule and Pt thus allowed the organic molecules to be pumped off by the vacuum system whereas the Pt was adsorbed to the target surface. Finally, the Pt atoms formed nanocrystals on the surface of the target. The application of gas injection systems has been described in more detail elsewhere (Giannuzzi et al., 2005; Wirth, 2009, 2004).

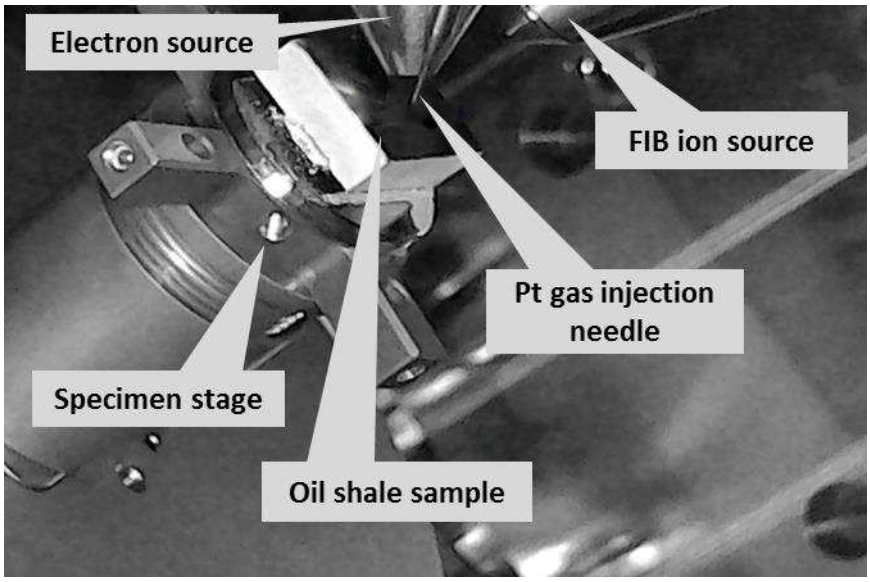

Figure 3.25 FIB-SEM setup consisting of an (1) electron source, FIB ion source (Ga^+), Platinum (Pt) gas injection needle, specimen stage and oil shale sample for analysis. The ion beam and electron beam were set a 52° angle to each other.

After the initial preparation steps, the sputtering procedure was started. Given that sputtering material with Ga^+ induces re-deposition of the sputtered material and amorphization due to Ga^+ implantation in the surface, two parallel trenches were sliced on both sides of the oil shale sample, which served as a repository for sputtered material. Fiducial markers were placed as visual reference points for image processing to ensure correct alignment between slices (Figure 3.26).

Following the complete cleaning of the fresh surface normal to the sample surface, the three dimensional volume imaging is achieved by repeating the sputtering process (slicing), and viewing, meaning imaging the frontal microstructure with the electron beam until the whole selected volume has been processed by subsequent slicing and viewing.

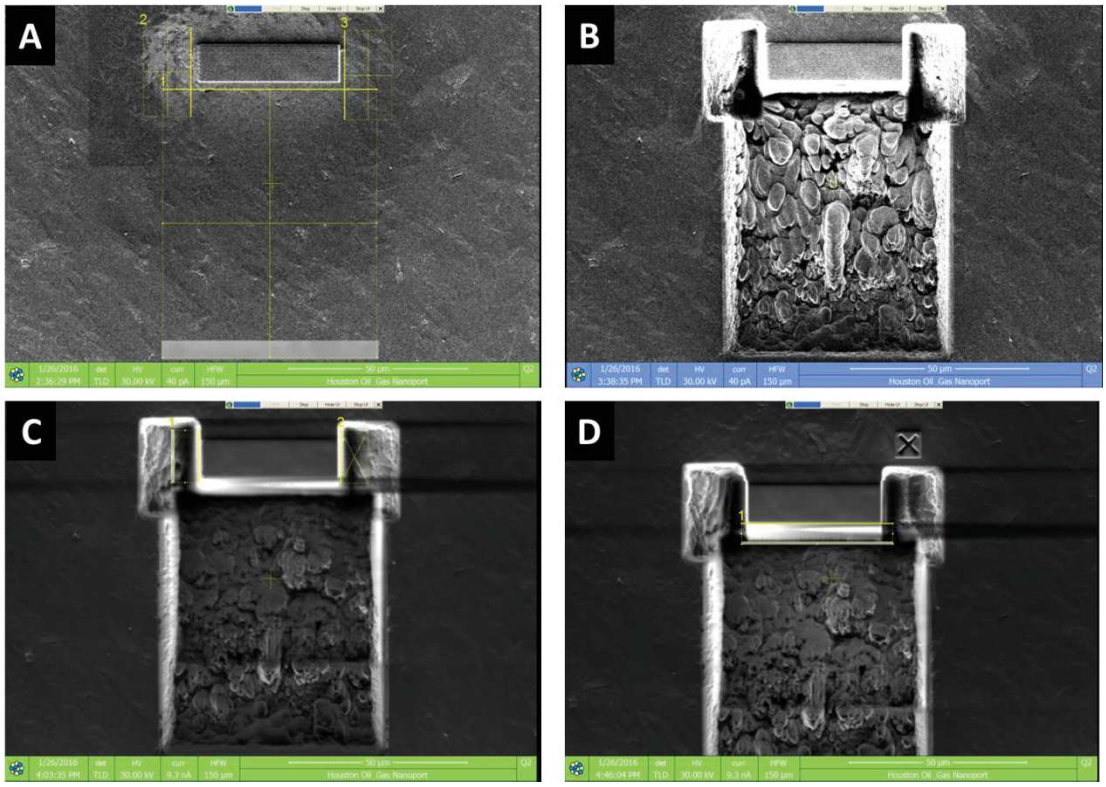

Figure 3.26 (A) SEM image following platinum deposition of 40 µm × 5 µm × 2µm, which act as a protective layer. This is vital to protect the area of interest from any stray ions and prevent any damage to the area, which will otherwise cause curtaining artefacts. (B) and (C) Trenches milled around region of interest for debris / redeposited material to collect in which would otherwise cause obscuration of the region of interest or shadowing effects. (D) A 7 µm x 7 µm × 2 µm platinum pad was deposited above the right side of the trench and an X placed in the centre. This is a fiducial marker, which acts as a reference point and allows for image alignment.

The efficiency of the sputtering process, or sputtering yield, is a function of the accelerating voltage, the angle of incidence of the ion beam and the beam current. A focused beam of gallium ions (Ga^{+}) operating at 30 keV and 2.5 nA beam was used for the sputtering/slicing process and each new milled surface was image at a 2 keV accelerating voltage and a 0.4 nA beam current under BSE mode. The entire process resulted in a 2-D stack of 600 slices, with each slice having a thickness of 10nm. The 2-D image stacks were collected using a *slice-and-view* imaging module.

3.7 X-ray Micro-tomography

X-ray micro-tomography (micro-CT) is a powerful non-destructive technique for material characterization that provides 3-D visualizations of the internal structure of an object. Micro-CT scans combine information from a series of 2-D X-ray absorption images recorded as the object is rotated about a single axis. By using mathematical principles of tomography, these 2-D images record the variation of X-ray attenuation within the sample and are reconstructed to produce a 3-D image where each voxel (smallest volume element, equivalent to a 3-D pixel) represents the X-ray attenuation at each single point (Landis and Keane, 2010). Given the relationship between X-ray absorption and material density, the 3-D internal structure can be inferred from the images. The resulting 3-D images are typically displayed as a series of 2-D slices. This process is illustrated in Figure 3.27.

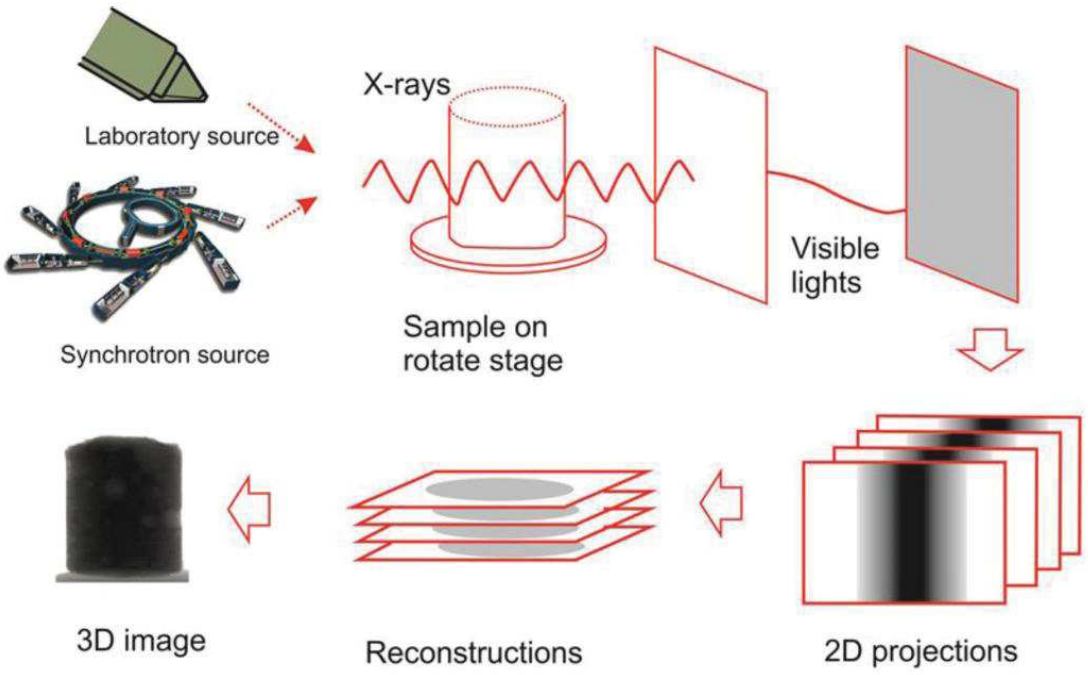

Figure 3.27 Schematic illustration of X-ray micro- tomography images acquisition and reconstruction (adapted from Landis & Keane 2010). X-ray micro-tomography images are generated based on the principle that X-ray intensity is linearly attenuated when passing through different materials. A decrease in X-ray intensity is a function of the X-ray energy, path length and material linear attenuation coefficient. The sample rotates around a specific axis and the detector measures the degree of attenuation, creating 2-D radiographs (projections) in greyscale. Individual 2-D projections are then reconstructed to produce a 3-D volume.

The principle of micro-CT is the attenuation of X-rays in the sample due to scattering and absorption when it passes through. The amount of attenuated radiation on an infinitely small distance is described by a linear attenuation coefficient, and the final attenuation indicates the sum of all local attenuation along the X-ray path (Stauber and Müller, 2008).

Photoelectric absorption, Compton scattering and Pair production are the three dominant processes that contribute to the attenuation of X-rays, with each being dominant in a different energy range (Figure 3.28) (Ketcham and Carlson, 2001). In photoelectric absorption, the electron is ejected and released when the full energy of an incoming X-ray photon is transferred to an inner electron. Compton scattering takes place when the incoming X-ray photon interacts with an outer electron, causing an electron to be ejected and lose part of its energy due to the deflection in another direction.

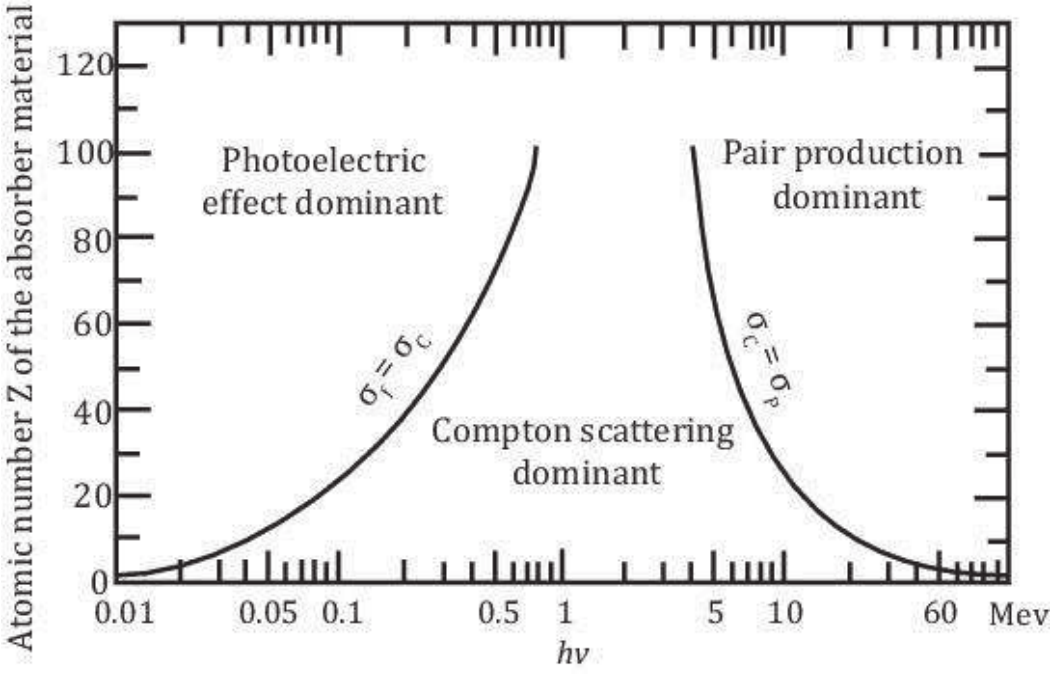

Figure 3.28 The interaction modes of X-rays with matter depending on elemental atomic number Z and the X-ray photon energy h*v*. There are three dominant physical processes responsible for attenuation of an X-ray signal: photoelectric absorption, Compton scattering, and pair production. In general, for geological materials, the photoelectric effect is the dominant attenuation mechanism at low X-ray energies, up to approximately 50–100 keV. Compton scatter is dominant at higher energies up to 5– 10 MeV, after which pair production predominates. Thus, unless higher-energy sources are used, only photoelectric absorption and Compton scattering need to be considered (Ketcham and Carlson, 2001).

In pair production, the photon interacts with a nucleus and is transformed into a positron-electron pair, with any excess photon energy transferred into kinetic energy in the produced particles. Photoelectric effect becomes the dominant attenuation mechanism at low X-ray energies, up to approximately 50-100 keV, followed by up to 5-10 MeV for Compton scattering, after which pair production dominates (Ketcham and Carlson, 2001).

For geological materials such as oil shale, the dominant attenuation mechanism is the photoelectric effect when a relatively low range of the energy spectrum is applied. A trend of the photoelectric effect is that the mass attenuation coefficient is approximately proportional to the third power of the attenuating material atomic number while being inversely proportion to the third power of the photon energy:

$$\text{photoelectric effect} \sim \frac{(\text{atomic number})^3}{(\text{photon energy})^3} \tag{3.3}$$

A useful method to get insight into the expectation of scanning an oil shale sample is to plot the linear attenuation coefficients of the materials over the range of X-ray energy spectrum. The linear attenuation coefficients can be obtained by multiplying mass attenuation coefficient by mass density (Berger et al., 2010). Figure 3.29 illustrates the relationship between linear attenuation coefficients and incident X-ray energy for four common materials found in oil shale rock samples: pyrite, calcite, dolomite, illite, quartz and carbon. By understanding the linear attenuation coefficient as a function of X-ray energy, it is possible to predict the ability of distinguishing minerals in micro-CT images. According to Figure 3.29, pyrite and organic matter (carbon) can be easily differentiated from other materials whereas calcite, dolomite, illite and quartz are harder to distinguish from one another.

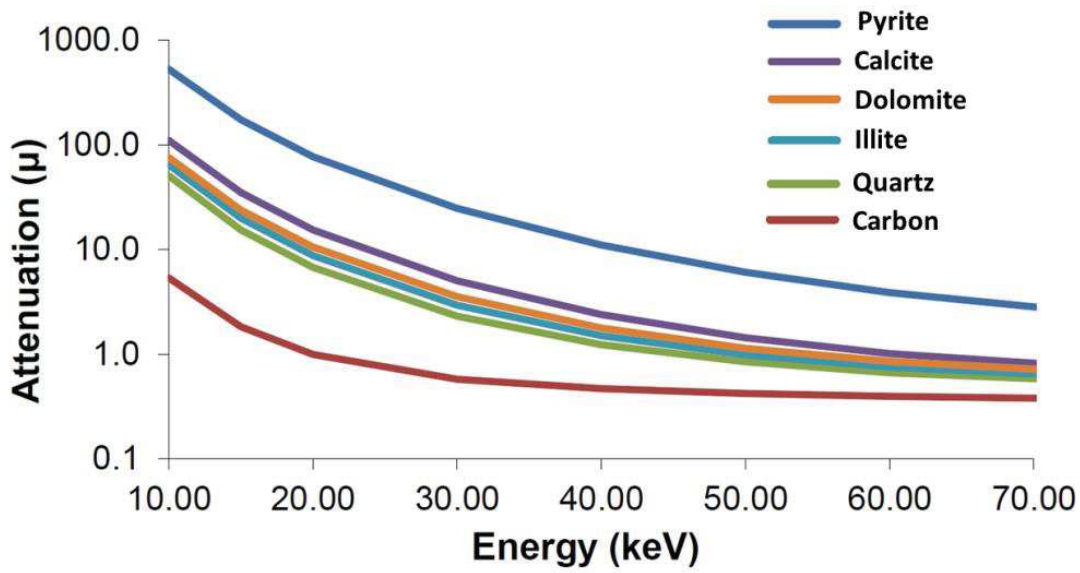

Figure 3.29 Linear attenuation coefficient as a function of incident X-ray energy for four common materials found in oil shale rock samples: pyrite, calcite, dolomite, illite, quartz and carbon. Note that the linear attenuation coefficients for calcite, dolomite, illite and quartz are very similar but rather different from pyrite and carbon (organic matter).

The intensity of attenuated transmitted X-ray beam (I) through a homogeneous material can be expressed using the Beer-Lambert Law (Cnudde and Boone, 2013; Ketcham and Carlson, 2001):

$$I = I_0 \exp(-\mu x) \tag{3.4}$$

where I is the attenuated intensity of X-ray beam, I_0 is the initial intensity of the X-ray beam, x is the thickness of the object material and μ is the linear attenuation coefficient with units of inverse distance. If the sample is composed of different materials such as in oil shale, the equation becomes (Ketcham and Carlson, 2001):

$$I = I_0 \exp[\sum_i (-\mu x)] \tag{3.5}$$

where each increment i reflects a single material with attenuation coefficient μ_i over a linear extent x_i. Equation (3.5) can be written by applying mass attenuation coefficient given as μ/ρ with unit of $cm^{-2}g^{-1}$ (Hubbell and Seltzer, 1996):

$$I = I_0 \exp[(\frac{-\mu}{\rho})\rho x)] \tag{3.6}$$

$$\frac{\mu}{\rho} = -(\rho x)^{-1} \ln(\frac{I}{I_0}) \tag{3.7}$$

where ρx is a term known as mass thickness and can be defined as the mass per unit area, being obtained by density multiplied by thickness x. The attenuation to each small thickness, dx, can be obtained by differentiating Equation (3.6):

$$\frac{dI}{I} = -\frac{\mu}{\rho} \rho dx = -\mu dx \tag{3.8}$$

There is a more general expression to define attenuated intensity of X-ray beam by adding the increments of attenuation along the direction of X-ray propagation:

$$I = I_0 \, exp[-\int \mu(s) ds] \tag{3.9}$$

where $\mu(s)$ is the linear absorption coefficient at position s along ray s. One of the key problems in computed tomography is to assign the correct value of μ to each position along the ray (and along all the other rays traversing the sample) knowing only the values of the line integral for the various orientations of s. This process is known as reconstruction (Stock, 1999):

$$\int \mu(s) ds = \ln(\frac{I_0}{I}) \tag{3.10}$$

Reconstruction is the mathematical process for converting 2-D projections into 3-D volumes. The most often used reconstruction technique is called filtered back-projection (Figure 3.30), where the micro-CT data is first convolved with a filter and each view is successively superimposed over a square grid at an angle corresponding to its acquisition angle (Feldkamp et al., 1989; Pan et al., 2009). The output of the reconstruction process is a 3-D image with its quality often determined by contrast and spatial resolution, depending on the scanning parameters used. In this study, scanned oil shale samples were reconstructed using the software Zeiss XMReconstructor, a Zeiss proprietary software accompanying the Zeiss Versa XRM-500 μ-CT instrument (Section 3.7.1.1). Examples of the reconstruction results for an oil shale sample are provided in Figure 3.31 Figure 3.33.

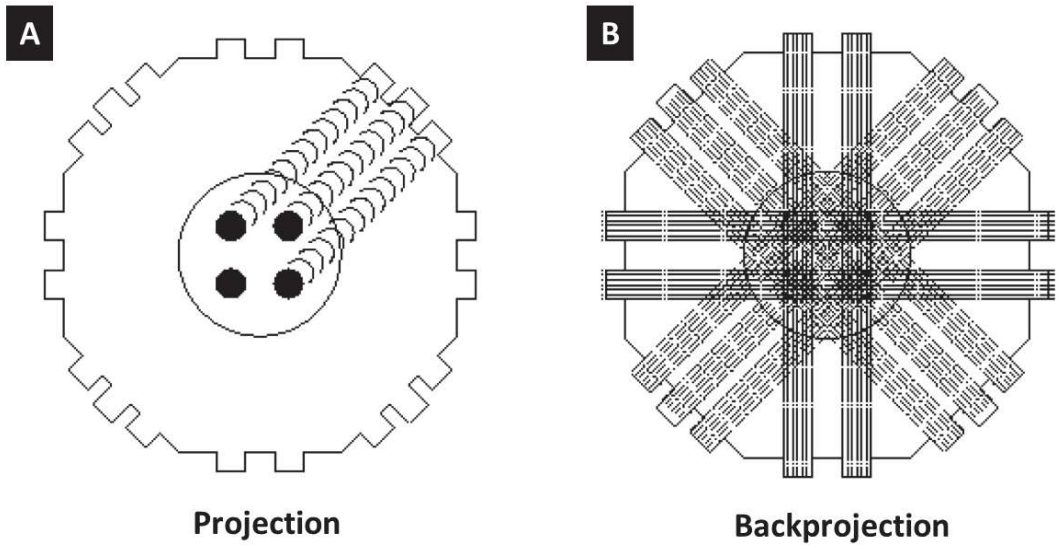

Figure 3.30 Illustration of (A) Projection, and (B) Backprojection. The object is rotated, pausing at discrete angles to collect 2-D projection images. The projection images are combined together to produce a 3-D reconstruction of the object's volume. Simple back-projection reconstructs an image by taking each projection and smearing (or backpojecting) it along the line it was acquired. As a result of this simple procedure, the backprojected image is blurred. In filtered backprojection (FBP), a filter is applied to each projection before the backprojection is done to counteract the blur. FBP is the most commonly used algorithm for computed tomography systems.

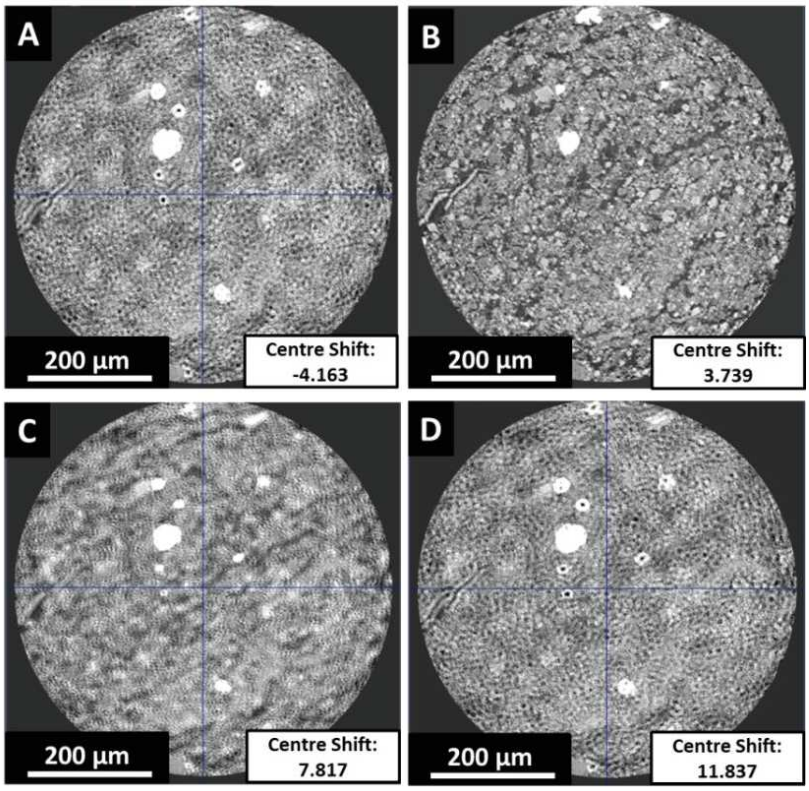

Figure 3.31 Reconstruction process using Zeiss proprietary software (Zeiss XMReconstructor) with centre shift at (A) -4.163, (B) 3.739, (C) 7.817 and (D) 11.837. For this oil shale dataset, a centre shift of 3.739 resulted in the best image quality.

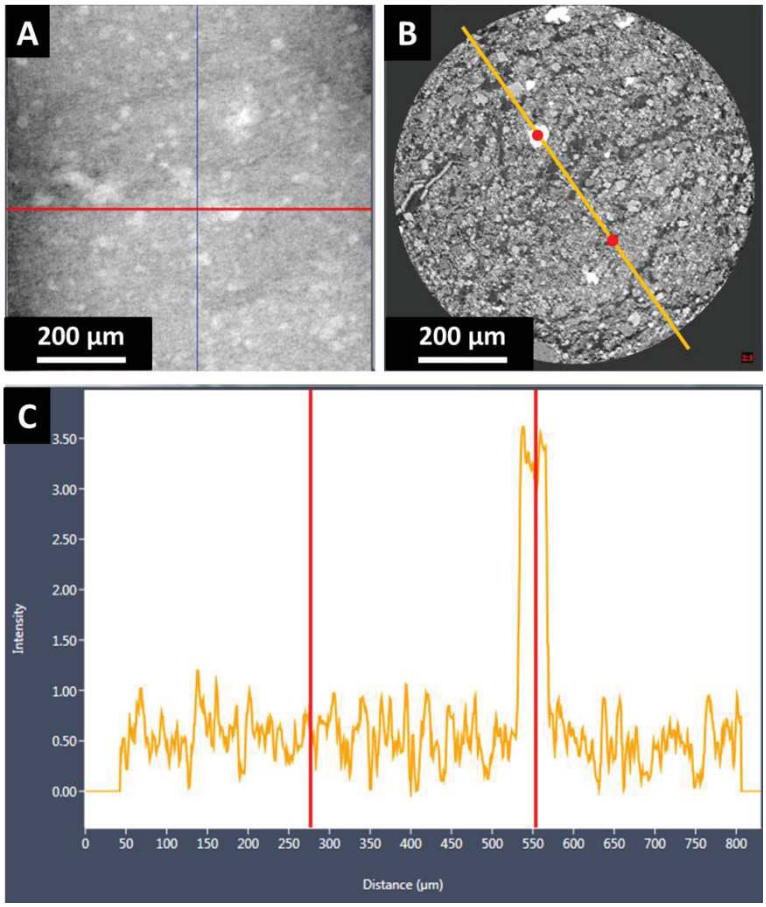

Figure 3.32 Oil shale sample (A) 2-D projections, (B) 2-D grey-level and (C) Line-plot indicating the intensity along the yellow line across image (B) with red markers for reference

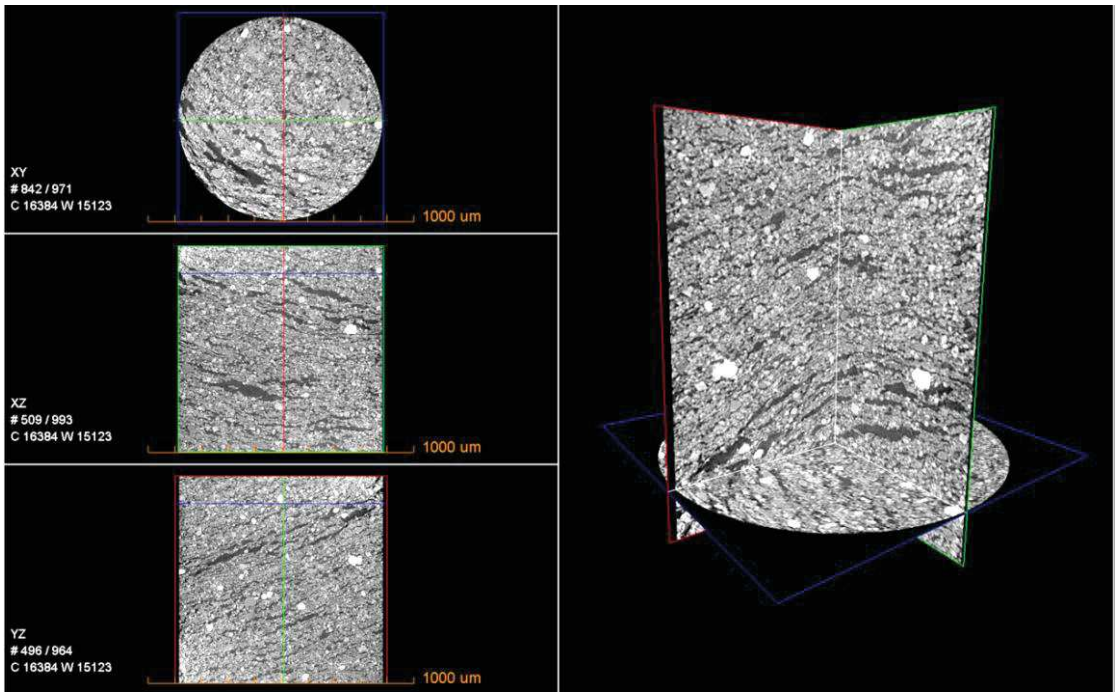

Figure 3.33 Example of oil shale laboratory-based X-ray micro-CT data visualization showing XY, XZ and YZ slices and a tri-planar image revealing 3-D microstructure of the scanned sample.

The selection of the X-ray energy is predominantly affected by the sample attenuation, including material and thickness. The X-ray energy can significantly impact the image quality, in particular the contrast of the images. Contrast is defined as the ratio of the difference in signal between feature (sample) and background to the signal from the background (Stock, 1999). It can also be expressed in a similar using the intensity of X-ray beam, shown in Equation (3.11). The higher the contrast, the better the distinction between two phases in an image:

$$Contrast = \frac{|sig_f - sig_b|}{sig_b} = \frac{|I_f - I_b|}{I_b} \tag{3.11}$$

where *sig* and *I* are the signal observed and intensity respectively and *f* and *b* refers to feature (sample) and background. Higher energy permits better penetration through materials with higher density while lower energy results in better contrast and image quality. Therefore, to achieve the optimal energy of X-rays, contrast and the intensity need to be suitably balanced.

3.7.1 X-ray Beam Sources

Micro-CT sources can be divided into two categories: (1) Micro focus X-ray cone beam tube sources used for laboratory micro-CT instrument and (2) parallel beam synchrotron radiation sources (Figure 3.34). Micro focus X-ray tubes generate X-rays by having high speed electrons directed at a target material with a high atomic number such as tungsten (Lifshin, 2008). In such a system, a projected cone beam is typically used as the point source. In the cone beam system, the spot size of the X-ray source plays a significant role. A smaller spot size results in a more accurate image while a larger spot size means that photons hitting a particular pixel can be traced back through different ray paths through the specimen, thus adding more noise and reducing image quality (Landis and Keane, 2010).

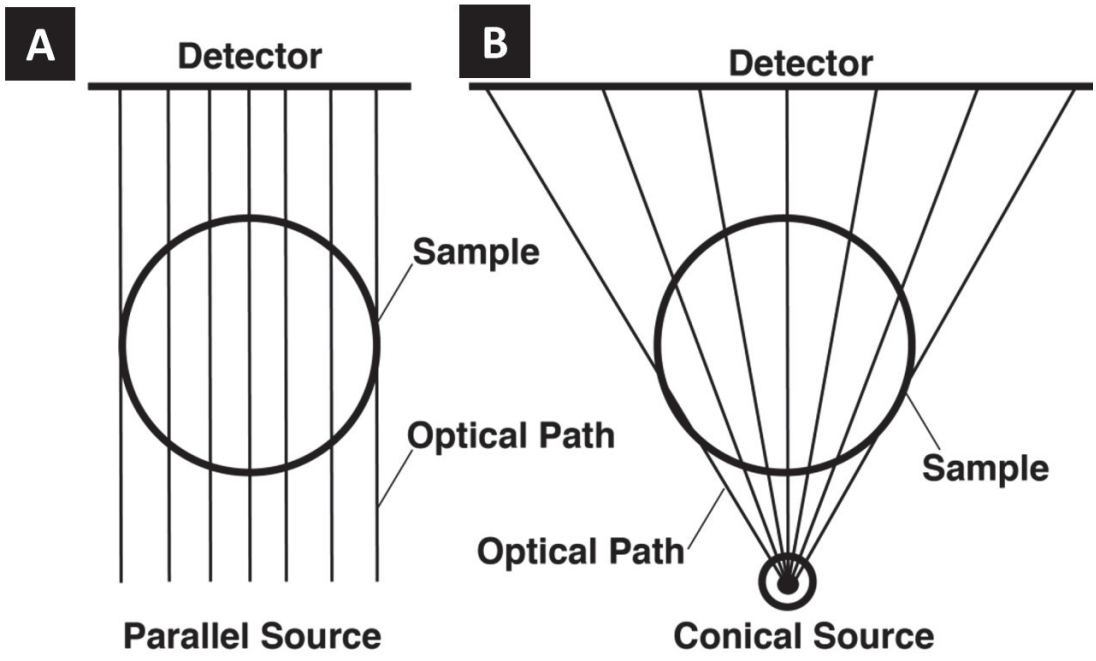

Figure 3.34 X-ray optical geometries. Illustration of a (A) parallel X-ray beam, (B) conical X-ray beam (Menke, 2015). Conical beams are typical used in bench-top X-ray μCT systems and parallel beams are typical of synchrotron X-ray μCT systems.

Synchrotron radiation as an X-ray source has provided significant development in imaging geological materials (Cnudde et al., 2006; Mees et al., 2003). Instead of a point source, synchrotron radiation consists of a parallel beam of infinite cross-section and involves the use of magnets to bend a beam of rapidly moving electrons (Lifshin, 2008; Winick, 1995). The photon flux from a synchrotron source is several orders of magnitude higher than for conventional X-ray sources. High flux density simultaneously reduces exposure times and improves the signal to noise ratio (SNR). Therefore, a key advantage of using a synchrotron source is the reduced scanning times where high quality images can be acquired at a time resolution on the order of 10 seconds, compared to traditional laboratory setups which can acquire images within a time frame of minutes to hours. Additional benefits of using synchrotron radiation include a simplified tomographic reconstruction algorithm due to the use of parallel beam, and the tunability of the X-ray energy to a narrow energy band (Bultreys et al., 2016; Landis and Keane, 2010). Using a parallel beam system, the reconstruction of each slice is independent from the other and can be conducted by a 2-D filtered back projection algorithm. On the other hand, for a cone beam system,

information on different slices are mixed, and therefore a truly 3-D reconstruction algorithm is required such as that provided by Feldkamp et al. (1984).

Although there are clear advantages of using synchrotron radiation, the numbers of synchrotron facilities are limited as the operational costs can be very high. In recent years, major steps in hardware components such as X-ray tube technology and the development of highly efficient and large flat panel detectors have allowed the development of very versatile and high resolution laboratory micro-CT systems that produce X-ray beams with an emission spot diameter down to well below one μm which is essential for micro-CT examination with voxels in the sub-micron range. Recent developments in X-ray optics have made laboratory-based micro-CT systems comparable to synchrotron-based micro-CT in terms of spatial resolution but at are still at the disadvantage of a significantly reduced X-ray flux and therefore increased image acquisition time. In this study, both lab-based micro-CT system and synchrotron radiation are used to investigate the microstructure and evolution of pore space during oil shale pyrolysis for Green River (Mahogany Zone) oil shale samples.

3.7.1.1 Laboratory-based μ-CT

In this study, the Zeiss Versa XRM-500 μ-CT was used to image oil shale before, during and after pyrolysis (Figure 3.35). The system consists of an X-ray source, scintillator, objective lens and a camera centred around a rotation stage that is encompassed by a lead X-ray enclosure and controlled by Zeiss proprietary imaging software (Figure 3.36). X-rays are produced by the source and directed through the oil shale sample mounted on the rotation stage. Parts of the X-rays are absorbed by the oil shale sample while others pass through the sample and hit the iodine scintillator which fluoresces in the visible light spectrum. This visible light is then focused by an objective onto the charge-coupled device (CCD), which translates that light into a pixel-based digital image where the pixel intensity value is a function of the number of X-rays that absorbed by the scintillator (CT number).

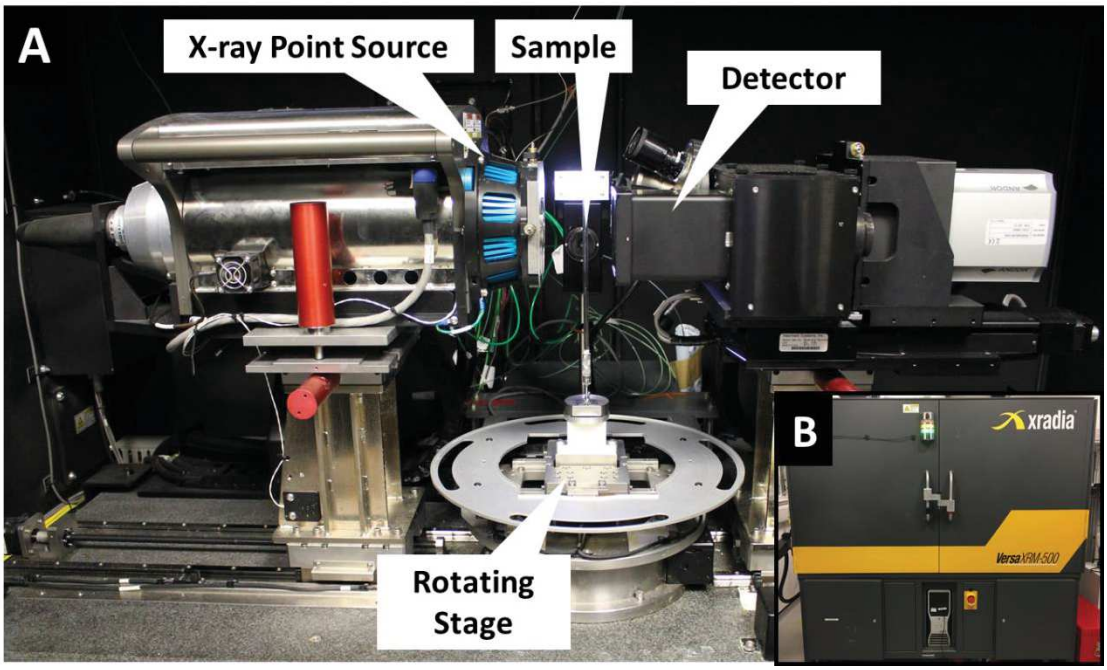

Figure 3.35 X-ray micro-tomography (μCT) apparatus used to capture 3-D scans of Green River (Mahogany Zone) oil shale samples. (A) The laboratory-based μCT consists of three main components: an X-ray micro-focus source, a rotation stage to mount and control the sample and an X-ray detector. (B) Zeiss Versa XRM-500 μ-CT system used in this research study.

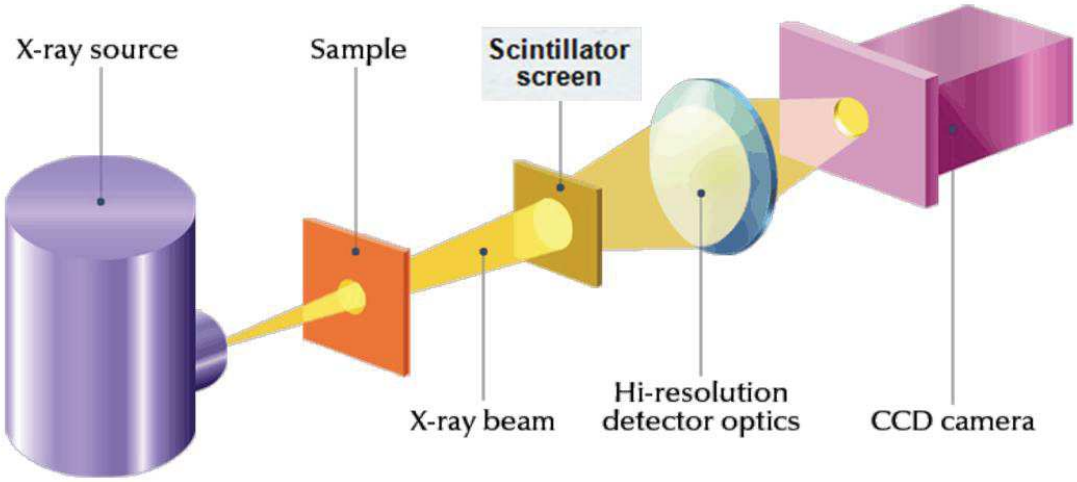

Figure 3.36 Zeiss Versa XRM-500 μ-CT schematic. An X-ray source fires X-rays through the sample which fluoresce when they hit the scintillator. The visible light is focused by the objective lens and digitised by the CCD array.

A series of images (projections) of the oil shale sample are taken at incrementally spaced angles from 0° to 360° as the sample is rotated. This set of [x,y] projections is then converted to sinograms [x, θ], where theta is the rotation angle, and is back projected into the 3-D intensity map using a group of transformation algorithms including the Radon Transform (Radon, 2005) and others which are discussed in further detail in the ASTM Standard Guide for Computed Tomography (CT) Imaging (ASTM, 1992).

An advantage of using a cone beam is that it is possible to magnify the image both optically and geometrically (Figure 3.37). Geometric magnification makes high-resolution scans possible at long sample distances. Optimal sample placement depends on desired magnification and acquisition time.

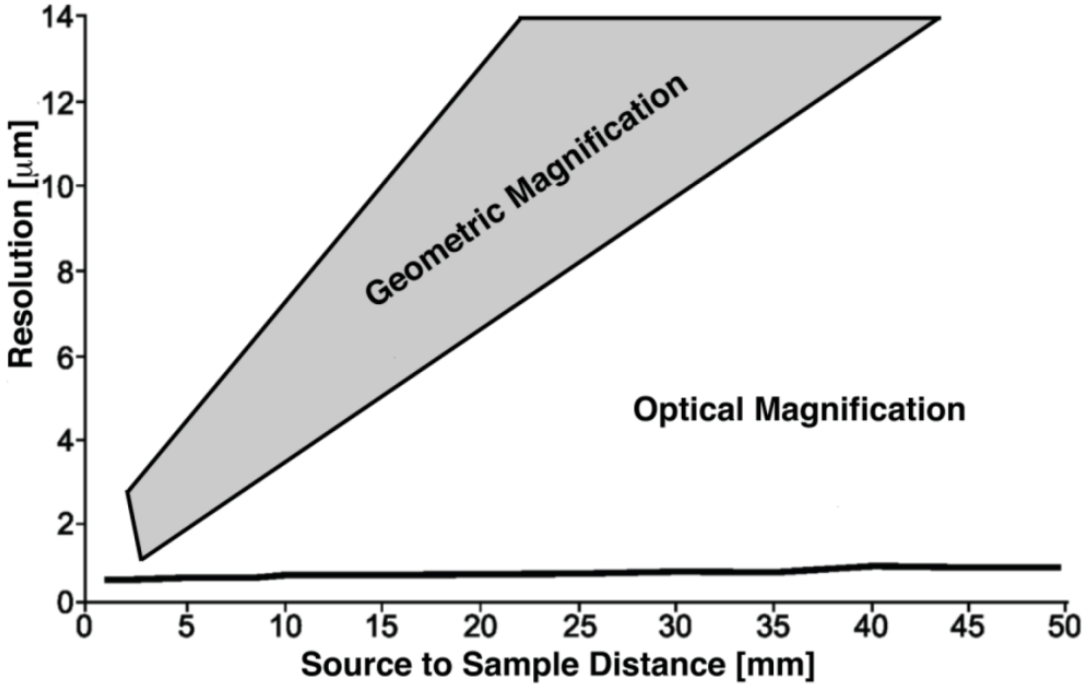

Figure 3.37 The geometric and optical magnification capabilities available in a laboratory-based micro-CT. Geometric magnification allows for high resolution scans at shorter source distances than traditional optical magnification (Menke, 2015).

Image resolution is mainly defined by optical and geometric magnification:

$$Total\ magnification = Optical\ magnification \times Geometric\ magnification \quad (3.12)$$

$$Geometric\ magnification = \frac{Source\ to\ Detector\ Distance}{Source\ to\ Sample\ Distance} = \frac{a+b}{a} \quad (3.13)$$

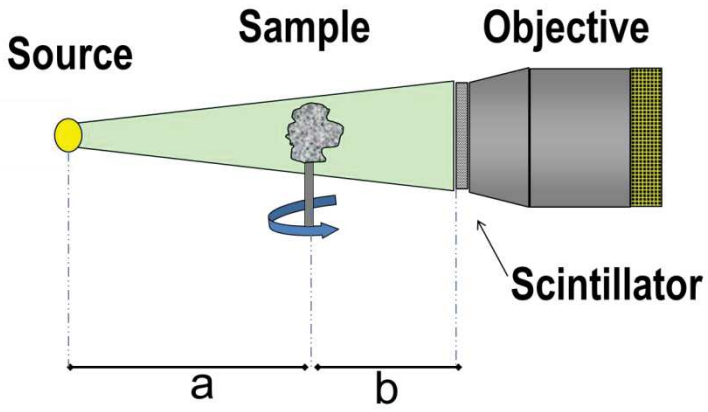

Figure 3.38 Illustration of the Zeiss Versa XRM-500 µ-CT source-sample-detector setup with *a* representing the source to sample distance and *b* representing sample to detector distance.

3.7.1.2 Synchrotron-based X-ray Micro-tomography

A synchrotron is circular particle accelerator that employs a guiding magnetic field to accelerate, direct, focus, and synchronize charged particles into a particle beam of increasing kinetic energy (Chao et al., 2013). In this study, oil shale samples were analysed using the Diamond Light Source (DLS) synchrotron facility in Harwell (UK). Synchrotrons consist of an electron gun that fire electrons through a linear accelerator (or linac) and into a booster ring where electrons receive a boost in energy from approximately 250 MeV to approximately 2.9 to 6 GeV and are then transferred into the storage ring The storage ring typically has many separate branching beam lines that extract small quantities of energy and apply them for various experimental needs including imaging (Figure 3.39).

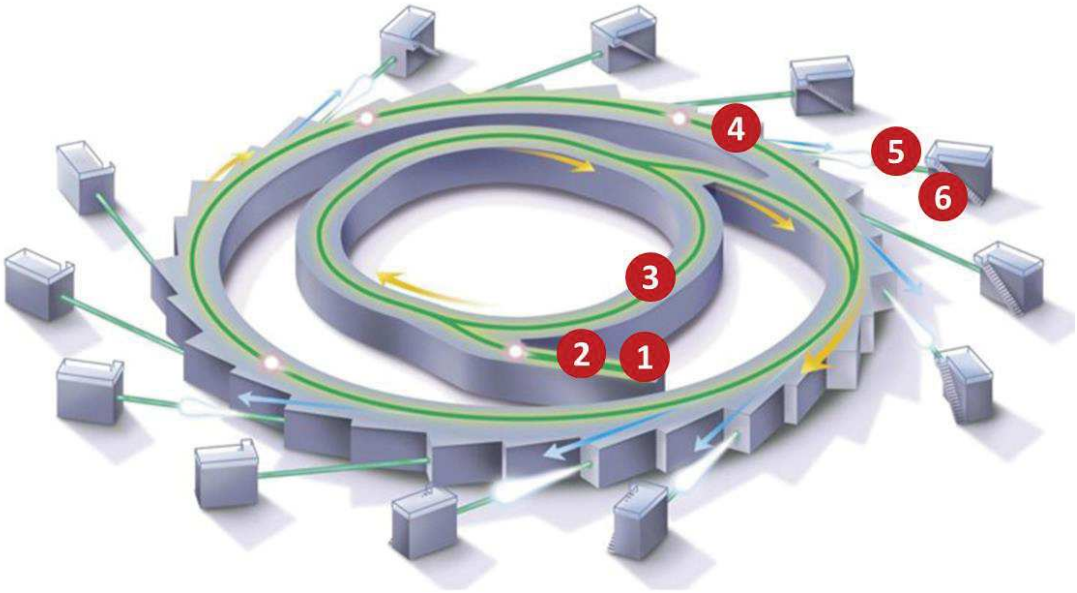

Figure 3.39 A schematic of a typical synchrotron consisting of: (1) Electron gun, (2) Linear accelerator (Linac), (3) Booster ring, (4) Storage ring, (5) Beamline, and (6) End station.

A Synchrotron consists of the electron gun, linear accelerator (LINAC), booster ring, storage ring (or rings), bending magnets (not shown in diagram), beam lines and the end station It is possible to use an undulator that consists of a periodic structure of dipole magnets (Figure 3.40). The electron beam is forced to undergo oscillations as it traverses the magnets and thus radiates energy (Luchini and Motz, 1990). The energy generated is concentrated to narrow energy bands and is very intense.

Mirrors and various filters are then used to narrow the energy spectrum depending on experimental requirements (Figure 3.41). Mirrors absorb the high-energy spectrum while filters absorb the lower energies. Therefore, it is possible to narrow the spectrum to the desired band of radiation using these devices. Once the beam has passed through the oil shale sample the unabsorbed light is picked up by the detector assembly. The detector of a synchrotron is similar to a laboratory source detector setup except that the scintillator must be able to cope with higher energy fluxes and the camera needs be able to take and transmit images at high rates.

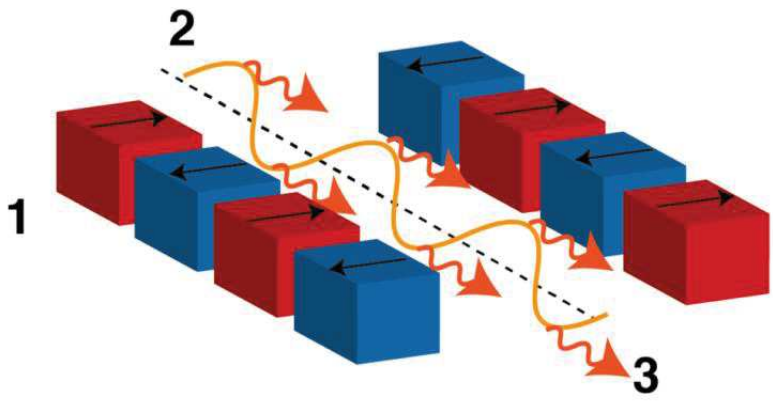

Figure 3.40 A synchrotron undulator. (1) The periodic structure of magnets, (2) Bending the electron beam, and (3) Generation of intense light (Menke, 2015).

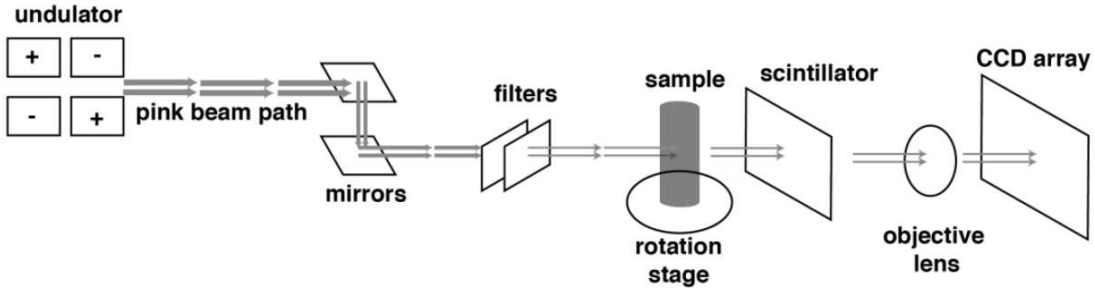

Figure 3.41 The Diamond Lightsource pink beam apparatus. The beam passing through the undulator generates intense light. The spectrum is narrowed by mirrors and filters and is then transmitted through the sample. The scintillator fluoresces in the visible spectrum and the light is focused and measured by the objective lens and CCD camera array (Menke, 2015).

3.7.2 Artefacts

Although the reconstructed 3-D image allow for the visualization of the internal structure of oil shale samples, there are several artefacts and that can render the data more problematic and make any quantification more challenging. The most common artefacts are beam hardening and ring artefacts.

3.7.2.1 Beam Hardening

Beam hardening is one of the most common artefacts encountered in micro-CT scanning. Beam hardening from a polychromatic beam (a range of energy spectrum) occurs because various components of the energy spectrum are not attenuated uniformly when passing through a sample. The lower energy component of the X-ray spectrum is more easily attenuated or even completely adsorbed when traveling

through a dense part. Based on the photoelectric effect, the X-ray absorption is approximately inversely proportion to the third power of the photon energy, which means that lower-energy X-rays are attenuated more readily and absorbed much more easily than higher-energy X-rays (Ketcham and Carlson, 2001; Stauber and Müller, 2008). In a micro-CT image, this process can be seen as an artificial darkening at the centre and a brightening near edges (Figure 3.42).

Various methods can reduce or correct beam hardening effects including: (1) Pre-harden the beam - using a filter, typically a thin metal plate (copper, aluminium) between the X-ray source and the object to reduce the amount of "soft" X-rays, (2) beam hardening can also be corrected/reduced during reconstruction using various algorithms.

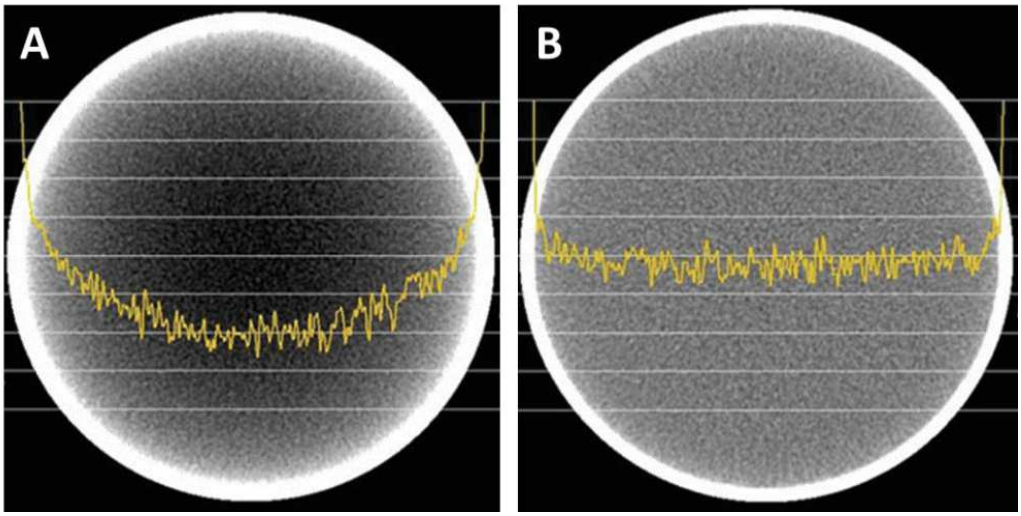

Figure 3.42 (A) Uncorrected initial image of a water phantom showing beam hardening (B) corrected image using reconstruction software (Kyriakou et al., 2009).

3.7.2.2 Ring Artefacts

Micro-CT images can be corrupted by ring artefacts, prohibiting quantitative analysis and hindering post processing such as noise reduction or image segmentation. Ring artefacts can be observed as full or partial circles in the 3-D image around the centre of the rotational axis. The ring artefacts can be caused by a defective pixel on the CCD detector, a defect in the scintillator which converts X-rays to visible light, or dust on the detector (Stauber and Muller, 2008). There are several methods to avoid ring artefacts. If the rings are caused by dust on the detector, it can be easily solved

by cleaning the detector. For defective pixels, most ring artefacts can be detected and removed by using software tools (Figure 3.43) (Axelsson et al., 2006; Kyriakou et al., 2009; Vlassenbroeck et al., 2007).

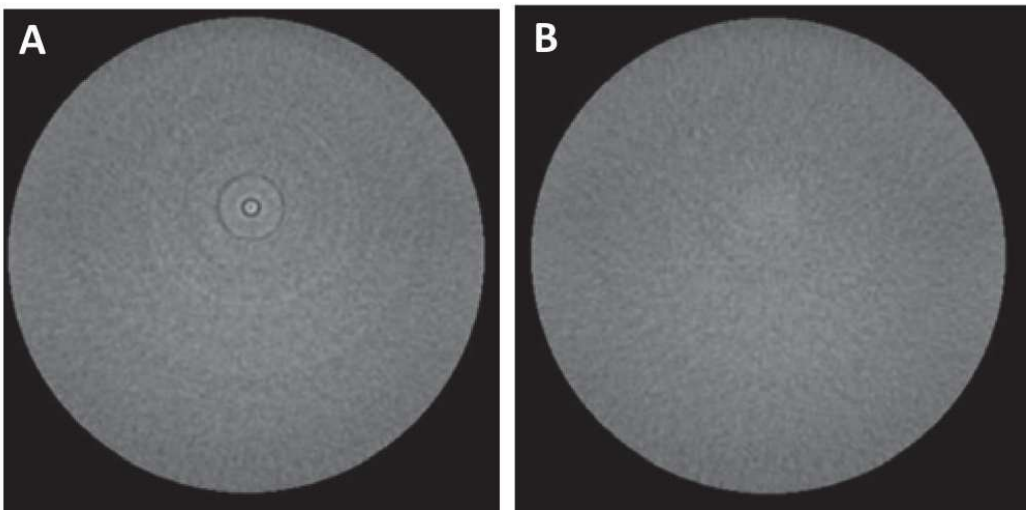

Figure 3.43 (A) Uncorrected initial image of a water phantom showing ring artefacts sand (B) corrected image based on median filtering of the reconstructed image and working on a transformed version of the reconstructed images in polar coordinates. This post-processing method reduced ring artefacts in the reconstructed images and improved image quality (Kyriakou et al., 2009).

3.7.3 Image Processing

3.7.3.1 Image Filtering

The raw images obtained using micro-CT can have noise as a result of several factors including low energy, flux and insufficient projections. An image can be filtered to reduce the noise or enhance the contrast. Numerous filters can be applied, with the simplest filter being the mean filter, which substitutes each voxel's greyscale value with the mean value of its neighbours (Ataman et al., 1981). The Gaussian filter operates in a similar way using the Gaussian weighted mean. Although these filters work well in reducing noise, they do tend to blur phase boundaries and therefore are not best suited to images that need to be segmented into multiple phases.

The median filter is the simplest edge preserving filter and works by replacing the greyscale voxel value with the median value of the local group. The greyscale value is associated with the initial voxel position, and therefore edges are preserved with conservative local groups. However, the edges can worsen when the local group is

increased. A more recent algorithm known as non-localized means (NLM) has been developed to tackle the limitations of local filters (Buades et al., 2008, 2005). NLM uses the mean of all voxels in the search window (which could be as large as the entire image) and then weights them using a Gaussian function by how similar they are to the target pixel. Using this method the edges are preserved. However, NLM filtering can be time consuming and is often only used in two-dimensions and with a relatively small search window. An example of NLM filtering applied to a pyrolysed oil shale sample is shown in Figure 3.44. A search window of 21 pixels, local neighbourhood of 5 pixels and similarity value of 0.6 was used. In this study, a two phase segmentation was applied and the impact of filtering was considered to be relatively less significant comapred to multiphase segmentation.

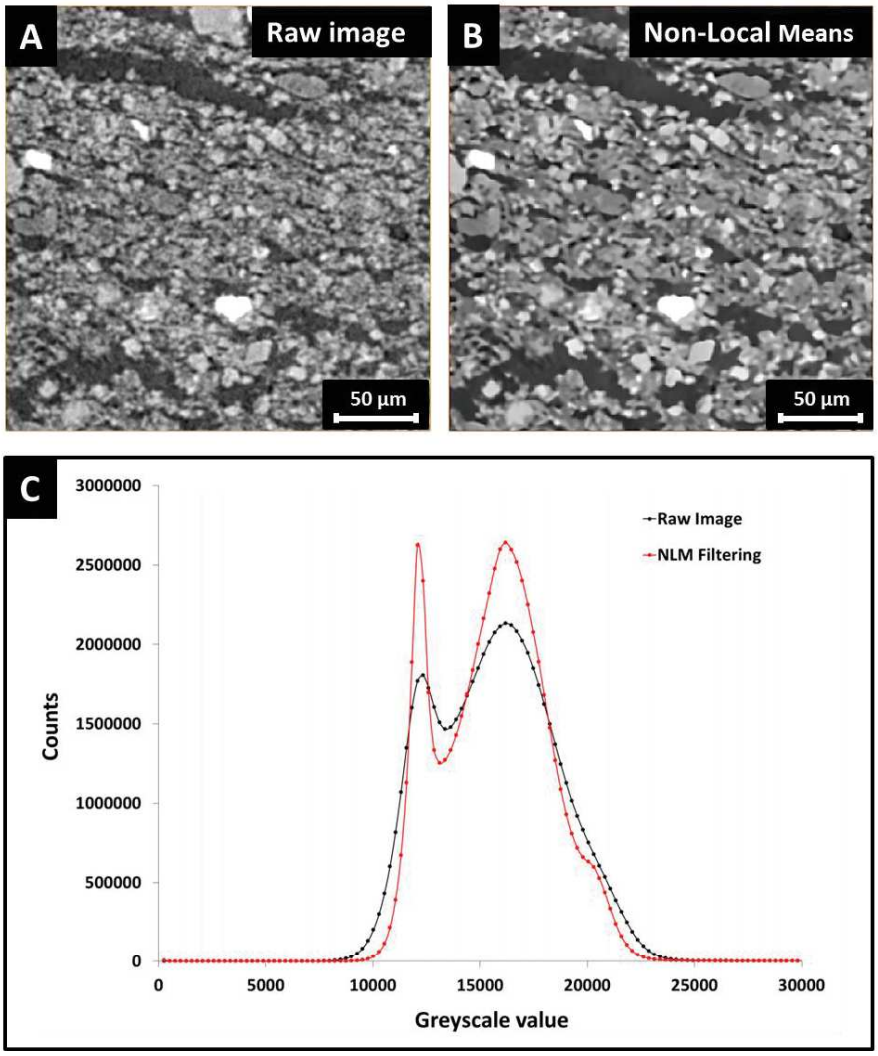

Figure 3.44 (A) Oil shale raw image, (B) Non-local means filtered image and (C) Histogram of the tomography data indicating the number of voxels (counts) with a particular grey value. A clear

separation is observed in the histogram peaks corresponding to the pore space (left peak) and the solid phase (right peak).

3.7.3.2 Image Segmentation

Before quantifying the petrophysical properties of an oil shale rock image, the phases within the image must be appropriately identified. Image segmentation is the process of dividing a digital image into multiple parts or segments and is an important step in the X-ray µCT imaging and analysis workflow (Figure 3.45). Many segmentation algorithms exist to assist in the automated segmentation process, with the most common being global thresholding and watershed segmentation.

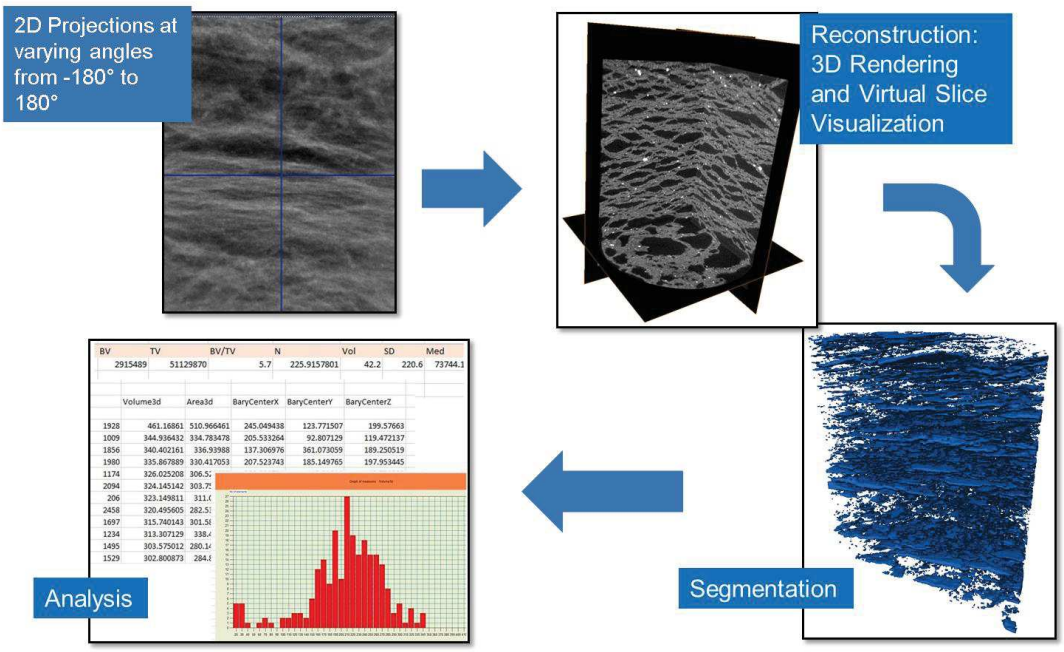

Figure 3.45 Overview of X-ray micro-CT imaging and analysis workflow for an oil shale sample: 2-D projections are acquired, followed by reconstruction to generate a 3-D volume, then segmentation is completed to separate key phases and finally analysis of the segmented volume is done to compute petrophysical properties.

Global thresholding is considered the simplest method of segmentation where greyscale values within a range are segmented as a particular phase. This method is rather effective with an image that has a high signal-to-noise ratio and comprises only two phases. On the other hand, for a noisy image, voxel misidentification can occur, particularly at the phase boundary where the voxel greyscale values are similar.

To identify phase boundaries, the watershed method of segmentation is better than global thresholding (Sheppard et al., 2004). The term watershed is applied because the gradient image computed on the image is analogous to the height map of a catchment basin (Figure 3.46). Firstly, the gradients between neighbouring voxels are computed and a new gradient image is generated. Areas of a relatively high gradient that correspond to the phase boundaries are removed from regional seeding. The user then seeds the areas of low gradient by eye and ascertains the range of greyscale values for each phase. The watershed algorithm then grows the user-defined seed basins successively up the intensity map into the high gradient regions. In this way voxel misidentification due to noise is minimized and the phase boundaries are created.

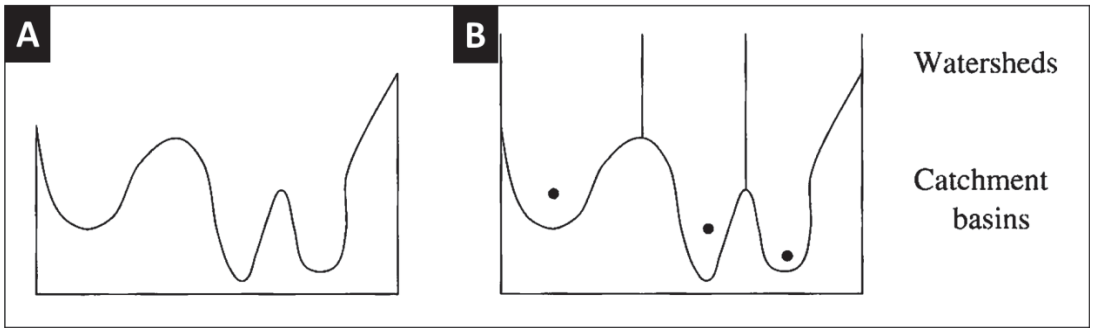

Figure 3.46 One-dimensional example of watershed segmentation. (A) Grey-level profile of image data. (B) Watershed segmentation - local minima of grey-level (altitude) yield catchment basins with local maxima defining the watershed lines (Sonka et al., 2014).

3.8 Pyrolysis of Oil Shale Samples

In this study, the Green River (Mahogany Zone) oil shale samples were pyrolysed both *ex situ* and *in situ*. For *ex situ* experiments, the samples were heated outside of the imaging instrument using a Carbolite ELF 11/14B furnace. For *in situ* experiments using a synchrotron light source, a custom-built cylindrical furnace was used (Figure 3.47). This bespoke furnace consisted of X-ray windows on either side to allow the passage of the X-ray beam and an access hole at the bottom to allow the insertion of the sample, which was affixed to the rotation stage of the beamline.

For both *ex situ* and *in situ* experiments in this study, pyrolysis was conducted under vacuum conditions (0.1 kPa absolute) as it has been shown to improve both oil yield and quality compared to pyrolysis under atmospheric pressure. Vacuum pressures

accelerate the transport of pyrolysis products by providing faster escape of primary oil from the reaction zone, therefore reducing the occurrence of secondary cracking reactions (Hoekstra et al., 2012; Pakdel et al., 1999; Roy et al., 1985; Siramard et al., 2016). In addition, Li et al. (1993) reported the increase of tar yield and the less aromatic species in the generated tar under vacuum conditions. This indicates the improvement on the oil production by having higher yield and better quality through pyrolysis under reduced pressures.

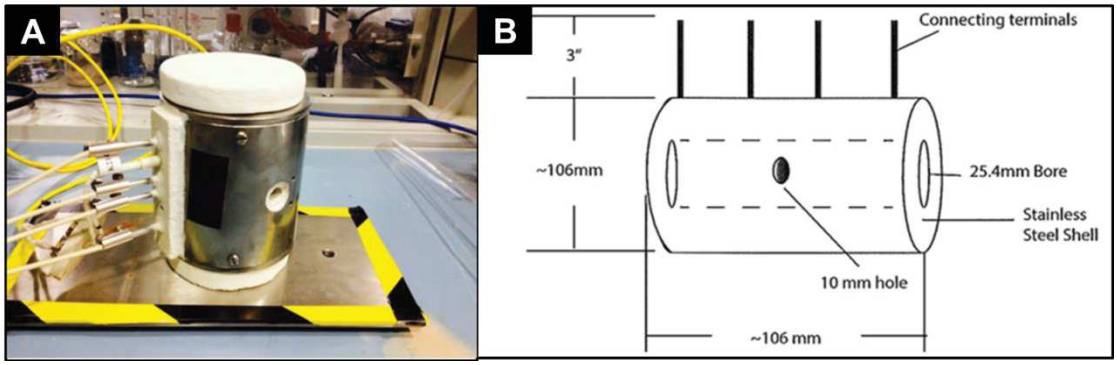

Figure 3.47 (A) Custom-built furnace designed for use at a synchrotron facility, (B) Schematic of furnace indicating key dimensions including 10 mm holes to allow the X-ray beam to directly pass through the sample during heating.

3.9 Summary

In this chapter, the experimental methods and analytical techniques used as part of the multi-scale multi-dimensional imaging and characterization of oil shale pyrolysis in this research were discussed. Results from geochemical and rock analysis methods (XRD, TOC, Programmed Pyrolysis, TGA, Elemental analysis and MFA) along with 2-D optical microscopy, SEM analysis and laboratory-based X-ray μCT are presented in Chapter 4. Chapter 5 reports studies using sub-micron X-ray μCT, Automated Ultra-high Resolution SEM, MAPS Mineralogy and FIB-SEM. Moreover, in Chapter 6 results from synchrotron-based X-ray μCT are discussed.

Chapter 4

Microstructural Imaging and Characterization of Oil Shale Pyrolysis using 2-D Optical Microscopy, SEM and 3-D Lab-based X-ray Micro-tomography

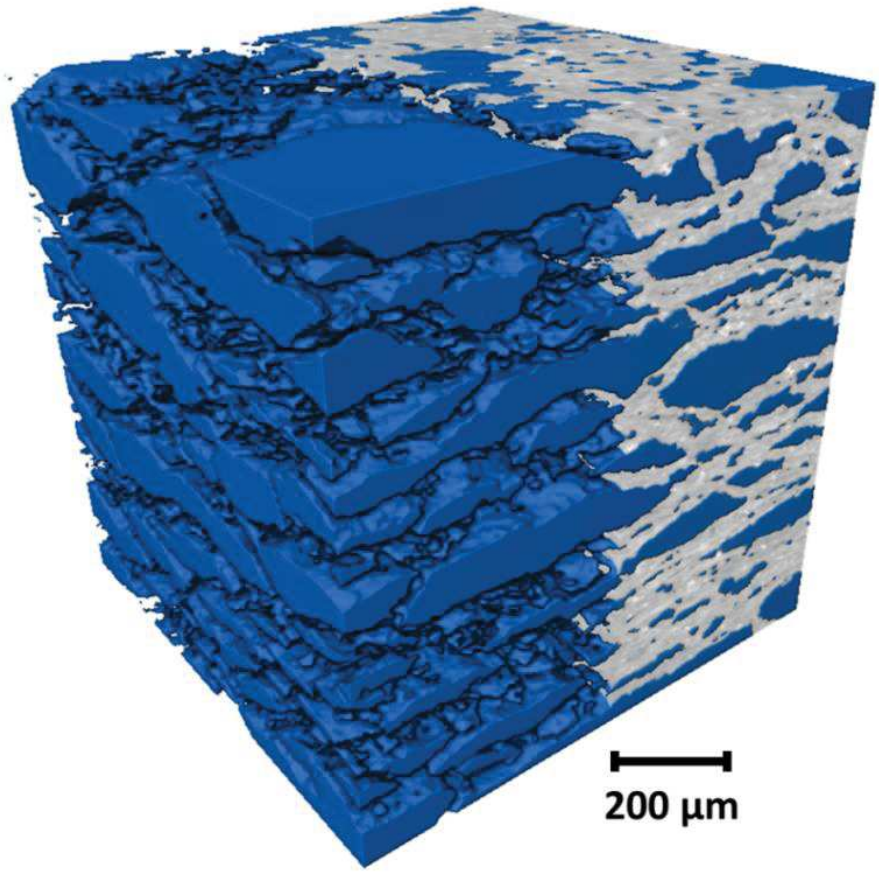

3-D representation of the pore space following pyrolysis of oil shale

Publication:

Saif, T., Lin, Q., Bijeljic, B. and Blunt, M.J., (2017). Microstructural Imaging and Characterization of Oil shale before and after Pyrolysis. *Fuel*, 197, 562-574.

4.1 Introduction

Given that microstructural evaluation of oil shale is challenging, this chapter provides an improved insight into the pore network structure and connectivity before, during and after oil shale pyrolysis, which is crucial to understanding hydrocarbon flow behaviour and enhancing recovery. In this chapter, bulk analyses are combined with traditional and advanced imaging methods to comprehensively characterise the internal microstructure and chemical composition of the world's richest oil shale deposit, the Green River Formation (Mahogany Zone). Image analysis in two dimensions (2-D) using optical (Section 4.3) and scanning electron microscopy (SEM) (Section 4.4), and in three dimensions (3-D) using X-ray micro-tomography (μCT) (Section 4.5) reveals a complex and variable fine grained microstructure dominated by organic-rich parallel laminations of the order of 10 μm thick which are tightly bound in a highly calcareous and heterogeneous mineral matrix. The results of a detailed X-ray μCT study of the Mahogany oil shale with increasing pyrolysis temperature (300-500°C) at 12 μm and 2 μm voxel sizes are also reported. The 3-D volumes of pyrolysed oil shale were reconstructed and image processed (Section 4.5.3) to visualize and quantify the volume and connectivity of the pore space. The results in Section 4.5.4 and 4.5.5 show a significant increase in directional anisotropic porosity associated with pyrolysis between 400-500°C with the formation of micro-scale connected pore channels developing principally along the kerogen-rich lamellar structures. Given the complexity and heterogeneity of oil shale, the representative size at which porosity remains constant is also studied. The results in this chapter provide a direct observation of pore and micro-fracture development during oil shale pyrolysis and the petrophysical measurements from this work serve as valuable input parameters to modeling oil shale pyrolysis processes.

4.2 Oil Shale Composition Analysis

4.2.1 X-ray Diffraction (XRD)

X-ray diffraction (XRD) is a laboratory-based analytical technique for identifying minerals and other crystalline phases in a wide range of materials, including oil shale samples (Al-Otoom et al., 2005; Bhargava et al., 2005; Tong et al., 2011). Details on the fundamental principles of XRD are provided in Section 3.3.1. In this work, the

oil shale rock sample was first disaggregated gently using a pestle and mortar. A representative 2 g split of this material was then micronized using a McCrone Micronizing Mill to obtain a powder with a mean particle diameter of between 5-10 μm. The fine powder was then backpacked into an aluminium cavity mount producing a randomly orientated sample suitable for XRD. Samples were analysed using a Bruker D8 Advance X-ray diffractometer with scattering angles, 2θ, between 5° and 75° with a step size of 0.05°/sec using CuKα radiation (λ = 1.54 Å) at a tube voltage of 35 kV and a current of 30 mA. Quantitative identification of the minerals in the oil shale sample was achieved using the full pattern analysis technique known as the Rietveld method (Rietveld, 1969) using the Inorganic Crystal Structure Database (ICSD) (Bergerhoff et al., 1983).

XRD analysis of oil shale from the Green River Formation (Mahogany Zone) reveals a complex mineral signature. The dominant mineral phases were dolomite, calcite, quartz, and feldspars with small amounts of illite, analcime and pyrite (Figure 4.1). Although kerogen is the most important component of oil shale, it cannot be detected by direct XRD analysis. However, XRD results provide valuable information in characterizing bulk oil shale mineralogy with previous studies establishing that minerals in oil shale can have both catalytic and inhibitory effects on pyrolysis reactions (Espitalie et al., 1980; Karabakan and Yürüm, 1998).

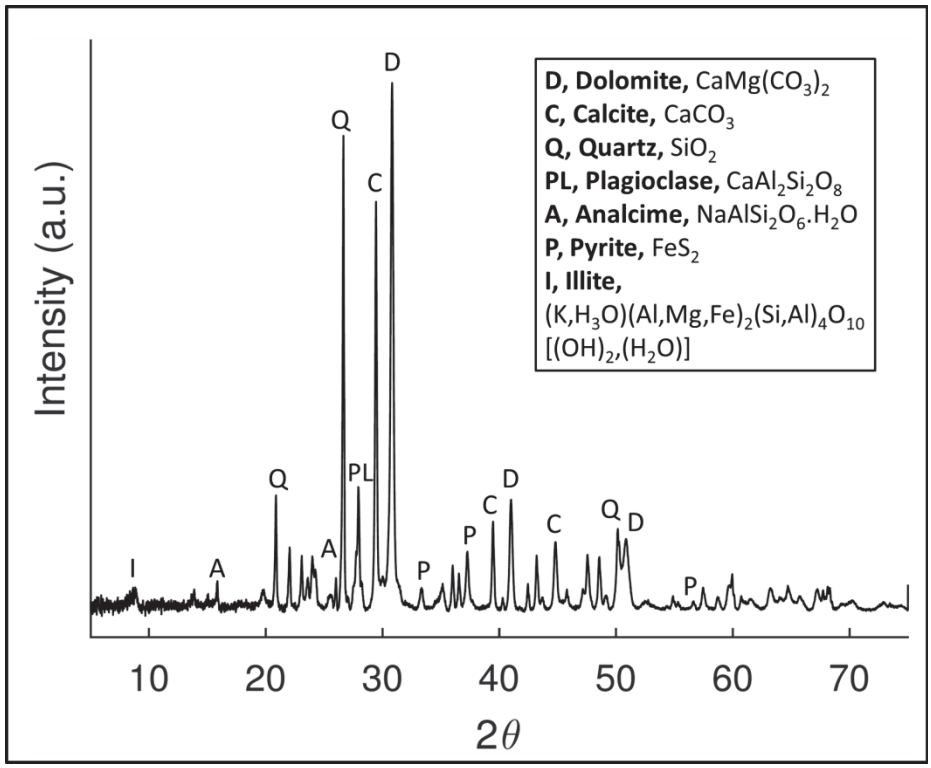

Figure 4.1 XRD pattern (diffractogram) for the Green River oil shale sample (Mahogany Zone) with characteristic mineral peaks identified.

4.2.2 Total Organic Carbon (TOC)

The oil shale sample was ground, homogenized and sieved to 60 mesh (<250 μm). 100 mg of the crushed sample was then treated for two hours with concentrated hydrochloric acid to remove carbonate minerals. The acid was removed from the sample with a filtration apparatus fitted with a glass microfiber filter paper. The filter was placed in a LECO crucible and dried at 110° C for one hour. After drying, the sample was analysed with a LECO 744 Carbon Analyser with detection limits to 0.01 wt%. The result reveals a TOC of 30.15% for the Mahogany zone oil shale indicating an organic rich sedimentary rock (Table 4.1). Details on the fundamental principles of TOC measurements are provided in Section 3.3.2.

4.2.3 Programmed Pyrolysis (Rock-Eval, Source Rock Analyser)

Programmed pyrolysis (Rock-Eval II and SRA) was performed to assess source rock quality and thermal maturity Details on the fundamental principles of programmed pyrolysis are provided in Section 3.3.3. A 100 mg of crushed rock sample was heated in an inert environment to obtain the parameters S1, S2, S3, T_{max}, hydrogen index

(HI), oxygen index (OI) and production index (PI). Sample heating at 300°C for 3 minutes produces the S1 peak by vaporizing the free (unbound) hydrocarbons. The temperature then increases by 25°C/minute to 600°C and the S2 and S3 peaks are measured from the pyrolytic degradation of the kerogen in the sample. The S2 peak is proportional to the amount of hydrogen-rich kerogen in the oil shale rock, and the S3 peak measures the amount of carbon dioxide released (to 390°C) providing an assessment of the oxygen content of the rock. The temperature at which the S2 peak reaches a maximum, T_{max}, is a measure of the source rock maturity. The pyrolysis data indicates a Type I kerogen and the results obtained from the Rock-Eval II instrument showed good agreement with the results obtained from the SRA method (Table 4.1).

Table 4.1 Composition analysis for the Green River oil shale sample (Mahogany Zone) including mineralogy, TOC and elemental analysis.

Mineralogy by XRD		
Dolomite (wt%)	39.0	
Calcite (wt%)	18.0	
Quartz (wt%)	14.2	
Plagioclase (wt%)	13.6	
Illite (wt%)	10.7	
K-Feldspar (wt%)	2.7	
Analcime (wt%)	1.8	
Pyrite (wt%)	1.2	
LECO		
TOC (wt%)	30.15	
	Rock-Eval	**SRA**
S1 (mg HC/g rock)	6.09	16.56
S2 (mg HC/g rock)	210.27	197.25
S3 (mg CO_2/g rock)	1.44	2.07
T_{max} (°C)	437	432
HI[a] (mg HC/g TOC)	697.41	654.23
OI[b] (mg HC/g TOC)	4.78	6.87
PI[c]	0.03	0.08
Elemental Analysis (Kerogen Isolate)		
Carbon (wt%)	65.22	
Hydrogen (wt%)	8.79	
Nitrogen (wt%)	2.33	
Oxygen (wt%)	19.86	
Iron (wt%)	0.12	
Sulphur $_{total}$ (wt%)	0.87	
Sulphur $_{pyrite}$ (wt%)	0.73	
Sulphur $_{organic}$ (wt%)	0.14	
H/C (molar)	1.62	
O/C (molar)	0.23	

[a] HI, Hydrogen Index = (S2 x 100) / TOC
[b] OI, Oxygen Index = (S3 x 100) / TOC
[c] PI, Production Index = S1/(S1+S2)

4.2.4 Elemental Analysis (CHNOS)

Kerogen was isolated from the raw oil shale using a standard hydrochloric and hydrofluoric acid treatment which is effective in removing carbonate and silicate minerals. The remaining material contained primarily kerogen as well as pyrite (FeS_2) which is particularly resistant to these methods. Carbon, hydrogen and nitrogen were determined using a Flash EA 1112 Series Analyser according to ASTM D5291. Oxygen was determined using a Leco RO-478 Oxygen Analyser with the method described in ASTM D5622. Further details on the elemental analysis procedure are provided in Section 3.3.5. Sulphur and iron contents were determined

by analysis on a Perkin Elmer DV 5300 ICP-AES following a modified EPA 200.7 method for ICP-AES analysis. Iron in isolated kerogen is considered to exist entirely as pyrite and the pyrite sulphur content can be determined given the stoichiometric relationship between the sulphur and iron contents of pyrite (S_{pyrite}/Fe_{pyrite}= 1.148). The organic sulphur content is then calculated by subtracting the pyrite sulphur from the total sulphur (Table 4.1).

4.2.5 Modified Fisher Assay (MFA)

A Modified Fischer Assay (MFA) method was used to measure the potential oil yield from the Mahogany oil shale sample outlined in ASTMD3904. A 100 g of 8 mesh (< 2.38 mm) oil shale was heated in an aluminium retort to 500 °C at 12 °C/min and held at this temperature for 40 min. The evolved hydrocarbons were passed through a condenser system and analysed. Further details on the MFA methodology are provided in Section 3.3.6. The quantity of oil was measured directly and the gas fraction was analysed by gas chromatography. The MFA results are summarised in Figure 4.2.

Modified Fischer Assay (MFA)	
Mineral Decomposition Products (wt%)	
$CO + CO_2$ Gas	1.0
Inert Mineral	67.1
Organic (Kerogen) Products (wt%)	
C3- Gas incl. H_2 +H_2S	2.0
Total C4+	22.0
Coke	7.9
MFA Parameters	
Oil density (g/ml)	0.87
Oil Yield (L/t)	241.6
Total organic products (wt%)	31.9

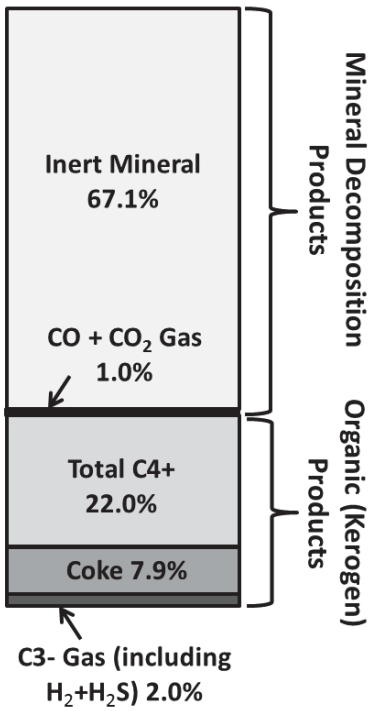

Figure 4.2 Modified Fisher Assay (MFA) results for the Green River oil shale sample (Mahogany Zone) including mineral decomposition and organic products, oil density and oil yield. The clean oil density represents the density of the oil recovered as liquid in the receiver following the test. The oil yield represents the amount of potentially extractable shale oil present in the sample as determined the MFA method.

4.3 Visualization using Optical Microscopy

Petrographic analyses provide a starting point to digitally characterise the mineral composition, texture and the fine-grained structure of shale rocks. In this study, geological thin sections from Green River Formation were prepared perpendicular to the laminations. The oil shale samples were air dried followed by epoxy vacuum impregnation. The samples were then hand lapped and polished using progressively finer alumina suspension (1 μm, 0.3 μm and 0.05 μm) alongside a high-purity hydrocarbon lubricant. Thin sections of 20 μm thickness were optically examined using a Zeiss SteREO Discovery.V12 microscope with accompanying AxioVision LE64 software (Carl Zeiss, Germany) using plane-polarized light (PPL). A mosaic photomicrograph was created by the automated stitching of 1152 individual images at 100× magnification (Figure 4.3). Further details on optical microscopy are provided section 3.4.

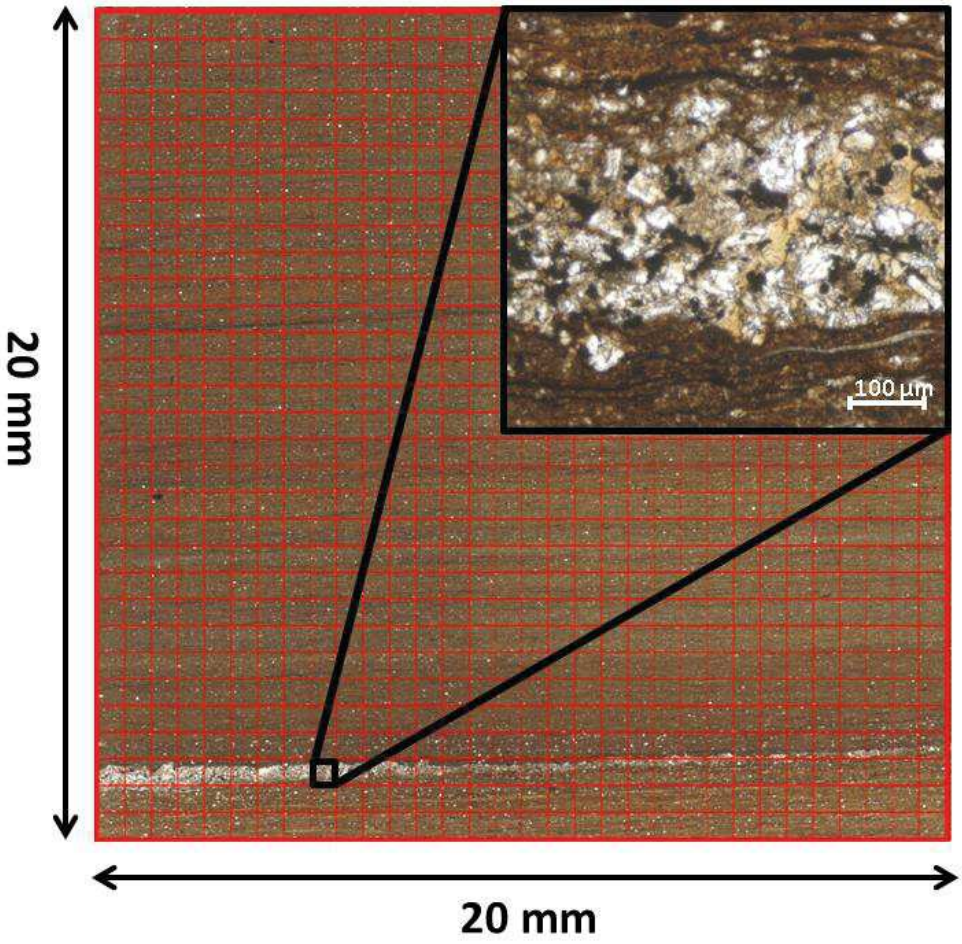

Figure 4.3 Thin section mosaic images of the Green River oil shale sample (Mahogany Zone) generated by digitally stitching 1152 individual images into one all-encompassing view.

Green River Mahogany Zone oil shale thin sections examined by optical microscopy reveal a fabric that is well defined by micro-laminations (Figure 4.4). The laminations are due to an alternation of layers rich and lean in organic matter. The organic rich layers appear as dark brown under transmitted light whilst the organic lean regions appear lighter and are dominated by inorganic minerals. The organic-rich laminae, primarily in the form of kerogen, are of the order of 10 μm thick, alternating with thicker layers of predominantly carbonate minerals in the form of dolomite and calcite. The fine kerogen laminae are both continuous and discontinuous laterally with the occasional presence of wavy laminations. This bipartite rhythmic structure, referred to as varves, is related to the seasonal changes in organic productivity and is one of the characteristic features of lacustrine sediments (Boyer, 1982; Bradley, 1931; Crowley et al., 1986; Surdam and Stanley, 1979). With optical microscopy, a useful initial visualization of the microstructure can be acquired to examine and explore minerals and microscopic features in 2-D. However, with traditional optical petrography, the resolution is limited to approximately 0.23 μm (diffraction barrier of visible light) which prevents the fine grain characteristics and nano-scale pores of oil shales from being characterised.

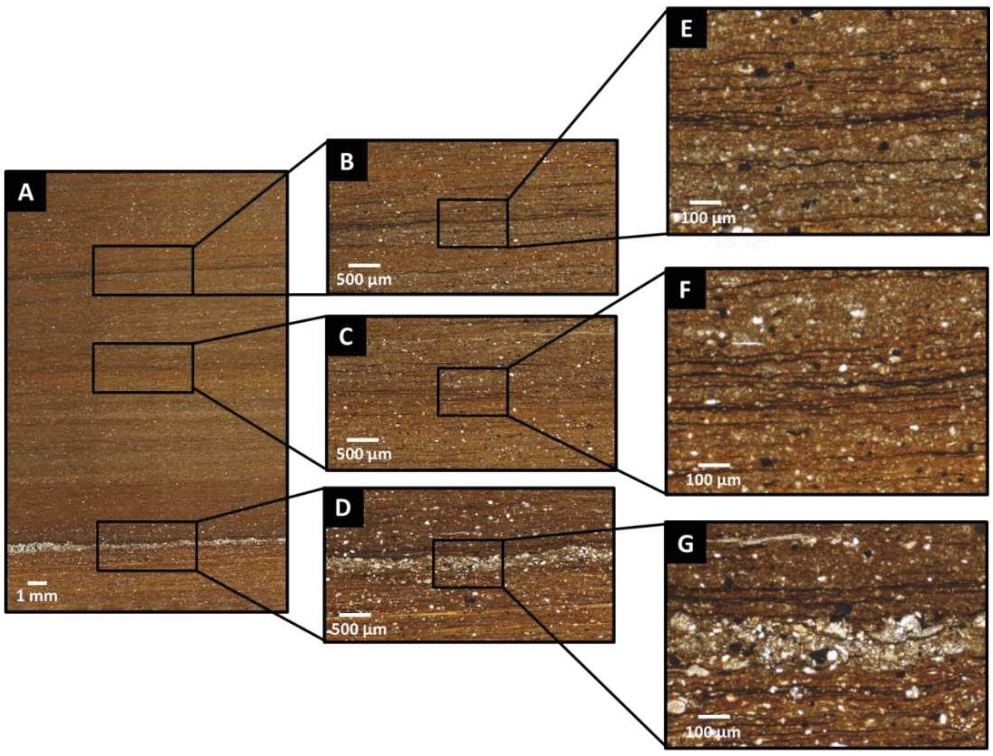

Figure 4.4 Thin section images of oil shale from the organic –rich Green River Formation (Mahogany Zone) at low (A), medium (B-D) and high (E-G) magnification. The images taken in plane polarized light (PPL) show a series of laminated structures of organic material in a distribution of fine grained inorganic minerals.

4.4 Visualization using Scanning Electron Microscopy (SEM)

Scanning electron microscopy (SEM) was performed on the Mahogany oil shale samples to obtain 2-D high-resolution images down to several nanometres and to achieve better contrast between the pore and solid phases. SEM coupled with Energy-dispersive X-ray spectroscopy (EDS) was also used to acquire a localized chemical analysis. SEM-EDS data was collected using a Zeiss EVO MA 10 with a Bruker XFlash Silicon Drift Detector. Images were captured under a backscattered electron detection mode (BSE) with an accelerating voltage of 20 kV and working distances of 10-11 mm. Further details on the principles of SEM are provided in Section 3.5. The oil shale samples were imaged at a range of magnifications to characterise the morphology of the oil shale rock fabric and the distribution of minerals and organic material. BSE imaging allows for compositional contrast to be recorded as BSE intensity which is a function of the mean atomic number of the specimen volume that interacts with the electron beam. Material with a low mean atomic number such as organic matter appears dark (black), and minerals with a high mean atomic number such as pyrite appear light (white) in standard greyscale digital images. Although the BSE intensity of organic matter is very low, void spaces, such as pores and fractures, exhibit even lower BSE intensity, allowing for pore identification in BSE images of shales.

Backscattered scanning electron microscopy (BSE) of the Mahogany Zone oil shale sample reveals the structure and distribution of organic matter, inorganic minerals and porosity at the micron to nano-scale. The sample is characterised by alternating horizontal organic-rich layers and inorganic minerals (Figure 4.5 A, B and F). The image contrast (greyscale variation) reflects compositional variations (mean atomic number) of the sample. Domains of darker grey levels represent organic matter (verified by EDS analysis), primarily as kerogen with a predominantly amorphous structure. The brighter grey level reflects higher density carbonate phases, and the brightest grey level represents pyrite. Micro-granular dolomite and calcite are the predominant minerals in the oil shale samples, mostly with characteristic rhombohedral structures and relatively equidimensional grains ranging in diameter from about 1 μm up to 30 μm (Figure 4.5 C and D).

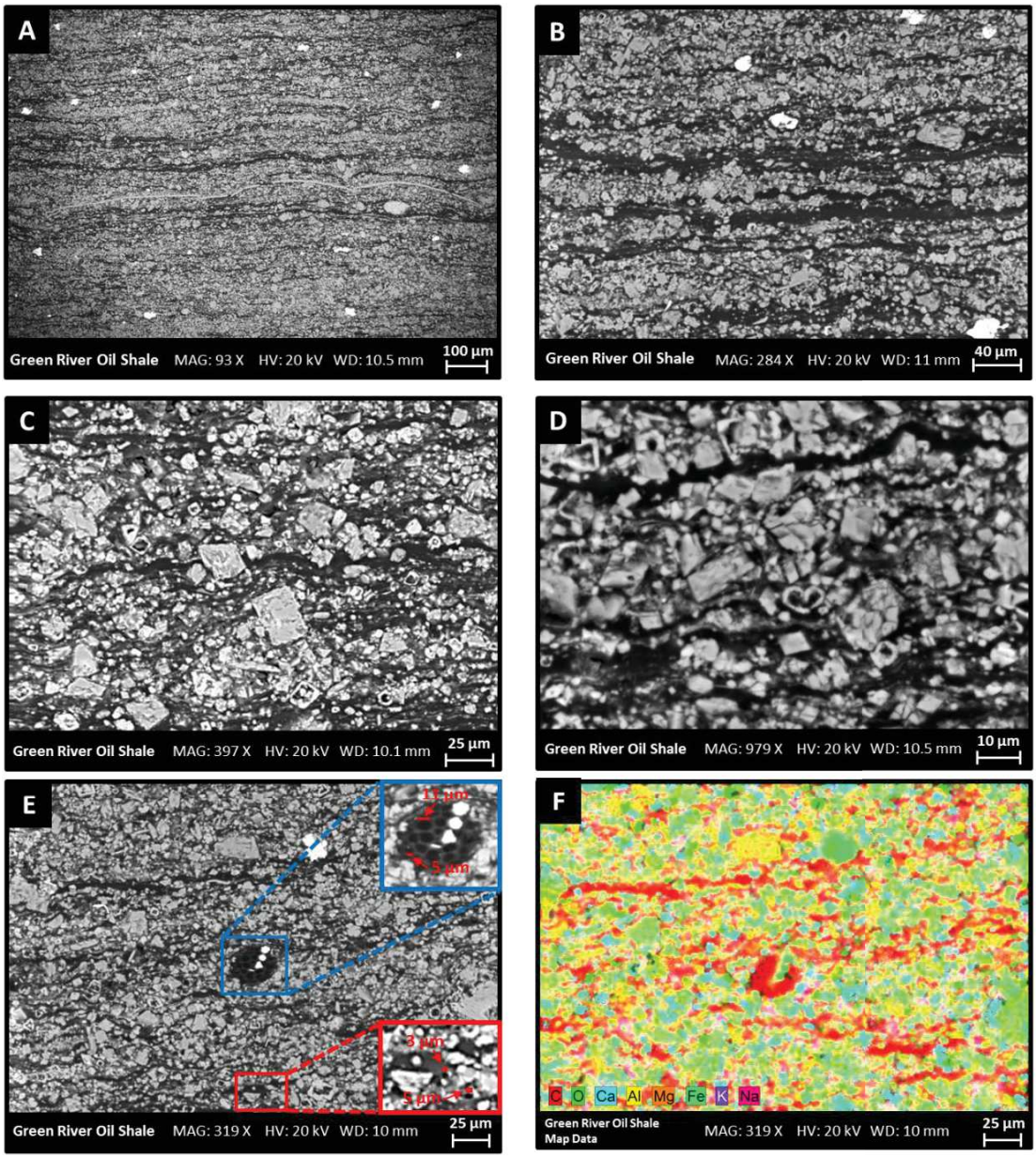

Figure 4.5 BSE images revealing organic matter, inorganic minerals and porosity with increasing magnification (A-E). The Oil Shale of the Green River Formation is characterised by alternating horizontal and folded layers of organic (black) and inorganic (grey) minerals. (F) Composite elemental map for the Green River Oil Shale displaying the spatial distribution of elements in the sample with organic-rich regions shown in red.

Authigenic clay minerals in the form of illite-mica are commonly present as a matrix constituent between the kerogen laminations and inorganic minerals, occurring as exceedingly fine-grained lathlike flakes. The high resolution BSE images reveal isolated nano-scale pores which are not accessible by mercury porosimetry even at high pressures (Figure 4.5 E). Pores identified in raw Mahogany oil shale include*:* *intra-organic pores*, referring to organic matter bounded pores; *organic interface pores*, referring to pores at the interface of organic matter and minerals; *intra-*

mineral pores, referring to pores fully bounded within mineral grains and *inter-mineral pores*, referring to pores lying between inorganic minerals. Although substantial information on the 2-D microstructure and chemical composition of oil shale can be acquired using SEM-EDS, a complementary imaging method to examine the nature of the 3-D microstructure is required to better predict oil shale pyrolysis processes.

4.5 Visualization and Quantification using X-ray Micro-tomography

4.5.1 Pyrolysis of Oil Shale Samples

Core samples of size 10 mm diameter by 70 mm length and 2 mm by 2 mm were selected from the same bulk Mahogany oil shale rock. The samples were loaded into borosilicate glass tubes allowing for vertical and radial expansion and placed under vacuum pressure at 0.1 kPa absolute. Isothermal experiments at 300, 350, 400, 450 and 500°C were conducted using a heating rate of 10°C/min to achieve the reaction temperature, where the cores were held for one hour. A thermocouple measured sample temperature and a proportional integral differential (PID) controller regulated the temperature to ±1°C. Following pyrolysis at each temperature stage, the samples were cooled to ambient temperature, removed from the furnace and subjected to micro-CT analysis. Photographs of the raw oil shale and pyrolysed samples from isothermal pyrolysis are shown in Figure 4.6.

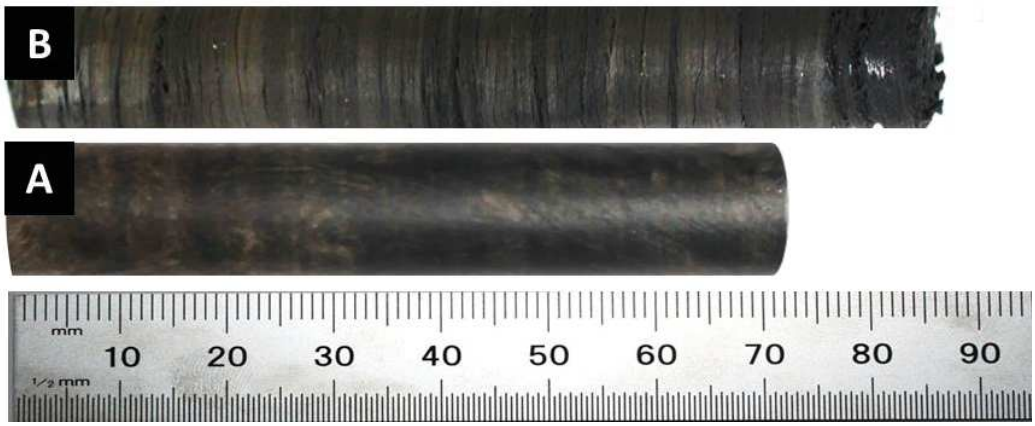

Figure 4.6 Photograph of the raw and pyrolysed Green River oil shale sample (Mahogany Zone) (A) Raw oil shale sample of size 10 mm (diameter) by 70 mm (length) (B) Oil shale sample pyrolysed at 500°C, note the vertical expansion linked to development porous layers predominantly along the kerogen-rich laminations.

4.5.2 X-ray Micro-tomography

A Zeiss Versa XRM-500 X-ray Microscope was used to image the Mahogany oil shale samples. The samples were mounted on a rotary stage, irradiated by a micro-focus polychromatic X-ray source and imaged in transmission onto a detector. The X-rays transmitted through the sample hit the scintillator crystals to give off visible light, which is then focused by the optical objective lens and converted into a digital image by the visible light charge-coupled device (CCD). Further details on the principles of laboratory-based X-ray micro-tomography are provided Section 3.7.1.1. A series of images (projections) are taken at incrementally spaced angles over 360° as the sample is rotated. The μCT acquisition settings at 12 μm and 2 μm voxel sizes are shown in Table 2.1.

4.5.3 Image Visualization and Processing

The tomograms were reconstructed using proprietary software provided by Zeiss and image processed using the Avizo 9.0 program (FEI, Visualization Sciences Group) and MATLAB (MathWorks). Multiple tomograms recorded at different locations along the vertical axis were reconstructed separately and the volumes stitched together. The total image size for the 12 μm and 2 μm scans was 727 × 754 × 7212 voxels and 1080 × 1131 × 5736 voxels respectively. The images (16-bit unsigned) were represented using unsigned grey scale value integers in the range 0 - 65,535. The grey scale values for each voxel correspond to X-ray attenuation, which varies as a function of density and atomic number. The less dense organic-rich material is shown as the darker coloured regions, while the denser mineral-rich matrix appears lighter. The images were processed using a non-local means edge preserving filter (Buades et al., 2008, 2005) and segmented to generate a binarised representation of the pore space. Further details on image processing are provided in Section 3.7.3. In this study Otsu's thresholding method (Otsu, 1979) was used, where the between-class variance (BCV) is defined, and the grey level at the BCV maximum determines the optimal threshold. It is an attractive method due to its simplicity in computation for bilevel thresholding. For this dataset, Otsu's method is applicable as upon pyrolysis the pore space in the oil shale sample can be separated from the rest of the solid phase as observed by the distinct peaks in the histogram of grey scale values (Figure 4.7 E).

Table 4.2 Oil shale μCT acquisition settings.

	μ-CT scan at 10 um voxel size	μ-CT scan at 2 um voxel size
X-ray source Energy (keV)	80	60
Power (W)	7	5
Optical Magnification	0.4 ×	4 ×
Number of Projections	1601	2001

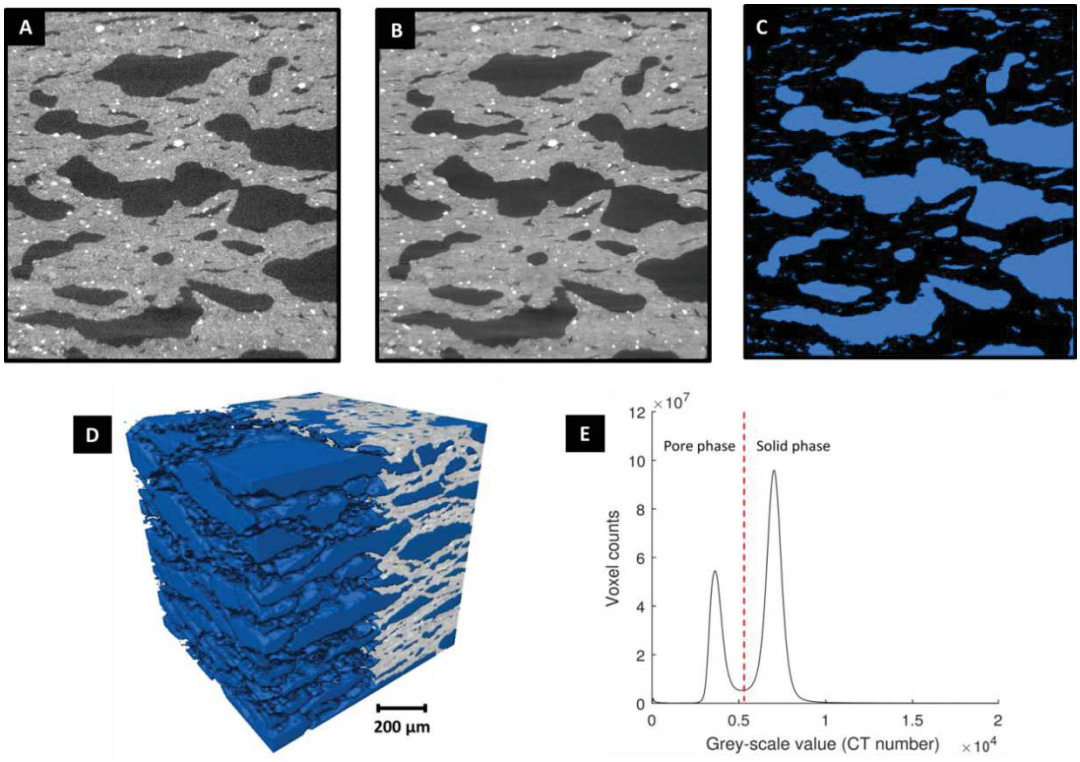

Figure 4.7 (A) Raw 2-D grey scale image at a 2 μm voxel size, (B) Non-local means filtered 2-D grey scale image, (C) Segmented image with pore space shown in blue (D) 3-D volume rendered image the pore space shown in blue and the matrix in grey, (E) Histogram of the tomography data showing the number of voxels with a particular grey value. A clear separation is observed in the histogram peaks corresponding to the pore space and the rest of the solid phase.

4.5.4 12 μm 3-D μCT analysis

Figure 4.8 A displays a 2-D image of a 3-D reconstructed grey scale image acquired at a 12 μm voxel size, with the grey scale values for each pixel corresponding to X-ray attenuation which varies as a function of density and atomic number. The less dense kerogen-rich layers are displayed as the darker coloured regions, while the denser mineral-rich layers appear lighter. The μCT image acquired reveals the spatial variation in organic content and the compositional and structural heterogeneity in oil shale of the Green River Formation. These results further validate results obtained from optical microscopy, which showed different minerals distributed in very thin and parallel laminae (Figure 4.4). Figure 4.8 B reveals the pore space that evolved following pyrolysis at 500°C with Figure 4.8 C depicting the spatial distribution of porosity (white) within the sample in the remaining solid phase (black) following binary segmentation. Micro-fracture networks developed during the pyrolysis process are evident and can be well defined. Large anisotropic (direction and geometry) micro-fractures are developed inside the kerogen-rich lamellar structures.

The computed porosity per slice is shown in Figure 4.8 D reveal a significant variation in porosity across the sample. These increased porosities constitute essentially the combined spaces represented predominantly by the loss of the organic matter. The internal vapour pressure of isolated pores increases to an extent that the mechanical strength can no longer contain. From 20°C to 500°C the oil shale sample experienced thermal expansion. Before pyrolysis, the distance between the top and bottom surfaces of the core was 5947 voxels or 71.36 mm. After pyrolysis, the distance between the top and bottom surfaces increased to 7212 voxels or 86.54 mm due to the development of pores during pyrolysis. This increase of 15.18 mm corresponds to a 21.27% increase in length. The expansion observed is due to the transformation of kerogen to oil and gas where during oil shale pyrolysis, the oil vaporizes and along with the gas supplies the driving force for structural expansion. The increase corresponds well with research into the linear expansion of oil shale cores by Duvall et al. (1983) where they achieved an increase of near 20% for their richest sample (Duvall et al., 1983).

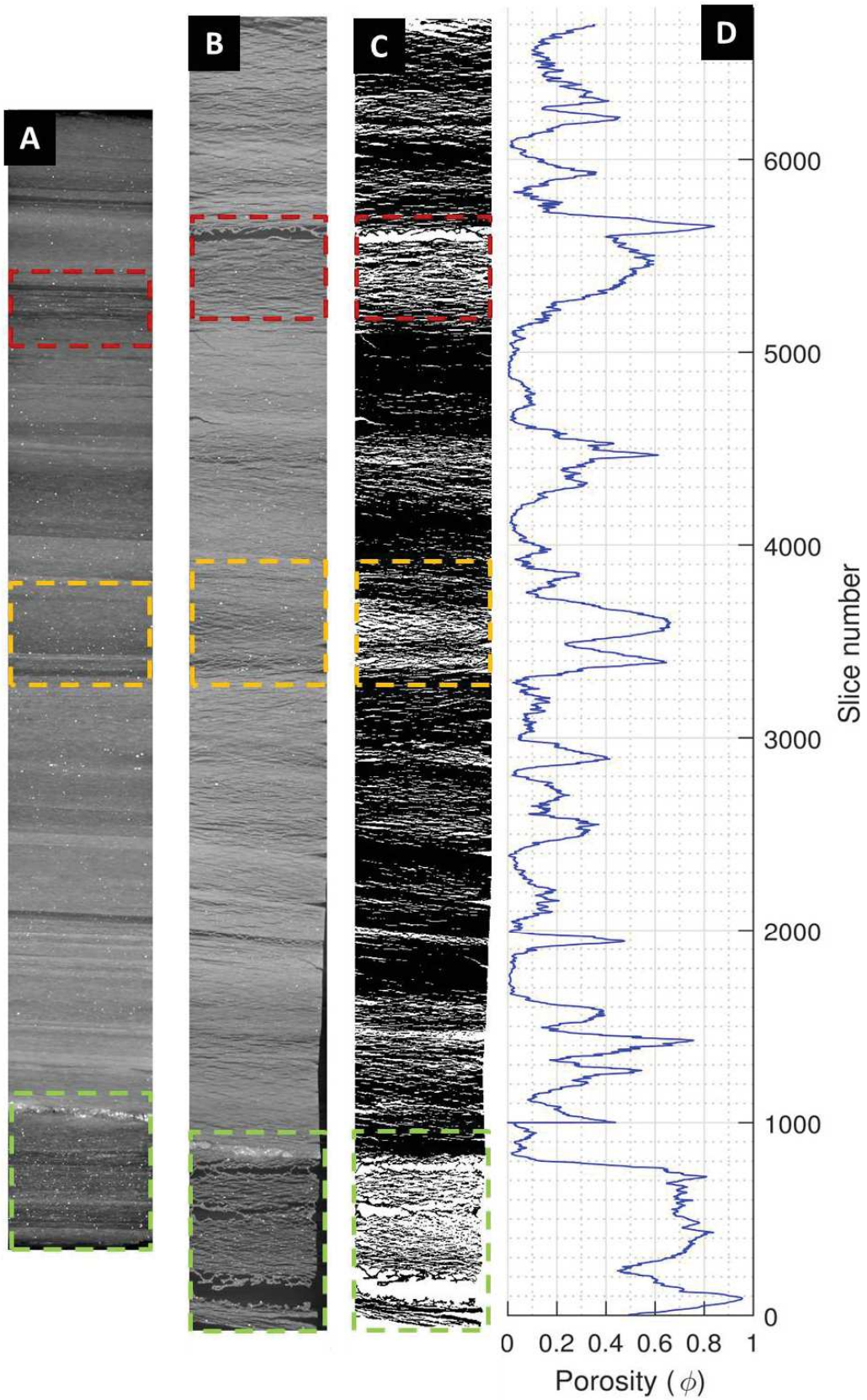

Figure 4.8 2-D grey scale images following reconstruction of the μCT 12 μm voxel size dataset for (a) raw oil shale, (b) pyrolysed oil shale at 500°C. (c) Segmented image with pore space shown in white. (d) The porosity profile per slice. The grey scale level indicates variations in the X-ray attenuation coefficients which depend on the density and atomic number of the material within each voxel. Pores and micro-fractures are observed in the kerogen-rich laminations.

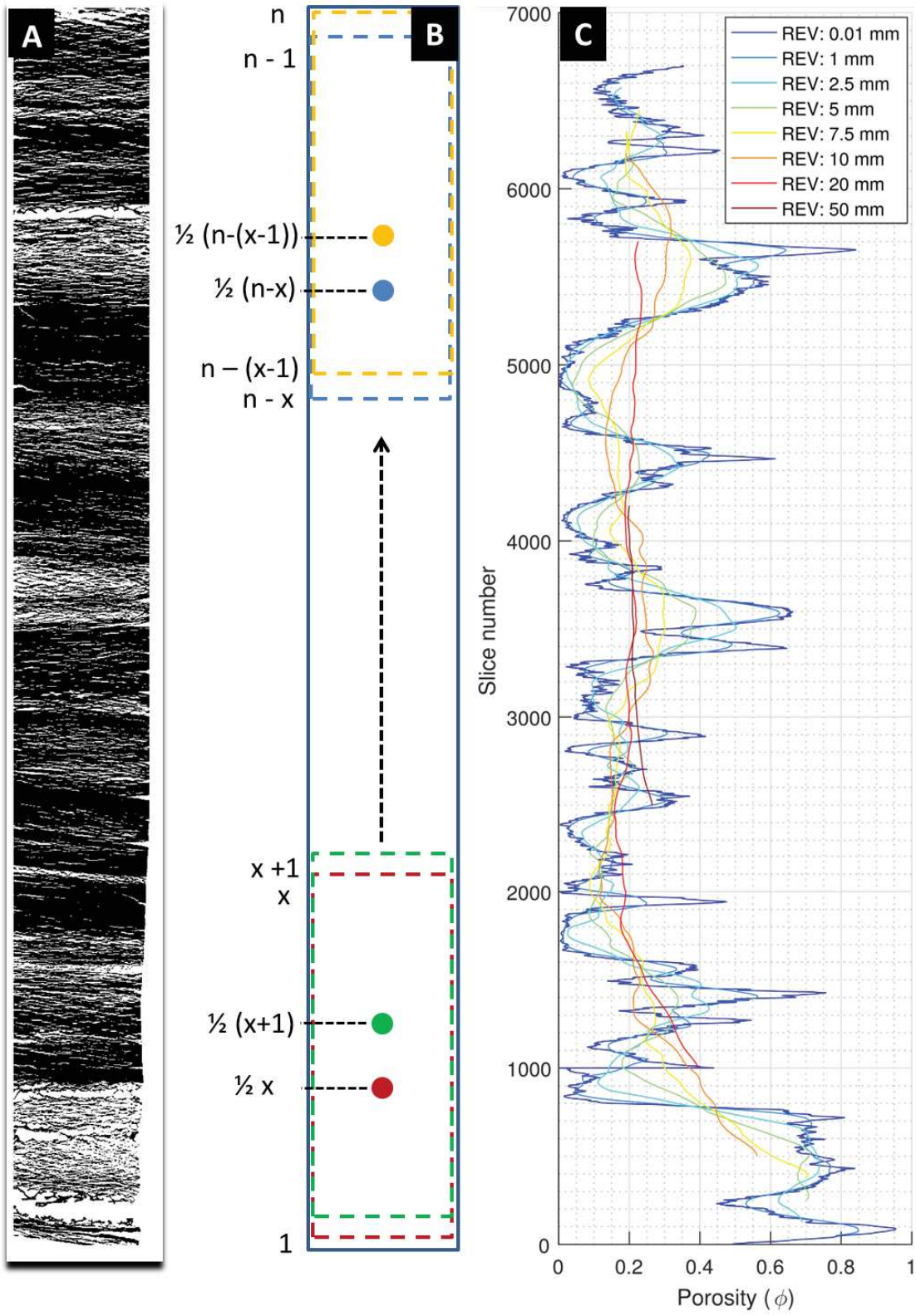

Figure 4.9 (A) 2-D segmented image with pore space shown in white and solid material in black. (B) REV analysis method where a volume of *x* thickness is moved up by one slice up to slice *n*, with each slice representing one voxel of 12 μm and porosity computed at each stage. (C) Porosity profile for analysed REV thicknesses.

Quantifying the representative sample size is essential for up-scaling the image analysis results to larger scales. The representative elementary volume (REV) was examined, defined here as the minimum averaging volume over which porosity remains constant. For examining laterally laminated oil shale samples, the REV is principally dependent on the vertical thickness where there is variation in organic material and mineral matter distribution. Therefore, in this study, the concept of REV is restricted to a representative elementary thickness (RET). RET analysis was conducted on the segmented 3-D image (Figure 4.9 A) for vertical thicknesses of 0.01, 1, 2.5, 5, 7.5, 10, 20 and 50 mm using porosity as the parameter of interest due its implication on hydrocarbon flow during oil shale pyrolysis. The analysis involved taking a sampling volume *x* thickness, moving up by 1 slice up to slice *n*, with each slice representing one voxel of 12 μm and computing the moving average porosity for each volume. From the porosity profile plot in Figure 4.9 C, it can be deduced that for thickness values of 0.01 – 5 mm there is significant fluctuation in porosity with the moving sampling volume. A relatively constant porosity profile is observed at a minimum RET of 10 mm. In addition, towards the bottom of the sample an increase in porosity was observed.

4.5.5 2 μm 3-D μCT analysis

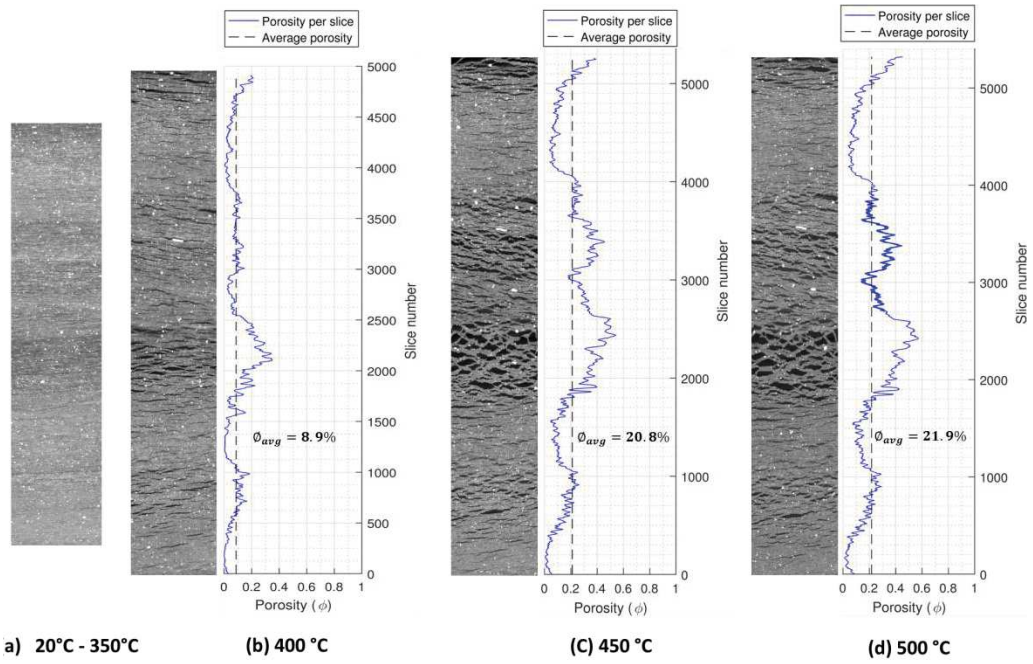

Figure 4.10 2-D grey scale images for oil shale sample at 20°C, 400°C, 450°C and 500°C with their respective porosity profiles per slice.

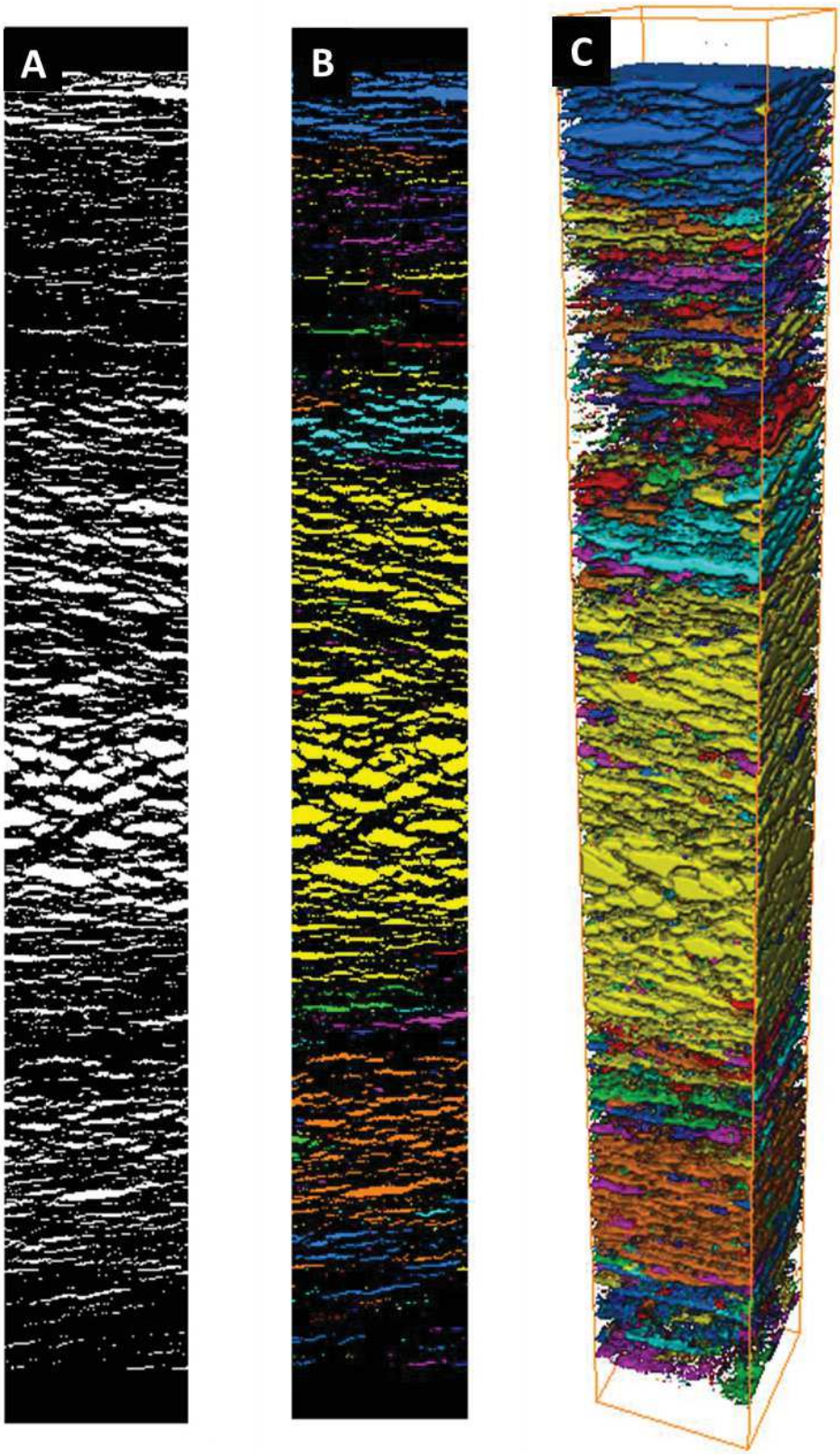

Figure 4.11 (A) 2-D segmented image for pyrolysed oil shale sample at 500°C with pore space shown in white and solid material in black. (B) 2-D image where pores of the same color are connected, (C) 3-D rendering of the pore space revealing the extensive laterally connectivity of the pore space following pyrolysis.

Following the determination of a minimum RET of 10 mm, a sample of 2 mm (diameter) by 10 mm (length) was imaged at 2 μm voxel size in 3-D using μCT before and pyrolysis at 300-500°C. The 2-D grey scale images with corresponding plots of porosity per slice are shown in Figure 4.10. Between 20°C and 350°C no change in porosity was identified in the oil shale sample at the 2 μm voxel size. At 400°C the first microscale pores are detected parallel to the kerogen-rich laminations resulting in an average sample porosity of 8.6% with a maximum slice porosity of 34.9%. A further increase in temperature to 450°C resulted in a further increase in average porosity to 20.8% and a maximum slice porosity of 54.3%. At 500°C a smaller increase in average porosity is computed to 21.9% and a maximum porosity of 57.3%. Figure 4.11, shows a 3-D rendering of the connectivity of the pore space following pyrolysis at 500°C where pores of the same colour are connected. To quantify connectivity, the image was cropped from 1080 × 1131 × 5736 voxels to 750 × 750 × 5736 voxels. Horizontally, 85.4% of the pore space is connected whilst vertically no connectivity was detectable at the 2 μm voxel size. The results obtained in this study were compared with those obtained in Chapter 7, where dynamic imaging of oil shale pyrolysis using a synchrotron X-ray source with a 2 μm voxel size was conducted on a 2 mm length Green River (Mahogany Zone) sample with a mixed composition of organic-rich and organic-lean laminations (Figure 4.12). The comparison reveals a similar trend in the evolution of porosity with temperature, with a resolvable change in porosity taking place between 390-400°C.

To assess the porosity range that results following pyrolysis at 500°C, 10 samples were selected at random from the bulk oil shale specimen. The samples were imaged, reconstructed, filtered and segmented to compute the porosity. Figure 4.13 shows the porosity results obtained with the highest value obtained as 37.9%, the lowest 12.8% and an average porosity of 23.1% for the 10 samples. The 3-D volume rendering of organic-rich, lean and mixed samples are shown in Figure 4.13 E-G. These results further validate that the final oil shale porosity values after pyrolysis are directly related to the organic matter content.

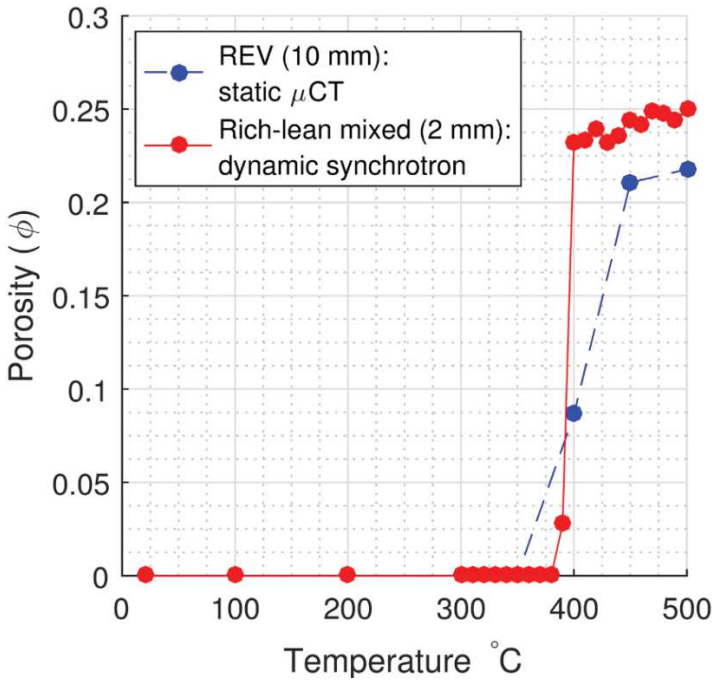

Figure 4.12 Oil shale porosity as a function of pyrolysis temperature. A comparison between static laboratory based analysis, presented here, and dynamic synchrotron μCT data (Saif et al., 2016).

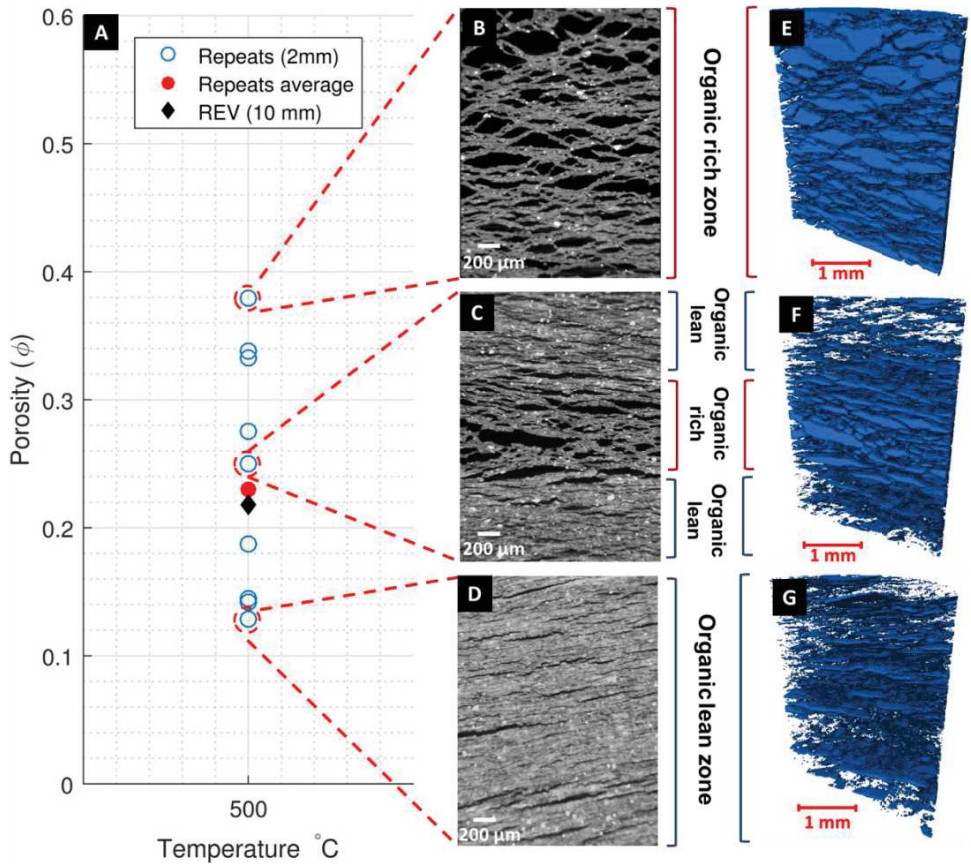

Figure 4.13 (A) Porosity of 10 oil shale samples after pyrolysis at 500°C, (B) – (D). 2-D grey scale images for organic-rich, organic-mixed and organic-lean regions respectively. (E) – (G) 3-D rendered volumes with the pore space visualized in blue.

4.6 Summary

Fluid flow through porous structures is a crucial aspect of hydrocarbon recovery during oil shale pyrolysis. The quantification of effective material properties is of paramount importance. The results from this chapter further our knowledge of the internal microstructure of the organic-rich Green River Formation (Mahogany Zone) and the changes in porosity and connectivity during oil shale pyrolysis. Initially the Mahogany oil shale was characterised by determining bulk properties including mineralogy (XRD), total organic carbon (TOC), thermal maturity (Rock-Eval and Source Rock Analyser (SRA)), elemental analysis (CHNOS) and oil yield (Modified Fischer Assay (MFA)). However, given the complexity and heterogeneity of oil shale, samples were also characterised using optical microscopy, SEM-EDS and X-X-ray μCT at 12 μm and 2 μm voxel sizes. These imaging techniques provided local information on the spatial distribution of organic material, mineral phases and pore structures.

This work has extended previous studies by examining oil shale pyrolysis at higher spatial resolutions and analysing the representative elementary thickness given the heterogeneity of oil shale. Thin section analysis showed a micro-laminated structure of organic material whilst SEM characterization with increasing magnification reveals the structure of a carbonate-rich matrix, the distribution organic matter and the nature of isolated pores in raw oil shale. On increasing the pyrolysis temperature from 20°C to 350°C no resolvable pore space was identified at 2 μm voxel size. At 400°C the development of the pore space was visualized and quantified showing that the increased porosity was primarily related to the thermal decomposition of organic matter. The porosity continued to increase to 450°C with a smaller increase between 450°C and 500°C leading to laterally connected pores along the kerogen-rich laminations. From μCT scans at 12 μm a minimum representative elementary thickness of 10 mm was determined based on porosity values.

These techniques are complementary: by combining bulk analytical techniques with traditional (2-D) and advanced (3-D) imaging methods, this chapter presented a more comprehensive characterization than current existing literature for this important oil shale, which subsequently allows for improved modelling and prediction of fluid

flow during oil shale pyrolysis. In addition, the experimental determination of petrophysical properties for oil shale can be uncertain, often producing inconsistent results. In this thesis it is proposed that multiple random 3-D images are required to perform a statistically representative analysis for oil shale rocks. This chapter also characterised the representative size for the Mahogany oil shale by analysing the sample size over which porosity remains constant, recommending 10 mm as the minimum representative elementary thickness.

The experimental data presented on oil shale before, during and after pyrolysis, serve as valuable input parameters to effectively model oil shale pyrolysis processes and permit a more knowledgeable appraisal of engineering problems associated with both *ex situ* and *in situ* operations. Chapter 5 extends this work by applying sub-micrometre X-ray micro-tomography to characterise both organic matter and porosity networks along with ultra-high resolution SEM approaching 3nm pixel size FIB-SEM analysis of un-pyrolysed and pyrolysed samples at a spatial resolution of 10 nm. Chapter 6 also extends this work by providing a visualization and quantification of the dynamics of pore evolution during pyrolysis using synchrotron-based X-ray micro-tomography at a time resolution of 160 seconds and voxel size of 2 μm.

Chapter 5

Imaging and Analysis of Oil Shale Pyrolysis using Sub-micron X-ray Micro-tomography, Automated Ultra-high Resolution SEM, MAPS Mineralogy and FIB-SEM

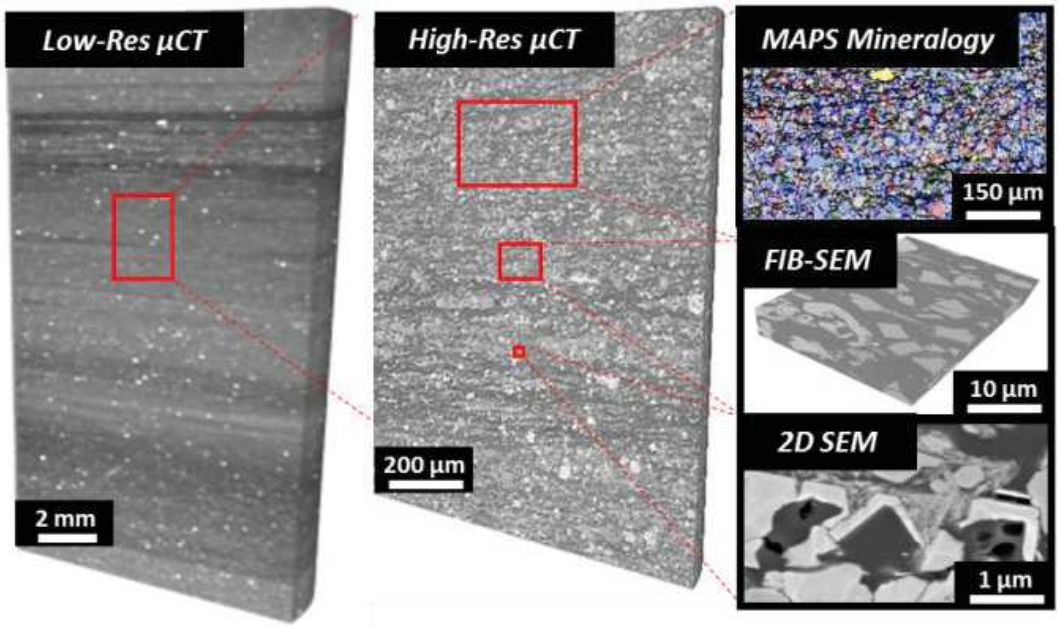

Multi-scale multi-dimensional oil shale characterization workflow

Publication:

Saif, T., Lin, Q., Butcher, A.R, Bijeljic, B. and Blunt, M.J., (2017). Multi-scale Multi-dimensional Microstructure Imaging of Oil Shale Pyrolysis using X-ray Micro-tomography, Automated Ultra-high Resolution SEM, MAPS Mineralogy and FIB-SEM, *Applied Energy*, 202, 628-647.

5.1 Introduction

The complexity of unconventional rock systems is expressed both in the compositional variance of the microstructure and the extensive heterogeneity of the pore space. This chapter extends previous work discussed in Chapter 4 by characterizing the microstructural heterogeneity of oil shale using sub-micron X-ray Micro-tomography (μCT) (Section 5.2), automated ultra-high resolution Scanning Electron Microscopy (SEM) (Section 5.3), MAPS Mineralogy (Modular Automated Processing System) and Focused Ion Beam Scanning Electron Microscopy (FIB-SEM) (Section 5.4). Observations in 2-D and 3-D and across nm-μm-mm length scales demonstrate both heterogeneity and anisotropy at every scale. The application of these techniques to worldwide oil shale deposits will allow significant insights into estimating mechanical and chemical proprieties of oil shale formations for modelling and designing oil shale pyrolysis processes.

5.2 3-D Organic Matter (Kerogen) and Pore Structure Analysis using Sub-micron X-ray Micro-tomography (μCT)

A Zeiss Versa XRM-500 X-ray Microscope (Carl Zeiss, CA, USA) was used to image the Green River (Mahogany Zone) oil shale samples. Samples of size 1.0 mm diameter by 5.0 mm length were mounted on a rotary stage, irradiated by a micro-focus polychromatic X-ray source and imaged in transmission onto a detector. The X-rays transmitted through the sample hit the scintillator crystals to give off visible light, which is then focused by the optical objective lens and converted into a digital image by the visible light charge-coupled device (CCD). A series of images (projections) were taken at incrementally spaced angles over 360° as the sample is rotated. The μCT scans of the oil shale samples were taken with the X-ray source operating at 50 keV and acquired at 0.8 μm voxel sizes with 2001 projections (Table 5.1), collected on a 2000 × 2000 pixel CCD detector with the pixel size binned to 1000 × 1000 pixels. A qualitative comparison between oil shale samples scanned at 12 μm and 2 μm (Section 4.5), and at 0.8 μm in this section is presented in Figure 5.1. Further details on the principles of laboratory-based X-ray micro-tomography are provided in Section 3.7.1.1.

The tomograms were reconstructed into 3-D volumes using proprietary software (Zeiss XMReconstructor, Carl Zeiss X-ray Microscopy Inc., Pleasanton, CA) based on filtered back-projection (FBP) algorithms and image processed using Avizo 9.0 software (FEI, Hillsboro, OR, USA) and MATLAB (MathWorks, Inc., Natick, USA). Following image processing, the total image size for the 0.8 μm scans was 964 × 993 × 970 voxels. The images (16-bit unsigned) were represented using unsigned greyscale value integers in the range 0 - 65,535. The images were processed using a non-local means edge preserving filter (Buades et al., 2008, 2005) and segmented using global thresholding to generate a binarised representation of the organic matter network (Figure 5.2). Further details on image filtering and image segmentation are provided in Section 3.7.3.1 and 3.7.3.2 respectively.

Figure 5.2A and B display a 2-D image of a 3-D reconstructed greyscale image acquired at a 0.8 μm voxel size. The greyscale values for each pixel correspond to X-ray attenuation, which varies as a function of density and atomic number. The less dense kerogen-rich layers within the oil shale sample are displayed as the darker coloured regions, while the denser mineral-rich layers appear lighter. Figure 5.2 C and D illustrate the segmented organic matter revealing a 99.8% well-connected organic network in the analysed 3-D oil shale volume that consists of 36.9% organic content. Figure 5.3 shows BSE and segmented images of organic matter content within the same analysed sample, revealing a TOC variation from 23.52% to 48.85%.

To study the impact of pyrolysis temperature on the evolution of the pore space, the Green River (Mahogany Zone) oil shale sample was imaged before and after pyrolysis from 20°C to 420°C in 10°C increments. The sample was heated *ex situ* in an electrically heated furnace (Carbolite ELF 11/14B) at each set temperature point and then allowed to cool to ambient temperature before being placed in a sample holder and imaged using the Zeiss Versa XRM-500 μCT scanner.

Table 5.1 Oil shale μCT acquisition settings.

	μ-CT scan at 10 μm voxel size	μ-CT scan at 2 μm voxel size	μ-CT scan at 0.8 μm voxel size
X-ray source Energy (keV)	80	60	50
Power (W)	7	5	4
Optical Magnification	0.4×	4×	20×
Number of Projections	1601	2001	2001

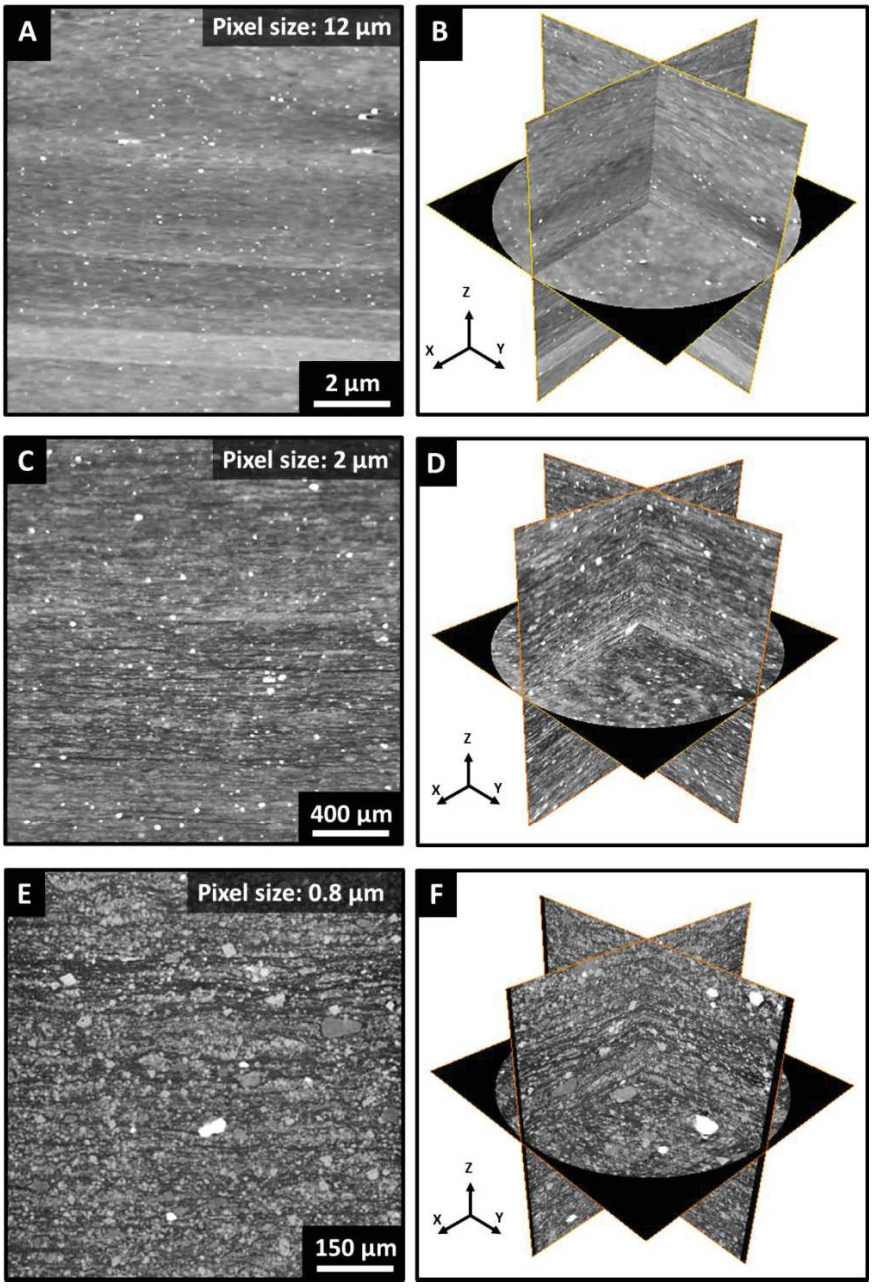

Figure 5.1 2-D greyscale and tri-planar images of Green River (Mahogany Zone) oil shale before pyrolysis acquired at (A)-(B) 12 μm, (C)-(D) 2 μm and (E)-(F) 0.8 μm voxel size.

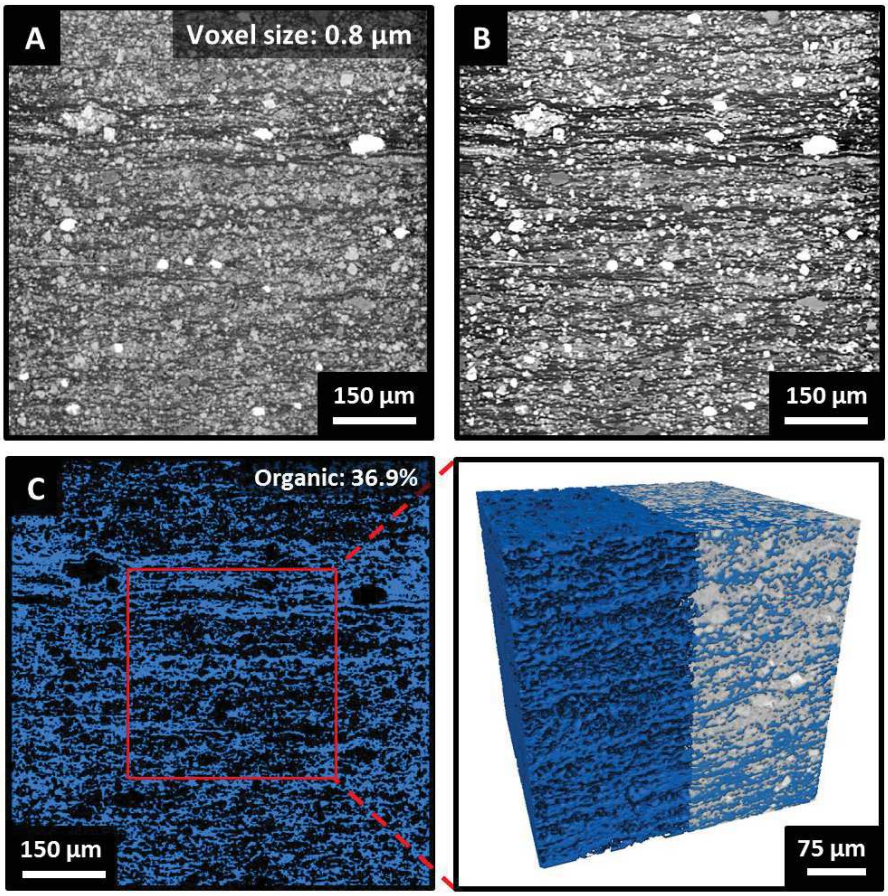

Figure 5.2 X-ray micro-tomography (μCT) for immature Green River (Mahogany Zone) oil shale acquired at a 0.8 μm voxel size. (A) Raw 2-D greyscale image, (B) Non-local means filtered 2-D greyscale image, (C) Segmented image with organic matter (kerogen) shown in blue (D) 3-D volume rendered image with the organic matter shown in blue and the mineral matrix in grey.

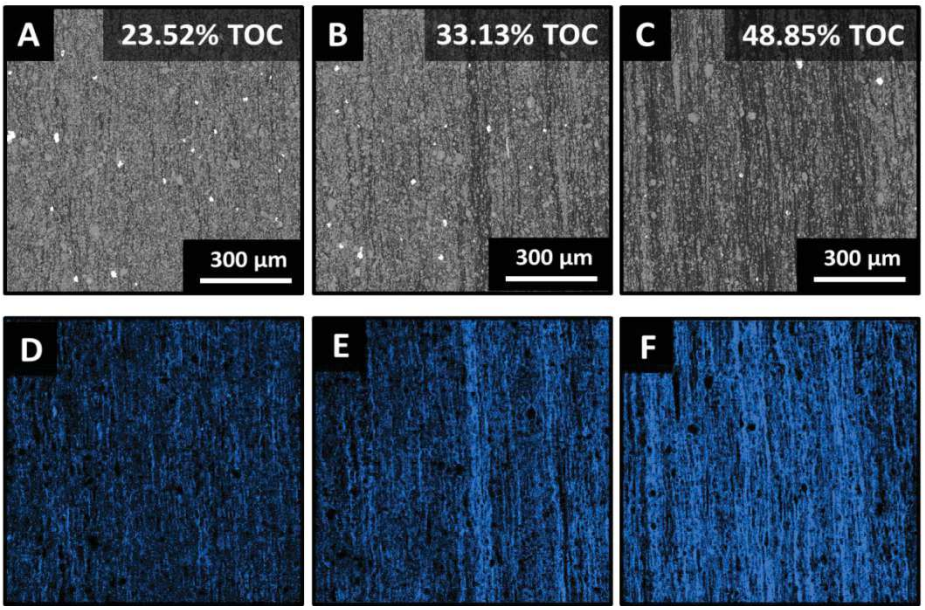

Figure 5.3 (A)-(C) Backscattered electron (BSE) images of the Green River (Mahogany Zone) oil shale with increasing amount of organic matter (total organic carbon (TOC)) within the same sample. (D)-(F) Segmented images with organic matter shown in blue.

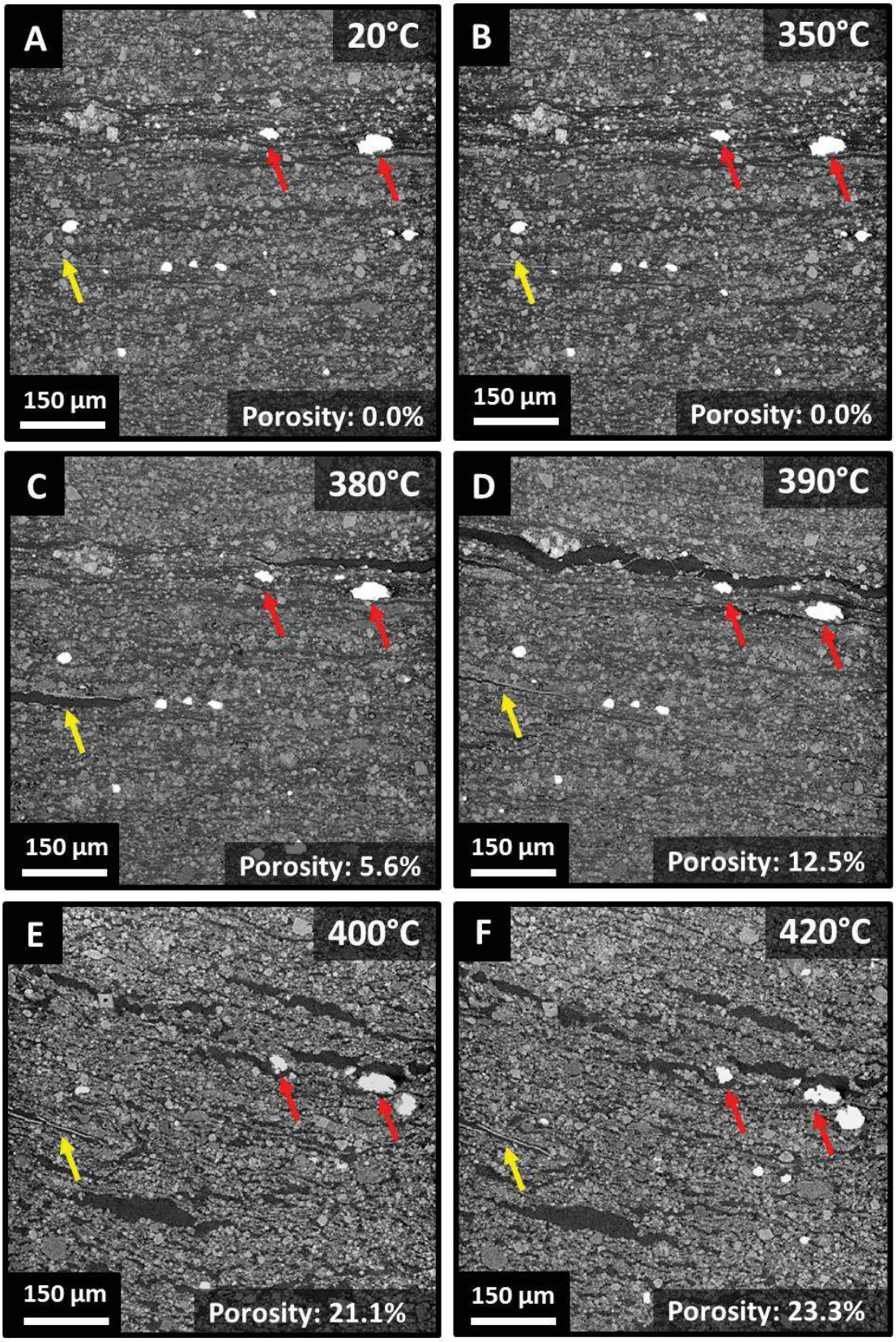

Figure 5.4 Micro-fracture development in the Green River (Mahogany Zone) oil shale sample during pyrolysis at (A) 20°C, (B) 350°C, (C) 380°C, (D) 390°C, (E) 400°C and (F) 420°C. The red arrows indicate reference pyrite minerals used to monitor the same 2-D μCT image slice, and the yellow arrows show developing micro-fractures within the oil shale sample.

Between 20°C and 350°C no change in porosity was identified in the oil shale sample at the 0.8 μm voxel size (Figure 5.4 A and B). In Figure 5.4 C, at 380°C, the first micro-fractures are observed parallel to the organic-rich laminations resulting in a sample porosity of 5.6%. A further increase in temperature to 390°C resulted in the propagation of the major fracture along the kerogen-rich bedding and the temporary closure of the minor fracture due to local compressive stresses (Figure 5.4 D). At 390°C the computed sample porosity was 12.5%. At 400°C (Figure 5.4 E) and 420°C (Figure 5.4 F), the growth of multiple major and minor pores and micro-fractures continues,c which is accompanied by a volume increase, resulting in a porosity of 21.1% and 23.3% respectively. The development of these pores and fractures within the organic-rich sample is due to the thermally-induced breakdown of kerogen into hydrocarbon fluids. The increase in fluid pressure during the transformation process causes local stress concentrations within the organic matter and at a critical stress, fractures start to nucleate and propagate. With increasing temperature, growing micro-fractures coalesce leading to an interconnected fracture network within the pyrolysed oil shale sample.

The results obtained in this study were compared with those obtained in Chapter 6, where dynamic imaging of oil shale pyrolysis using a synchrotron X-ray source with a 2 μm voxel size was performed on a Green River (Mahogany Zone) sample with a mixed composition of organic-rich and organic-lean zones. The comparison between *ex situ* (static X-ray μCT) and *in situ* (dynamic synchrotron X-ray μCT) results reveal a similar trend in the evolution of porosity with temperature, with a resolvable change in porosity taking place between 380-400°C.

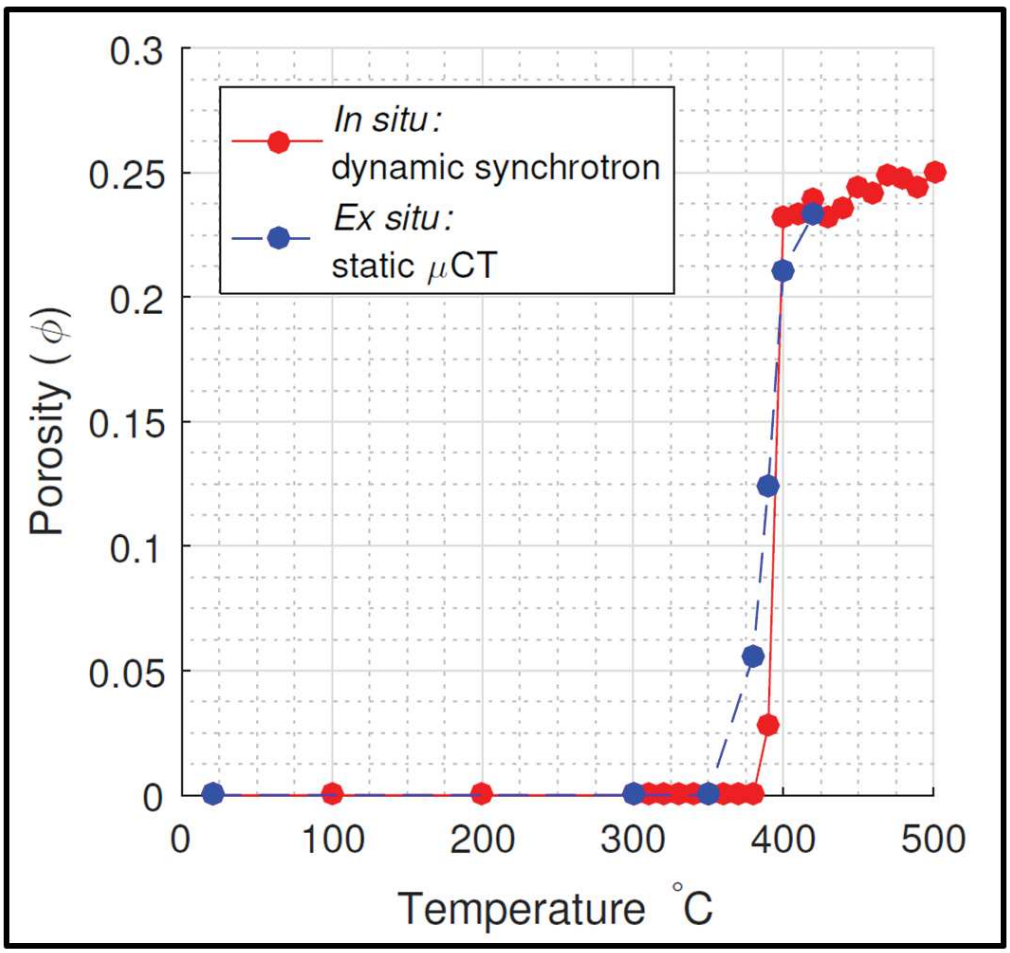

Figure 5.5 Oil shale porosity for the Green River (Mahogany Zone) samples as a function of pyrolysis temperature. A comparison is made between static laboratory based analysis, presented here, and dynamic synchrotron μCT data (Saif et al., 2016).

5.3 2-D Ultra-high resolution SEM and MAPS Mineralogy

Ultra-high resolution Scanning Electron Microscopy (SEM) was performed on Green River (Mahogany Zone) oil shale samples to characterise the complex distribution and association of organic, mineral, and pore phases at the nano-to-micro scales. In this study, Mahogany zone samples of about 18 mm × 14 mm × 5 mm were initially hand-polished using sandpaper (600, 1200 and 2000 grit) and diamond lapping film (6 μm, 3 μm and 1 μm). The resulting Mahogany oil shale sample surfaces were then attached to 25 mm diameter pin-type stubs using carbon tape and then coated with less than a 100-Å thick elemental carbon film via a vacuum evaporator (Quorum Q150T) to mitigate charge build up (Figure 5.6 A). Each sample surface was then argon ion milled using a Fischione 1060 SEM Mill under a 2° incident angle and 360° sample rotation at 6 keV for 22 hours. In this process, argon is ionized and

accelerated towards the sample surface where the impinging ions sputter material from the surface at a controlled rate (Figure 5.6 B). The oil shale polished sample surfaces were then examined using a Quanta FEG 650 SEM (FEI) equipped with two Bruker XFlash 6 series detectors for energy dispersive spectroscopy (EDS). Details on the fundamental principles of SEM-EDS are provided in Section 3.5.

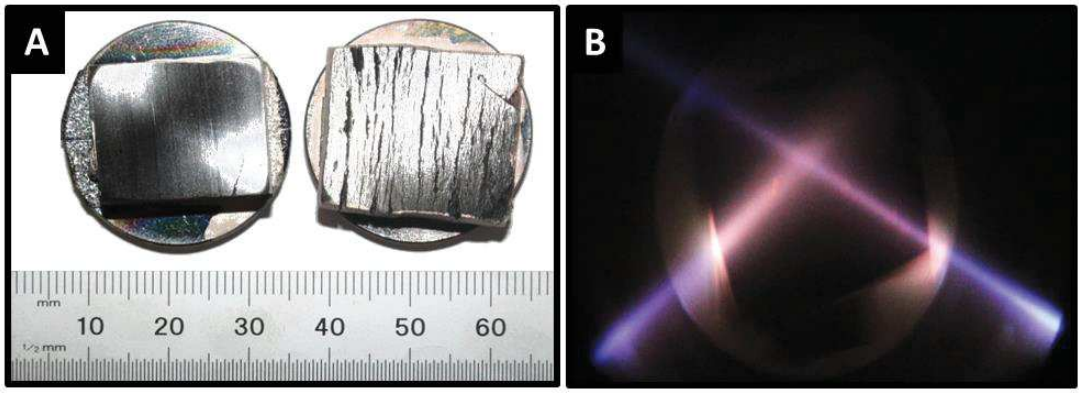

Figure 5.6 (A) Carbon-coated argon ion milled Green River (Mahogany zone) oil shale samples, un-pyrolysed (sample 1, left) and pyrolysed (sample 2, right), prepared for large-area automated SEM imaging and MAPS Mineralogy, (B) Two independently adjustable ion sources used to rapidly mill the oil shale samples creating highly polished ultra-flat surfaces for ultra-high resolution SEM imaging.

MAPS (Modular Automated Processing System) software was used for automated acquisition of high-resolution large-format mosaic images. The surface area of interest was divided into a grid format with 19 × 16 tiles and a sequence of BSE images were acquired in real-time with a 10% overlap (Figure 5.7). This resulted in images of 34,733 × 28,839 pixels for sample 1 (un-pyrolysed) and 35,417 × 29,216 pixels for sample 2 (pyrolysed) each with a pixel size 500 nm captured at an energy of 15 keV. The stitched mosaic of images allows for the systematic investigation of fine-grained microstructures from the nm to the mm scales. Further details on large scale automated SEM imaging are discussed in Section 3.5.2.

Electron beam analysis points return secondary X-ray spectra that are compared with a large database, allowing the assignment of each analysis point to a specific mineral or elemental category. Nanomin software (FEI, Hillsboro, OR, USA) was used to analyse SEM-EDS data, and to map the chemical, mineral composition and textural features in the rock samples at an X-ray spacing of 10 μm and an acquisition time of 8ms per pixel. Regions of interest were further explored by acquiring ultra-high

resolution mosaic BSE images at beam energies of 3-5 keV generating images with 3, 10, 20, 30 and 50 nm pixel sizes.

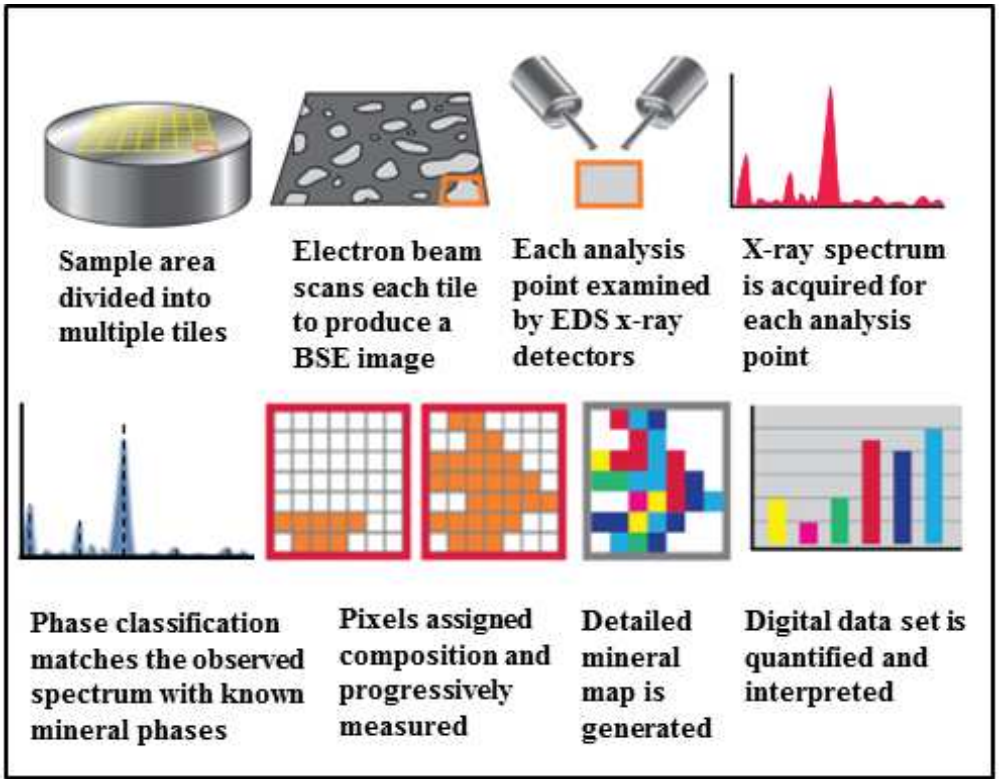

Figure 5.7 Automated SEM and MAPS Mineralogy measurement and analysis workflow. The area of interest is divided into multiple tiles and backscattered electron (BSE) images are recorded in sequence and subsequently stitched to generate 7one single image. The full surface is also mapped using energy-dispersive (EDS) X-ray analysis with a user-defined spacing. The EDS X-ray spectrum for each analysis point is compared to a database of known mineral species. This process is automated on a pixel by pixel basis to create high resolution mineral maps.

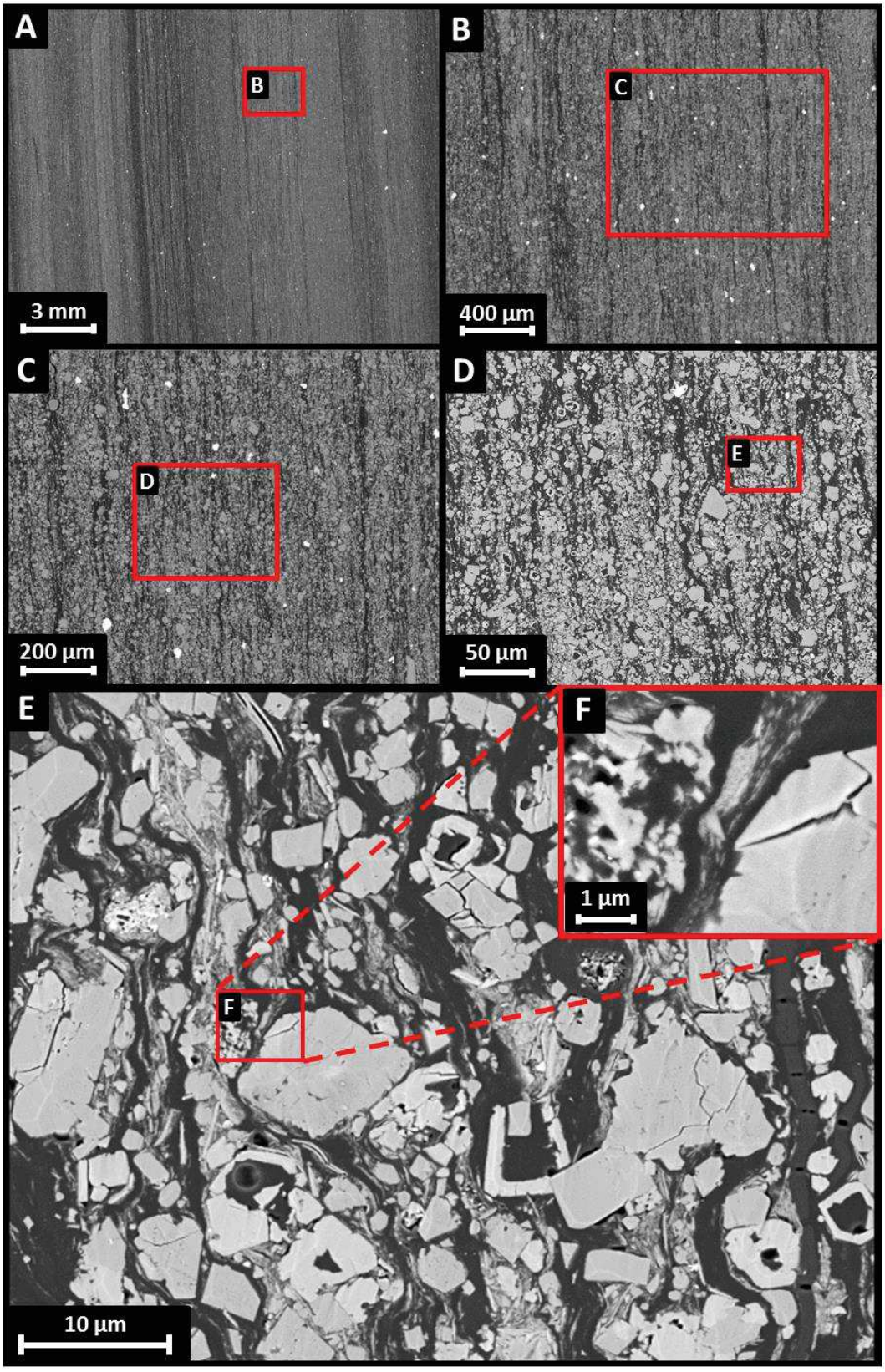

Figure 5.8 (A) Stitched BSE image of 18 mm × 14 mm raw Green River (Mahogany zone) oil shale. The large area image has been created by stitching 19 × 16 tiles, resulting in an image of 34,733 × 28,839 pixels with a pixel size of 500 nm captured at 15 keV. (B) - (D) From the full overview of the stitched image of a sample, zooming exposes the high resolution details without losing correlation and allows regions of interest to be located for further investigation. (E) - (F) Higher resolution BSE images acquired at 5 keV with a 10 nm pixel size.

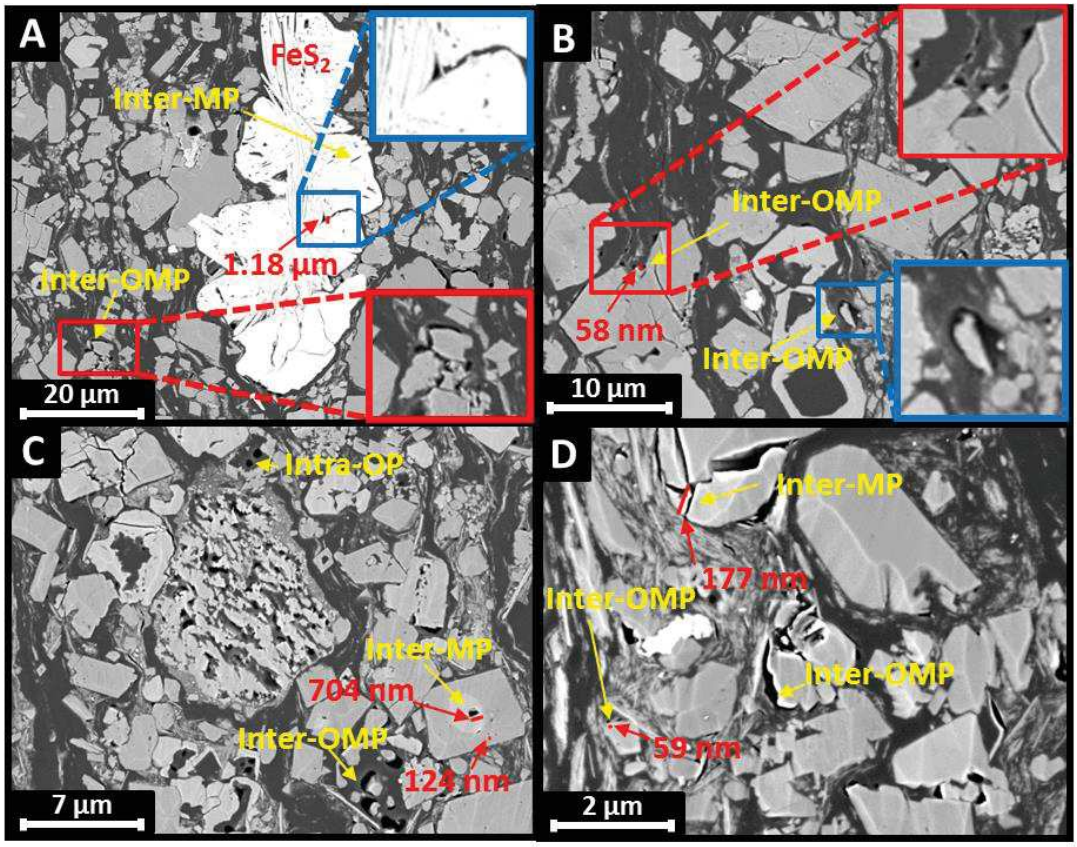

Figure 5.9 The pores identified in the un-pyrolysed Green River (Mahogany Zone) oil shale sample can be categorized into: Intra-OP (Organic Pore), Inter-OMP (Organic-Mineral Pore), Intra-MP (Mineral Pore), Inter-MP (Mineral Pore). (A) Marcasite grain (FeS_2, orthorhombic), the dimorph of pyrite with characteristic tabular-bladed morphology, BSE image captured at 5 keV with a 15 nm pixel size. (B) Individual rhomboid shaped grains characteristic of dolomite, BSE image captured at 5 keV with a 15 nm pixel size. (C) Porous carbonate grain, BSE image captured at 5 keV with a 10 nm pixel size. (D) Clay platelets with local ordering within organic matter and submicron-scale pores between clay mineral platelets, BSE image captured at 3 keV with a 3 nm pixel size.

Figure 5.8 shows greyscale mosaic BSE images that display compositional contrast in the heterogeneous Green River (Mahogany Zone) oil shale sample. Automated tiling and stitching BSE images into mosaics enable pore-scale resolution over the entire sample surface in one image allowing the simultaneous retrieval of microstructural fabric heterogeneity and nanometre-scale structures without losing correlation. The gigapixel size mosaic can expose higher resolution features within a deceased field of view to uncover structural features that constitute the rock fabric (Figure 5.8 A-F). In these SEM images, compositional contrast is recorded as BSE intensity which is a function of the mean atomic number of the specimen volume that interacts with the electron beam. Kerogen, which is predominantly composed of relatively low atomic number elements in the form of carbon, hydrogen, and oxygen translates to darker image pixels. This organic matter is dispersed within a matrix of

inorganic minerals such as iron-rich pyrite, calcium-rich dolomite, and silicon-rich quartz, which appear as brighter (light grey to white) image pixels due to higher atomic number elements. The Green River oil shale exhibits a layered structure of alternating kerogen-rich and lean laminations at both the millimetre (Figure 5.8 A) and micron scales (Figure 5.8 B-D).

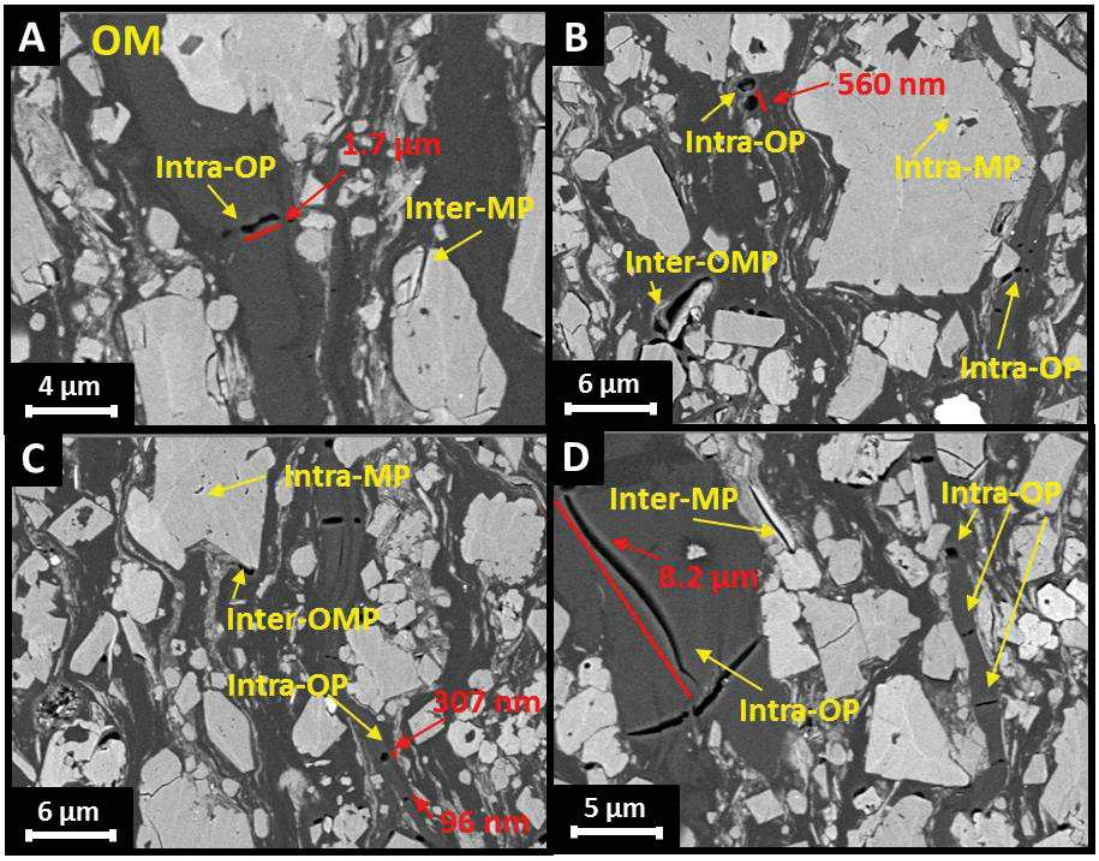

Figure 5.10 (A) Lenticular shaped intra-OP (Organic Pore) of micron-scale, BSE image captured at 5 keV with a 50 nm pixel size, (B) Intra-MP (Mineral Pore) within dolomite grain and inter-OMP (Organic-Mineral Pore) between organic matter and potassium feldspar grain, BSE image captured at 5 keV with a 50 nm pixel size, (C) Intra-OP within the range from several tens to a few hundred nanometres, BSE image captured at 5 keV with a 50 nm pixel size, (D) Fracture pores within organic matter of a few micrometres, BSE image captured at 5 keV with a 10 nm pixel size.

Although the BSE intensity of kerogen is low, void spaces, such as pores and fractures, display even lower BSE intensity, allowing for pore identification and quantification in BSE images of oil shale samples (Figure 5.9 and Figure 5.10). The EDS performed on the oil shale surfaces combined with the mineral identification software package NanoMin confirm that the darker areas are organic kerogen, with the lighter grey inorganic mineral matrix being primarily composed of varying amounts of dolomite, calcite, quartz and clays (Figure 5.12 and Figure 5.13).

Figure 5.9 - 5.11 show pores present in the oil shale sample which range from a few nanometres to several micrometres in diameter and from simple to complex geometries. These pores form by both depositional and diagenetic processes as well as through multiple stages related to deposition, compaction, cementation, and dissolution. In the Green River (Mahogany Zone) oil shale sample four types of porosity are observed: *intra-organic pores*, referring to pores bounded by organic matter; *inter-organic-mineral pores*, referring to pores between organic matter and minerals; *intra-mineral pores*, referring to pores fully bounded within mineral grains and inter-mineral pores, referring to pores lying between inorganic minerals. For the Mahogany oil shale sample, a key observation was that organic matter hosted pores, rather than mineral-hosted pores, were the dominant contributors to total porosity and are predominantly sub-μm in size with typically irregular geometries.

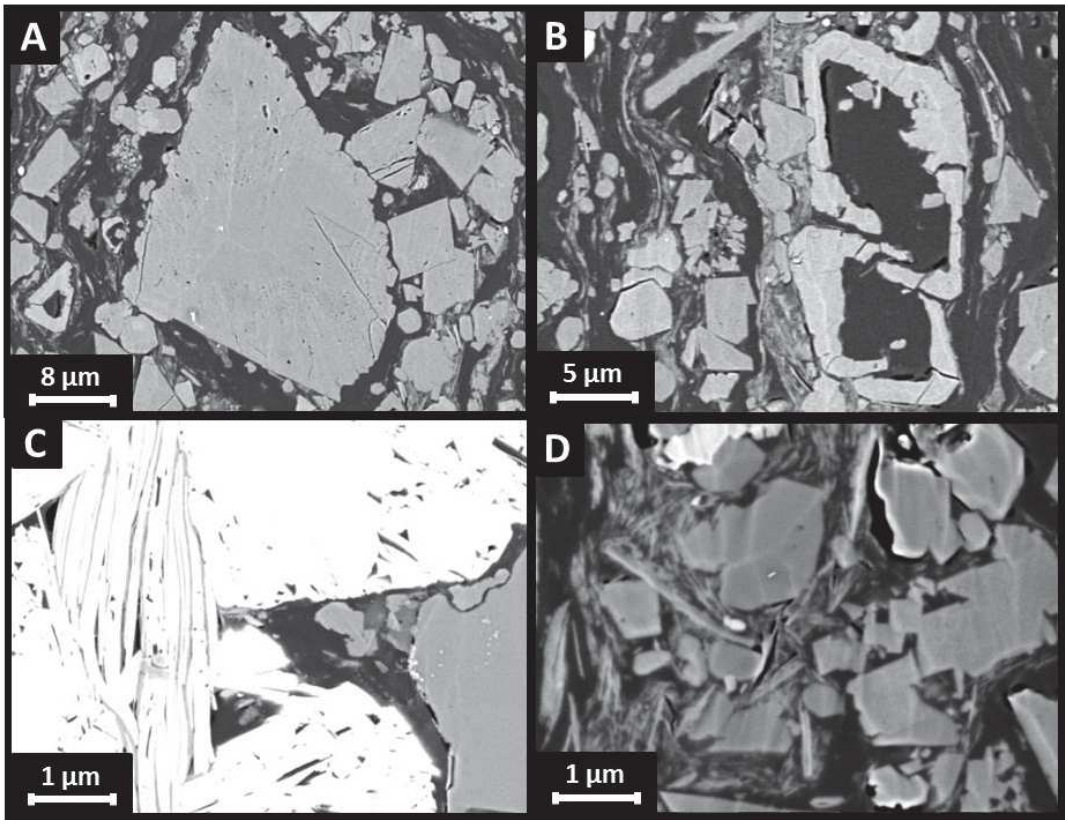

Figure 5.11 High-resolution BSE images for immature Green River (Mahogany Zone) oil shale, (A) Dolomite grain with sub-μm pores, (B) Kerogen encapsulated within calcite minerals, (C) Mineral hosted nano-porosity within a Marcasite (FeS_2) grain, and (D) Nano-scale clay platelets within kerogen.

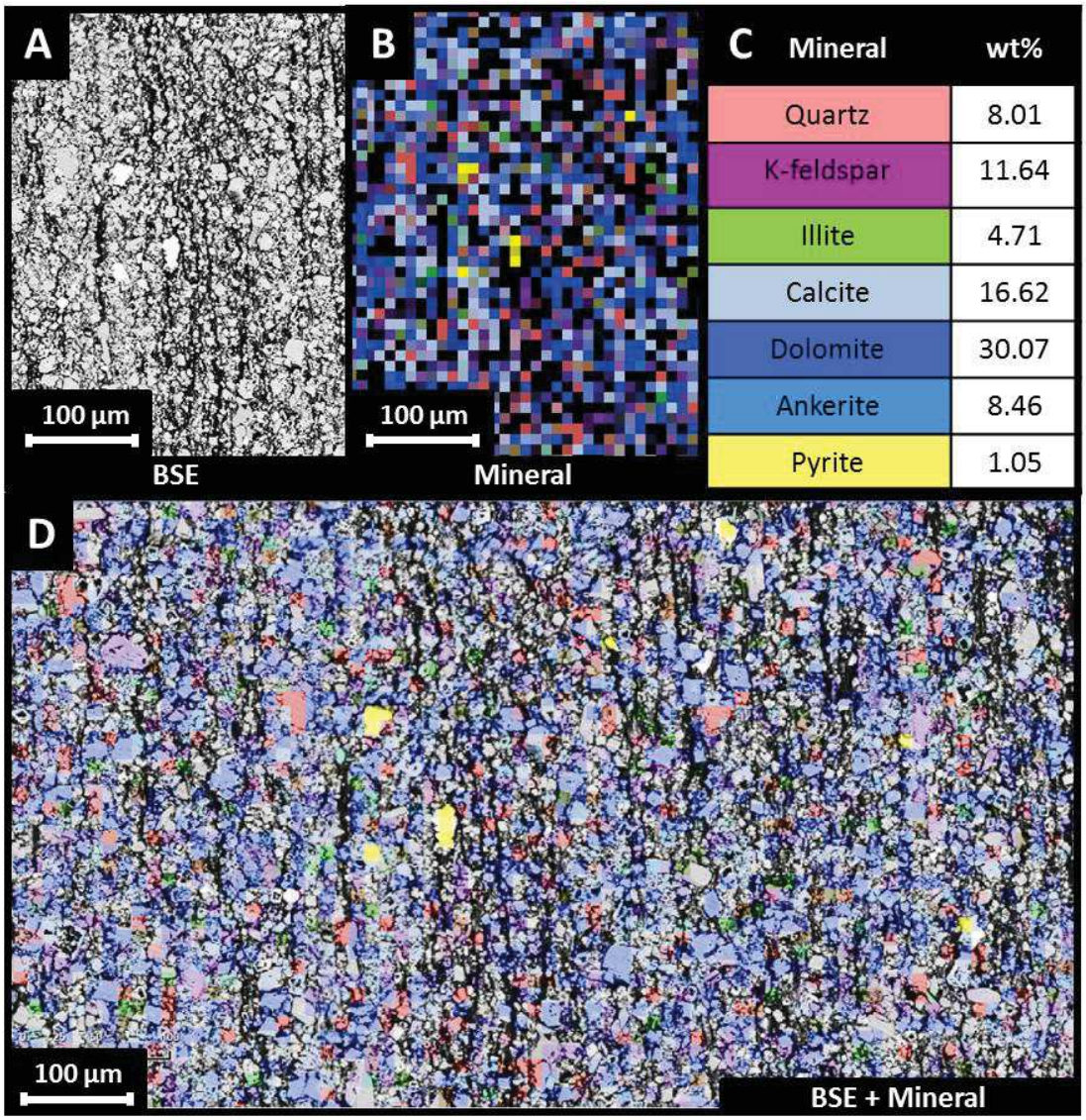

Figure 5.12 (A) Backscattered electron (BSE) greyscale mosaic image; (B) Mineral map based on EDS analysis with an X-ray spacing of 10 µm and acquisition time of 8ms per pixel with automated mineral identification performed using NanoMin software; and (C) Quantification of minerals present in the Green River (Mahogany Zone) oil shale sample indicating a highly calcareous mineral matrix. (D) An overlay of (a) and (b) showing the spatial distribution of minerals and the micro-texture of the inorganic mineral grains dispersed within organic matter (kerogen).

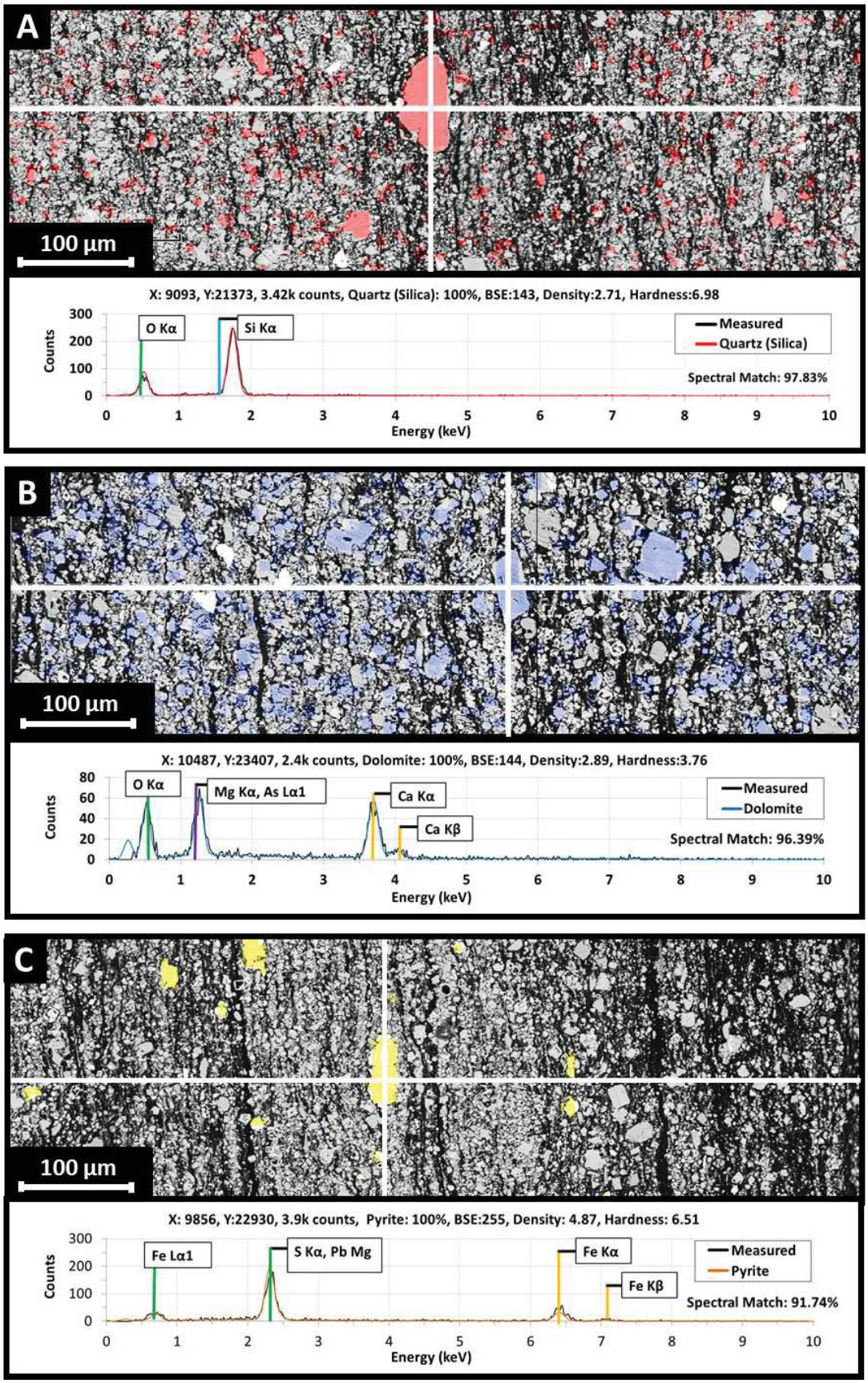

Figure 5.13 Backscattered electron (BSE) images of Green River (Mahogany Zone) with point identification of inorganic mineral grains by comparing measured X-ray spectra with a mineral spectral library: (A) Quartz (SiO_2), (B) Dolomite ($CaMg(CO_3)_2$) and (C) Pyrite (FeS_2).

To assess the impact of BSE pixel size on segmented organic, mineral and pore phases, a 50 μm (height) × 60 μm (width) region of interest (ROI) within the oil shale sample was selected consisting of a range of mineral grains, substantive organic matter and the presence of pores (Figure 5.14 A-C). BSE images were taken at pixel sizes of 500 nm, 50 nm and 10 nm. For each greyscale image, global threshold segmentation was applied to generate a three-phase segmented image constituting organic matter, minerals and pore pores (Figure 5.14 D-F). At a 500 nm pixel size, the computed organic and mineral relative quantities were 28.1% and 71.9% respectively, with no pores identified at this pixel size. At a 50 nm pixel size, the percentage of resolvable organic matter increased significantly to 40.7%, and mineral relative amounts decreased to 58.8%. Both organic-hosted and mineral-hosted pores were successfully resolved at a 50 nm pixel size with an ROI porosity of 0.5%. At a 10 nm pixel size, the percentage of resolvable organic, mineral and pore phases was computed at 42.2%, 57.1% and 0.7% respectively, indicating a very small change from the relative quantities computed at 50 nm.

Figure 5.15 and Figure 5.16 show BSE mosaic images following pyrolysis of the Green River (Mahogany Zone) oil shale at 500°C. The development of micro-fracture networks are well defined and occur parallel to the oil shale bedding plane. At high resolutions, an intricate network of well-connected nano-pores and fractures surrounding the inorganic mineral grains is observed. Both nano- and micro-fractures fractures constitute the void spaces generated by the thermal breakdown of the kerogen macromolecular structure that resulted in local overpressure build-up during kerogen maturation and subsequently the preferential propagation of fractures along the kerogen-rich laminations allowing the generated hydrocarbon fluids to escape. In addition to the pore space, at the micron-scale regions are observed where the organic matter had partially decomposed during pyrolysis as well as regions where kerogen still remains unconverted. This observation illustrates that not all the solid kerogen thermally transforms to fluid hydrocarbons at the same rate or to the same extent which accentuates the complexity in kerogen pyrolysis kinetics.

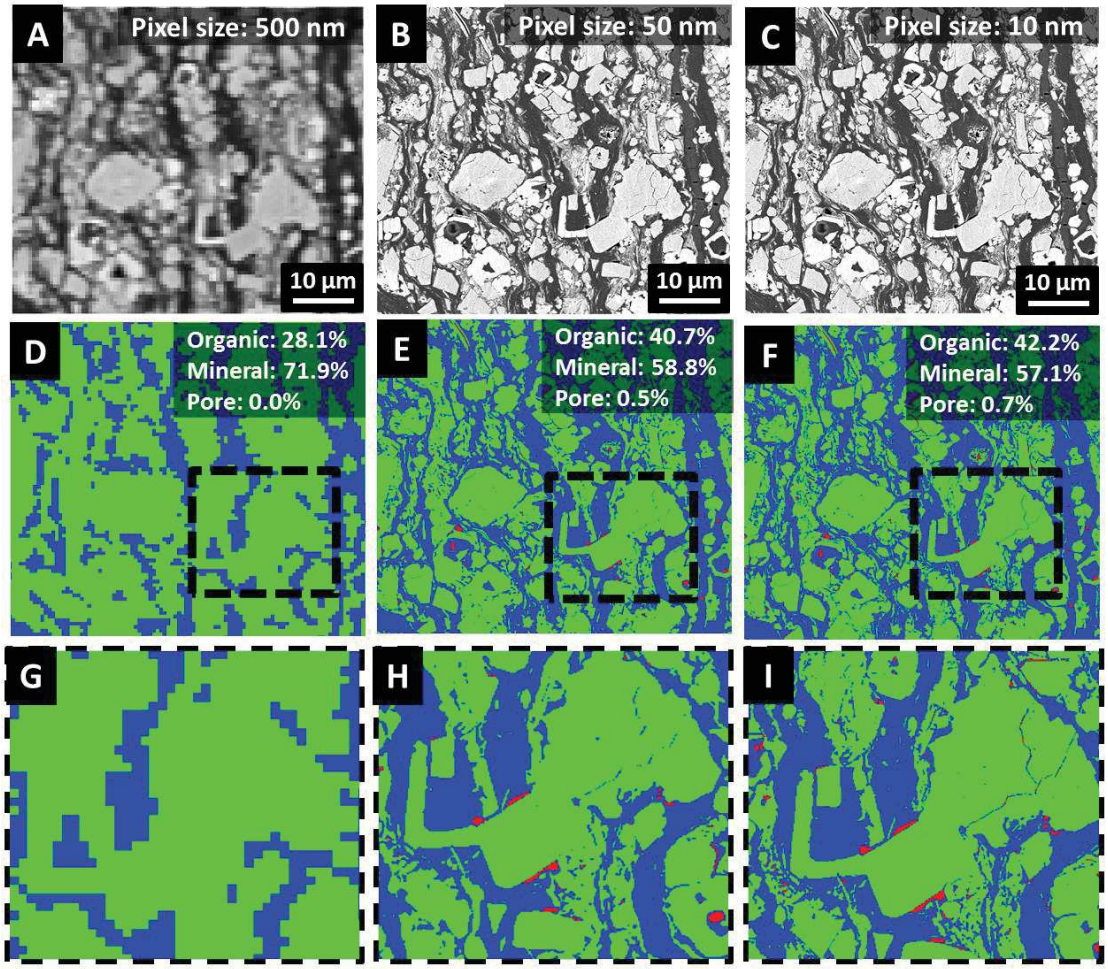

Figure 5.14 (A)-(C) Backscattered electron (BSE) images of the Green River (Mahogany Zone) oil shale of same region of interest with decreasing pixel size: (A) 500 nm, (B) 50 nm and (C) 10 nm. (D)-(F) Three-phase segmented images with organic matter shown in blue, mineral phases in green and pores in red, (G)–(I) Zoom-in within segmented images with finer pixel size revealing more well-defined boundaries between organic, mineral and pore phases.

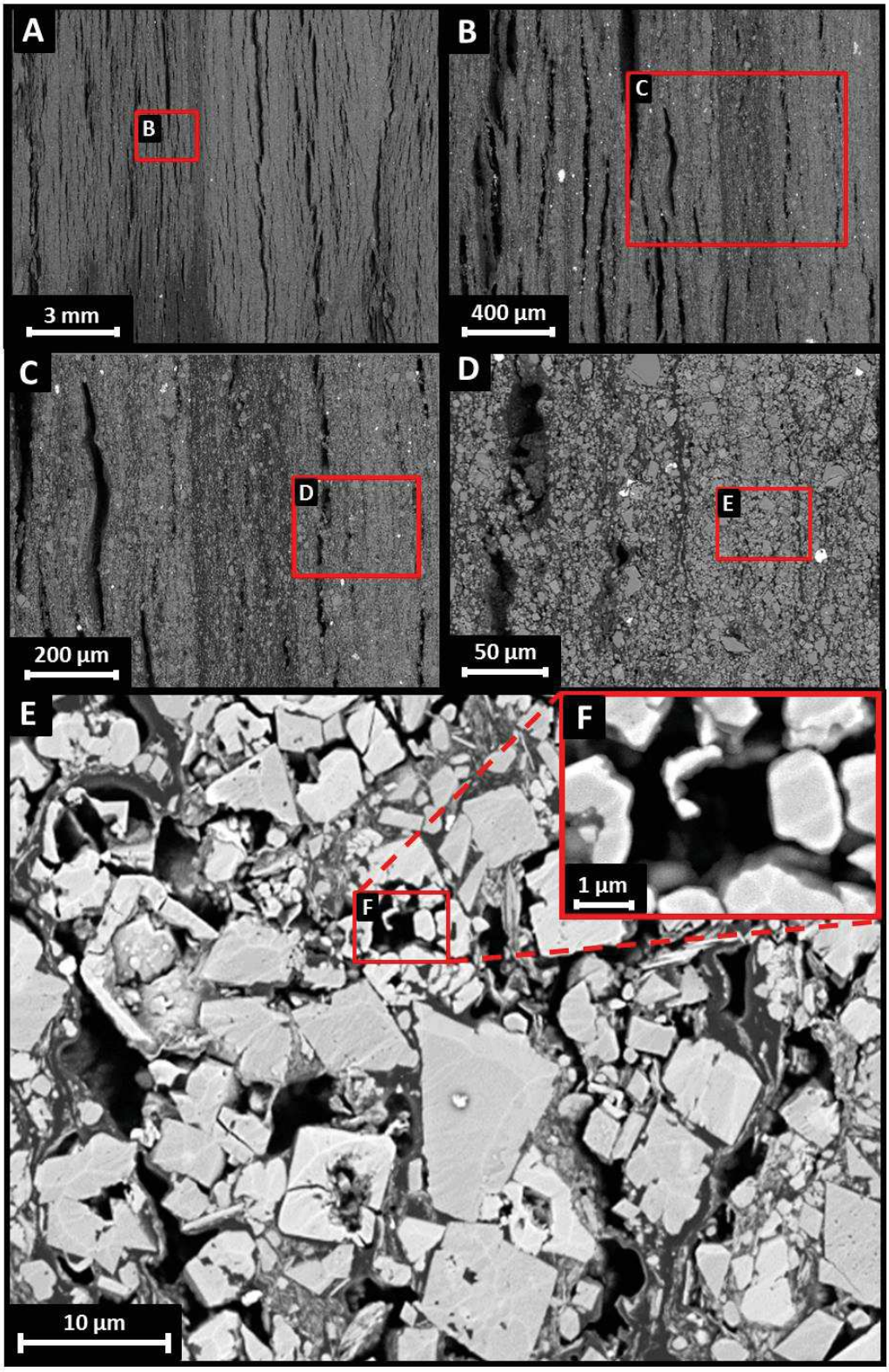

Figure 5.15 (A) Stitched BSE image of 18 mm × 14 mm Green River (Mahogany zone) oil shale pyrolysed at 500°C. The large area image has been created by stitching 19 × 16 tiles, resulting in an image of 35,417 × 29,216 pixels with a pixel size of 500 nm captured at 15 keV. (B) - (D) From the full overview of the stitched image of a sample, zooming exposes the high resolution details without losing correlation and allows regions of interest to be located for further investigation. Fractures formed during oil shale pyrolysis, which essentially constitute the loss of organic matter, are observed from the μm-to- mm scales. (E) - (F) Higher resolution BSE images acquired at 5 keV with a 10 nm pixel size.

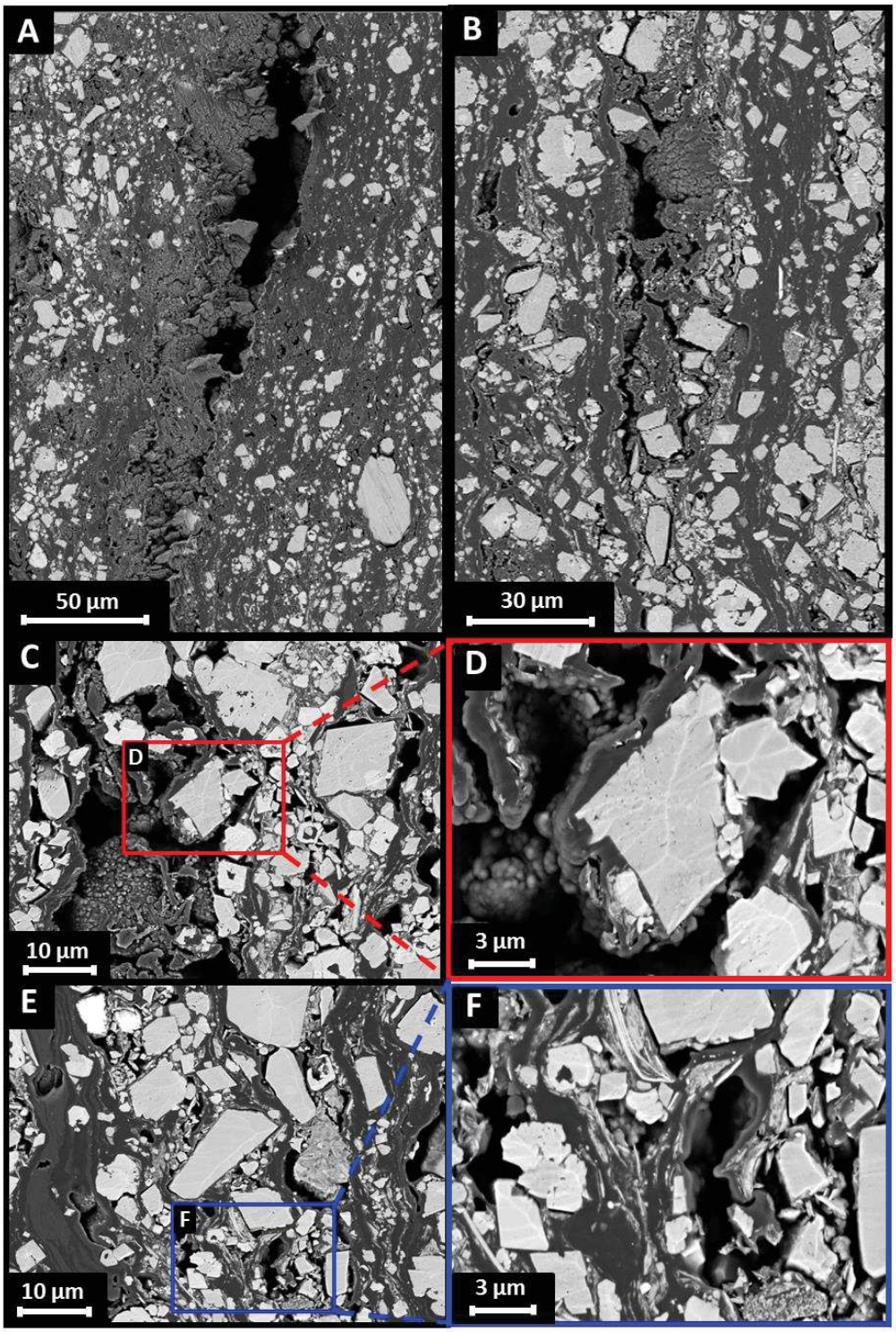

Figure 5.16 BSE images of the Green River (Mahogany Zone) oil shale pyrolysed at 500°C. (A) An open micro-fracture of approximately 200 µm in length as the solid kerogen is converted to fluid hydrocarbons, image captured at 5 keV with a 30 nm pixel size. (B) A fracture of approximately 80 µm in length with connecting smaller fractures as the organic matter thermally decomposes, BSE image captured at 5 keV with a 20 nm pixel size. (C) - (D) Partially decomposed organic matter, with solid kerogen remaining attached to inorganic mineral grains, BSE image captured at 5 keV with a 10 nm pixel size. (E) - (F) Images showing the formation of pores within the oil shale microstructure from tens of nanometres to a few micrometres in size and varying in shape from nearly circular to irregular polygon pores hosted within the organic matter and between the organic material and inorganic mineral grains, BSE image captured at 5 keV with a 10 nm pixel size.

5.4 3-D Nano-scale imaging using Focused Ion-Beam Scanning Electron Microscopy (FIB-SEM)

The FEI Helios NanoLab 660 DualBeam system was used to obtain 3-D data sets for nano- to micron scale structural characterization of the Green River (Mahogany zone) oil shale samples (un-pyrolysed and pyrolysed). This technology combines automated sequential FIB (Focused Ion Beam) milling and SEM (Scanning Electron Microscope) imaging to create a series of 2-D images (Figure 5.17 A), which in turn leads to 3-D volume reconstructions. Further details on the principles of FIB-SEM are provided in Section 3.6. A focused beam of gallium ions (Ga^+) operating at 30 keV and 2.5 nA beam current milled regions of interest in the oil shale samples by sputtering away material via momentum transfer causing the ejection of target atoms and the exposure of a fresh oil shale surface. The SEM imaged the newly milled oil shale cross-sectional surface at a 2 keV accelerating voltage and a 0.4 nA beam current under BSE mode to achieve excellent contrast between inorganic minerals, organic matter and the pore space. The ion beam and electron beam were set a 52° angle to each other (Figure 5.17 B), resulting in parallel cuts and 600 evenly spaced slices. A fiducial reference mark was placed on the oil shale surface next to the region of interest for alignment and registration of the individual slices (Figure 5.17 C). Prior to milling a 4 μm strip of platinum was deposited over the site of interest to protect from excessive beam damage and minimize curtaining artefacts (Ishitani et al., 2004; Wirth, 2009). Auto Slice and View G3 software (FEI) was used for serial sectioning of the oil shale samples creating 2048 × 1155 × 600 voxel volumes with a voxel size of 14.63 × 18.32 × 10.0 nm for both sample 1(un-pyrolysed) and sample 2 (pyrolysed) (Figure 5.18).

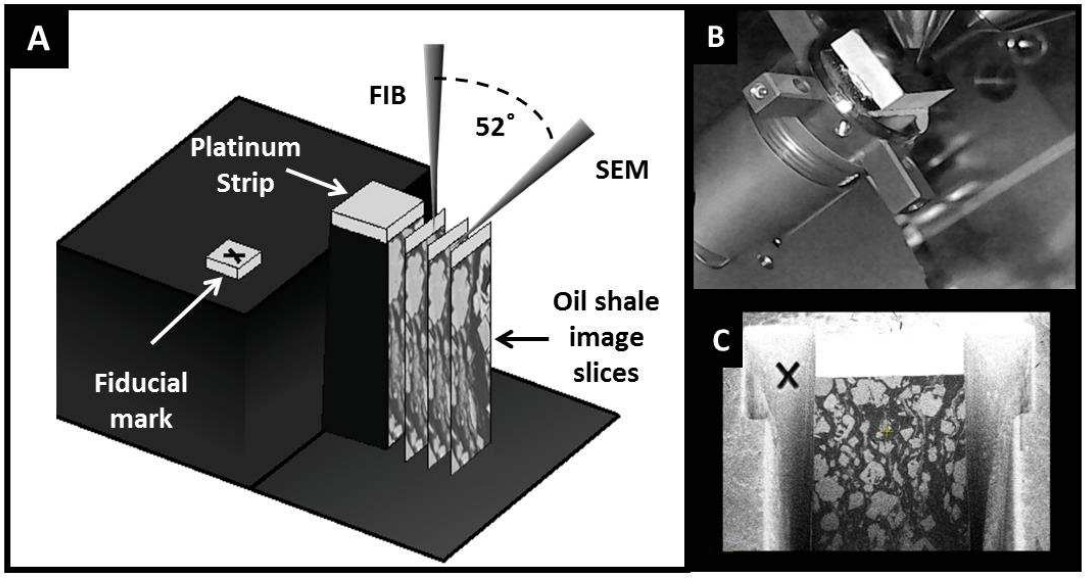

Figure 5.17 (A) Schematic diagram of the sectioning and imaging procedure in a focused ion beam–scanning electron microscopy (FIB-SEM) system, (B) FIB-SEM configuration, and (C) FIB-SEM site preparation: first, a trench is milled around the volume that will be analyzed; then, FIB milling and SEM imaging are used sequentially to generate a 3-D data set of parallel, high-resolution images. Fiducial markers are placed as reference features to allow for image alignment/registration.

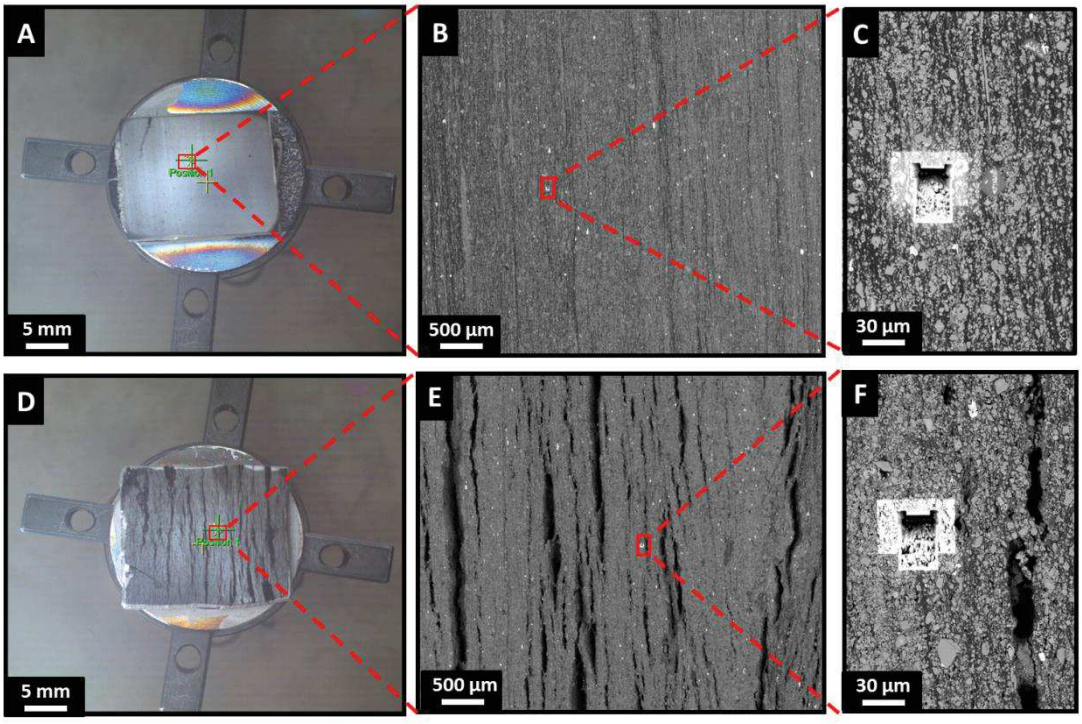

Figure 5.18 FIB-SEM locations selected for sample 1 (un-pyrolysed, top) and sample 2 (pyrolysed, bottom) of the Green River (Mahogany Zone) oil shale. (A) Immature oil shale in the SEM sample chamber. (B) BSE mosaic image revealing a moderately organic-rich region. (C) An enlarged section of the FIB-SEM image with trenches milled by FIB around the region of interest (ROI) prior to serial sectioning and imaging of the ROI using the FIB and SEM. (D) Pyrolysed oil shale sample (500°C). (E) BSE image revealing a network of parallel fractures. (F) FIB-SEM region precisely selected to capture developed pores/fractures, the solid phase of minerals and remaining organic material.

Each FIB-SEM data set was then imported to PerGeos software (FEI, Hillsboro, OR, USA) for image processing. A major challenge in processing FIB-SEM shale image data is the presence of pore-back or shine-through artefacts arising when structures lying below the milling plane are visible through pores with electrons going behind an imaging plane and hitting the back-side of the pore. The signal reflected from the pore-back leads to difficulties in image segmentation where the pore space should be separated from the solid material. In a typical shale sample, the greyscale of the matrix is similar to the greyscale of the pore backs. The specific FIB-SEM pore-back problem, caused by the electrons reflected, depends on a number of parameters such as the size, the depth, and the orientation of the pore. The traditional approach of global thresholding breaks down, particularly in regions of high porosity where more electrons can be detected from deeper regions in the sample leading to higher greyscale values in the pore space. In this study, the data sets were pre-processed using a Fast Fourier transform (FFT) and a non-local means edge preserving smoothing filter (Buades et al., 2008, 2005). Following this, a three-phase segmentation method was applied to separate organic matter, minerals and the pore space (including pore-back artefacts), relying on 3-D gradient and marker-based watershed transforms (Figure 5.19).

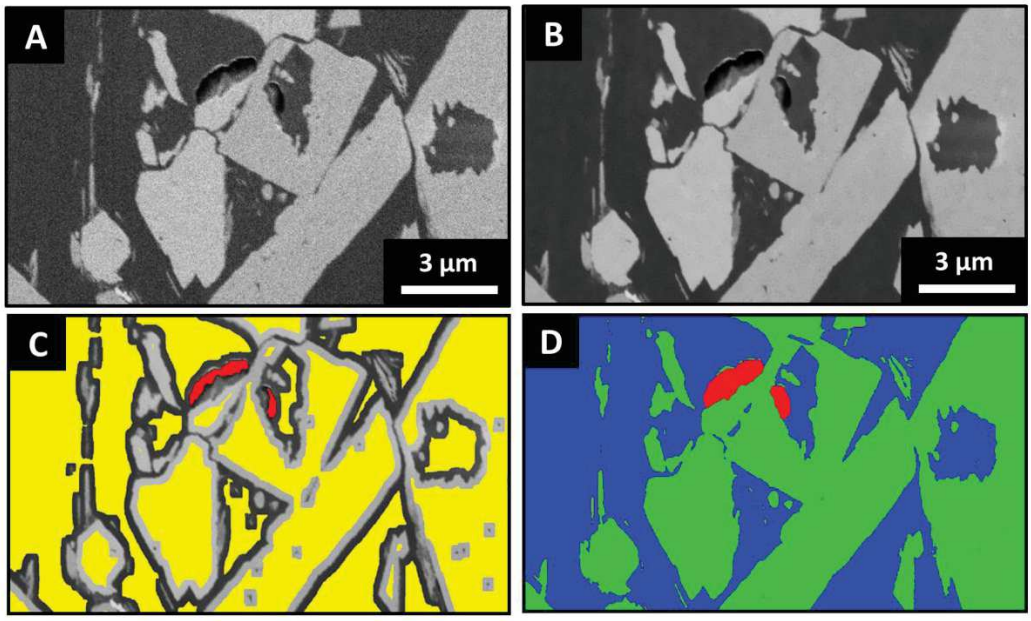

Figure 5.19 (A) Raw greyscale image acquired using FIB-SEM. (B) The filtered image processed using a non-local means edge preserving smoothing filter. (C) Placement of markers with pore phase (including pore backs) marked in red and solid phase (organic + mineral) marked in yellow followed by the application of 2-D watershed segmentation. (D) Pore phase (red) is locked in place and a 2-D watershed segmentation is applied to separate the organic phase (blue) from the mineral phase (green).

From a stack of 2-D images, the kerogen, minerals and pore phases were serially reconstructed to render 3-D FIB-SEM volumes from sample 1 (un-pyrolysed) and sample 2 (pyrolysed) (Figure 5.20 A and Figure 5.21 A respectively). Figure 5.20 B represents the 3-D segmented visualization for the immature Green River (Mahogany Zone) oil shale (sample 1) which reveals that the organic matter network is complex and that connectivity occurs across the 30 μm × 20 μm × 6 μm volume. The pore space is isolated with pores ranging in length scale from a several nanometres to a few micrometres and in shape from spherical to elongated geometries. The volume contributions of kerogen, minerals and pores for the reconstructed raw oil shale volume were 51.8%, 47.7% and 0.5% respectively (Figure 5.20 C-E). Figure 5.21 B represents the 3-D segmented visualization for the Green River (Mahogany Zone) oil shale following pyrolysis at 500°C (sample 2) revealing a dominant pore space with connecting micro-fractures parallel to the kerogen laminations but limited connection between layers. The FIB-SEM volume also reveals a residual connected kerogen network following pyrolysis. The volume contributions of kerogen, minerals and pores for the reconstructed raw oil shale volume were 39.6%, 42.2% and 18.2% respectively (Figure 5.21 C-E).

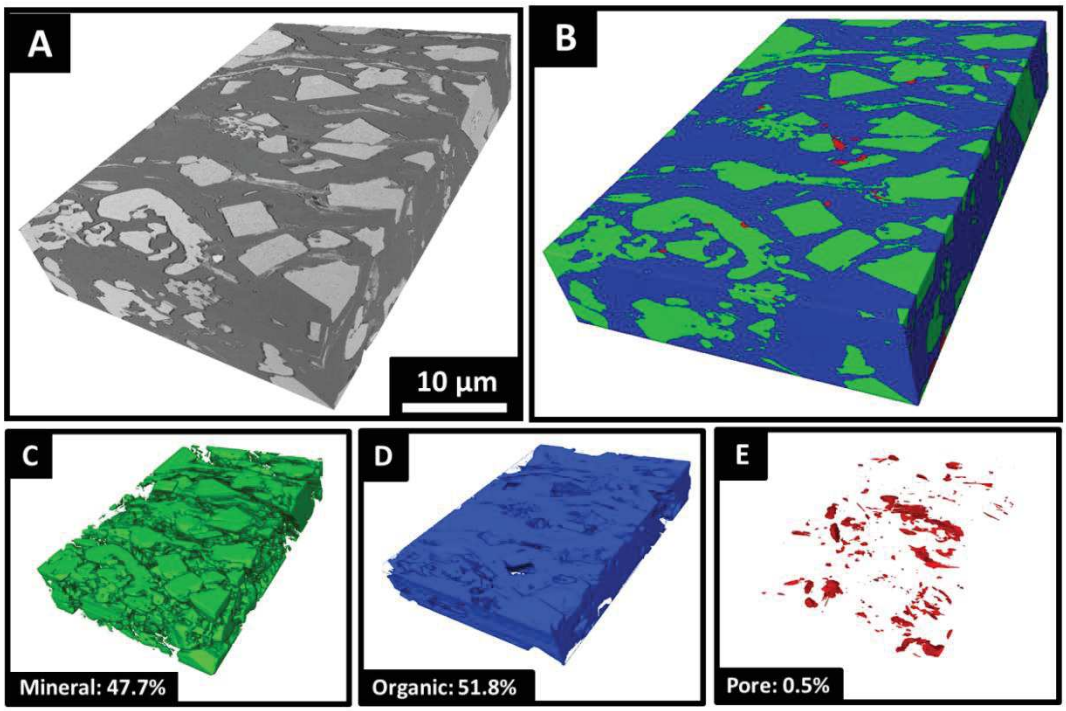

Figure 5.20 (A) 3-D reconstructed greyscale FIB-SEM volume of the raw Green River (Mahogany Zone) oil shale, sample 1. (B) Three-phase segmentation of minerals (green), organic matter (blue) and pores (red). (C) Mineral grains representing 47. 7% of the FIB-SEM volume. (D) Fully connected organic matter (kerogen) representing 51.8% of the FIB-SEM volume. (E) Isolated pores from nano to micron-scales representing 0.5% of the total FIB-SEM volume.

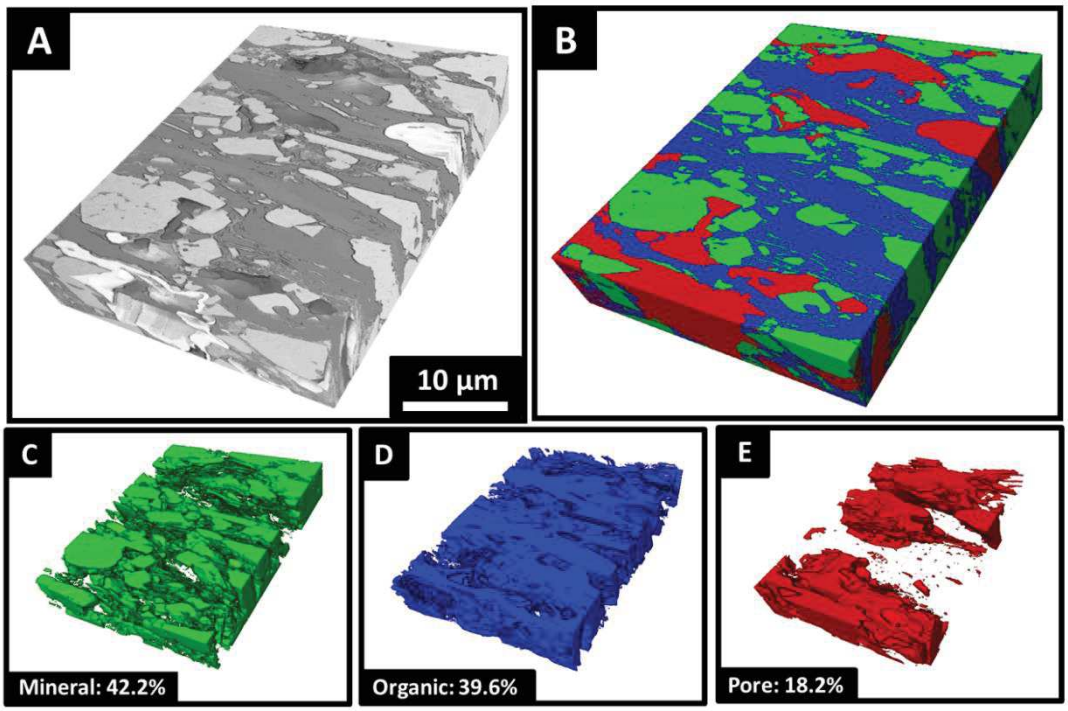

Figure 5.21 (A) 3-D reconstructed greyscale FIB-SEM volume of the Green River (Mahogany Zone) oil shale pyrolysed at 500°C, sample 2. (B) Three-phase segmentation of minerals (green), organic matter (blue) and pores (red). (C) Mineral grains representing 42.2% of the FIB-SEM volume. (D) Residual organic matter representing 39.6% of the FIB-SEM volume. (E) Pores predominantly in the form of micro-fractures along the organic-rich laminations representing 18.2% of the total FIB-SEM volume.

The number of individual pore-body sizes was computed from the FIB-SEM reconstructed volumes. Figure 5.22 shows a 3-D rendering of the connectivity of the pore space for both the un-pyrolysed and pyrolysed samples. For the un-pyrolysed sample, all the pore space appears disconnected, as indicated by the wide range of colours (Figure 5.22 A). However, for the pyrolysed sample, the pore space is well-connected laterally across the sample. The volume fraction of interconnected pores in the X plane was 28.7%, Y plane 0% and Z plane 98.9% (Figure 5.22 B).

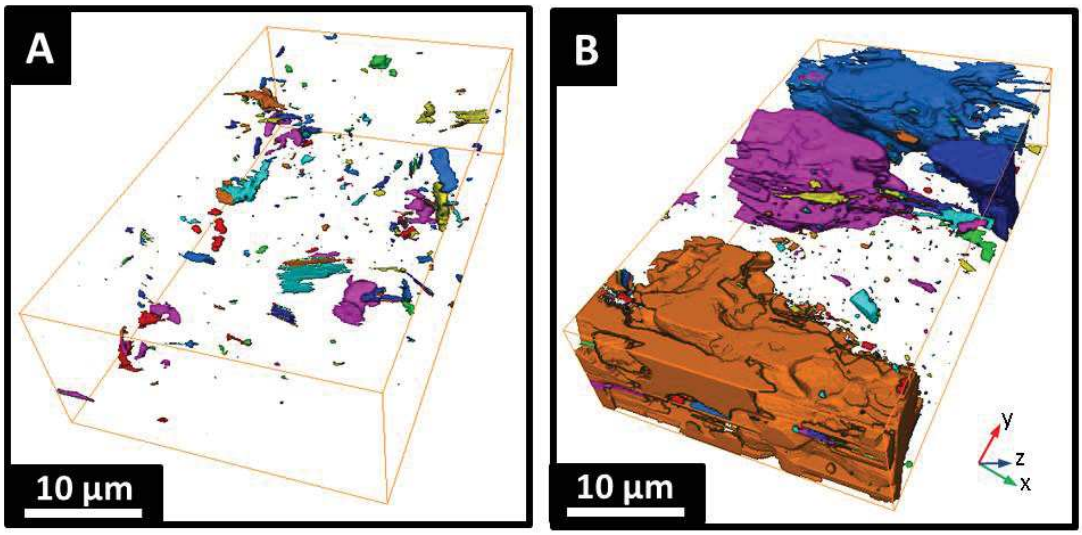

Figure 5.22 3-D FIB-SEM rendering of the pore space where the colors indicate clusters of connected pores. (A) Immature Green River (Mahogany Zone) oil shale where the pore space appears disconnected —the large range of colors indicates a poorly connected pore network. (B) Pyrolysed (500°C) Green River (Mahogany Zone) oil shale displaying a well-connected pore space in the form of micro-fractures predominantly along the organic-rich laminations. Percentage of connected pores in the X direction was 28.7%, Y direction 0% and Z direction 98.9%

Pore sizes were computed as the radii of spheres of equivalent volume for each pore-body. All the pore bodies, defined as connected void space, have been divided into different size categories each of which is represented by a mean equivalent radius. Histograms of the pore size distribution for the Green River (Mahogany Zone) oil shale for the both the un-pyrolysed and pyrolysed samples were constructed, along with the cumulative percent of the pore size distribution. For the un-pyrolysed oil shale FIB-SEM volume, the histogram indicates that pores having an equivalent radius approximately between 15 nm and 22 nm dominate the distribution (Figure 5.23 A). Although from Figure 5.23 A it is quantified that relatively smaller pores dominate in number, Figure 5.23 B shows that pores approximately ranging from

140 nm to 390 nm in equivalent radius have the greatest volumetric contribution, occupying 75.9% of the total pore volume. For the pyrolysed oil shale, the histogram in Figure 5.24 A indicates that pores having an equivalent radius of approximately between 9 nm and 18 nm dominate in number. while Figure 5.24 B reveals that pores with an approximate equivalent radius between 1.6 μm and 2.0 μm significantly dominate in the volumetric contribution taking 98.7% of the pore space within the analysed 30 μm × 20 μm × 6 μm FIB-SEM volume.

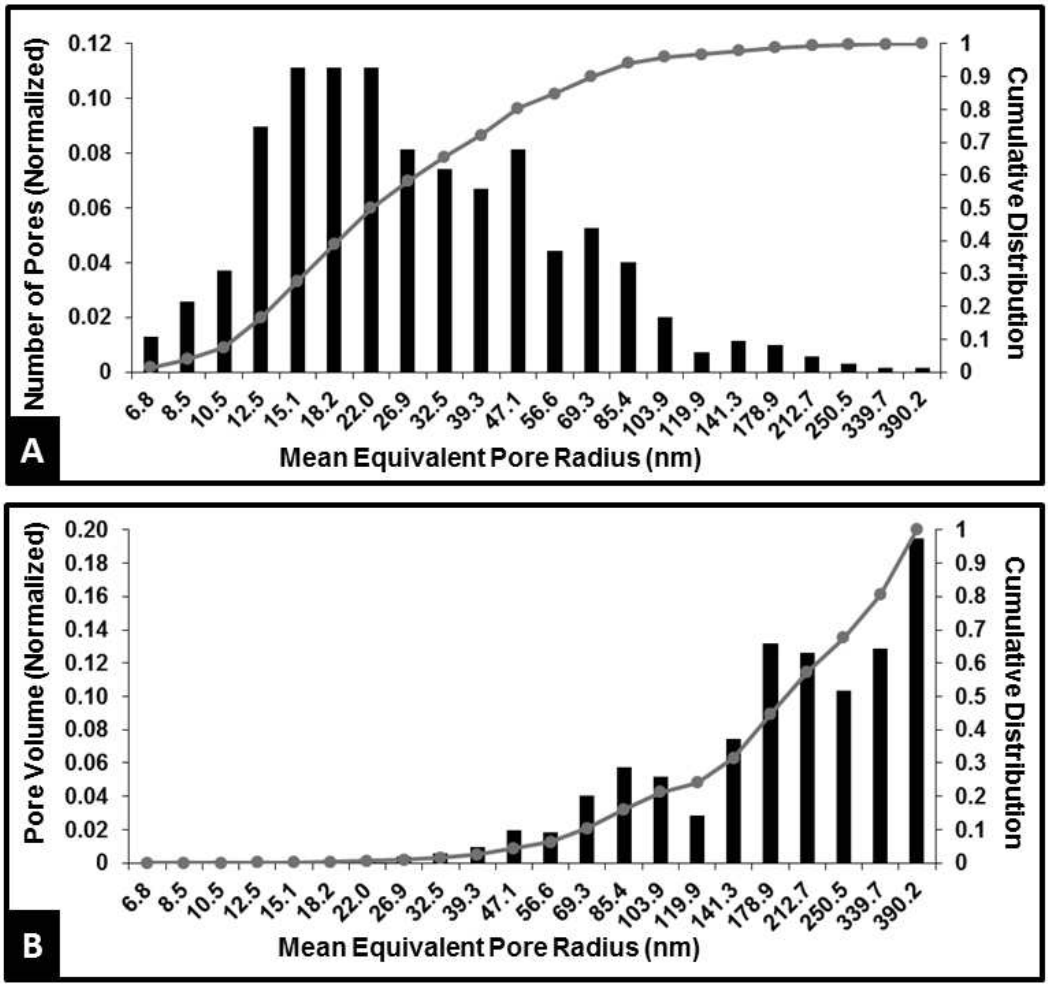

Figure 5.23 (A) Immature Green River (Mahogany Zone) Oil Shale pore size distribution showing that pores between 15 nm and 22 nm in equivalent radius dominate in number. (B) Pore volume contribution, showing that pores approximately ranging from 140 nm to 390 nm in equivalent radius have the greatest volumetric contribution occupying 75.9% of the pore volume.

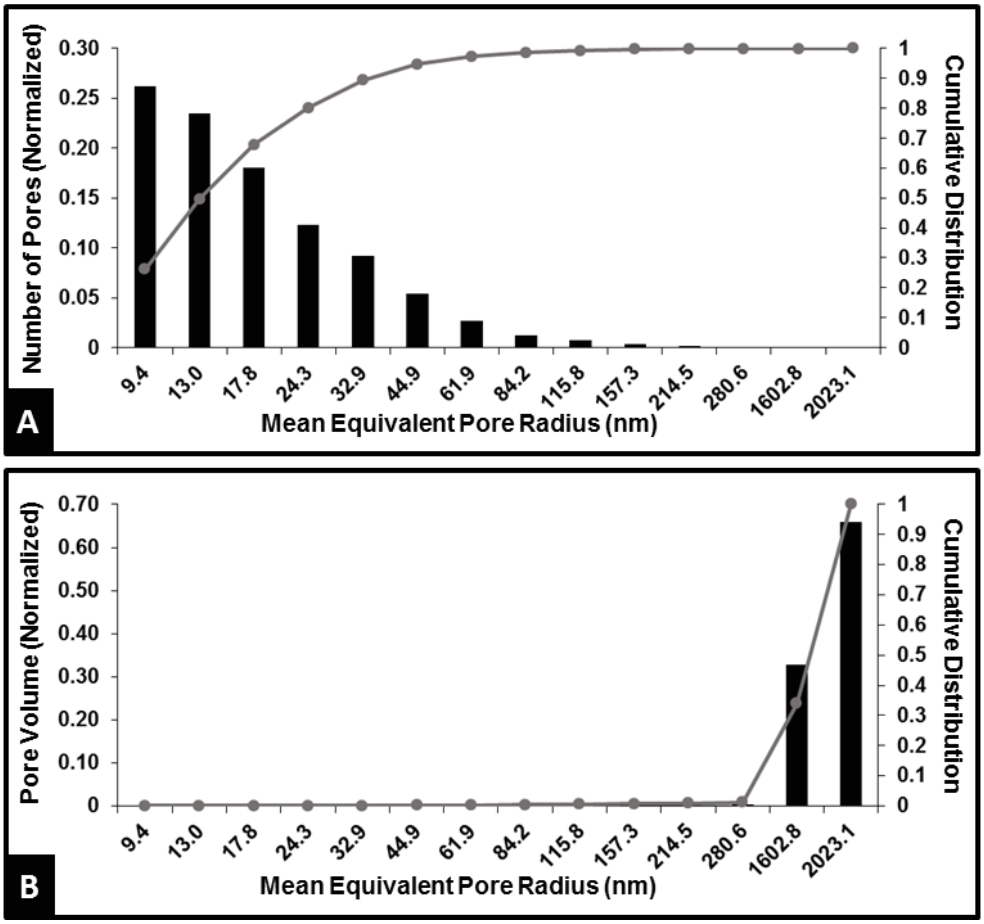

Figure 5.24 (A) Pyrolysed Green River (Mahogany Zone) Oil Shale pore size distribution showing that pores between approximately 9 nm and 18 nm in equivalent radius dominate in number. (B) Pore volume contribution, showing that pores approximately ranging from 1.6 μm and 2 μm in equivalent radius have the greatest volumetric contribution occupying 98.7% of the pore volume.

Each oil shale FIB-SEM dataset in this study represents a volume of approximately 3600 μm^3. It is important to note that the gain in resolution to detect nano-scale features comes at the expense of the volume analysed. The volumetric contribution and spatial distribution of organic matter, minerals and pores in FIB-SEM oil shale datasets represent a tiny fraction of large oil shale formations. Upscaling petrophysical values computed from FIB-SEM volumes requires an understanding of the representative elementary volume for oil shale, which can vary among different oil shale deposits. In addition, multiple oil shale sampling volumes will be required to achieve statistical significance. Moreover, by correlating FIB-SEM data sets with large-area automated SEM imaging and X-ray μCT which offers lower resolution but larger field of view imaging, a more comprehensive understanding can be acquired of both the oil shale macro- and micro fabric heterogeneity and the association of nano-scale structures within the fabric domains.

5.5 Summary

The data presented in this chapter demonstrates that combining X-ray μCT with automated ultra-high resolution SEM, MAPS Mineralogy and FIB-SEM contributed to a powerful and synergistic multi-scale and multi-dimensional workflow. This integrated imaging strategy delivers crucial petrophysical characterization of heterogeneous fabrics in oil shales revealing important microstructural and mineralogical complexities. 2-D and 3-D imaging, allows for the visualization and quantification of pores, organic matter and inorganic mineral phases over mm-μm-nm scales before and after pyrolysis.

Oil shale samples from the organic-rich Green River Formation (Mahogany Zone) - the world's largest oil shale deposit - were scanned using X-ray μCT at a 0.8 μm voxel size revealing a well-connected organic network within a heterogeneous inorganic mineral matrix. 3-D X-ray μCT scans following incremental *ex situ* oil shale pyrolysis up to 420°C captured the propagation and coalescence of micro-fractures, with the first observed fractures nucleating at 380°C and substantive volume expansion occurring at 400°C.

Automated tiling and stitching of ultra-high resolution SEM images into mosaics of gigapixel size were captured for un-pyrolysed and pyrolysed samples over 18 mm × 14 mm areas. Argon (Ar) ion milling was used to prepare ultra-flat surfaces with minimal artefacts. BSE mosaic images enabled pore-scale resolutions over the entire sample surface in one image allowing the simultaneous retrieval of microstructural fabric heterogeneity and nanometre-scale structures without losing correlation. The stitched mosaic of images allowed for the systematic exploration of fine-grained microstructures within oil shale samples from the nm to mm scales.

BSE images revealed that organic matter hosted pores, rather than mineral-hosted pores, were the dominant contributors to total porosity and were predominantly sub-μm in size with irregular polygonal geometries. Following pyrolysis, multiple fractures were observed along with regions of partially decomposed and unconverted kerogen. MAPS mineralogy indicated that the Mahogany oil shale is calcareous in composition with a complex distribution of dolomite, calcite, K-feldspar, quartz, pyrite and illitic clay platelets within the dispersed organic matter.

FIB-SEM volumes of 30 μm × 20 μm × 6 μm for un-pyrolysed and pyrolysed samples were acquired. 3-D gradient and marker-based transforms provided successful three-phase segmentation to separate organic matter, minerals and the pore space (including pore-back artefacts). The results revealed unconnected pores occupying 0.5% of the analysed volume, with pores between 15 nm and 22 nm in equivalent radius dominating in number. The pyrolysed oil shale showed well-connected pores across the volume with a total sample porosity of 18.2%. Pores with an equivalent radius between 1.6 μm and 2.0 μm made up the bulk of the pore volume in the pyrolysed sample.

Correlating FIB-SEM data sets with large-area automated SEM imaging and X-ray μCT provides a comprehensive framework to capture oil shale micro-fabric heterogeneity and the association of nano-scale structures within the fabric domains. Multiple 2-D images are needed to qualitatively and quantitatively characterise pores and fine clay minerals at the nano-scale. The grain sizes, identification and distribution of inorganic minerals can be achieved by combining sub-μm BSE imaging with MAPS mineralogy. Several 3-D image analyses are necessary to substantiate the extent of the organic matter network and pore-space connectivity. Integrating 2-D and 3-D rock fabric analysis provided in this chapter and in Chapter 4 along with 4-D synchrotron-based imaging detailed in Chapter 6, provides a promising pathway towards understanding, predicting and modelling hydrocarbon transport and production during oil shale pyrolysis.

Chapter 6

Dynamic Imaging of Oil Shale Pyrolysis using Synchrotron X-ray Micro-Tomography

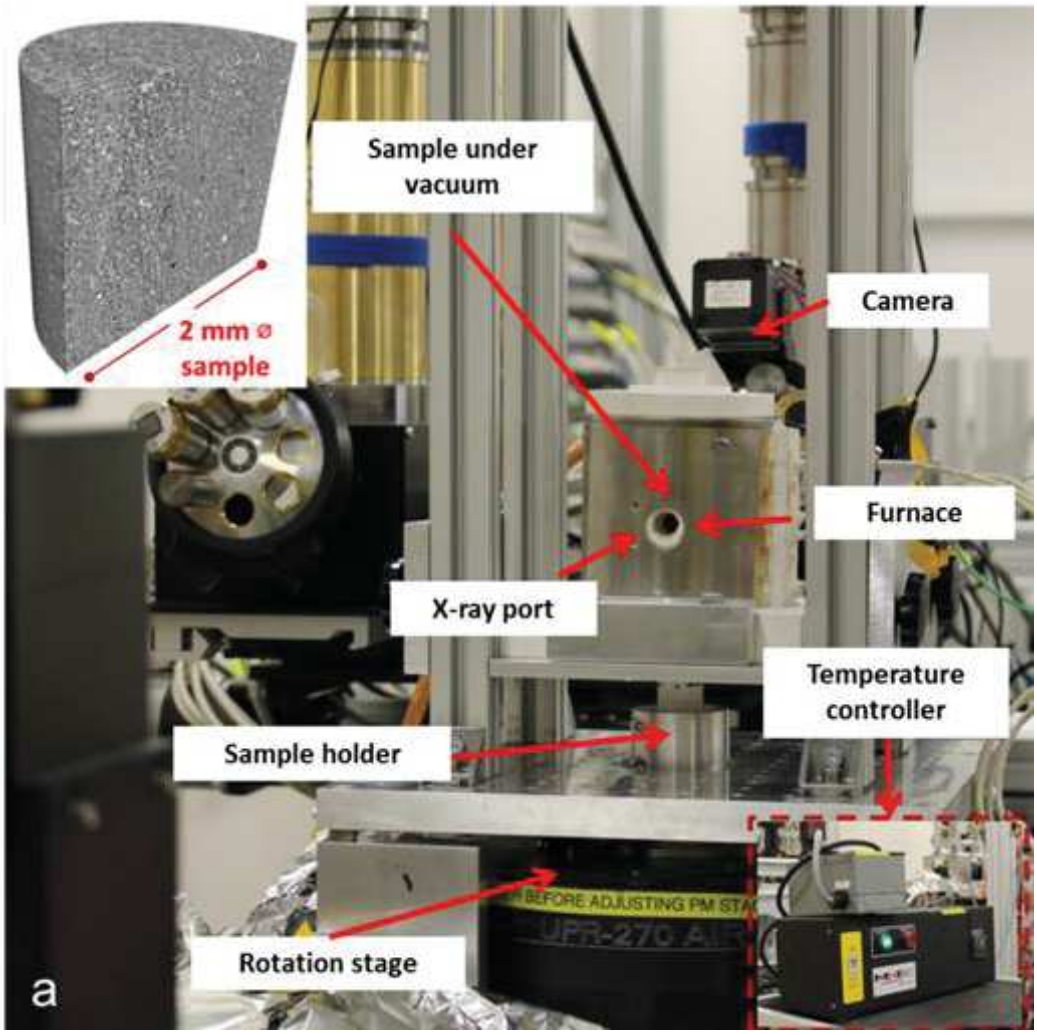

Apparatus used at Diamond Light Source (DLS) Beamline I13-2

Publication:

Saif T., Lin, Q., Singh, K., Bijeljic, B. and Blunt, M.J. (2016). Dynamic imaging of oil shale pyrolysis using Synchrotron X-ray micro-tomography. *Geophysical Research Letters*, 43(13), 6799-6807

6.1 Introduction

Previous work in Chapters 4 and 5 provided valuable insight into the microstructural changes of oil shale before and after pyrolysis (static imaging). In this chapter, earlier work is extended by directly visualizing the temporal evolution of the pore space and micro-fracture networks during pyrolysis using synchrotron X-ray micro-tomography (dynamic imaging). Immature Green River (Mahogany Zone) shale samples were thermally matured under vacuum conditions at temperatures up to 500°C while being periodically imaged with a 2 μm voxel size. The structural transformation of both organic-rich and organic-lean layers within the shale was quantified. The images reveal a dramatic change in porosity accompanying pyrolysis between 390-400°C with the formation of micron-scale heterogeneous pores. With a further increase in temperature, the pores steadily expand resulting in connected micro-fracture networks that predominantly develop along the kerogen-rich laminations.

X-ray micro-computed tomography (μCT) has provided direct visualization and quantitative assessment of geological samples (Andrä et al., 2013; Andrew et al., 2013; Berg et al., 2013; Cnudde and Boone, 2013; Dann et al., 2010; Ketcham and Carlson, 2001; Lin et al., 2015; Mahabadi et al., 2012; Menke et al., 2015; Singh et al., 2016; Wildenschild and Sheppard, 2013), including oil shale rocks (Coshell et al., 1994; Kang et al., 2011; Tiwari et al., 2013). The advantage of μCT is that it allows non-destructive access to the internal structure of objects, providing qualitative and quantitative data about the structure and morphology of 3-D samples and features (pores, fractures, grains etc.). To capture dynamic processes, recent work has focused on X-ray imaging of geological materials using synchrotron X-ray micro-tomography (Andrew et al., 2015; Berg et al., 2014; Fusseis et al., 2014; Madonna et al., 2013; Menke et al., 2016; Panahi et al., 2014). This can be considered as four-dimensional (4-D) tomography (three spatial coordinates plus time evolution), where 3-D tomograms are recorded over a short period of time.

Although valuable, previous work in Chapters 4 and 5 is limited to the extent that they analyse samples before and after an experiment, providing an incomplete understanding of a spatially and temporally dynamic process. To capture this time dependence, fast scanning times, high resolution, at high temperatures and anaerobic

conditions are required. To meet all of these challenges is currently experimentally difficult using lab-based μCT systems. In this chapter, results are presented based on a novel experimental technique using synchrotron imaging to dynamically visualize and quantify the 3-D pore network structure and connectivity for the pyrolysis.

6.2 Operating Parameters

The oil shale sample was obtained from an outcrop of the organic-rich Mahogany zone of the Green River Shale Formation (Uinta Basin, Utah) (further detail on sample selection is provided in Section 3.2). In this study, TGA of the oil shale sample was conducted using a Perkin-Elmer Pyris 1 instrument (Perkin Elmer, USA) to establish the mass loss profile allowing for comparison with segmented pore volumes from image analysis. A 100 g sample of the oil shale rock was crushed and milled, and 20 mg of this powdered sample was heated to 850°C at a heating rate of 10°C/min using nitrogen as the purge gas.

A 2.5 mm diameter by 10 mm length core was selected from the same oil shale rock which contained organic rich and lean laminations tightly bound in an inorganic mineral-rich matrix. A custom built furnace was used to heat the sample during the experiment. The cylindrical furnace consisted of two viewports on opposite sides to allow the X-ray beam to directly pass through. The sample was loaded into a borosilicate glass tube and placed under vacuum pressure at 0.1 kPa absolute. A thermocouple measured sample temperature and a PID controller regulated the temperature to ±1°C. A detailed schematic of the experimental apparatus is shown in Figure 6.2.

The experiment was performed at the Diamond Light Source I13-2 beamline with a polychromatic beam energy that ranges from 8 to 30 KeV with a maximum photon flux of 4 x 10^9 Ph/s. The low energy X-rays were filtered by passing the beam through 2 mm Al and 0.1 mm Au filters. A 250 μm-thick $CdWO_4$ scintillator with a 4× objective lens and a PCO EDGE 5.5 camera were used.

The 3-D scans had an exposure time of 80 ms, capturing 2001 projections as the sample was rotated 180° around an axis perpendicular to the quasi-parallel incident

polychromatic X-ray beam. The total acquisition time was 160 seconds per scan. Figure 6.3 illustrates the experimental temperature with each point indicating a tomography scan at the centre of the core with a 2 mm × 2 mm field of view. The sample was heated from 20°C to 500°C with the temperature held constant at key pyrolysis stages where scans were recorded.

Each reconstructed image had $1{,}000^3$ voxels with a voxel size of 2 μm. A non-local means edge preserving filter [Buades et al., 2005; Buades et al., 2008] was applied to reduce noise (Figure 6.4 A-D). The pore space was segmented (Figure 6.4 E-F) using Otsu's algorithm [Otsu, 1979] which maximizes the between-class variance of voxel intensity. For this dataset, the algorithm provided consistent segmentation to separate the pore space from the rest of the solid phase. All image processing was conducted using the Avizo 9.0 program (FEI, Visualization Sciences Group) and MATLAB (MathWorks).

6.3 Pore Space Segmentation

Image thresholding is often a necessary step during image processing with the aim of classifying an image ensemble into two or more object images so that features can be extracted and analysed. In this study, Otsu's (Otsu 1979) thresholding method was used where the between-class variance (BCV) is defined, and the grey level at the BCV maximum determines the optimal threshold. It is an attractive method due to its simplicity in computation for bilevel thresholding. For this dataset, Otsu's method is applicable as upon pyrolysis the pore space in the oil shale sample can be separated from the rest of the solid phase.

The pore-space segmentation results by Otsu's thresholding were compared with the watershed segmentation module in the Avizo 9.0 program, with the results indicating observing less than 2% difference in the segmented pore volume between the two methods. Moreover, the segmentation algorithm does not influence the trend in porosity with increasing pyrolysis temperature. Further details on image segmentation is provided in Section 3.7.3.2.

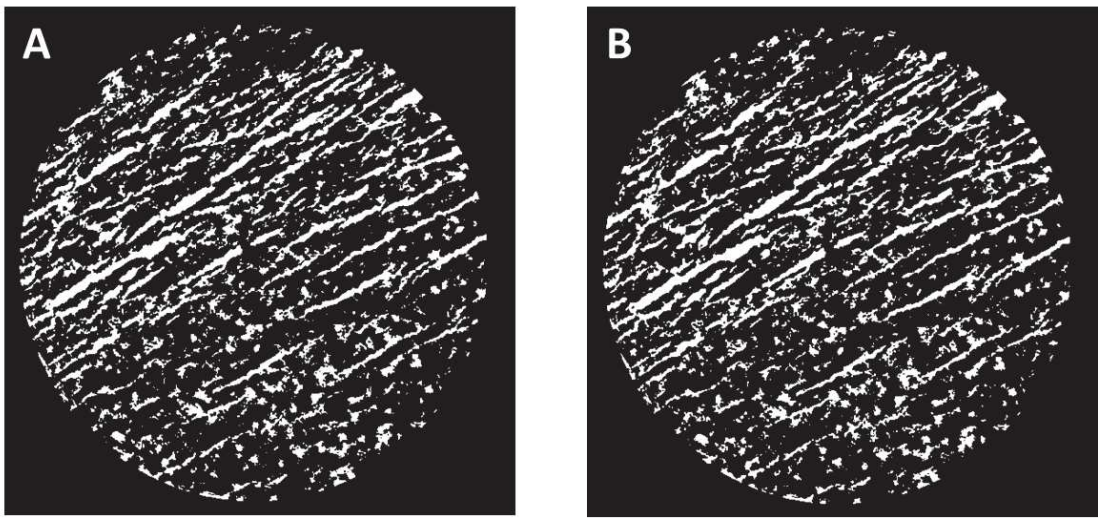

Figure 6.1 A comparison of segmentation results between Otsu's thresholding method and watershed segmentation. The results indicate a difference in segmented pore volume of less than 2%.

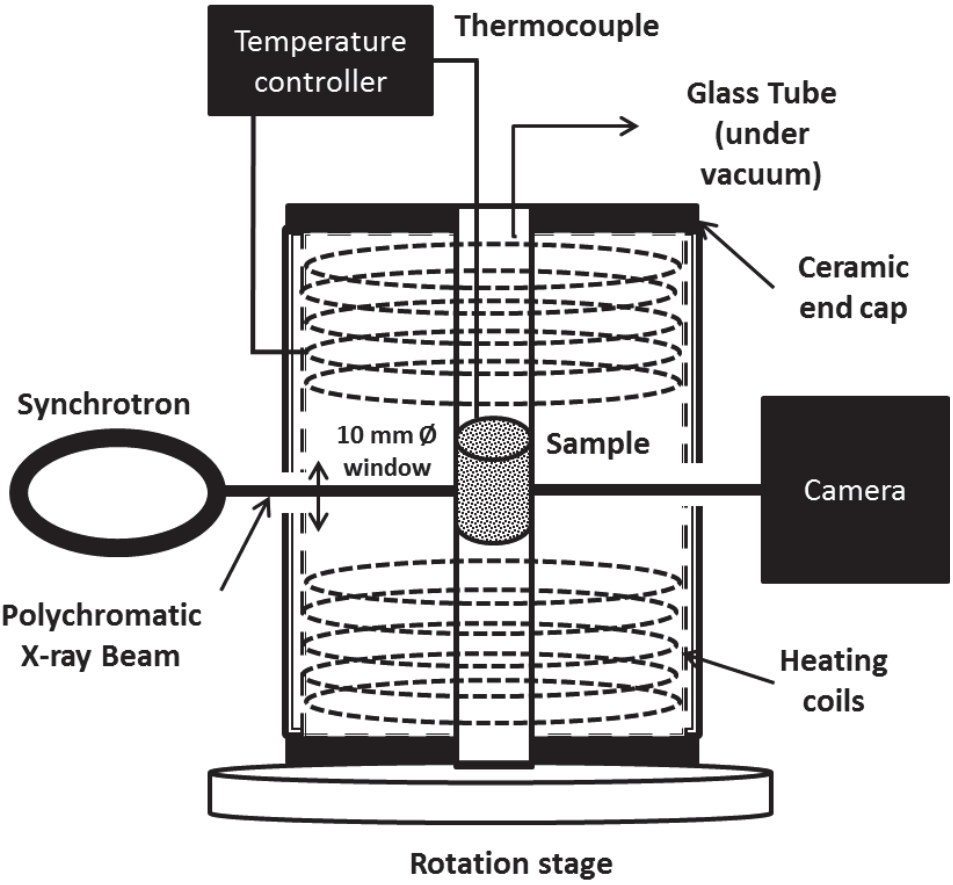

Figure 6.2 Schematic of experimental apparatus used at Diamond Light Source (DLS).

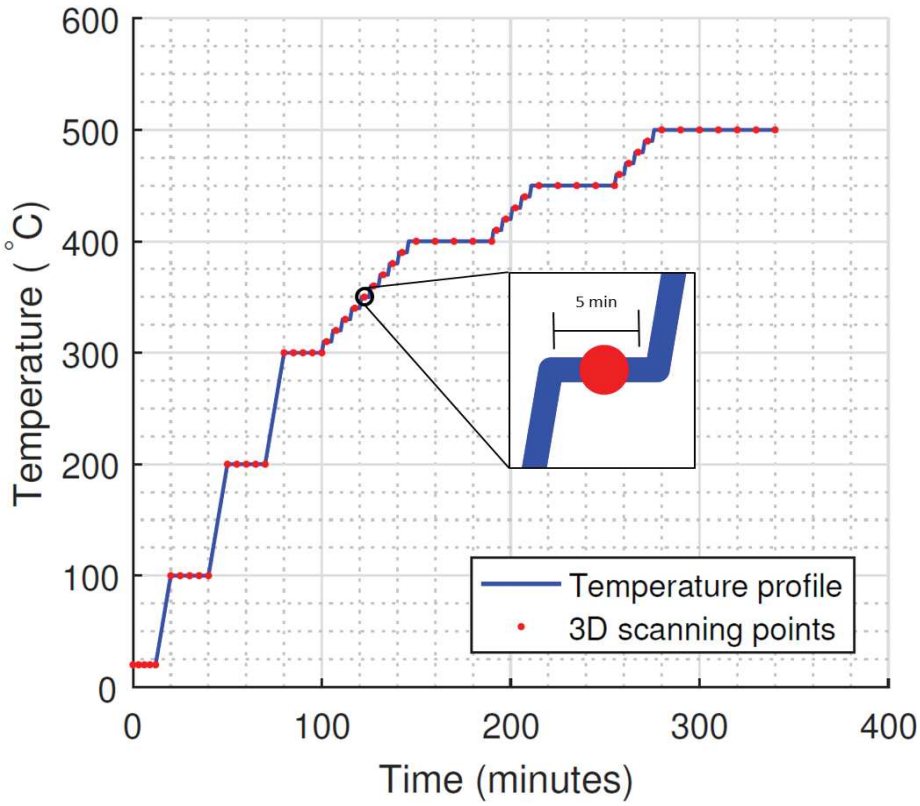

Figure 6.3 Temperature profile used in the experiment, with each point (red) representing an acquisition of a 3-D tomogram. In total 52 scans were recorded.

6.4 Pore Structure Evolution

Figure 6.4 A-D show 2-D cross-sectional slices of 3-D images of the Green River (Mahogany Zone) oil shale sample, with the greyscale values for each pixel corresponding to X-ray attenuation, which varies as a function of density and atomic number. In Figure 6.4A, the less dense organic-rich material is shown as the darker coloured regions, while the denser mineral-rich matrix appears lighter.

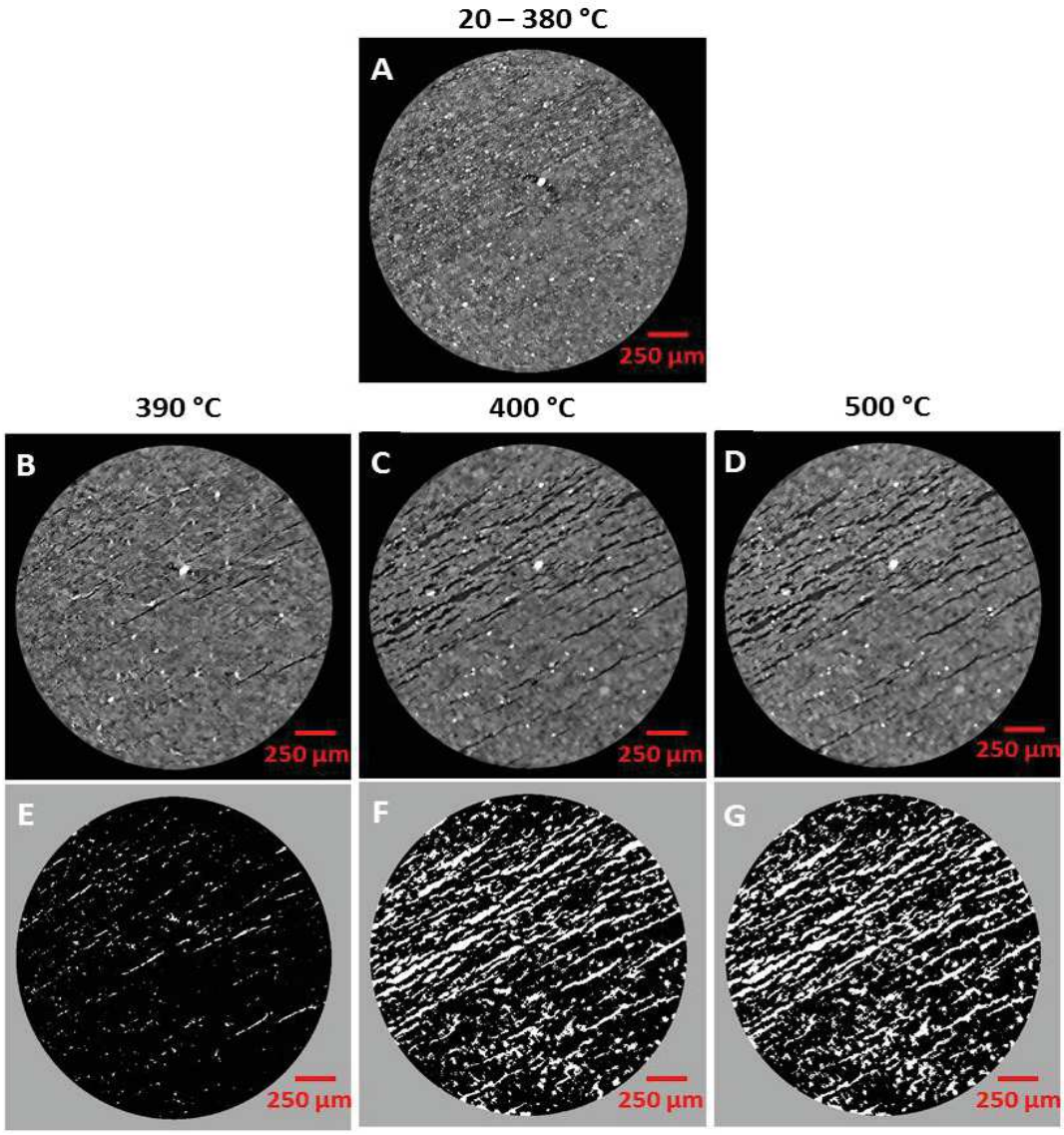

Figure 6.4 (A) – (D) Filtered greyscale images at different temperatures. (E) - (G) segmented images with pore space shown white. The greyscale cross-sections show organic-rich laminations (dark grey) tightly bound in an inorganic mineral matrix (light grey) with no resolvable pore space between 20°C and 380°C. The first resolvable pore space appears at 390°C. There then follows a dramatic increase in porosity to form micro-fracture networks along the organic-rich laminations (c and f) with a small but detectable increase in porosity with a further increase in sample temperature to 500°C (D and E).

Organic rich laminations (darker areas in the image) were observed qualitatively by analysing individual slices (Figure 6.4). However, due to the limited image quality and voxel size, it was challenging to accurately separate the organic and non-organic regions quantitatively. SEM-EDS analysis was performed to confirm that the darker regions in the greyscale images are indeed organic rich (41% carbon content) relative to matrix material (Figure 6.5 - 6.7).

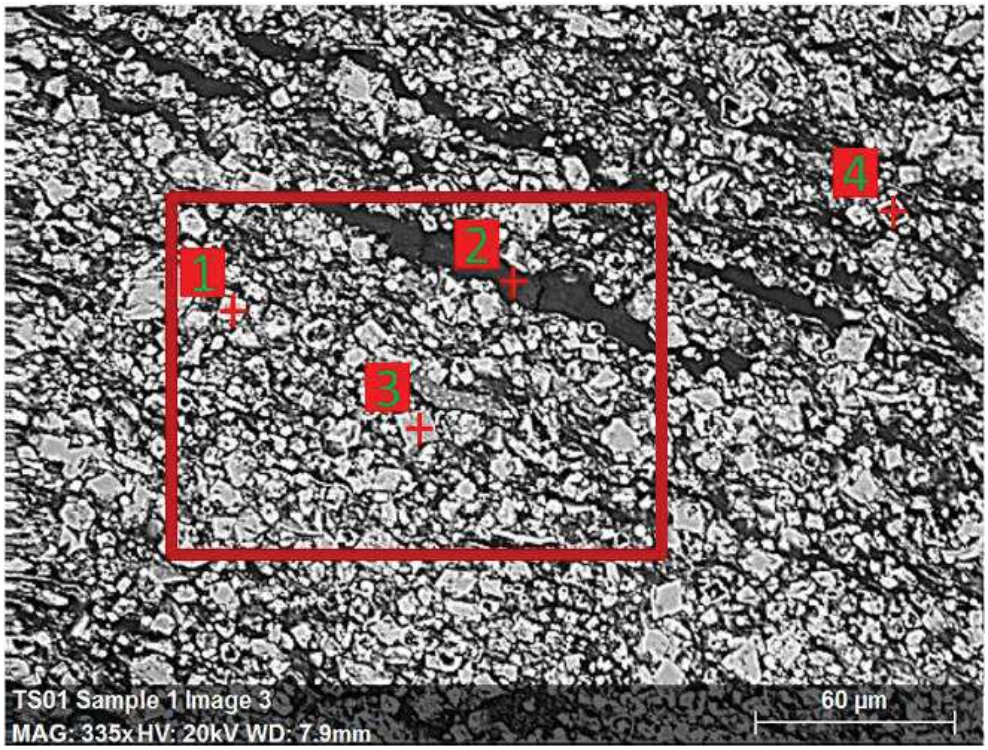

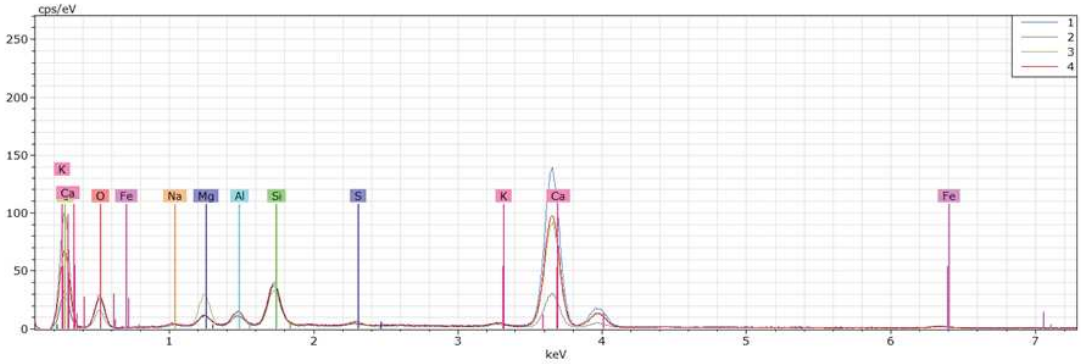

Mass percent (%)

Spectrum	C	O	Na	Mg	Al	Si	S	K	Ca	Fe	Mo
1	21.88	29.03	-	1.61	1.21	3.92	0.08	1.28	25.46	0.50	-
2	40.53	12.89	-	0.71	0.48	2.09	-	0.32	4.24	0.45	0.33
3	23.90	28.66	-	5.59	2.09	3.69	0.16	1.03	17.24	0.76	-
4	32.94	23.94	0.48	1.12	1.21	3.04	0.22	0.46	13.50	0.48	-
Mean value:	29.81	23.63	0.48	2.26	1.25	3.18	0.15	0.77	15.11	0.55	0.33
Sigma:	8.61	7.52	0.00	2.25	0.66	0.82	0.07	0.46	8.80	0.14	0.00
Sigma mean:	4.31	3.76	0.00	1.13	0.33	0.41	0.04	0.23	4.40	0.07	0.00

Figure 6.5 BSE image of the Green River Oil Shale sample with four EDS spot analysis points and corresponding spectra results. The organic-rich material is shown as the darker coloured area and the denser mineral mineral-rich matrix appears lighter. The red box represents the area used to acquire an elemental map.

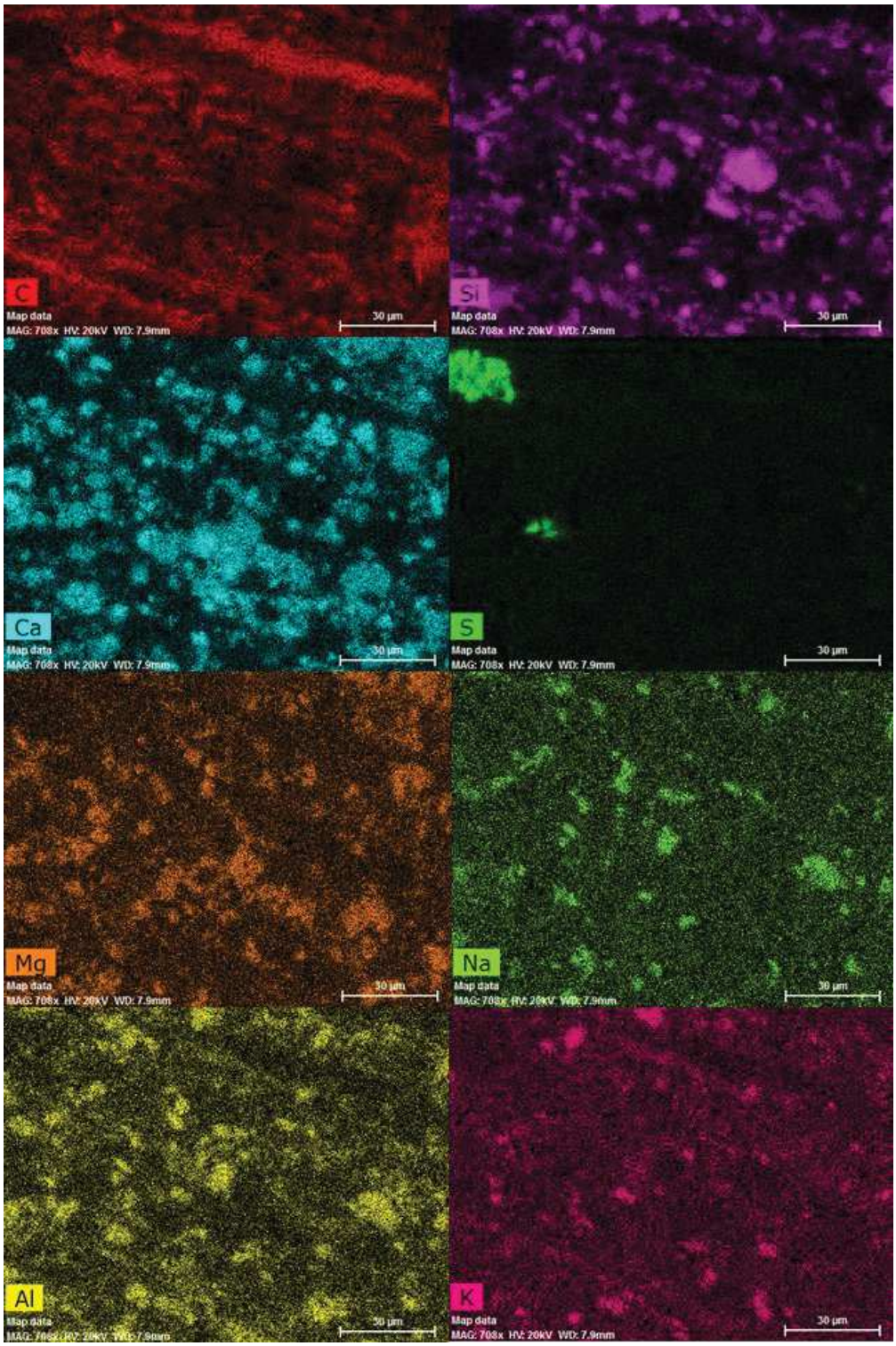

Figure 6.6 Individual elemental maps for the Green River Oil Shale displaying the spatial distribution of carbon (C), silicon (Si), Ca (calcium), sulphur (S), magnesium (Mg), sodium (Na), aluminium (Al) and potassium (K).

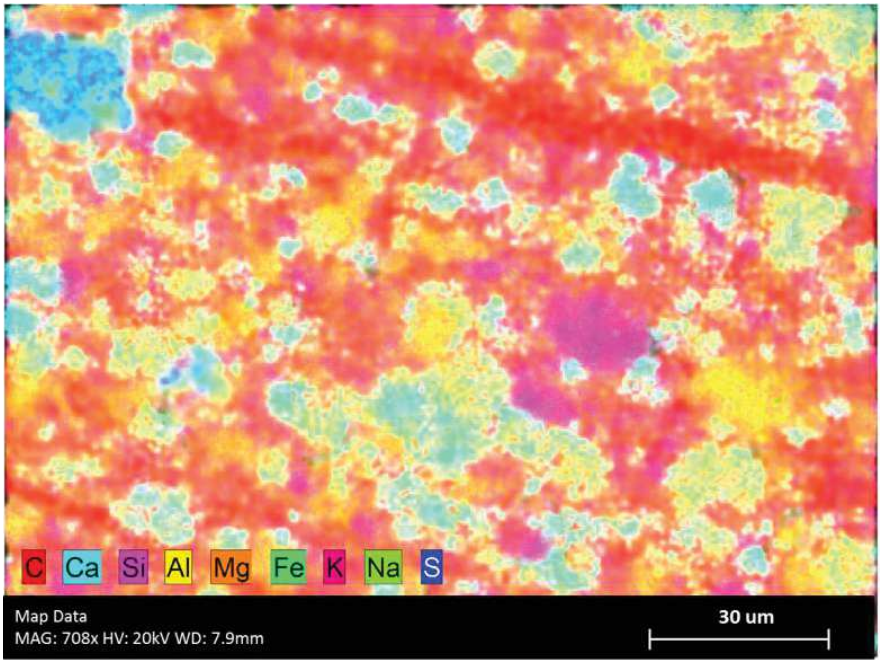

Figure 6.7 Composite elemental map for the Green River Oil Shale displaying the spatial distribution of elements in the sample. Organic-rich areas are shown in red, calcium-rich minerals in blue and silicon-rich minerals in pink.

Figure 6.8 shows the porosity as a function of experimental time given the experimental temperature profile (Figure 6.2C). Between 20°C and 380°C no visible change in porosity was detected for a 2 μm voxel size. The cross-sections (Figure 6.4 B and E) reveal the onset of resolvable pores at 390°C in the organic-rich layers of the shale sample with a total sample porosity of 2.7% (Figure 6.8). To illustrate this, Figure 6.9 presents 3-D visualizations of the segmented pore structure (Figure 6.4 E and F) at 390°C and 400°C. A dramatic increase in total porosity to 21.9% is observed at 400°C as the pores expand resulting in micro-fracture networks parallel to the shale bedding which provide a pathway for the outgoing hydrocarbons. In Figure 6.9C, the computed porosity values are plotted for each vertical slice (A to B) at 390°C and 400°C, revealing a well-defined variation in the spatial porosity distribution after pyrolysis. Greater porosity is observed in the organic-rich regions (which are assumed to be the darker areas at the beginning of the experiment) compared to the organic-lean regions. SEM-EDS analysis was performed to confirm that the darker regions in the greyscale images are indeed organic rich (41% carbon content) relative to matrix material. The increased porosities in the organic-rich regions fundamentally constitute the combined volumes represented primarily by the loss of organic material. With increasing temperature, devolatilization of kerogen

increases the internal vapour pressure of large unconnected pores to such an extent that the mechanical strength of the surrounding material can no longer retain the gas, leading to the dramatic porosity changes observed between 390°C and 400°C. A further increase in temperature to 500°C results in only a 3% increase in average porosity to 24.9%.

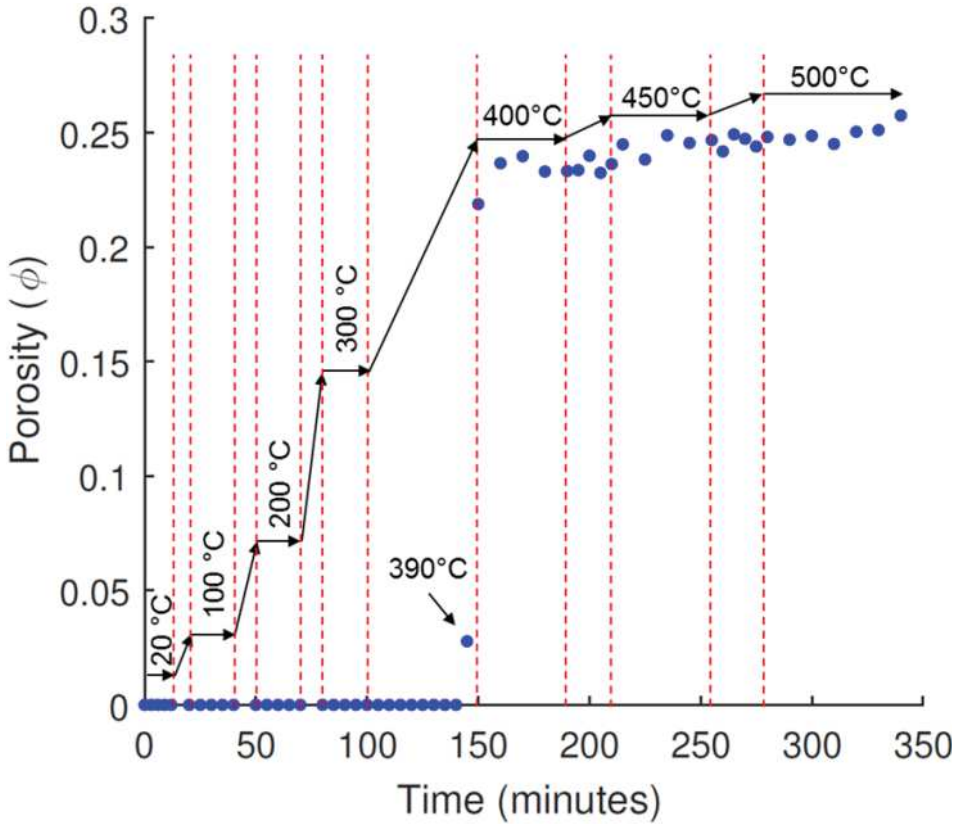

Figure 6.8 Porosity as a function of experimental time. The temperature is indicated by the arrows. Between 20°C and 380°C no resolvable porosity was observed; at 390°C the first micro-scale pores were detected contributing to a porosity of 2.7%; at 400°C a dramatic increase in porosity is observed resulting in a total porosity of 21.9%; and a further increase in pyrolysis temperature to 500°C leads to a smaller increase in porosity to 24.9%.

The first scan at 400°C revealed a total porosity of 21.9% (Figure 6.8). The sample was held at 400°C with the acquisition of a further four scans every 10 minutes to examine the impact of time at a constant temperature. A small but noticeable increase of 2.2% in average porosity to 24.1% over a period of 40 minutes is observed. This indicates the majority of the pore space transformation occurs within the first 10 minutes of the temperature stabilizing at 400°C.

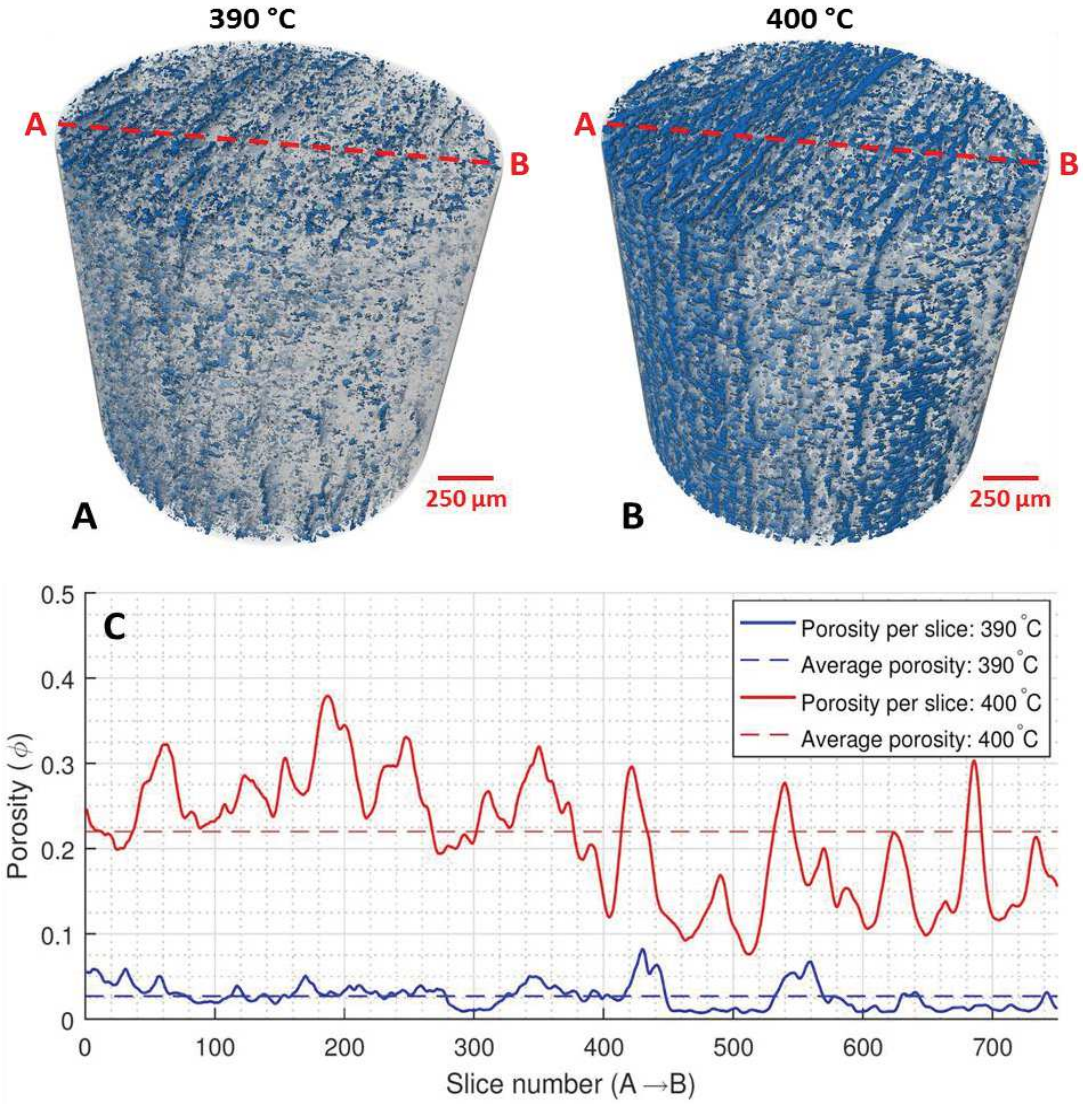

Figure 6.9 3-D rendered volumes of the oil shale sample at 390°C (A) and 400°C (B). The dramatic increase in porosity is visualized with the pore phase (blue) and remaining matrix phase (grey). The porosity profile across the sample from line A to B for both 390°C and 400°C reveals a variable porosity distribution related to the thermal decomposition of organic material.

6.5 Pore Space Connectivity

Figure 6.9 shows a 3-D rendering of the connectivity of the pore space: at 390°C all the pore space appears disconnected at the resolution of the scan, as indicated by the wide range of colours. However, at 400°C, 96.5% of the pore space is connected and a further increase in temperature to 500°C results in a 97.8% connected pore space. Figure 6.11A shows the mass loss for the bulk sample from TGA analysis, and the fractional mass loss change between two points which indirectly represents the pyrolysis reaction rate. At temperatures less than 200°C, a small mass loss is observed, primarily due to the evaporation of water, including adsorbed and interlayer water from clay minerals. At a temperature between 250°C and 500°C a major mass loss of 35.4% is observed. Although a mass loss of 22.6% from the TGA experiment at 380°C is obtained, no pore space development is observed in the images at 2 μm voxel size until a slightly higher temperature is reached (Figure 6.4A). This can be attributed to pore structure transformation at sub-micron resolution. The first mass loss stage in Figure 6.11A represents the decomposition of organic material where chemical bonds linking the organic compounds to the rock matrix are broken and the kerogen macromolecular structure is pyrolysed yielding simpler and lighter molecules. A single major trough for organic decomposition suggests that one distinguishable process occurs in this temperature range governed by a single global reaction mechanism. At temperatures above 600°C, a further mass loss of 15.2% is observed related to the decomposition of carbonate and clay minerals. In total, a mass loss of 50.6% is observed.

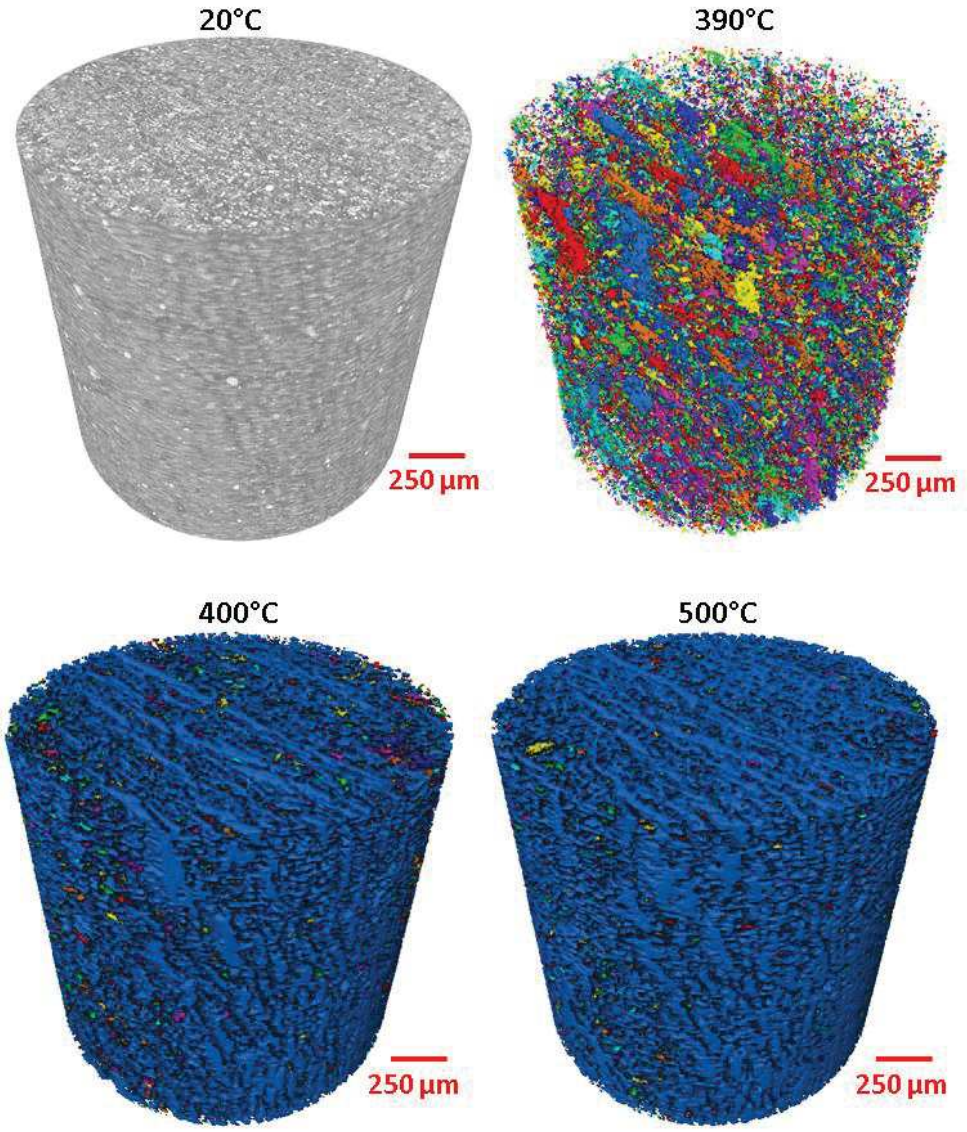

Figure 6.10 3-D rendering of the pore space where the colors indicate clusters of connected pores. At 20°C no pores can be resolved. At 390°C all the pore space appears disconnected at the resolution of the image - the large range of colors indicates a poorly connected pore network. At 400°C and 500°C the vast majority of the pore space is connected, 96.5% and 97.8% respectively, shown in blue.

6.6 Pore Volume Analysis: Imaging vs TGA

The fractional mass loss in the TGA analysis can be related to the change in pore volume from the images. Assuming that organic material of a constant density is produced, it can be assumed that the mass loss is proportional to the increase in pore volume. The fractional change in pore volume as determined from the 3-D images is compared to the change in mass in Figure 6.11. The maximum change in oil shale matrix volume is obtained at 400°C which is comparable to the maximum change in mass loss for the bulk oil shale sample as measured by TGA. At the 2 µm voxel

resolution the mid-to-late stage of pore space development related to the thermal breakdown of organic matter has been captured. To characterise the pore structure evolution at earlier stages of mass loss, images with nano-scale resolution are required.

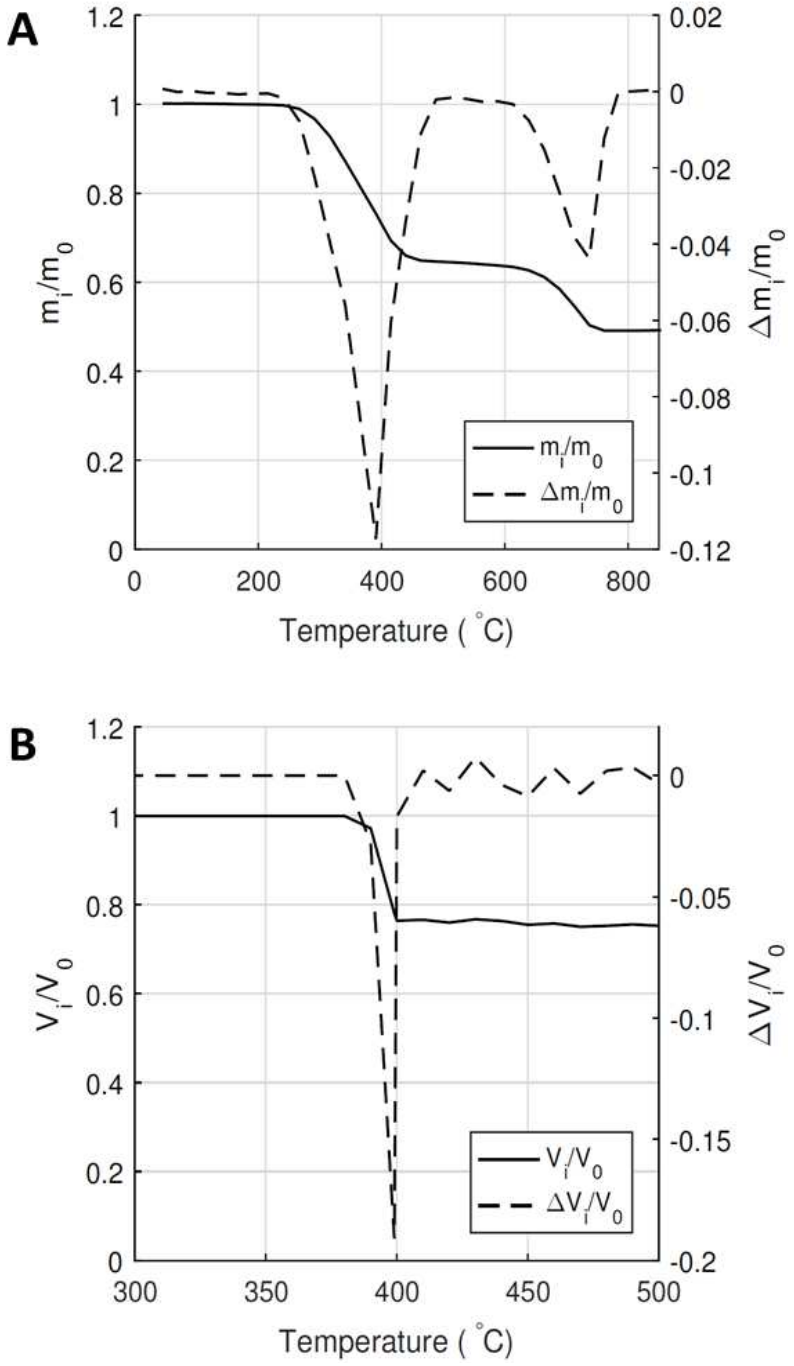

Figure 6.11 (A) Thermogravimetric (TGA) data showing the fraction of the mass remaining as a function of temperature (solid line) and the fractional change in mass (dashed line) between two measured temperature points. $\boldsymbol{m_0}$ is the initial mass, $\boldsymbol{m_i}$ is the mass at some temperature and $\boldsymbol{\Delta m_i}$ is the change in mass for a 10°C temperature increase. (B) Image derived data showing the matrix (non-pore) volume loss due to pore space development (solid line) and the fractional change in matrix volume. $\boldsymbol{\Delta V_i}$ is the change in volume for a 10°C temperature increase.

6.7 Summary

In this chapter, a novel technique combining synchrotron X-ray tomography with a custom-built furnace was designed and applied to visualize and quantify dynamic pore space development for Green River Oil Shale of the organic-rich Mahogany zone at temperatures representative of oil shale pyrolysis technologies (300 – 500°C). The development in oil shale pore structure during pyrolysis was not resolvable at a voxel size of 2 μm for temperatures between 20°C and 380°C. The onset of resolvable pore space occurred at 390°C in the organic-rich phases with a dramatic increase in porosity and connectivity at 400°C. This striking change in porosity was corroborated by mass loss change determined by TGA. Increasing the temperature further to 500°C resulted in only a small increase in porosity. On holding the temperature constant, it is observed that the majority of the pore space development took place within the first 10 minutes. It has been shown that pore development is directly related to the initial spatial distribution of organic matter. These results provide a direct observation of dynamic pore and micro-fracture development for oil shale pyrolysis to better understand the mechanisms that govern the process to ultimately enhance pyrolysis performance.

Chapter 7

Conclusions and Future Work

7.1 Conclusions

In this thesis, it has been demonstrated that multi-scale multi-dimensional imaging and quantification methods are powerful tools for the petrophysical characterization of oil shales, especially the geometry, sizes, network and distribution of fine-grained minerals, organic matter and the evolution of pore structure with increasing pyrolysis temperature. Laboratory and synchrotron based X-ray μCT combined with automated ultra-high resolution SEM, MAPS Mineralogy and FIB-SEM have provided valuable microstructural information in 2-D and 3-D at multiple length scales over three orders of magnitude, with voxel/pixel sizes of 12 μm, 2 μm, 0.8 μm, 0.5 μm, 50 nm, 10 nm and 3 nm.

Key contributions include:

(1) High-resolution 2-D and 3-D imaging of oil shale microstructures.
(2) Visualization and quantification of organic-hosted porosity, organic distribution and connectivity in 3-D before and after oil shale pyrolysis.
(3) Capturing the dynamic evolution of the pore space during pyrolysis using 4-D imaging.

This multi-scale multi-dimensional workflow was applied to the Green River (Mahogany Zone) oil shale formation, the world's largest oil shale deposit. Key microstructural features were analysed including pores, organic matter, clay minerals and non-clay minerals. Using ultra-high resolution SEM under backscattered secondary electron (BSE) mode with automated tiling and stitching, porosity in the oil shale samples was classified into four types: intra-organic pores, referring to pores bounded by organic matter; inter-organic-mineral pores, denoting pores between organic matter and minerals; intra-mineral pores, referring to pores fully bounded within mineral grains and inter-mineral pores, signifying pores lying between inorganic minerals. For the Mahogany oil shale sample, a key finding was

that organic matter hosted pores, rather than mineral-hosted pores, were the dominant contributors to total porosity and are predominantly sub-μm in size with typically irregular geometries. In addition, the results from BSE image and automated spatial mineralogy revealed a complex and variable fine-grained microstructure dominated by organic-rich parallel laminations of the order of 10 μm thick which are tightly bound in a highly heterogeneous mineral matrix of predominantly dolomite and calcite.

A comprehensive X-ray μCT study analysed Mahogany zone oil shale samples with increasing pyrolysis temperature from 300 to 500°C. On increasing the pyrolysis temperature from 20°C to 350°C no resolvable pore space was identified at a 2 μm voxel size. At 400°C the development of pore space was visualized and quantified showing that increased porosity was primarily related to the thermal decomposition of organic matter. The porosity continued to increase to 450°C with a smaller increase between 450°C and 500°C leading to laterally connected pores along the kerogen-rich laminations. From μCT scans at 12 μm a minimum representative elementary thickness of 10 mm was determined based on porosity values. In addition, FIB-SEM volumes of 30 μm × 20 μm × 6 μm for un-pyrolysed and pyrolysed (500°C) samples were acquired, reconstructed followed by three-phase segmentation to separate the pore space, organic matter and inorganic minerals. Results showed that for the un-pyrolysed sample, unconnected pores occupied 0.5% of the analysed volume, with pores between 15 nm and 22 nm in equivalent radius dominating in number. For the pyrolysed oil shale FIB-SEM volume, it was shown that there were well-connected pores across the volume with a total sample porosity of 18.2% with pores of an equivalent radius between 1.6 μm and 2.0 μm made dominating the bulk of the pore volume.

Given that the pyrolysis of oil shale is an inherently dynamic process, a 4-D (3-D + time) synchrotron X-ray μCT study was conducted to visualize and quantify the evolution of the pore structure with increasing pyrolysis temperature (300 - 500°C). The development in oil shale pore structure during pyrolysis was not resolvable at a voxel size of 2 μm for temperatures between 20°C and 380°C. The onset of resolvable pore space occurred at 390°C in the organic-rich phases with a dramatic increase in porosity at 400°C. The internal pressure within the organic matter

increases as the pyrolysis temperature increases causing the sharp eruption of shale oil vapour and combustible gas, that results in results of pore. This striking change in porosity was corroborated by mass loss change determined by thermogravimetric analysis (TGA). Increasing the temperature further to 500°C resulted in only a small increase in porosity. It was shown that the dominant mechanisms of pore space development during oil shale pyrolysis are the thermal decomposition of organic matter and thermal deformation of pores. These results provide valuable pore and micro-fracture datasets to better model, understand and ultimately enhance the production of hydrocarbons from oil shale pyrolysis.

7.2 Future Work

7.2.1 Correlative imaging

Although imaging techniques have been proven to be powerful tools to visualize and quantify spatial distribution of significant features in oil shale, they cannot be used alone for the complete understanding of petrophysical properties before and after pyrolysis. Complementary techniques such as optical microscopy, SEM and TEM, as well as physical measurements including XRD, nitrogen adsorption, helium porosimetry, and chemical measurements including TOC, vitrinite reflectance (Ro) and EDS could be employed to produce valuable information for the same sample. Full correlative imaging techniques can be applied. A typical FIB-SEM dataset volume is 10 × 10 × 10 μm in size and is acquired by means of a destructive technique, meaning the same volume cannot be analysed using another method. As part of a correlative imaging workflow, it would be best to conduct 2-D and 3-D non-destructive techniques followed by a destructive technique such as FIB-SEM to obtain high-resolution microstructural information. In addition, Diffraction Contrast Tomography (DCT) could be applied which combines the concepts of image reconstruction from projections (tomography) and X-ray diffraction imaging (topography) to reveal 3-D mineral distributions. Although image registration could be greatly challenging, these correlative imaging techniques together with bulk geochemical analyses can facilitate understanding and quantification of pore-organic-mineral- associations and oil shale rock fabrics.

7.2.2 Dynamic Imaging

In this study, dynamic imaging using synchrotron-based X-ray micro-tomography at 2 μm voxel size was conducted on oil shale samples with increasing temperature. This research can be further extended to examine the oil shale pyrolysis process at the sub-μm voxel size. In addition, a core-holder system could be developed that would allow confining pressure to be applied to the sample to better characterise in situ oil shale pyrolysis processes. In addition to quantifying the porosity evolution, digital volume correlation (DVC) analysis could be used to build up 3-D displacement and strain maps that would allow for better prediction of micro-fracture propagation.

There is also an opportunity for dynamic SEM imaging, using an Environmental Scanning Electron Microscope (ESEM). Using an ESEM and a programmable heating stage would allow nano-scale visualizations of kerogen thermal decomposition under laboratory conditions and the opportunity to address key questions related to the growth of pores within the organic material and at the organic-mineral interfaces and the percolation threshold point at which the pores become connected.

7.2.3 Modelling

Modelling methods can be applied to estimate the flow properties in the pyrolysed oil shale pore network structures. Flow properties such as absolute and relative permeabilities can be estimated. There are different numerical approaches that are used to compute pore-space properties. These can be divided into two categories: network modelling and direct simulation on image voxels. In network modelling a topological representative network is extracted from a 3-D image of the pore space obtained from techniques such as X-ray micro-CT imaging through which the relevant displacement and transport equations are computed (Blunt et al., 2013; Øren and Bakke, 2003; Piri and Blunt, 2005; Raeini et al., 2017; Valvatne and Blunt, 2004). In general, the pore-space can be defined by pores which correspond to the larger voids in the rock and throats which are narrower pathways connecting the pores. One advanced pore network extraction method is the maximal ball approach where spheres are grown in the pore space, centred on each void voxel. The largest

spheres represent pores, and chains of smaller spheres connecting them define throats (Dong and Blunt, 2009). Once the topologically representative network is extracted, flow and transport are computed semi-analytically through this network. Despite a number of approximations concerning the pore space geometry, the significant advantage of pore-network modelling is its superior computational efficiency over direct simulation approaches.

On the other hand, in direct simulation, the governing equations of flow and transport are computed on the image voxels. The voids are discretized with flow and transport computed on a voxel-based grid. This approach is dependent on the resolution (voxel size) and image size. Both of these approaches, pore network modelling and direct simulation, will be considered when modelling the two-phase flow of oil and gas during the oil shale pyrolysis process. From network extraction, parameters can be obtained including pore-size distribution and connectivity (in terms of coordination number distribution) and permeability parameters can be determined from network and direct simulations.

It may also be possible to model the chemical and physical changes that occur during pyrolysis. This, however, requires a quantitative pore-scale description of these processes which is, at present, lacking. In particular chemical variations are significant, explored in the next section.

7.2.4 Chemical Variations in Oil Shales

An interesting chemical variation in oil shales that can explored is sulphur-rich versus sulphur poor kerogens. It is found that sulphur-rich kerogens are able to generate liquid hydrocarbons at lower temperatures because carbon-sulphur bonds are weaker than any bonds in sulphur-poor kerogens. The effect of clay-rich versus carbonate-rich matrices can also be considered in future work along with the effect of Type I versus Type II kerogen matrices on the mechanism of pore formation as the latter are expected to produce waxier products.

7.2.5 Hydrous Pyrolysis

Hydrous pyrolysis involves heating organic-rich rocks in the presence of liquid water. The presence of water in the pyrolysis of oil shale has been shown to improve the quality of the oil product (Burnham 1995, Lewan 2002). The water acts as a source of hydrogen which terminates free-radical sites and therefore minimises recombination and subsequent char formation. The presence and absence of water on oil shale pyrolysis can be investigated particularly in terms of the pore-structure changes and fluid distribution.

References

Aguilera, R.F., Radetzki, M., 2013. Shale gas and oil: fundamentally changing global energy markets. Oil Gas J. 111, 54–61.

Ahmad, N., Williams, P.T., 1998. Influence of particle grain size on the yield and composition of products from the pyrolysis of oil shales. J. Anal. Appl. Pyrolysis 46, 31–49.

Al-Harahsheh, A., Al-Ayed, O., Al-Harahsheh, M., Abu-El-Halawah, R., 2010. Heating rate effect on fractional yield and composition of oil retorted from El-lajjun oil shale. J. Anal. Appl. Pyrolysis 89, 239–243. doi:10.1016/j.jaap.2010.08.009

Al-Khulaifi, Y., Lin, Q., Blunt, M.J., Bijeljic, B., 2017. Reaction Rates in Chemically Heterogeneous Rock-Coupled Impact of Structure and Flow Properties Studied by X-ray Microtomography. Environ. Sci. Technol.

Al-Otoom, A.Y., Shawabkeh, R. a., Al-Harahsheh, A.M., Shawaqfeh, A.T., 2005. The chemistry of minerals obtained from the combustion of Jordanian oil shale. Energy 30, 611–619. doi:10.1016/j.energy.2004.05.024

Allen, J.L., Johnson, C.L., Heumann, M.J., Gooley, J., Gallin, W., 2012. New technology and methodology for assessing sandstone composition: A preliminary case study using a quantitative electron microscope scanner (QEMScan). Geol. Soc. Am. Spec. Pap. 487, 177–194.

Allred, V.D., 1966. Shale oil developments: Kinetics of oil shale pyrolysis. Chem. Eng. Prog.;(United States) 62.

Alstadt, K.N., Katti, D.R., Katti, K.S., 2012. An in situ FTIR step-scan photoacoustic investigation of kerogen and minerals in oil shale. Spectrochim. Acta Part A Mol. Biomol. Spectrosc. 89, 105–113.

Amelinckx, S., Van Dyck, D., Van Landuyt, J., Van Tendeloo, G., 2008. Electron microscopy: principles and fundamentals. John Wiley & Sons.

American Society for Testing and Materials, 1984. Designation D 3904-80—Standard test method for oil from oil shale: Annual Book of ASTM Standards.

Andrä, H., Combaret, N., Dvorkin, J., Glatt, E., Han, J., Kabel, M., Keehm, Y., Krzikalla, F., Lee, M., Madonna, C., Marsh, M., Mukerji, T., Saenger, E.H., Sain, R., Saxena, N., Ricker, S., Wiegmann, A., Zhan, X., 2013. Digital rock physics benchmarks—Part I: Imaging and segmentation. Comput. Geosci. 50, 25–32. doi:http://dx.doi.org/10.1016/j.cageo.2012.09.005

Andrew, M., Bijeljic, B., Blunt, M.J., 2013. Pore-scale imaging of geological carbon dioxide storage under in situ conditions. Geophys. Res. Lett. 40, 3915–3918. doi:10.1002/grl.50771

Andrew, M., Menke, H., Blunt, M., Bijeljic, B., 2015. The Imaging of Dynamic Multiphase Fluid Flow Using Synchrotron-Based X-ray Microtomography at Reservoir Conditions. Transp. Porous Media 1–24. doi:10.1007/s11242-015-0553-2

ASTM, E., 1992. 1441 Standard Guide for Computed Tomography (CT) Imaging. Am. Soc. Test. Mater. Philadelphia, PA.

Ataman, E., Aatre, V., Wong, K., 1981. Some statistical properties of median filters. IEEE Trans. Acoust. 29, 1073–1075.

Avid, B., Purevsuren, B., Dugarjav, J., 2000. Pyrolysis and thermogravimetric investigation of the Mongolian Khoot oil shale. Oil shale 17, 241–251.

Axelsson, M., Svensson, S., Borgefors, G., 2006. Reduction of ring artifacts in high resolution X-ray microtomography images. Lect. Notes Comput. Sci. 4174, 61.

Bae, J.H., 1969. Some effects of pressure on oil-shale retorting. Soc. Pet. Eng. J. 9, 287–292.

Bai, F., Guo, W., Lü, X., Liu, Y., Guo, M., Li, Q., Sun, Y., 2015. Kinetic study on the pyrolysis behavior of Huadian oil shale via non-isothermal thermogravimetric data. Fuel 146, 111–118.

Bartis, J.T., LaTourrette, T., Dixon, L., Peterson, D.J., Cecchine, G., 2005. Oil shale development in the United States: prospects and policy issues. Rand Corporation.

Bartke, J., Duvall, J., 1977. Topical Meeting, Energy and Minerals Resources Recovery. p. 516.

Behar, F., Vandenbroucke, M., 1987. Chemical modelling of kerogens. Org. Geochem. 11, 15–24.

Bera, B., Mitra, S.K., Vick, D., 2011. Understanding the micro structure of Berea Sandstone by the simultaneous use of micro-computed tomography (micro-CT) and focused ion beam-scanning electron microscopy (FIB-SEM). Micron 42, 412–418. doi:10.1016/j.micron.2010.12.002

Berg, S., Armstrong, R., Ott, H., Georgiadis, A., Klapp, S.A., Schwing, A., Neiteler, R., Brussee, N., Makurat, A., Leu, L., 2014. Multiphase flow in porous rock imaged under dynamic flow conditions with fast X-ray computed microtomography. Petrophysics 55, 304–312.

Berg, S., Ott, H., Klapp, S.A., Schwing, A., Neiteler, R., Brussee, N., Makurat, A., Leu, L., Enzmann, F., Schwarz, J.-O., Kersten, M., Irvine, S., Stampanoni, M., 2013. Real-time 3D imaging of Haines jumps in porous media flow. Proc. Natl. Acad. Sci. 110, 3755–3759.

Berger, M.J., Hubbell, J.H., Seltzer, S.M., Chang, J., Coursey, J.S., Sukumar, R., Zucker, D.S., Olsen, K., 2010. XCOM: Photon cross sections database, 2010. URL http//www. nist. gov/pml/data/xcom.

Bergerhoff, G., Hundt, R., Sievers, R., Brown, I.D., 1983. The inorganic crystal structure data base. J. Chem. Inf. Comput. Sci. 23, 66–69.

Bhargava, S., Awaja, F., Subasinghe, N.D., 2005. Characterisation of some Australian oil shale using thermal, X-ray and IR techniques. Fuel 84, 707–715.

Biglarbigi, K., Killen, J.C., Mohan, H., Carolus, M.J., 2009. SS: Unlocking the Unconventional Oil and Gas Reservoirs: Potential for Oil Shale Development in the United States, in: Offshore Technology Conference. Offshore Technology Conference.

Birdwell, J.E., Mercier, T.J., Johnson, R.C., Brownfield, M.E., 2012. In-place oil shale resources examined by grade in the major basins of the Green River Formation, Colorado, Utah, and Wyoming. US Geol. Surv. Fact Sheet 3145, 2013.

Blackson, J., Todd, C.S., Bar, G., Reuschle, D., Janus, M., Darus, M., Nickles, A., 2008. Automated Image Acquisition at High Spatial Resolutions in a Field Emission Gun Scanning Electron Microscope. Microsc. Microanal. 14, 1210–1211.

Blunt, M.J., Bijeljic, B., Dong, H., Gharbi, O., Iglauer, S., Mostaghimi, P., Paluszny, A., Pentland, C., 2013. Pore-scale imaging and modelling. Adv. Water Resour. 51, 197–216. doi:10.1016/j.advwatres.2012.03.003

Borrego, A.G., Prado, J.G., Fuente, E., Guillén, M.D., Blanco, C.G., 2000. Pyrolytic behaviour of Spanish oil shales and their kerogens. J. Anal. Appl. Pyrolysis 56, 1–21.

Bousige, C., Ghimbeu, C.M., Vix-Guterl, C., Pomerantz, A.E., Suleimenova, A., Vaughan, G., Garbarino, G., Feygenson, M., Wildgruber, C., Ulm, F.-J., 2016. Realistic molecular model of kerogen/'s nanostructure. Nat. Mater. 15, 576–582.

Boyer, B.W., 1982. Green River laminites: Does the playa-lake model really invalidate the stratified-lake model? Geology 10, 321–324.

Boyer, C., Kieschnick, J., Suarez-rivera, R., Lewis, R.E., Waters, G., 2006. Producing Gas from Its Source. Oilf. Rev. 36–49.

BP, 2016. Energy Outlook to 2035. [WWW Document]. URL available: https://www.bp.com/content/dam/bp/pdf/energy-economics/energy-outlook-2016/bp-energy-outlook-2016.pdf [Accessed 10 January 2010]

Bradley, W.H., 1931. Origin and microfossils of the oil shale of the Green River Formation of Colorado and Utah. US Govt. Print. Off.

Brandt, A.R., 2008. Converting oil shale to liquid fuels: Energy inputs and greenhouse gas emissions of the shell in situ conversion process. Environ. Sci. Technol. 42, 7489–7495. doi:10.1021/es800531f

Braun, R.L., Rothman, A.J., 1975. Oil-shale pyrolysis: Kinetics and mechanism of oil production. Fuel 54, 129–131.

Brunauer, S., Emmett, P.H., Teller, E., 1938. Adsorption of gases in multimolecular layers. J. Am. Chem. Soc. 60, 309–319.

Buades, A., Coll, B., Morel, J.-M., 2008. Nonlocal Image and Movie Denoising. Int. J. Comput. Vis. 76, 123–139. doi:10.1007/s11263-007-0052-1

Buades, A., Coll, B., Morel, J.M., 2005. A non-local algorithm for image denoising. doi:10.1109/CVPR.2005.38

Buckman, J., 2014. Use of automated image acquisition and stitching in scanning electron microscopy: Imaging of large scale areas of materials at high resolution. Microsc. Anal. 28(1), 13–15.

Bultreys, T., De Boever, W., Cnudde, V., 2016. Imaging and image-based fluid transport modeling at the pore scale in geological materials: A practical introduction to the current state-of-the-art. Earth-Science Rev. 155, 93–128.

Burnham, A., Singleton, M., 1983. High-pressure pyrolysis of Green River oil shale. ACS Publications.

Burnham, A.K., 2017a. Structures of Coal, Kerogen, and Asphaltenes, in: Global Chemical Kinetics of Fossil Fuels. Springer, pp. 75–105.

Burnham, A.K., 2017b. GLOBAL CHEMICAL KINETICS OF FOSSIL FUELS. Springer.

Burnham, A.K., 2017c. Pyrolysis in Open Systems, in: Global Chemical Kinetics of Fossil Fuels. Springer, pp. 107–169.

Burnham, A.K., 2015. A simple kinetic model of oil generation, vaporization, coking, and cracking. Energy & Fuels 29, 7156–7167.

Burnham, A.K., Happe, J.A., 1984. On the mechanism of kerogen pyrolysis. Fuel 63, 1353–1356.

Burwell, E.L., Carpenter, H.C., Sohns, H.W., 1969. Experimental in situ retorting of oil shale at Rock Springs, Wyoming.

Burwell, E.L., Sterner, T.E., Carpenter, H.C., 1970. Shale Oil Recovery by In-Situ Retorting-A Pilot Study. J. Pet. Technol. 22, 1–520.

Caillé, A., Al-Moneef, M., de Castro, F.B., Bundgaard-Jensen, A., Fall, A., de Medeiros, N.F., Jain, C.P., Kim, Y.D., Nadeau, M.-J., Testa, C., 2007. 2007 Survey of Energy Resources. World Energy Counc. 2007.

Cameron, I.T., Gani, R., 2011. Product and process modelling: a case study approach. Elsevier.

Cane, R.F., 1976. The origin and formation of oil shale. Dev. Pet. Sci. 5, 27–60.

Chao, A.W., Mess, K.H., Tigner, M., Zimmermann, F., 2013. Handbook of accelerator physics and engineering. World scientific.

Chilingarian, G. V, Yen, T.F., 2011. Oil shale. Elsevier.

Clarkson, C.R., Solano, N., Bustin, R.M., Bustin, A.M.M., Chalmers, G.R.L., He, L., Melnichenko, Y.B., Radliński, A.P., Blach, T.P., 2013. Pore structure characterization of North American shale gas reservoirs using USANS/SANS, gas adsorption, and mercury intrusion. Fuel 103, 606–616. doi:10.1016/j.fuel.2012.06.119

Cnudde, V., Boone, M.N.N., 2013. High-resolution X-ray computed tomography in geosciences: A review of the current technology and applications. Earth-Science Rev. 123, 1–17. doi:10.1016/j.earscirev.2013.04.003

Cnudde, V., Masschaele, B., Dierick, M., Vlassenbroeck, J., Hoorebeke, L. Van, Jacobs, P., 2006. Recent progress in X-ray CT as a geosciences tool. Appl. Geochemistry 21, 826–832. doi:10.1016/j.apgeochem.2006.02.010

Conner, W.C., Cevallos-Candau, J.F., Weist, E.L., Pajares, J., Mendioroz, S., Cortes, A., 1986. Characterization of pore structure: porosimetry and sorption. Langmuir 2, 151–154.

Cook, A.C., Sherwood, N.R., 1991. Classification of oil shales, coals and other organic-rich rocks. Org. Geochem. 17, 211–222.

Coshell, L., Mclver, R.G., Chang, R., 1994. X-ray computed tomography of Australian oil shales: non-destructive visualization and density determination. Fuel 73, 1317–1321. doi:10.1016/0016-2361(94)90307-7

Crawford, P., Biglarbigi, K., Dammer, A., Knaus, E., 2008a. Advances in World Oil Shale Production Technologies. Proc. SPE Annu. Tech. Conf. Exhib. 1–11. doi:10.2118/116570-MS

Crawford, P., Biglarbigi, K., Dammer, A., Knaus, E., 2008b. Advances in world oil-shale production technologies, in: SPE Annual Technical Conference and Exhibition. Society of Petroleum Engineers.

Crowley, K.D., Duchon, C.E., Rhi, J., 1986. Climate record in varved sediments of the Eocene Green River Formation. J. Geophys. Res. Atmos. 91, 8637–8647.

Curtis, M.E., Ambrose, R.J., Sondergeld, C.H., Rai, C.S., 2010. Structural Characterization of Gas Shales on the Micro- and Nano-Scales. Can. Unconv. Resour. Int. Pet. Conf. 1–15. doi:10.2118/137693-MS

Dann, R., Turner, M., Close, M., Knackstedt, M., 2010. Multi-scale characterisation of coastal sand aquifer media for contaminant transport using X-ray computed tomography. Environ. Earth Sci. 63, 1125–1137. doi:10.1007/s12665-010-0788-8

De Leeuw, J.W., Largeau, C., 1993. A review of macromolecular organic compounds that comprise living organisms and their role in kerogen, coal, and petroleum formation, in: Organic Geochemistry. pp. 23–72.

Deo, M.D., Tiwari, P., 2008. Kinetics of oil shale pyrolysis and oil composition, in: 2008 AIChE Annual Meeting, AIChE 100. pp. 1–11.

Derenne, S., Largeau, C., Casadevall, E., Damsté, J.S.S., Tegelaar, E.W., De Leeuw, J.W., 1990. Characterization of Estonian Kukersite by spectroscopy and pyrolysis: Evidence for abundant alkyl phenolic moieties in an Ordovician, marine, type II/I kerogen. Org. Geochem. 16, 873–888.

Desbois, G., Urai, J.L., Kukla, P.A., Konstanty, J., Baerle, C., 2011. High-resolution 3D fabric and porosity model in a tight gas sandstone reservoir: a new approach to investigate microstructures from mm-to nm-scale combining argon beam cross-sectioning and SEM imaging. J. Pet. Sci. Eng. 78, 243–257.

Dobson, K.J., Harrison, S.T.L., Lin, Q., Ní Bhreasail, A., Fagan-Endres, M.A., Neethling, S.J., Lee, P.D., Cilliers, J.J., 2017. Insights into Ferric Leaching of Low Grade Metal Sulfide-Containing ores in an Unsaturated Ore Bed Using X-ray Computed Tomography. Minerals 7, 85.

Dong, H., Blunt, M.J., 2009. Pore-network extraction from micro-computerized-tomography images. Phys. Rev. E 80, 36307.

Duncan, D.C., 1976. Geologic setting of oil-shale deposits and world prospects. Dev. Pet. Sci. 5, 13–26.

Durand, B., 1980. Kerogen: Insoluble organic matter from sedimentary rocks. Editions technip.

Durand, B., Monin, J.C., 1980. Elemental analysis of kerogens (C, H, O, N, S, Fe). Kerogen Paris, Ed. Tech. 113–142.

Duvall, F.E.W., Sohn, H.Y., Pitt, C.H., Bronson, M.C., 1983. Physical behaviour of oil shale at various temperatures and compressive loads: 1. Free thermal expansion. Fuel 62, 1455–1461.

Dyni, J.R., 2003. Geology and resources of some world oil-shale deposits. Oil Shale 20, 193–252.

Dyni, J.R., U.S. Geological Survey, 2010. Oil Shale. 2010 Surv. Energy Resour. 93–122.

Energy, R., 2008. Competent Persons Report Assets of Great South Land Minerals Limited, Tasmania.

Espitalie, J., Madec, M., Tissot, B., 1980. Role of mineral matrix in kerogen pyrolysis: influence on petroleum generation and migration. Am. Assoc. Pet. Geol. Bull. 64, 59–66.

ExxonMobil, 2017. 2017 Outlook for Energy: A View to 2040. [WWW Document]. URL available: http://cdn.exxonmobil.com/~/media/global/files/outlook-for-energy/2017/2017_outlook_for_energy.pdf [Accessed 10 January 2010]

Feldkamp, L.A., Davis, L.C., Kress, J.W., 1984. Practical cone-beam algorithm. JOSA A 1, 612–619.

Feldkamp, L.A., Goldstein, S.A., Parfitt, M.A., Jesion, G., Kleerekoper, M., 1989. The direct examination of three-dimensional bone architecture in vitro by computed tomography. J. bone Miner. Res. 4, 3–11.

Fletcher, T.H., Pugmire, R.J., 2016. Oil Shale Pyrolysis Rates and Mechanisms. Utah Oil Shale Sci. Technol. Policy Perspect. 119.

Fox, J.P., 1980. Water-related impacts of in-situ oil shale processing. California Univ., Berkeley (USA). Lawrence Berkeley Lab.

Francu, J., Harvie, B., Laenen, B., Siirde, A., Veiderma, M., Collins, P., Steiger, F., 2007. A study on the EU oil shale industry–viewed in the light of the Estonian experience. A report by EASAC to the Committee on Industry, Research and Energy of the European Parliament. Eur. Acad. Sci. Advis. Counc.

Fusseis, F., Xiao, X., Schrank, C., De Carlo, F., 2014. A brief guide to synchrotron radiation-based microtomography in (structural) geology and rock mechanics. J. Struct. Geol. 65, 1–16. doi:http://dx.doi.org/10.1016/j.jsg.2014.02.005

Gallin William, Day Roger L, Keiter Robert, 2010. Oil Shale: A Solution to the Liquid Fuel Dilemma. doi:10.1021/bk-2010-1032

Gao, J., 2009. COAL, OIL SHALE, NATURAL BITUMEN, HEAVY OIL, AND PEAT.

Gavin, J.M., 1924. Oil shale. U.S. Gov. Print. Off. Washington.

Giannuzzi, L.A., Kempshall, B.W., Schwarz, S.M., Lomness, J.K., Prenitzer, B.I., Stevie, F.A., 2005. FIB lift-out specimen preparation techniques, in: Introduction to Focused Ion Beams. Springer, pp. 201–228.

Gibson, P.J., 1989. Petrology of two Tertiary oil shale deposits from Queensland, Australia. J. Geol. Soc. London. 146, 319–331.

Glorioso, J.C., Rattia, A., 2012. Unconventional reservoirs: Basic petrophysical concepts for shale gas, in: SPE/EAGE European Unconventional Resources Conference & Exhibition-From Potential to Production.

Golubev, N., 2003. Solid oil shale heat carrier technology for oil shale retorting. Oil Shale 20, 324–332.

Grauch, R.I., Eberl, D.D., Butcher, A.R., Botha, P.W.S.K., 2008. Quantitative mineralogy of fine-grained sedimentary rocks: a preliminary look at QEMSCAN®. Microsc. Microanal. 14, 532–533.

Gregg, M.L., Campbell, J.H., Taylor, J.R., 1981. Laboratory and modelling investigation of a Colorado oil-shale block heated to 900 C. Fuel 60, 179–188.

Gregg, S.J., Sing, K.S.W., 1982. Adsorption, surface area and porosity academic. New York 242–245.

Gu, Y., 2003. Automated scanning electron microscope based mineral liberation analysis an introduction to JKMRC/FEI mineral liberation analyser. J. Miner. Mater. Charact. Eng. 2, 33.

Guffey, F.D., McLendon, T.R., 1984. Evaluation of oil yield losses during the retorting of oil shale at low void fractions. Part 1. The effect of particle size and resource grade. Liq. Fuels Technol. 2, 439–461.

Hajizadeh, A., Safekordi, A., Farhadpour, F.A., 2011. A multiple-point statistics algorithm for 3D pore space reconstruction from 2D images. Adv. Water Resour. 34, 1256–1267.

Han, X., Jiang, X., Cui, Z., 2008. Change of pore structure of oil shale particles during combustion. 2. Pore structure of oil-shale ash. Energy and Fuels 22, 972–975. doi:10.1021/ef700645x

Han, X., Jiang, X., Yu, L., Cui, Z., 2006. Change of pore structure of oil shale particles during combustion. Part 1. Evolution mechanism. Energy & fuels 20, 2408–2412. doi:10.1021/ef0603277

Han, X., Kulaots, I., Jiang, X., Suuberg, E.M., 2014. Review of oil shale semicoke and its combustion utilization. Fuel 126, 143–161. doi:http://dx.doi.org/10.1016/j.fuel.2014.02.045

Han, X.X., Jiang, X.M., Cui, Z.G., 2009. Studies of the effect of retorting factors on the yield of shale oil for a new comprehensive utilization technology of oil shale. Appl. Energy 86, 2381–2385. doi:http://dx.doi.org/10.1016/j.apenergy.2009.03.014

Harak, A., Dockter, L., Long, A., Sohns, H.W., US, B.R.I., 1974. 7995. US Bur. Mines, Laramie, Wyoming.

Hascakir, B., Babadagli, T., Akin, S., 2008. Experimental and numerical simulation of oil recovery from oil shales by electrical heating. Energy & Fuels 22, 3976–3985.

Haswell, R., Zeile, U., Mensch, K., 2008. Van Gogh's painting grounds: an examination of barium sulphate extender using analytical electron microscopy–SEM/FIB/TEM/EDX. Microchim. Acta 161, 363–369.

Hoekstra, E., van Swaaij, W.P.M., Kersten, S.R.A., Hogendoorn, K.J.A., 2012. Fast pyrolysis in a novel wire-mesh reactor: Design and initial results. Chem. Eng. J. 191, 45–58.

Huang, J., Cavanaugh, T., Nur, B., 2013. 1 An Introduction to SEM Operational Principles and Geologic Applications for Shale Hydrocarbon Reservoirs. Electron Microsc. shale Hydrocarb. Reserv. AAPG Mem. 102 1–6. doi:10.1306/13391699M1023580

Hubbard, A.B., Robinson, W.E., 1950. A thermal decomposition study of Colorado oil shale. US Dept. of the Interior, Bureau of Mines.

Hubbell, J.H., Seltzer, S.M., 1996. Tables of X-Ray Mass Attenuation Coe $ cients and Mass Energy-Absorption Coe $-cients from 1 keV to 20 MeV for Elements.

Hutton, A., 1991. Fluorescence microscopy in oil shale and coal studies.

Hutton, A., Bharati, S., Robl, T., 1994. Chemical and petrographic classification of kerogen/macerals. Energy & Fuels 8, 1478–1488.

Hutton, A.C., 1995. Organic petrography of oil shales, in: Composition, Geochemistry and Conversion of Oil Shales. Springer, pp. 17–33.

Hutton, A.C., 1988. The lacustrine Condor oil shale sequence. Geol. Soc. London, Spec. Publ. 40, 329–340.

Hutton, A.C., 1987. Petrographic classification of oil shales. Int. J. Coal Geol. 8, 203–231.

Hutton, A.C., 1982. Organic petrology of oil shales.

IEA, 2015. World Energy Outlook [WWW Document]. URL available: http://www.worldenergyoutlook.org/weo2015/ [Accessed 10 January 2010]

Ishitani, T., Umemura, K., Ohnishi, T., Yaguchi, T., Kamino, T., 2004. Improvements in performance of focused ion beam cross-sectioning: aspects of ion-sample interaction. J. Electron Microsc. (Tokyo). 53, 443–449.

Jaber, J.O., Probert, S.D., 1999. Pyrolysis and gasification kinetics of Jordanian oil-shales. Appl. Energy 63, 269–286.

Jaber, J.O., Probert, S.D., Williams, P.T., 1999. Evaluation of oil yield from Jordanian oil shales. Energy 24, 761–781.

Jiang, H., Song, L., Cheng, Z., Chen, J., Zhang, L., Zhang, M., Hu, M., Li, J., Li, J., 2015. Influence of pyrolysis condition and transition metal salt on the product yield and characterization via Huadian oil shale pyrolysis. J. Anal. Appl. Pyrolysis 112, 230–236.

Johnson, H.R., Crawford, P.M., Bunger, J.W., 2004. Strategic significance of America's oil shale resource: Volume 2--oil shale resources technology and economics.

Johnson, R.C., Mercier, T.J., Brownfield, M.E., Pantea, M.P., Self, J.G., 2009. Assessment of In-Place Oil Shale Resources of the Green River Formation, Piceance Basin, Western Colorado.

Jordens, A., Marion, C., Grammatikopoulos, T., Waters, K.E., 2016. Understanding the effect of mineralogy on muscovite flotation using QEMSCAN. Int. J. Miner. Process. 155, 6–12.

Kang, Z., Zhao, J., Yang, D., Zhao, Y., Hu, Y., 2017. Study of the evolution of micron-scale pore structure in oil shale at different temperatures. Oil Shale 34, 42.

Kang, Z.Q., Yang, D., Zhao, Y.S., Hu, Y.Q., 2011. Thermal cracking and corresponding permeability of Fushun oil shale. Oil Shale 28, 273–283. doi:10.3176/oil.2011.2.02

Karabakan, A., Yürüm, Y., 2000. Effect of the mineral matrix in the reactions of shales. Part 2. Oxidation reactions of Turkish Göynük and US Western Reference oil shales. Fuel 79, 785–792.

Karabakan, A., Yürüm, Y., 1998. Effect of the mineral matrix in the reactions of oil shales: 1. Pyrolysis reactions of Turkish Göynük and US Green River oil shales. Fuel 77, 1303–1309.

Ketcham, R.A., Carlson, W.D., 2001. Acquisition, optimization and interpretation of x-ray computed tomographic imagery: Applications to the geosciences. Comput. Geosci. 27, 381–400. doi:10.1016/S0098-3004(00)00116-3

Koel, M., Ljovin, S., Hollis, K., Rubin, J., 2001. Using neoteric solvents in oil shale studies. Pure Appl. Chem. 73, 153–159.

Kök, M. V., Iscan, a. G., 2007. Oil shale kinetics by differential methods. J. Therm. Anal. Calorim. 88, 657–661. doi:10.1007/s10973-006-8027-y

Kok, M. V, Pamir, R., 2003. Pyrolysis kinetics of oil shales determined by DSC and TG/DTG. Oil Shale 20, 57–68.

Krueger, R., 1999. Dual-column (FIB–SEM) wafer applications. Micron 30, 221–226.

Kyriakou, Y., Prell, D., Kalender, W.A., 2009. Ring artifact correction for high-resolution micro CT. Phys. Med. Biol. 54, N385.

Landis, E.N., Keane, D.T., 2010. X-ray microtomography. Mater. Charact. 61, 1305–1316.

Lee, S., 1990. Oil shale technology. CRC Press.

Lee, S., Speight, J.G., Loyalka, S.K., 2014. Handbook of alternative fuel technologies. crc Press.

Lee, S., Speight, J.G., Loyalka, S.K., 2007. Handbook of Alternative Fuel Technologies, Green Chemistry and Chemical Engineering. CRC Press.

Lekas, M.A., Lekas, J.M., Strickland, F.G., 1991. Initial evaluation of fracturing oil shale with propellants for in situ retorting, Phase 2. Western Research Inst., Laramie, WY (United States).

Lemmens, H., Butcher, A., Botha, P., 2011. FIB/SEM and SEM/EDX: a New Dawn for the SEM in the Core Lab? J. Petrophysics SPWLA 52, 1–12.

Li, C.-Z., Bartle, K.D., Kandiyoti, R., 1993. Vacuum pyrolysis of maceral concentrates in a wire-mesh reactor. Fuel 72, 1459–1468.

Lifshin, E., 2008. X-ray Characterization of Materials. John Wiley & Sons.

Lin, Q., Al-Khulaifi, Y., Blunt, M.J., Bijeljic, B., 2016. Quantification of sub-resolution porosity in carbonate rocks by applying high-salinity contrast brine using X-ray microtomography differential imaging. Adv. Water Resour. 96, 306–322.

Lin, Q., Bijeljic, B., Rieke, H., Blunt, M., 2017. Differential imaging of porous plate capillary drainage in laminated sandstone rock using X-ray micro-tomography, in: 79th EAGE Conference and Exhibition 2017-Workshops.

Lin, Q., Neethling, S.J., Dobson, K.J., Courtois, L., Lee, P.D., 2015. Quantifying and minimising systematic and random errors in X-ray micro-tomography based volume measurements. Comput. Geosci. 77, 1–7. doi:http://dx.doi.org/10.1016/j.cageo.2014.12.008

Liu, X., Zhan, J.-H., Lai, D., Liu, X., Zhang, Z., Xu, G., 2015. Initial pyrolysis mechanism of oil shale kerogen with reactive molecular dynamics simulation. Energy & Fuels 29, 2987–2997.

Loucks, R.G., Reed, R.M., Ruppel, S.C., Hammes, U., 2012. Spectrum of pore types and networks in mudrocks and a descriptive classification for matrix-related mudrock pores. Am. Assoc. Pet. Geol. Bull. 96, 1071–1098.

Loucks, R.G., Reed, R.M., Ruppel, S.C., Jarvie, D.M., 2009. Morphology, genesis, and distribution of nanometer-scale pores in siliceous mudstones of the Mississippian Barnett Shale. J. Sediment. Res. 79, 848–861.

Lü, X., Sun, Y., Lu, T., Bai, F., Viljanen, M., 2014. An efficient and general analytical approach to modelling pyrolysis kinetics of oil shale. Fuel 135, 182–187.

Luchini, P., Motz, H., 1990. Undulators and free-electron lasers. Clarendon Press.

Ma, L., Fauchille, A.-L., Dowey, P.J., Pilz, F.F., Courtois, L., Taylor, K.G., Lee, P.D., 2017. Correlative multi-scale imaging of shales: a review and future perspectives. Geol. Soc. London, Spec. Publ. 454, SP454-11.

Ma, L., Pilz, F.F., Dowey, P.J., Taylor, K.G., Lee, P.D., 2016. Multi-Scale Shale Imaging Challenges: Examples from US and European Plays.

Madonna, C., Quintal, B., Frehner, M., Almqvist, B.S.G., Tisato, N., Pistone, M., Marone, F., Saenger, E.H., 2013. Synchrotron-based X-ray tomographic microscopy for rock physics investigations. Geophysics 78, D53–D64.

Mahabadi, O.K., Randall, N.X., Zong, Z., Grasselli, G., 2012. A novel approach for micro-scale characterization and modeling of geomaterials incorporating actual material heterogeneity. Geophys. Res. Lett. 39. doi:10.1029/2011GL050411

Martignoni, W.P., Rodrigues, W.J.B., 2002. Petrosix oil shale technology learning curve, in: 26th Oil Shale Symposium, Proceedings, Poster. pp. 16–20.

Mastalerz, M., Schimmelmann, A., Drobniak, A., Chen, Y., 2013. Porosity of Devonian and Mississippian New Albany Shale across a maturation gradient: Insights from organic petrology, gas adsorption, and mercury intrusion. Am. Assoc. Pet. Geol. Bull. 97, 1621–1643.

Matzick, A., Dannenberg, R.O., Ruark, J.R., Phillips, J.E., Lankford, J.D., 1966. Development of the Bureau of Mines gas-combustion oil-shale retorting process. US, Bur. Mines, Bull.;(United States) 635.

McGlade, C., Speirs, J., Sorrell, S., 2013. Unconventional gas–a review of regional and global resource estimates. Energy 55, 571–584.

Mees, F., Swennen, R., Van Geet, M., Jacobs, P., 2003. Applications of X-ray computed tomography in the geosciences. Geol. Soc. London, Spec. Publ. 215, 1–6.

Menke, H., Andrew, M., Blunt, M., Bijeljic, B., 2016. Reservoir condition imaging of reactive transport in heterogeneous carbonates using fast synchrotron tomography—Effect of initial pore structure and flow conditions. Chem. Geol. 428, 15–26.

Menke, H., Bijeljic, B., Andrew, M., Blunt, M., 2015. Dynamic Three-Dimensional Pore-Scale Imaging of Reaction in a Carbonate at Reservoir Conditions. Environ. Sci. Technol. 49, 4407–4414. doi:10.1021/es505789f

Menke, H.P., 2015. Reservoir condition pore-scale imaging of reaction. Imp. Coll. London.

Milliken, K.L., Rudnicki, M., Awwiller, D.N., Zhang, T., 2013. Organic matter–hosted pore system, Marcellus formation (Devonian), Pennsylvania. Am. Assoc. Pet. Geol. Bull. 97, 177–200.

Milner, M., McLin, R., Petriello, J., 2010. Imaging texture and porosity in mudstones and shales: Comparison of secondary and ion-milled backscatter SEM methods, in: Canadian Unconventional Resources and International Petroleum Conference. Society of Petroleum Engineers.

Moore, D.M., Reynolds, R.C., 1989. X-ray Diffraction and the Identification and Analysis of Clay Minerals. Oxford university press Oxford.

Motlep, R., Kirsimae, K., Talviste, P., Puura, E., Jurgenson, J., 2007. Mineral composition of Estonian oil shale semi-coke sediments. Oil Shale 24, 405–423.

Nastasi, M., Mayer, J., Hirvonen, J.K., 1996. Ion-solid interactions: fundamentals and applications. Cambridge University Press.

Nazzal, J.M., 2008. The influence of grain size on the products yield and shale oil composition from the Pyrolysis of Sultani oil shale. Energy Convers. Manag. 49, 3278–3286.

Niu, M., Wang, S., Han, X., Jiang, X., 2013. Yield and characteristics of shale oil from the retorting of oil shale and fine oil-shale ash mixtures. Appl. Energy 111, 234–239.

Noble, R.D., Harris, H.G., Tucker, W.F., 1981. Isothermal oil shale pyrolysis. 2. Kinetics of product formation and composition at various pressures. Fuel 60, 573–576.

Ogura, K., Yamada, M., Hirahara, O., Mita, M., Erdman, N., Nielsen, C., 2010. Gigantic montages with a fully automated FE-SEM (serial sections of a mouse brain tissue). Microsc. Microanal. 16, 52–53.

Oja, V., Suuberg, E.M., 2012. Oil Shale oil shale Processing oil shale processing, Chemistry and Technology, in: Encyclopedia of Sustainability Science and Technology. Springer, pp. 7457–7491.

Okabe, H., Blunt, M.J., 2007. Pore space reconstruction of vuggy carbonates using microtomography and multiple-point statistics, in: Water Resources Research.

Okabe, H., Blunt, M.J., 2005. Pore space reconstruction using multiple-point statistics. J. Pet. Sci. Eng. 46, 121–137.

Okabe, H., Blunt, M.J., 2004. Prediction of permeability for porous media reconstructed using multiple-point statistics. Phys. Rev. E 70, 66135.

Olson, R.K., Grigg, M.W., 2008. Mercury injection capillary pressure (MICP) a useful tool for improved understanding of porosity and matrix permeability distributions in shale reservoirs. Am. Assoc. Pet. Geol. Search Discov. Artic. 40322.

Øren, P.-E., Bakke, S., 2003. Reconstruction of Berea sandstone and pore-scale modelling of wettability effects. J. Pet. Sci. Eng. 39, 177–199.

Orendt, A.M., Pimienta, I.S.O., Badu, S.R., Solum, M.S., Pugmire, R.J., Facelli, J.C., Locke, D.R., Chapman, K.W., Chupas, P.J., Winans, R.E., 2013. Three-dimensional structure of the Siskin Green River Oil Shale Kerogen Model: a comparison between calculated and observed properties. Energy & Fuels 27, 702–710.

Orloff, J., Swanson, L., Utlaut, M., 2003. High Resolution Focused Ion Beams: FIB and its Applications: Fib and Its Applications: The Physics of Liquid Metal Ion Sources and Ion Optics and Their Application to Focused Ion Beam Technology. Springer Science & Business Media.

Otsu, N., 1979. A threshold selection method from gray-level histograms. IEEE Trans. Syst. Man Cybern. 9, 62–66. doi:citeulike-article-id:1116982

Ozerov, I.M., Polozov, V.F., 1968. Principles of oil shale commercial classification, in: UN Symp. Dev. Util. Oil Shale Resources, Tallinn.(Preprint).

Pakdel, H., Roy, C., Kalkreuth, W., 1999. Oil production by vacuum pyrolysis of Canadian oil shales and fate of the biological markers. Fuel 78, 365–375.

Pan, X., Sidky, E.Y., Vannier, M., 2009. Why do commercial CT scanners still employ traditional, filtered back-projection for image reconstruction? Inverse Probl. 25, 123009.

Panahi, H., Kobchenko, M., Renard, F., Mazzini, A., Scheibert, J., Dysthe, D.K., Jamtveit, B., Malthe-Sørenssen, A., Meakin, P., 2014. A 4D synchrotron X-ray tomography study of the formation of hydrocarbon migration pathways in heated organic-rich shale. arXiv Prepr. arXiv1401.2448.

Parker, J.C., Zhang, F., 2006. Efficient formulations of heat and mass transfer in oil shale retort models, in: 26th Oil Shale Symposium, Colorado School of Mines, 16–19 October 2006.

Picard, M.D., 1955. Subsurface stratigraphy and lithology of Green River Formation in Uinta Basin, Utah. Am. Assoc. Pet. Geol. Bull. 39, 75–102.

Piri, M., Blunt, M.J., 2005. Three-dimensional mixed-wet random pore-scale network modeling of two-and three-phase flow in porous media. I. Model description. Phys. Rev. E 71, 26301.

Pirrie, D., Butcher, A.R., Power, M.R., Gottlieb, P., Miller, G.L., 2004. Rapid quantitative mineral and phase analysis using automated scanning electron microscopy (QemSCAN); potential applications in forensic geoscience. Geol. Soc. London, Spec. Publ. 232, 123–136.

Pitman, J.K., Pierce, F.W., Grundy, W.D., 1990. Thickness, oil-yield, and kriged resource estimates for the Eocene Green River formation, Piceance Creek basin, Colorado.

Pommer, M., Milliken, K., 2015. Pore types and pore-size distributions across thermal maturity, Eagle Ford Formation, southern Texas. Am. Assoc. Pet. Geol. Bull. 99, 1713–1744.

Probstein, R.F., Hicks, R.E., 2006. Synthetic fuels. Courier Corporation.

Puura, E., 1999. Technogenic minerals in the waste rock heaps of Estonian oil shale mines and their use to predict the environmental impact of the waste. Oil Shale 16, 99–107.

Qian, J., Wang, J., 2006. World oil shale retorting technologies, in: Int. Conf. on Oil Shale: ⌈ Recent Trends in Oil Shale. pp. 7–9.

Qian, J., Wang, J., Li, S., 2008. World's Oil Shale Available Retorting Technologies And The Forecast Of Shale Oil Production. International Society of Offshore and Polar Engineers.

Qing, W., GUOJUN, J., Hongpeng, L., JINGRU, B., Shaohua, L., 2010. Variation of the pore structure during microwave pyrolysis of oil shale. Oil Shale 27, 135–146. doi:10.3176/oil.2010.2.04

Radon, J., 2005. 1.1 über die bestimmung von funktionen durch ihre integralwerte längs gewisser mannigfaltigkeiten. Class. Pap. Mod. diagnostic Radiol. 5, 21.

Raeini, A.Q., Bijeljic, B., Blunt, M.J., 2017. Generalized network modeling: Network extraction as a coarse-scale discretization of the void space of porous media. Phys. Rev. E 96, 13312.

Raja, M.A., Zhao, Y., Zhang, X., Li, C., Zhang, S., 2017. Practices for modeling oil shale pyrolysis and kinetics. Rev. Chem. Eng.

Rajeshwar, K., Nottenburg, R., Dubow, J., 1979. Thermophysical properties of oil shales. J. Mater. Sci. 14, 2025–2052. doi:10.1007/BF00688409

Reyes, F., Lin, Q., Udoudo, O., Dodds, C., Lee, P.D., Neethling, S.J., 2017. Calibrated X-ray micro-tomography for mineral ore quantification. Miner. Eng. 110, 122–130.

Rietveld, H., 1969. A profile refinement method for nuclear and magnetic structures. J. Appl. Crystallogr. 2, 65–71.

Rine, J.M., Smart, E., Dorsey, W., Hooghan, K., Dixon, M., 2013. 12 Comparison of Porosity Distribution within Selected North American Shale Units by SEM Examination of Argon-ion-milled Samples. AAPG Special Volumes.

Roy, C., de Caumia, B., Brouillard, D., Ménard, H., 1985. The pyrolysis under vacuum of aspen poplar. Springer, pp. 237–256.

Ruble, T.E., Lewan, M.D., Philp, R.P., 2001. New insights on the Green River petroleum system in the Uinta basin from hydrous pyrolysis experiments. Am. Assoc. Pet. Geol. Bull. 85, 1333–1371.

Rühl, C., 2008. BP Statistical Review of World Energy, June 2008. London BP.

Saif, T., Lin, Q., Bijeljic, B., Blunt, M.J., 2017a. Microstructural imaging and characterization of oil shale before and after pyrolysis. Fuel 197, 562–574.

Saif, T., Lin, Q., Butcher, A.R., Bijeljic, B., Blunt, M.J., 2017b. Multi-scale multi-dimensional microstructure imaging of oil shale pyrolysis using X-ray micro-tomography, automated ultra-high resolution SEM, MAPS Mineralogy and FIB-SEM. Appl. Energy 202, 628–647.

Saif, T., Lin, Q., Singh, K., Bijeljic, B., Blunt, M.J., 2016. Dynamic Imaging of Oil Shale Pyrolysis using Synchrotron X-ray Micro-tomography. Geophys. Res. Lett. doi:10.1002/2016GL069279

Schiffbauer, J.D., Xiao, S., 2009. Novel application of focused ion beam electron microscopy (FIB-EM) in preparation and analysis of microfossil ultrastructures: A new view of complexity in early Eukaryotic organisms. Palaios 24, 616–626.

Schlatter, L.E., 1968. Definition, Formation and Classification of Oil Shale, in: Preprint, United Nations Symposium on the Development and Utilization of Oil Shale Resources, Tallinn.

Scholten, J.J.F., 1967. Mercury porosimetry and allied techniques, in: Porous Carbon Solids. Academic Press New York, pp. 225–250.

Schrodt, J.T., Ocampo, A., 1984. Variations in the pore structure of oil shales during retorting and combustion. Fuel 63, 1523–1527.

Scouten, C.S., 1990. Oil Shale. Fuel Sci. Technol. Handb.

Seewald, J.S., 2003. Organic-inorganic interactions in petroleum-producing sedimentary basins. Nature 426, 327.

Seliger, R.L., Fleming, W.P., 1974. Focused ion beams in microfabrication. J. Appl. Phys. 45, 1416–1422.

Sheppard, A.P., Sok, R.M., Averdunk, H., 2004. Techniques for image enhancement and segmentation of tomographic images of porous materials. Phys. A Stat. Mech. its Appl. 339, 145–151.

Shuzhao, C., Liwen, G., Cangyan, X., Haijun, W., 2011. Utilization of oil shale retorting technology and underground overview, in: Computer Distributed Control and Intelligent Environmental Monitoring (CDCIEM), 2011 International Conference on. IEEE, pp. 2400–2403.

Singh, K., Bijeljic, B., Blunt, M.J., 2016. Imaging of oil layers, curvature and contact angle in a mixed-wet and a water-wet carbonate rock. Water Resour. Res. doi:10.1002/2015WR018072

Siramard, S., Lin, L., Zhang, C., Lai, D., Cheng, S., Xu, G., 2016. Oil shale pyrolysis in indirectly heated fixed bed with internals under reduced pressure. Fuel Process. Technol. 148, 248–255.

Siskin, M., Katritzky, A.R., 1995. Aqueous organic chemistry: Geochemical aspects, in: Composition, Geochemistry and Conversion of Oil Shales. Springer, pp. 313–327.

Sivel, V.G.M., Van den Brand, J., Wang, W.R., Mohdadi, H., Tichelaar, F.D., Alkemade, P.F.A., Zandbergen, H.W., 2004. Application of the dual-beam FIB/SEM to metals research. J. Microsc. 214, 237–245.

Sohns, H.W., Long, A., 1975. In situ oil shale proceeding research. NSF (RANN)-75-001 8, 35.

Solum, M.S., Mayne, C.L., Orendt, A.M., Pugmire, R.J., Adams, J., Fletcher, T.H., 2014. Characterization of Macromolecular Structure Elements from a Green River Oil Shale, I. Extracts. Energy & Fuels 28, 453–465. doi:10.1021/ef401918u

Sondergeld, C.H., Ambrose, R.J., Rai, C.S., Moncrieff, J., 2010. Micro-structural studies of gas shales, in: SPE Unconventional Gas Conference. Society of Petroleum Engineers, p. 17. doi:10.2118/131771-MS

Sonka, M., Hlavac, V., Boyle, R., 2014. Image processing, analysis, and machine vision. Cengage Learning.

Speight, J.G., 2014. The chemistry and technology of petroleum. CRC press.

Speight, J.G., 2012a. Shale oil production processes. Gulf Professional Publishing.

Speight, J.G., 2012b. Origin and Properties of Oil Shale, Shale Oil Production Processes. doi:10.1016/B978-0-12-401721-4.00001-1

Stanfield, K.E., Frost, I.C., 1949. Method of Assaying Oil Shale by a Modified Fischer Retort: Revision of RI 3977. United States. Bureau of Mines.

Stauber, M., Müller, R., 2008. Micro-computed tomography: a method for the non-destructive evaluation of the three-dimensional structure of biological specimens. Osteoporos. Methods Protoc. 273–292.

Stock, S.R., 1999. X-ray microtomography of materials. Int. Mater. Rev. 44, 141–164.

Strizhakova, Y. a., Usova, T. V., 2008. Current trends in the pyrolysis of oil shale: A review. Solid Fuel Chem. 42, 197–201. doi:10.3103/S0361521908040022

Sugiyama, M., Sigesato, G., 2004. A review of focused ion beam technology and its applications in transmission electron microscopy. J. Electron Microsc. (Tokyo). 53, 527–536.

Sun, B.Z., Wang, Q., Li, S.H., Wang, H.G., 2008. Analysis of specific area and porous structure of oil shale and semi-coke. J. Power Eng. 28, 163–167.

Sun, C.L., 2006. The influential factor of pyrolysis of oil shale. Process. Util. Coal 1, 37–38.

Surdam, R.C., Stanley, K.O., 1979. Lacustrine sedimentation during the culminating phase of Eocene lake Gosiute, Wyoming (Green River Formation). Geol. Soc. Am. Bull. 90, 93–110.

Taylor, A.W., Ritts, B.D., 2004. Mesoscale Heterogeneity of Fluvial Lacustrine Reservoir Analogues: Examples from the Eocene Green River and Colton Formations, Uinta Basin, Utah, USA. J. Pet. Geol. 27, 3–25.

Tisot, P.R., 1962. Properties of Green River Oil Shale Determined from Nitrogen Adsorption and Desorption Isotherms. J. Chem. Eng. Data 7, 405–410.

Tissot, B., Welte, D.H., 1978. Petroleum occurrence and formation.

Tiwari, P., Deo, M., 2012. Compositional and kinetic analysis of oil shale pyrolysis using TGA – MS. Fuel 94, 333–341. doi:10.1016/j.fuel.2011.09.018

Tiwari, P., Deo, M., Lin, C.L., Miller, J.D., 2013. Characterization of oil shale pore structure before and after pyrolysis by using X-ray micro CT. Fuel 107, 547–554. doi:10.1016/j.fuel.2013.01.006

Tomutsa, L., Silin, D.B., Radmilovic, V., 2007. Analysis of chalk petrophysical properties by means of submicron-scale pore imaging and modeling. SPE Reserv. Eval. Eng. 10, 285–293.

Tong, J., Han, X., Wang, S., Jiang, X., 2011. Evaluation of structural characteristics of Huadian oil shale kerogen using direct techniques (solid-state 13C NMR, XPS, FT-IR, and XRD). Energy & fuels 25, 4006–4013.

Tovey, N.K., Wang, J., 1997. An Automatic Image Acquisition and Analysis System for a Scanning Electron Microscope. Scanning Microsc. 11, 211–227.

Tyson, R. V, 1995. Origin and Nature of the Amorphous Group, in: Sedimentary Organic Matter. Springer, pp. 169–180.

Valvatne, P.H., Blunt, M.J., 2004. Predictive pore-scale modeling of two-phase flow in mixed wet media. Water Resour. Res. 40.

Van Brakel, J., Modrý, S., Svata, M., 1981. Mercury porosimetry: state of the art. Powder Technol. 29, 1–12.

Van Den Berg, M.L.J., 1975. Some investigations on the chemical nature of kerogen.

Van Krevelen, D.W., 1950. Graphical-statistical method for the study of structure and reaction processes of coal. Fuel 29, 269–284.

Vandenbroucke, M., 2003. Kerogen: from Types to Models of Chemical Structure. Oil Gas Sci. Technol. 58, 243–269. doi:10.2516/ogst:2003016

Vandenbroucke, M., Largeau, C., 2007. Kerogen origin, evolution and structure. Org. Geochem. 38, 719–833.

Vitorovic, D., 1980. Structure elucidation of kerogen by chemical methods. Kerogen. Ed. Tech. Paris 301–338.

Vlassenbroeck, J., Dierick, M., Masschaele, B., Cnudde, V., Van Hoorebeke, L., Jacobs, P., 2007. Software tools for quantification of X-ray microtomography at the UGCT. Nucl. Instruments Methods Phys. Res. Sect. A Accel. Spectrometers, Detect. Assoc. Equip. 580, 442–445.

Wallman, P.H., Tamm, P.W., Spars, B.G., 1981. Oil shale retorting kinetics. ACS Publications.

Wang, D., Xu, Y., He, D., Guan, J., Zhang, O., 2009. Investigation of mineral composition of oil shale. Asia-Pacific J. Chem. Eng. 4, 691–697.

Wang, J., Liang, J., 2010. The influence of temperature on rapid pyrolysis feature. Coal Transform. 33, 66–69.

Wang, P., Jiang, Z., Ji, W., Zhang, C., Yuan, Y., Chen, L., Yin, L., 2016. Heterogeneity of intergranular, intraparticle and organic pores in Longmaxi shale in Sichuan Basin, South China: Evidence from SEM digital images and fractal and multifractal geometries. Mar. Pet. Geol. 72, 122–138.

Wang, Q., Ye, J., Yang, H., Liu, Q., 2016. Chemical Composition and Structural Characteristics of Oil Shales and Their Kerogens Using Fourier Transform Infrared (FTIR) Spectroscopy and Solid-State 13C Nuclear Magnetic Resonance (NMR). Energy & Fuels 30, 6271–6280.

Wang, Q., Zhao, W., Liu, H., Jia, C., Li, S., 2011. Interactions and kinetic analysis of oil shale semi-coke with cornstalk during co-combustion. Appl. Energy 88, 2080–2087.

Wang, W., Li, S., Li, L., Ma, Y., Yue, C., He, J., 2014. Pyrolysis characteristics of a North Korean oil shale. Pet. Sci. 11, 432–438. doi:10.1007/s12182-014-0358-x

Washburn, E.W., 1921. The dynamics of capillary flow. Phys. Rev. 17, 273.

Wildenschild, D., Sheppard, A.P., 2013. X-ray imaging and analysis techniques for quantifying pore-scale structure and processes in subsurface porous medium systems. Adv. Water Resour. 51, 217–246. doi:10.1016/j.advwatres.2012.07.018

Williams, P.T., Ahmad, N., 2000. Investigation of oil-shale pyrolysis processing conditions using thermogravimetric analysis. Appl. Energy 66, 113–133.

Williams, P.T., Ahmad, N., 1999. Influence of process conditions on the pyrolysis of Pakistani oil shales. Fuel 78, 653–662. doi:10.1016/S0016-2361(98)00190-2

Winick, H., 1995. Synchrotron Radiation Sources—A Primer. World Scientific.

Winter, D.A., DE, M., Schneijdenberg, C., Lebbink, M.N., Lich, B., Verkleij, A.J., Drury, M.R., Humbel, B.M., 2009. Tomography of insulating biological and geological materials using focused ion beam (FIB) sectioning and low-kV BSE imaging. J. Microsc. 233, 372–383.

Wirth, R., 2009. Focused Ion Beam (FIB) combined with SEM and TEM: Advanced analytical tools for studies of chemical composition, microstructure and crystal structure in geomaterials on a nanometre scale. Chem. Geol. 261, 217–229.

Wirth, R., 2004. Focused Ion Beam (FIB). Eur. J. Mineral. 16, 863–876.

y Leon, C.A.L., 1998. New perspectives in mercury porosimetry. Adv. Colloid Interface Sci. 76, 341–372.

Yen, T.F., 1976. Structural aspects of organic components in oil shales. Dev. Pet. Sci. 5, 129–148.

Yu, H.L., Jiang, X.M., 2007. The influence of particle size on retorting and dynamics parameter of oil shale. Acad. J. Zhongyuan Eng. Coll. 18, 1–4.

Zou, C., 2017. Unconventional petroleum geology. Elsevier.